University of Bath

UNIVERSITY OF BATH

PHD

VHF radar studies of mesosphere and thermosphere

Beldon, Charlie

Award date:
2008

Awarding institution:
University of Bath

[Link to publication](#)

VHF RADAR STUDIES OF THE MESOSPHERE & THERMOSPHERE

Charlotte L Beldon

A thesis submitted for the degree of Doctor of Philosophy
University of Bath
Department of Electronic and Electrical Engineering

2008

COPYRIGHT

_____
Charlotte L Beldon

Abstract

The dynamics of the Mesosphere and Lower Thermosphere (MLT) at polar and middle latitudes are investigated using VHF meteor radars. High-frequency gravity-wave activity and momentum fluxes are examined using Skiymet meteor radars based at Esrange, in Arctic Sweden (68°N, 21°E) and Rothera, Antarctica (68°S, 68°W). The 8-hour tide is investigated at middle latitudes using a meteor radar based in Castle Eaton, UK (52°N, 2°W).

A novel technique for studying high-frequency gravity-waves with meteor radar is developed and applied to data from the radars at Rothera and Esrange. This technique is used to investigate the activity of gravity-waves with periods between about 5 minutes and 2 hours and horizontal scales less than about 400 km. A strong semi-annual cycle is revealed with solsticial peaks and equinocial minima. This behaviour is explained in terms of the critical-level filtering imposed by the stratospheric winds. Strong inter-hemispheric differences are also revealed. The theory is advanced that this is the result of the smaller winds speeds in the northern hemisphere in spring (due to the more rapid break-up of the stratospheric vortex).

Variances calculated using this new technique are used to investigate interactions between the high-frequency gravity-wave field and tides and planetary-waves. Clear modulations of the gravity-wave field at tidal and planetary-wave frequencies are shown and reveal a relationship between the phase of the tide and the maxima in gravity-wave activity. It is proposed that the likely mechanism for this modulation is critical-level filtering by the tidal winds, acting on an anisotropic gravity-wave field.

Zonal and meridional variances and momentum fluxes are calculated using data from the radars at Rothera and Esrange. Monthly-mean variances confirm the semi-annual seasonal cycle and reveal higher meridional activity over Rothera, particularly in summer. Again this is explained in terms of interactions with the mean winds as the waves ascend to the MLT. Zonal and meridional momentum fluxes reveal a somewhat more variable seasonal cycle, which is clearer over Rothera and indicates that at heights of about 90 km and below, momentum flux has a north-west direction in winter and south-east in summer.

Data from the radar based at Castle Eaton is used to demonstrate that the 8-hour tide is of significant amplitude in both the mid-latitude and polar MLT. Climatologies reveal a seasonal cycle with a maxima in amplitude in autumn and a secondary maxima in winter. An interesting result is that the seasonal behaviour varies with latitude and the secondary winter-time maximum seen over the UK is not present in the Arctic. Analysis of hourly-mean amplitudes reveal possible interactions between the 8-hour tide, the 12- and 24-hour tides and planetary waves. An analysis based the 17 years of available data indicates a weak relationship between solar activity and the 8-hour tide. Tidal amplitudes tend to increase while phase tends to decrease as solar activity increases.

Acknowledgements

I would like to thank my family for all the support they have given me and for all they have had to put up with! I want to thank all my friends and labmates, particularly Pete Younger for never refusing to answer my questions, Dave Sandford for sharing the highs and lows of a PhD with me and Matt Foster for not giving up on me even through all the moaning.

Finally, I would like to thank Nick Mitchell, my supervisor for his support during this project and for pointing out all the incorrectly hyphenated words!

Contents

List of Figures

List of Tables

List of Acronyms

CIRA COSPAR International Reference Atmosphere

FCA Full Correlation Analysis

GSWM Global Scale Wave Model

HRDI High Resolution Doppler Imager

IDI Imaging Doppler Interferometer

IS Incoherent Scatter

LOS Line Of Sight

MF Medium Frequency

MLT Mesosphere and Lower Thermosphere

MST Mesosphere-Stratosphere-Troposphere

NLC Noctilucent Clouds

PMSE Polar Mesospheric Summer Echoes

QBO Quasi-Biannual Oscillation

ROSE Research for Ozone in the Stratosphere and its Evolution

SOR Starfire Optical Range

UARS Upper Atmosphere Research Satellite

URAP UARS Reference Atmosphere Project

VHF Very High Frequency

List of Symbols

z	Height
g	Acceleration due to gravity
H	Scale height
m	Vertical wavenumber
k	Zonal wavenumber
l	Meridional wavenumber
$\overline{u(z)}$	Mean winds at a height, z
C	Speed of sound
c	Phase speed of a wave with respect to the ground
$\hat{c}$	Intrinsic phase speed
N	Brunt-Väisälä frequency
ω	frequency
f	Coriolis force
R_i	Richardson number
λ	Wavelength
α	Angle between the vector between a line drawn between a meteor and the ground and a line drawn between the meteor and the radar, see Figure 2.17
u'^2	Zonal gravity-wave variance
v'^2	Meridional gravity-wave variance
$u'w'$	Zonal component of vertical momentum flux
$v'w'$	Meridional component of vertical momentum flux

Chapter 1

An Introduction to the Mesosphere and Lower Thermosphere

1.1 Introduction

The Mesosphere and Lower Thermosphere (MLT) is the region of the Earth's atmosphere at heights between about 50 and 120 km. It is bounded below by the stratopause and above by the mesopause. The MLT is a region where processes crucial for linking the different layers of the atmosphere occur. However, it is only in recent decades that continuous and reliable observations have been made. This lack of observations is due, in part, to the difficulty of obtaining *in situ* measurements at these heights. The air is too dense for satellite flight, yet it is too tenuous for aircraft or balloons. Although *in situ* measurements can be made with rocket-borne equipment, they are costly and only provide snapshots as the rocket passes through the region. However, ground based radars can provide reliable and continuous observations of the MLT region.

At MLT heights, there is a 'zoo' of different waves and tides propagating through the atmosphere. They play a vital role in the energetics and dynamics of the region. Waves excited in the lower atmosphere propagate upwards, traversing different regions of the atmosphere and propagating into progressively less dense layers. Wave amplitudes grow with the decreasing air density if the waves conserve energy per unit mass. Thus, waves with small amplitudes in their source regions can grow to very large amplitudes in the MLT. Strong non-linear interactions can occur between these large amplitude waves, tides and mean winds. These interactions result in a strongly coupled system which can in turn influence the propagation characteristics of the MLT and so influence the coupling of the lower, middle and upper parts of the atmosphere.

The large amplitude of the waves in the MLT promotes various forms of instability, causing some waves to 'break'. This transfers energy and momentum carried by the waves into the mean flow. This momentum drives the planetary-scale circulation of the middle atmosphere away from the

circulation predicted from pure radiative equilibrium.

The MLT region is increasingly believed to be a sensitive indicator of climate change (e.g. *Thomas*, 1996). Increasing carbon dioxide levels that have a small warming effect at ground level will have a much larger cooling effect in the mesosphere. Modelling studies suggest that a doubling in atmospheric CO_2 will result in a warming at sea level of 1 - 3 K, but a corresponding cooling at stratospheric heights of $\sim$ 14 K and a cooling of $\sim$ 8 K in the upper mesosphere (e.g., *Akmaev and Fomichev*, 1998). Understanding this region is therefore important, not only in understanding the behaviour of the atmosphere as a whole, but also in quantifying changes in the Earth's climate.

This Chapter will give an introduction to the MLT region. The structure of the atmosphere and the dynamics of the MLT region will be discussed in Section 1.2. Section 1.3 will discuss some of the waves and tides observed in the MLT. Section 1.4 will discuss some of the phenomena occurring in the polar atmosphere. Finally, Section 1.5 will describe the scope of this thesis and publications resulting from this work.

1.2 Dynamics of the Mesosphere and Thermosphere

The Earth's atmosphere can be separated into distinct layers defined by the temperature gradient within each layer. Figure 1.1 presents a vertical temperature profile of the Earth's atmosphere from the ground to 120 km in January at UK latitudes. The data is taken from COSPAR International Reference Atmosphere (CIRA)-86 model (*Flemming et al.*, 1988).

1.2.1 The Predictions of Radiative Equilibrium

To understand the behaviour of the MLT region it is important to understand the atmosphere as it would be, were it in *radiative equilibrium*. For an atmosphere to be in radiative equilibrium there is no net radiative heating or cooling at any point. Thus, the temperature everywhere assumes a steady state. In the case of the Earth's atmosphere, the radiative transfer is dominated by the heating and cooling of carbon dioxide, water vapour, molecular oxygen and ozone. These chemical species are concentrated at different heights in the atmosphere and so absorb and radiate most energy at these heights. Figure 1.2 shows the heating and cooling rates for the dominant species, in units of Kelvin per day.

In the MLT the dominant cooling comes from carbon dioxide and ozone. Note the peak in both heating and cooling rates that occurs at 50 km, highlighting the importance of ozone in heating and carbon dioxide in cooling the atmosphere. Using the heating rates from Figure 1.2
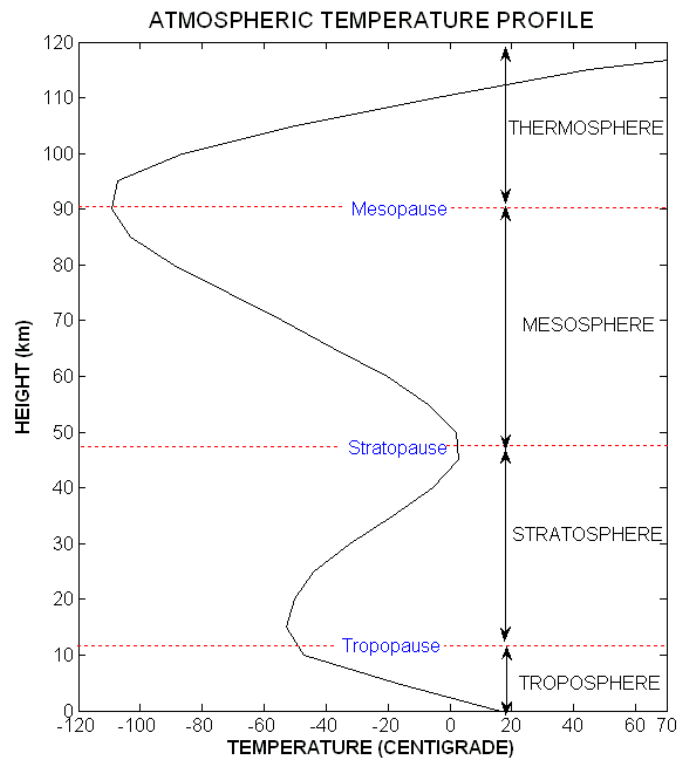
Figure 1.1: Temperature profile of the Earth's atmosphere from CIRA-86 for January conditions.
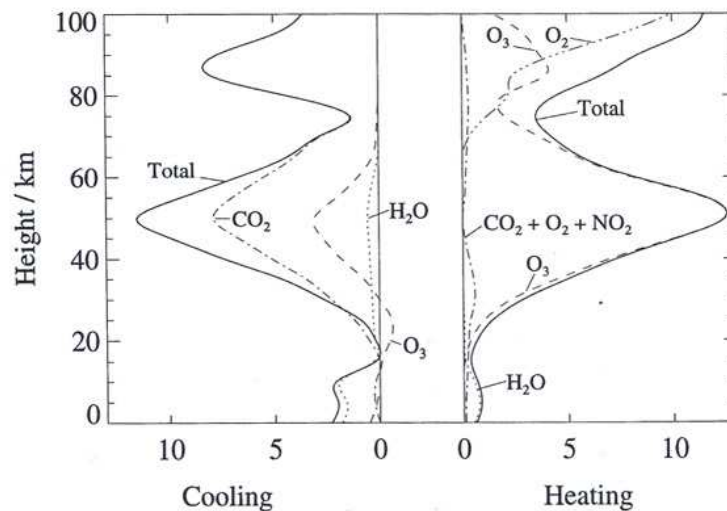
Figure 1.2: Heating and cooling rates (Kelvin per day) of chemical species in the Earth's atmosphere, after *London* (1980).

the temperature structure of the atmosphere in radiative equilibrium can be calculated. Figure 1.3 shows the zonally-averaged latitudinal temperature structure of the atmosphere calculated using only these heating and cooling rates under solstice conditions. After *Geller* (1983).

It is obvious from the figure that the temperature gradient in the stratosphere and mesosphere
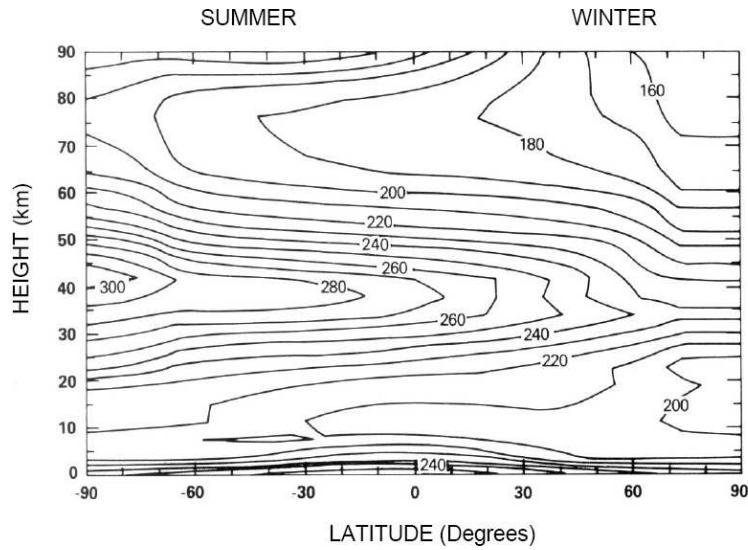
Figure 1.3: Temperatures calculated solely using radiative equilibrium, units are Kelvin, after *Geller* (1983).

is from a warm summer pole to a cold winter pole. This is a product of the heating in summer when the polar region is in continual sunlight and the absence of heating during winter when the polar region is in continual darkness.

The maximum temperatures occur at the stratopause. These reach $\sim$ 300 K at the summer pole and $\sim$ 220 K at the winter pole. This reflects the higher concentrations of ozone at these heights. The minimum temperature of $\sim$ 160 K occurs at the mesopause over the winter pole.

This temperature structure results in a steady-state planetary-scale circulation in the atmosphere as described by the thermal wind equation. Figure 1.4 shows the forces acing on an air parcel in these conditions and the resulting motion.
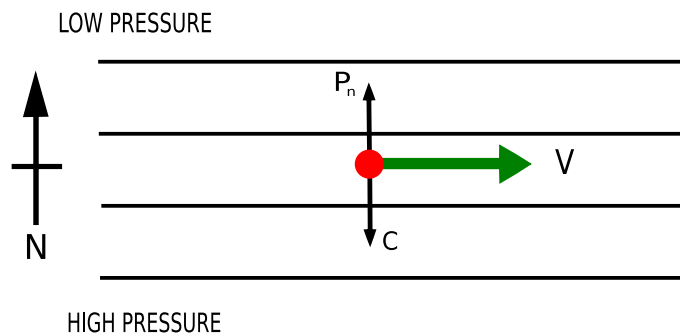
Figure 1.4: The forces required to generate geostrophic flow for northern hemisphere winter. P_n is the pressure gradient force, C is the Coriolis force and V is the resulting direction of motion. The parallel, horizontal lines represent isobars.

An air parcel will be acted upon by the pressure gradient force (P_n) as shown in Figure 1.4. This force is created by the unequal heating (strong at the summer pole, none at the winter pole) and acts to push the air parcel from the summer to winter pole, from high to low pressure.

The air parcel is also acted upon by the *Coriolis force*, acting at right angles to the direction of the air parcels motion. The Coriolis and pressure gradient forces balance each other and a *geostrophic* wind is formed. This flows parallel to the isobars, in an eastward direction in the winter hemisphere and a westward direction in the summer hemisphere.

The resulting winds are presented in Figure 1.5. Note that equatorial and tropical winds cannot be determined from the thermal wind equation due to the near zero Coriolis force close to the equator. There are also no meridional or vertical winds predicted.
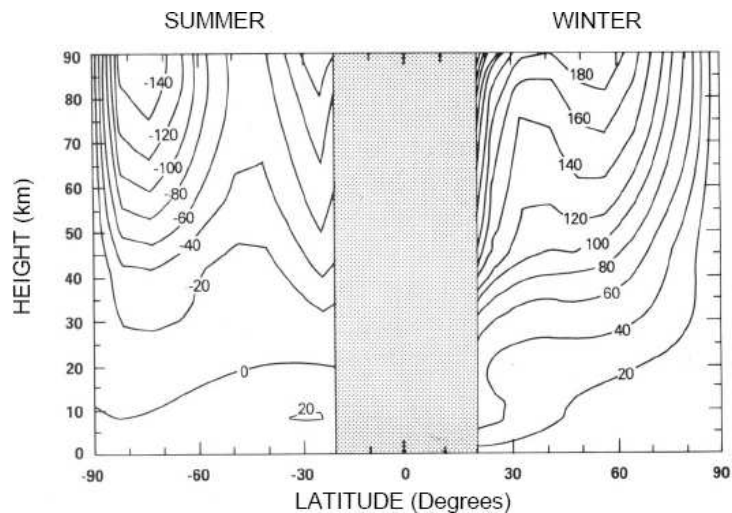
Figure 1.5: The zonal mean geostrophic winds predicted by radiative equilibrium. Positive wind values represent eastward winds, negative values represent westward winds. After *Geller* (1983).

Several things are immediately noticeable about the winds presented in Figure 1.5. These are:

1. There are strong zonal winds that increase with height in both hemispheres.

2. In the winter hemisphere there is an eastward jet centered near a latitude of 50°.

3. In the summer hemisphere there is westward jet centred near a latitude of -75°.

1.2.2 The Observed Circulation

The observed global temperatures and wind structure of the atmosphere differ greatly from those predicted by radiative equilibrium. Figure 1.6 presents the more realistic temperatures taken from the empirical CIRA-86 model for solstice conditions (*Flemming et al.*, 1988).

When compared to Figure 1.3, several differences are immediately obvious. These are:

1. Above heights of $\sim$ 60 km, the summer pole is no longer warmer than the winter pole. In
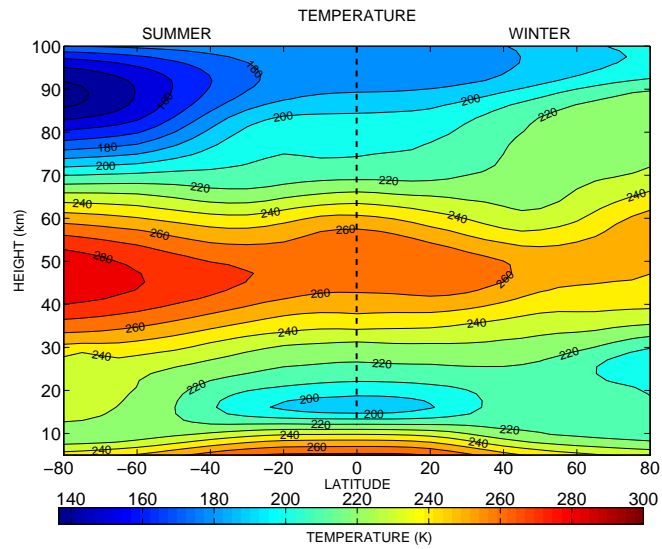
Figure 1.6: Zonally averaged temperatures predicted by the CIRA-86 model for solstice conditions

fact, above ~ 80 km the summer pole is *cooler* than the winter pole - a counter intuitive result since the summer pole is in continuous sunlight and the winter pole is in continuous darkness.

2. The tropospause temperatures show a minimum at the equator, differing from the predictions of radiative equilibrium where there is a gradual increase in temperature from the winter to summer pole.
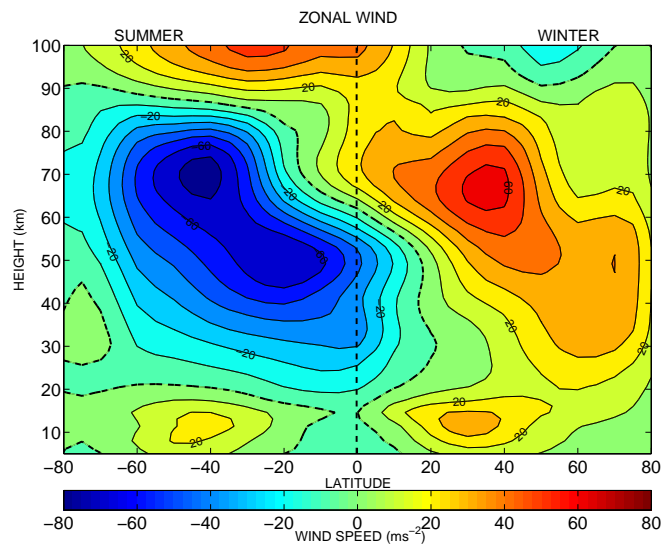
Figure 1.7: Zonal winds predicted by the CIRA-86 model for solstice conditions

There are also striking differences in the wind structure of the real atmosphere compared to that predicted by radiative equilibrium. Figure 1.7 presents the zonal winds taken from the CIRA-86 model for solstice conditions. The most notable differences are:

1. There are two pairs of jets evident at heights below ~ 90 km. The first pair are in the upper troposphere and lower stratosphere. They are both eastward. The second pair are in the stratosphere and mesosphere. They are directed westward in summer and eastward in winter.

2. In the radiative equilibrium model the strength of the winds increases with height. However, at heights near 90 km the observed strength of the winds reduces and the winds reverse.

To explain these differences we must consider the effect of dynamic forcing of the atmosphere by waves. In particular, we must consider the effect of energy and momentum deposited by breaking and dissipating waves.

1.2.3 Wave Drag Acting on the Middle Atmosphere

A 'frictional' force acting to slow the zonal winds would force the radiative equilibrium winds to more realistic speeds. This additional force would act on an air parcel in addition to the pressure gradient and Coriolis forces shown in Figure 1.4. This frictional force is believed to be *wave drag* and is thought to be caused by the dissipation or breaking of waves that ascend from the lower atmosphere.

The addition of wave drag to a radiative equilibrium model can replicate the observed cold summer mesopause as well as the reduction and reversal of the zonal winds. This additional force requires a rebalancing of the forces shown in Figure 1.4. The new balance is shown in Figure 1.8.
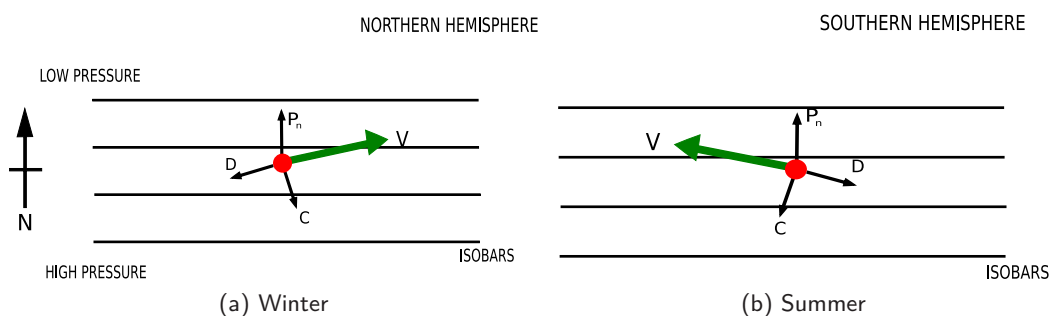
Figure 1.8: Forces acting on an air parcel in (a) the northern hemisphere (winter) and (b) the southern hemisphere (summer) when wave drag is considered. Here P_n is the pressure gradient force, C is the Coriolis force, D is the drag force and V is the resultant air parcel velocity. D and C act at right right angles to each other. The parallel lines represent isobars.

Note that when the effect of wave drag is considered, the resultant flow is no longer parallel to the isobars. The Coriolis force, C, and the drag force, D, combined, balance the pressure gradient force, P_n, so that $P_n = C + D$. The new balance of forces has produced an air parcel velocity that crosses isobars, producing a meridional flow. In *both* the summer (southern) and

winter (northern) hemispheres the flow is towards the winter (northern) pole. As a consequence there is a direct cross-equator meridional flow.

This meridional flow is vital in explaining why the predictions of radiative equilibrium do not match observations. The meridional flow is directed towards the winter pole in both hemispheres, resulting in a convergence of air on the winter pole. There is a corresponding divergence of flow over the summer pole. This means, by continuity that there must be vertical flows to replace the air lost at the summer pole and remove the air from the winter pole. An upwelling occurs at the summer pole, drawing air upwards from lower down in the atmosphere. This upwelling air cools adiabatically producing the observed *colder* temperatures at the summer mesopause. At the winter pole a downwelling occurs and air is heated adiabatically and produces *warmer* temperatures in the winter mesopause. The magnitude of the vertical winds are on the order of less than 1 cms^{-1} and can be inferred from the adiabatic heating and cooling they induce. This circulation is known as the *Dobson-Brewer* circulation and is illustrated in Figure 1.9.
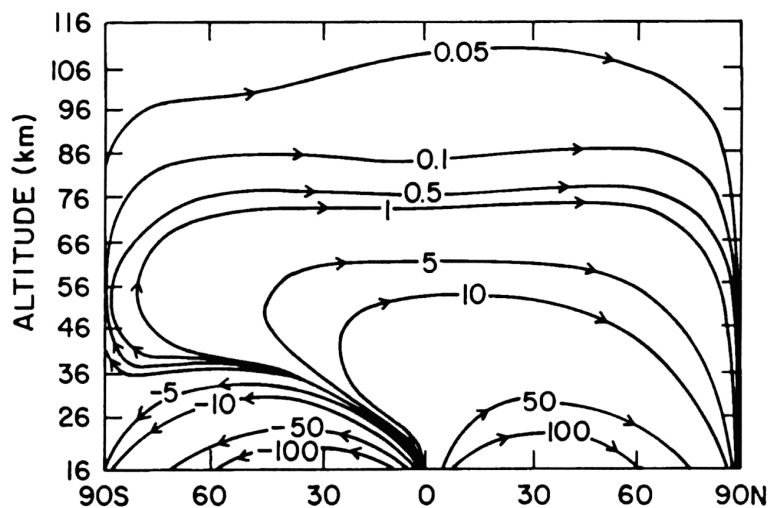
Figure 1.9: Calculated mass meridional stream function in units of kgm^{-1}s^{-1} during the Northern Hemisphere winter solstice. After *Garcia and Solomon* (1983).This is the Dobson-Brewer Circulation.

The reversal in the pole-to-pole temperature gradient in the mesosphere and lower thermosphere in turn influences the zonal winds through the thermal wind equation. This results in a eastward summer jet and a westward winter jet at mid-latitudes. It also leads to the strength of the zonal jets decreasing with height as the frictional force acts against the wind motion. At a height of about 90 km the winds reverse, closing off the mesospheric jets.

1.3 A Zoo of Waves

The Earth's atmosphere supports a large number of wave phenomena. MLT dynamics are dominated by large scale waves and tides, the largest amplitude of which are gravity waves, tides and planetary waves. Waves can reach very large amplitude in the MLT because as the waves

propagate upwards they grow in amplitude with height. This is a consequence of the decreasing air density and means that waves with small amplitudes in the lower atmosphere grow to have large amplitudes in the MLT. This is explained in more detail below.

Atmospheric density ρ, decreases exponentially with increasing height, z, as can be seen in equation 1.1.

$$\rho = \rho_0 \exp \frac{-z}{H} \tag{1.1}$$

The rate of decrease is determined by H, the scale height, defined as:

$$H = \frac{kT}{mg} \tag{1.2}$$

Where k is Boltzmann's constant, T is the temperature, m is mean molecular mass and g is acceleration due to gravity.

For waves ascending through the atmosphere, in the absence of dissipative effects, kinetic energy per unit volume is conserved. So as ρ decreases, A, the amplitude of the wave must increase to conserve energy per unit volume E, where $E = \frac{1}{2}\rho A^2$. Therefore, the amplitude of the wave grows exponentially to compensate for the decreasing density. This is described in equation 1.3.

$$A = A_0 \exp \frac{z}{H}, \tag{1.3}$$

where A_0 is the amplitude at a given height, z_0. Through this process, waves that have amplitudes of a few centimeters in the lower atmosphere can grow to significant amplitude in the MLT.

1.3.1 Gravity Waves

Gravity waves are some of the most important waves in the atmosphere. They occur in stably stratified fluids where the restoring force for the wave motion is buoyancy. They also occur in planetary atmospheres, stellar interiors and in the oceans.

Gravity waves play an important role in the dynamics of the middle atmosphere. Because of the growth of wave amplitude with height, gravity waves can reach large amplitudes in the MLT. The waves can then become unstable and break, depositing energy and momentum into the atmosphere. This transports energy away from the gravity-wave source regions into the MLT so coupling together different layers of the atmosphere (e.g., *Fritts and Alexander*, 2003).

Gravity waves are meso-scale waves with periods ranging between $\sim$ 5 minutes to many hours (from the Brunt-Väisälä frequency to the inertial period). They are mostly generated in the troposphere or lower stratosphere. Sources of gravity waves are varied but the most significant

are thought to be flow over topography, convection, wind shear, unbalanced flows and frontal systems (*Fritts and Alexander*, 2003). Gravity waves can also be generated by mechanisms such as geostrophic adjustment and wave-wave interactions, although these mechanisms remain less well understood.

Gravity waves can be *external* or *internal*. External waves are those trapped to be propagating on a density discontinuity or surface such as an inversion in the atmosphere or, as is the case with ocean waves, the discontinuity between the air and the ocean. Internal waves are not confined to a discontinuity and can propagate throughout the medium.

The presence of gravity waves depends on atmospheric stability. That is, whether the environmental lapse rate is greater or less than the adiabatic lapse rate. To understand why this is the case, consider an air parcel in an atmosphere where the environmental lapse rate is *less stable* than the adiabatic lapse rate, as illustrated in the left hand panel of Figure 1.10. In this case if the air parcel is displaced vertically upwards from a height Z_0 to a height of Z_U it will cool adiabatically from its starting temperature, T_0, to T_U. The air parcel is now at a higher temperature than its surroundings and hence will have a lower relative density. Therefore, it will experience an upwards force and so accelerate upwards. If the air parcel is displaced downwards to a height Z_D, it will have a correspondingly higher density than its surroundings at and will continue to sink. Thus the atmosphere is *unstable* and thus quickly results in convection which acts to remove the super-adiabatic lapse rate and return it to an adiabatic state.
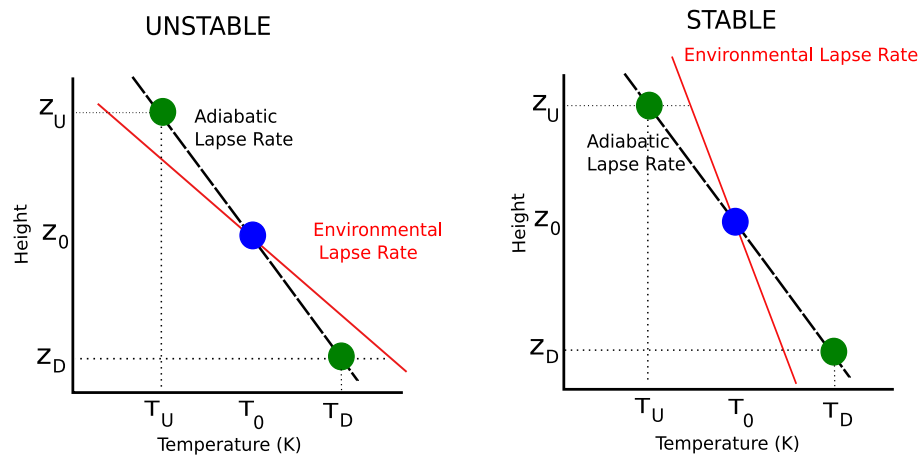
Figure 1.10: Schematic illustration of a vertically displaced air parcel, the dashed line represents the adiabatic lapse rate, the red line is the environmental lapse rate and the dots represent a theoretical air parcel.

Now consider an air parcel in an atmosphere where the environmental lapse rate is *more stable* than the adiabatic lapse rate, as illustrated in the right hand panel of Figure 1.10. In this case, as the air parcel is displaced vertically upwards it will cool adiabatically to a temperature T_U which is lower than the surrounding temperature. Hence it will have a higher relative density and it will experience a downwards force and sink. If the air parcel were to be displaced downwards it would be correspondingly lower density than its surroundings and will experience an upwards force.

Thus the difference between the environmental and adiabatic lapse rates provides a restoring force within the stable atmosphere. The restoring force is proportional to the displacement of the air parcel from its equilibrium position, Z_0. This results in vertical simple harmonic motion of the air parcel about Z_0. The frequency of the simple harmonic motion is determined by the environmental lapse rate and the upper limit to the frequency of an oscillation forced in this manner occurs when the air parcel is oscillating vertically. The frequency of this oscillation is known as the Brunt-Väisälä frequency. In the MLT region the Brunt-Väisälä frequency usually corresponds to a period of oscillation of approximately 5 minutes.

A better understanding of gravity waves can be gained by an examination of the *dispersion relation*. The dispersion relation describes the relationship between the wave frequency and the wave number. It can be derived by considering the following equations for an isothermal, stationary, adiabatic atmosphere (*Hines*, 1960).

The equation of hydrostatic balance:

$$\overline{\rho_0}\frac{\partial \mathbf{u}}{\partial t} = \rho' - \nabla\, p', \tag{1.4}$$

the equation of state:

$$\frac{\partial p'}{\partial t} + \mathbf{u}\,\nabla p_0 = C^2\left(\frac{\partial \rho'}{\partial t} + \mathbf{u}\,\nabla\rho_0\right), \tag{1.5}$$

and the equation of continuity:

$$\frac{\partial \rho'}{\partial t} + \mathbf{u}\,\nabla\rho_0 + \rho_0\,\mathrm{div}\,\mathbf{u} = 0. \tag{1.6}$$

Where ∇ is the grad operator, p_0 is the pressure of an unperturbed atmosphere, p' is a pressure perturbation and $p = p_0 + p'$. Similarly, ρ_0 is the unperturbed density, ρ' is the density perturbation and $\rho = \rho_0 + \rho'$. The steady state atmospheric velocity is 0 and $\mathbf{u}$ is the velocity perturbation vector, c is the speed of sound, where $C^2 = \gamma p_0/\rho_0$ and γ is the ratio of specific heats (C_p/C_v).

The wave solution of these equations gives the dispersion relation, equation 1.7 for gravity waves.

$$\omega^4 - \omega^2 C^2(k^2 + m^2) + (\gamma - 1)g^2 k^2 + i\gamma g \omega^2 m = 0, \tag{1.7}$$

where ω is the frequency, k is the zonal wavenumber, m is the vertical wavenumber, C is the speed of sound and g is the acceleration due to gravity.

Considering a zonally propagating wave, for it to propagate the vertical wavenumber, m, must be real. If m is purely imaginary, the wave is vertically evanescent and cannot propagate vertically. This describes an external wave propagating along a discontinuity such as an ocean surface wave. If m is complex or real, the resulting waves are internal and capable of vertical propagation. Forcing m to be complex and substituting back into the dispersion relation gives the dispersion

relation for internal gravity-waves shown below:

$$\omega^4 - \omega^2 C^2 (k^2 + m^2) + (\gamma - 1)g^2 k^2 - \frac{\gamma g^2 \omega^2}{4C^2} = 0. \tag{1.8}$$

This yields two solutions for ω^2 for any pair of real k and m. The first solution allows waves to exist at frequencies above ω_a, the *acoustic cut-off frequency*, where,

$$\omega_a = \frac{\gamma g}{2C}. \tag{1.9}$$

These are acoustic waves, longitudinal waves whose restoring force is pressure. They propagate in the same direction as the group and energy flow. Throughout the middle atmosphere ω_a, corresponds to a period of ~ 4.4 minutes.

The second solution allows waves to exist at frequencies below N, the Brunt-Väisälä frequency, where

$$N = \frac{(\gamma - 1)^{1/2} g}{c}. \tag{1.10}$$

Waves that exist at or below the Brunt-Väisälä frequency are called *gravity waves*, they are transverse waves with a restoring force of bouyancy. The Brunt-Väisälä frequency is the natural oscillation frequency of an air parcel if displaced vertically and released. Thus, for or waves with frequencies close to N the motions are mostly vertical. If the parcel is displaced at an angle to the vertical, it will oscillate at a lower frequency which is related to the angle of displacement. Throughout the middle atmosphere the Brunt-Väisälä frequency corresponds to a period of $\sim$ 5 minutes.

There is a lower limit of the frequency of gravity waves called the *inertial frequency* f (also known as the Coriolis parameter). This is defined by $f = 2\Omega sin\phi$ where Ω is the angular velocity of the Earth, ϕ is the latitude. The inertial frequency corresponds to a period of $\sim$ 12 hours at the poles to infinity at the equator.

Waves at the limiting inertial frequency, are called *inertial waves*. Below this frequency, the Coriolis force disrupts the motion. For inertia-gravity waves the horizontal wavelengths are usually much larger than the vertical wavelength. The motion of an air parcel disturbed by the wave is mostly horizontal and the transverse Coriolis forces are significant. Thus the Coriolis force plays a significant role in the motion of the air parcel. Because the vertical motion is very small there is little pressure perturbation and the dispersion relation can be approximated as equation 1.11.

$$m^2 = \frac{(k^2 + l^2)^{1/2} N^2}{\omega^2 - f^2} \qquad \text{or} \qquad \omega^2 = N^2 \frac{(k^2 + l^2)^{1/2}}{m^2} + f^2. \tag{1.11}$$

An interesting characteristic of internal propagating waves is that the group velocity and the phase velocity are perpendicular. As a consequence of this, the phase fronts of an upwardly

propagating wave appear to descend with time.

Critical-Level Filtering

The majority of gravity waves are generated in the lower atmosphere. The spectrum is largely determined by the characteristics of their source. However, as they propagate away from the source regions their spectrum is influenced by the factors in the propagation medium such as background winds and temperatures. Waves can be *filtered* by the mean winds and temperatures. For example, a wave of wavenumber k, propagating in the presence of a mean wind, U, has an intrinsic frequency of $\hat{\omega} = \omega - kU$, (the frequency measure with respect to the mean wind) where ω is the frequency with respect to the ground. As the wave propagates upward, ω remains constant so that a change in the mean wind induces a corresponding change in the intrinsic frequency and in the horizontal and vertical wavelengths. In terms of phase speeds this relation becomes equation 1.12.

$$\hat{c} = c - U, \tag{1.12}$$

where $\hat{c}$ is the intrinsic phase speed, c is the phase speed with respect to the ground and U is the background wind in the direction of propagation of the wave. When a wave encounters a level where $U - \hat{c}$ tends to zero, the vertical wavelength will also tend to zero (since it can be shown that $\hat{c} \sim \frac{N}{m}$) and the wave can no longer propagate. The wave is then said to have reached a *critical level*. The wave will either tend to break just below this critical level or be absorbed or reflected. If the wave breaks, energy and momentum are deposited into the mean flow. As the winds form critical levels for waves ascending through the atmosphere, waves with a range of phase speeds encounter different critical levels. As a result, only gravity waves with phase speeds outside a 'forbidden range' (defined by the background wind velocity) will reach the MLT.

Wave Breaking

Gravity waves grow in amplitude as they propagate vertically. When the waves reach large amplitude they can become unstable and 'break'. This acts to limit or reduce the amplitude of the wave. It can be shown that the wave becomes unstable when their amplitude in the direction parallel to the direction of horizontal wave propagation is greater than their intrinsic phase speed. When this condition is met the wave becomes unstable and breaks, dissipating energy and creating turbulence and small-scale mixing of the atmosphere. A number of mechanisms contribute to the dissipation of wave energy, including convective and dynamic instabilities, turbulent or radiative damping and non-linear interactions.

The dominant instability in the case of high-frequency gravity waves is believed to be convective instability (*Fritts and Rastogi*, 1985). In this type of instability the temperature perturbations of

the wave induce localised unstable regions in the atmosphere. As the wave perturbations depend of the wave amplitude, there is a limiting amplitude at which instabilities develop. This is called the *saturation or breaking amplitude*.

The dominant instability for low-frequency gravity waves is dynamical instability. This occurs when the vertical shear in the horizontal wind induced by the wave exceeds a critical value. The flow becomes unstable when the Richardson number is less than $\frac{1}{4}$ and turbulence is then generated, constraining the wave amplitude. The Richardson number is defined as :

$$R_i = \frac{N^2}{\left(\frac{du}{dz}\right)^2},$$ (1.13)

The threshold amplitudes for these processes are similar. However, convective instability occurs preferentially for high and medium frequency waves and dynamical instability occurs preferentially for low frequency waves (*Fritts and Rastogi*, 1985). This is because of the rapid onset of turbulence for convective instability in the first case and the additional contribution of shear from Coriolis force induced transverse velocities in the second case.

1.3.2 Tides

Atmospheric tides are global-scale oscillations with periods related to the solar day. They are primarily the result of periodic heating of the atmosphere by the Sun. This is in contrast to oceanic tides which are excited by the gravitational forcing from the moon. Gravitational tides forced by the Sun and moon do exist in the atmosphere but are of small amplitude. This section will give a brief introduction to atmospheric thermal and lunar tides.

The sun heats the atmosphere strongly during the day, but not at night. This results in what is effectively a 'square wave' profile of heating. To illustrate this heating, Figure 1.11 shows the distribution of heating with height (also showing chemical species), latitude and local time. This heating forces oscillations with periods that are harmonics of a day, that is for example, 24, 12, 8 and 6 hours. Due to the amplitude growth of waves with height, a tide generated with small amplitude in the lower atmosphere can reach amplitudes of many tens of ms^{-1} in the MLT. The upward propagation of tides can be inferred by their presence at MLT heights, far above their primary source regions as well as from the observed downward phase propagation for tides (corresponding to upward energy propagation).

Considering Figures 1.11(a) to (c), it can be seen that most solar heating occurs over the equator. Further, most heating occurs during the day and not the night, creating an approximate square-wave profile in local time. A Fourier analysis of this heating curve will thus result in a steady mean component, a diurnal component that forces the 24-hour tide, a smaller semi-diurnal component, (12-hour tide), and successively smaller high frequency components. Of these high-frequency
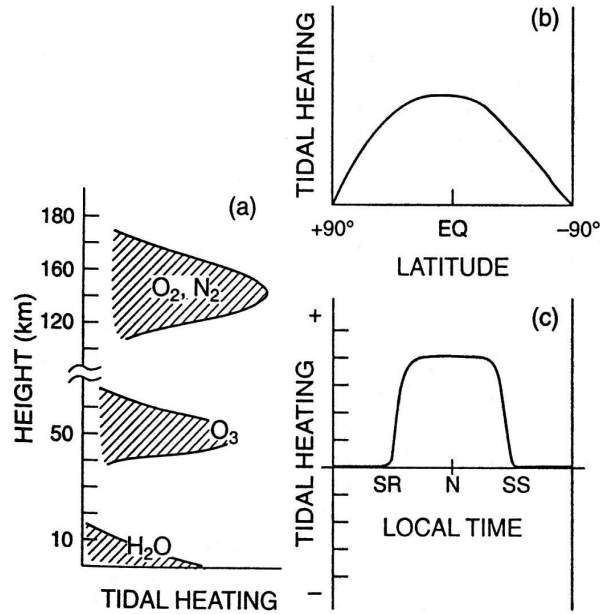
Figure 1.11: Diagram depicting the distribution of heating with (a) height, (b) latitude and (c) local time. After (*Forbes*, 1995)

components the 8- and 6-hour ones are the most significant.

The distribution of heating in latitude, i.e. strongest at the equator, would suggest that tidal amplitudes are largest at low latitudes. Although this is true for the 24-hour tide, the 12-hour tide maximises at mid-latitudes. This is because the 24-hour tide has a short vertical wavelength in comparison to the depth of atmosphere in which it is forced. This results in destructive interference, reducing the amplitude of the 24-hour tide before it leaves the excitation region.

The general structure of the tides can be described by an equation derived from the equation of motion on a rotating sphere, the adiabtic equation and the equation of continuity. This can then be resolved into Laplace's tidal equation and a vertical structure equation. Laplace's tidal equation describes the horizontal structure of the tides. Solutions consist of pairs of eigenfunctions, Θ_n, called *Hough functions* and eigenvalues, h_n, called the equivalent depths.

Hough functions describe the latitudinal structure of the tide. There are several Hough functions for each tide, known as *modes*. These correspond to eastward or westward propagating global-scale waves bounded at the poles. Each mode is identified by a zonal wavenumber, k, and a meridional index, l_i, where the meridional index is defined so that in the Hough function $(l_i - k)$ nodes appear between the poles. Negative values of l_i indicate that the wave is evanescent and not propagating.

Tides can be separated into migrating and non-migrating components. Migrating tides have the same local time variation at all longitudes - they are *sun following*. These tides are excited by absorption of solar radiation at various heights in the atmosphere. *Non-migrating* modes are

generated, for example, by strong longitudinal changes in topography such as land-sea contrast, non-linear interactions of tides and planetary waves and regions of strong localised gravity-wave drag. Non-migrating modes can propagate eastwards or westwards.

Decoupling the migrating and non-migrating components of the tide is impossible using data from only one ground station. Therefore, satellite based measurements or longitudinal chains of ground stations are used to study non-migrating tidal components.

Lunar Atmospheric Tides

Atmospheric tides generated by the gravitational pull of the moon have smaller amplitudes than tides forced by solar heating. They have amplitudes of about 5 - 20% of the solar tides (e.g., *Sandford et al.*, 2007; *Hagan et al.*, 2003). Lunar tides are mainly generated in the troposphere and a large proportion of the forcing comes from the vertical motion of the ocean surface. They have periods related to the moons orbital period, 24.84 hours, and the largest is the lunar semi-diurnal tide which has been shown to reach significant amplitudes in the MLT (e.g., *Sandford et al.*, 2006, 2007).

1.3.3 Planetary Waves

Planetary waves are also global-scale oscillations which, like tides, have an integer number of cycles 'wrapped around' a circle of latitude. These waves also reach large amplitudes in the MLT. For example, the quasi-two-day wave can reach amplitudes over 50 ms^{-1}. These waves produce purely horizontal air parcel motions, unlike tides or gravity waves and can displace an air parcel large horizontal distances. Because of these large meridional displacements planetary waves can transport chemical species great distances in the atmosphere. The well known Rossby waves are the idealisations of planetary waves on a plane (*Beer*, 1974).

Planetary waves exist due to the conservation of *absolute vorticity* and the restoring force for these waves is ultimately the poleward gradient of *planetary vorticity*.

The generation of a planetary wave can be illustrated by considering a displaced air parcel as shown in Figure 1.12. An air parcel initially moving eastwards along a line of latitude in the northern hemisphere has no rotation about a vertical axis and so has zero relative vorticity. If the air parcel is displaced poleward the planetary vorticity, f ($= 2\Omega \sin \phi$) increases. This results in a decrease of relative vorticity if absolute vorticity is conserved and causes the parcel to spin *clockwise* about a vertical axis. This spin in combination with the eastward motion cause a southward flow ahead of the parcel which pushes it equatorward, back to its equilibrium position. The parcel will overshoot and the reverse will occur setting up an oscillation about the

equilibrium position.
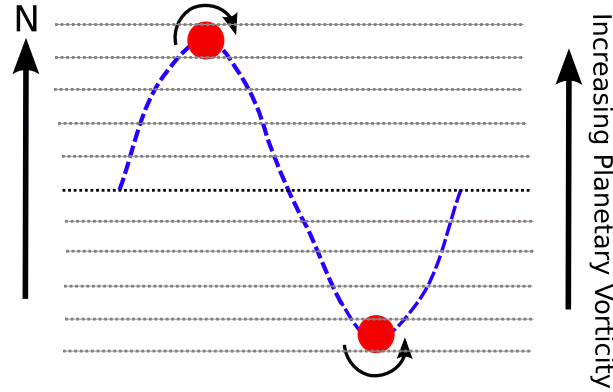
Figure 1.12: A schematic diagram showing the relationship between planetary vorticitiy, relative vorticity and an air parcel displaced by a planetary wave in the Northern Hemisphere

Further understanding of planetary waves can be obtained by examination of the dispersion relation. The derivation of this equation is beyond the scope of this work and a full derivation can be found in *Andrews et al.* (e.g., 1987). The dispersion relation for planetary waves is stated in equation 1.14.

$$c = -\frac{\omega}{k} = \overline{u} - \frac{\beta}{k^2 + l^2}. \tag{1.14}$$

Where k, l and m are the wavenumbers, $\overline{u}$ is a uniform flow, ω is the wave frequency and c is the phase velocity in the x direction, β is a constant $\beta = df/dy$ where f is the Coriolis force.

For equation 1.14 to be satisfied, the velocity of the wave relative to the flow $(c - \overline{u})$ must be negative (as $\frac{\beta}{k^2 + l^2}$ can only be positive). This means Rossby waves invariably propagate westwards with respect to the mean flow. However, if a Rossby wave has a westward phase speed less than the eastwards velocity of the mean flow, then the wave pattern may be advected eastwards by the flow (*Salby*, 1996).

Equation 1.14 included the simplification of an assumed two-dimensional structure. If a three-dimensional structure is considered, the dispersion relation becomes

$$c = -\frac{\omega}{k} = \overline{u} - \frac{\beta}{k^2 + l^2 + \frac{m^2 f_0^2}{gN}}. \tag{1.15}$$

This can be used to investigate the propagation of waves with respect to the mean flow. For a stationary planetary wave, $c = 0$, m^2 must be positive for vertical propagation of the wave. This sets the condition:

$$0 < \overline{u} < \frac{\beta}{(k^2 + l^2)}, \tag{1.16}$$

which means that when the flow is westward ($u < 0$), or strongly eastward ($u >> 0$), there will be no vertical propagation of the wave i.e., the wave will only propagate in weak to moderate eastward wind speeds. Thus stationary planetary waves cannot propagate through the westward winds in the summer stratosphere / mesosphere and only low wavenumber waves can propagate

through the eastward winds in the winter stratosphere, this condition is known as the *Charney-Drazin criterion*.

Stationary planetary waves are believed to be excited by flow over orography and differential heating between the land and ocean, so they are known as *forced modes* (*Charney and Eliassen*, 1949). There are also *free modes* such as global normal modes (e.g. the quasi-two-day wave and the 16-day wave). These are natural resonances of the Earth's atmosphere. Free modes may be generated by random departures from geostrophic balance and by baroclinic and barotropic instability (e.g., *Beer*, 1974).

1.4 The Polar Atmosphere

Much of the work in this thesis will focus on the polar MLT. The middle and upper atmosphere have been recognised as important and sensitive indicators of the atmosphere as a whole. This is particularly true for the polar atmosphere where changes in phenomena such as Noctilucent Clouds (NLC) and Polar Mesospheric Summer Echoes (PMSE) occur (*Jarvis et al.*, 1999). In spite of this, the polar atmosphere still remains a relatively poorly understood part of the atmosphere.

The Arctic MLT has been the subject of numerous studies using a variety of techniques (e.g., meteor radar, Medium Frequency (MF) radar, rockets and optical techniques). There are fewer studies of the Antarctic MLT. Studies that make comparisons between the polar regions are rare. The latter will be a particular focus of this thesis.

Some of the largest differences between the Arctic and Antarctic occur in winter and spring. During winter the polar regions remain in darkness and the lack of solar heating creates a cold low-pressure system over the pole. The eastwards winds that form around this system can be very strong and make up the *polar night vortex*. The vortex air reduces transport from the low latitudes into the polar region, effectively isolating the polar regions from the rest of the atmosphere.

The Arctic winter stratosphere is warmer than the Antarctic winter stratosphere by approximately 20 K (*Andrews et al.*, 1987). This combined with the fact that there is more planetary wave activity in the northern hemisphere, means that the vortex breaks down more rapidly over the Arctic. The Arctic atmosphere also regularly experiences sudden stratospheric warmings whereas there has only been one Antarctic warming in recorded history.

1.5   The Scope of this Thesis

This chapter gave a brief introduction to the general structure of the Earth's atmosphere and some of the many types of waves that propagate through it. As waves propagate upwards though different layers of the atmosphere they carry energy and momentum that is deposited when they break. Wave breaking in the MLT influences the temperature, chemistry and dynamics of this part of the atmosphere. The studies in this thesis explore the characteristics and behaviour of gravity waves and high-frequency tides through observations made using meteor wind radar. Much of this work will focus on the polar atmosphere using radars based in the Arctic and Antarctic.

Chapter 2 introduces some of the physics behind the operation of meteor radars and describes the radars and data analysis used in this work. Chapter 3 describes and implements the *variance technique*, a novel technique for studying high-frequency gravity waves with meteor radar. This technique is used to investigate and contrast high-frequency gravity-wave activity in the Arctic and Antarctic. It also reveals some effects of critical-level filtering on gravity-wave activity and investigates interactions between gravity waves and the background temperature structure and gravity waves and tides. Chapter 4 describes the zonal and meridional variance and the vertical flux of horizontal momentum within the Arctic and Antarctic gravity-wave fields. This Chapter also examines the effects on the MLT gravity-wave field of interactions with the mean winds lower down in the atmosphere. Chapter 5 considers the behaviour of the 8-hour tide at middle and high latitudes and reveals the significance of the high-frequency tidal components. Suggestions for future work are detailed in Chapter 6.

Publications resulting from the work contained in this thesis are listed below:

1. Beldon, C. L., H. G. Muller and N. J. Mitchell, The 8-hour tide in the mesosphere and lower thermosphere over the UK, 1988-2004. *Journal of Atmospheric and Solar-Terrestrial Physics*, 68, 655-668, 2006.

2. Beldon, C. L. and N. J. Mitchell, Gravity Waves in the Polar Mesopause Region observed by Meteor Radar. *Journal of Atmospheric and Solar-Terrestrial Physics*, (Submitted).

Chapter 2

VHF Meteor Radar

2.1 Introduction

Many different methods have been developed to study the Earth's atmosphere. However, the Mesosphere and Lower Thermosphere (MLT) region is difficult to observe directly. Although the development of rocket-borne instrumentation has allowed us to make increasingly frequent and accurate *in situ* measurements of the middle atmosphere, these techniques can only provide us with snapshots of the atmosphere at a particular time. In order to develop a long-term dataset from these techniques, a sustained series of such instantaneous measurements would be needed, which would be expensive and impractical. The locations available for rocket-borne experiments are also limited because measurements over oceans or densely-populated areas are impossible. Satellite observations can successfully study this part of the atmosphere and have the advantage of providing large spacial coverage. However, this often comes at the price of low temporal resolution, a lack of versatility and a large financial outlay.

For these reasons, effective observations of the MLT region are made using ground based remote sensing techniques, including radars. There are several advantages that make the use of radars attractive for this type of study:

1. They operate effectively in all weather conditions, including high levels of cloud cover

2. They have full diurnal sampling, that is they can operate during the day or night

3. They operate autonomously with little maintenance and so are suitable for use in remote or inhospitable locations

4. They are relatively cheap to purchase and maintain

5. They offer reasonable height and time resolution

6. They can operate continuously over many years

Meteor radars are specifically designed to use the ionised trail associated with meteors as a scatterer. Because these trails drift with the neutral winds at the height at which they are formed they can be used as tracers of the motion of the atmosphere in the MLT region.

Meteors will be briefly described in Section 2.2 and the principle of meteor radar will be described in Section 2.3. The method of calculating horizontal winds will be described in Section 2.5. Finally, radars used in this study and the data recorded by them will be presented in Section 2.6.

2.2 Meteors and the Atmosphere

A meteor or 'shooting star' is the bright streak of light emitted as a particle of interplanetary material, a meteoroid, burns up in the Earth's atmosphere. The majority of meteoroids that produce a meteor have diameters between $\sim$ 0.05 and 200 mm (*Ceplecha et al.*, 1998). The smallest particle that can produce a meteor has a diameter of approximately 0.01 mm, larger meteoroids (up to several kilometres) have impacted the Earth but these are much rarer.

Large amounts of energy are needed to create the bright streak of light we see as a meteor. This comes from the high entry speeds of the meteoroids. As they enter the atmosphere, meteoroids have speeds between 11.2 and 72.8 kms^{-1}. The average entry speed is $\sim$ 42 kms^{-1}. The lowest possible speed of 11.2 kms^{-1} corresponds to a meteor falling solely under the gravitational influence of the Earth. The highest possible speed of 72.8 kms^{-1} represents a head-on collision between a particle travelling at the escape velocity of the solar system, 42.5 kms^{-1}, and the Earth travelling with its orbital speed of 30.3 kms^{-1}. Although speeds higher than this have been recorded, such events are rare. These meteoroids are thought have originated from outside the solar system.

When a meteoroid enters the denser parts of the atmosphere, friction causes the temperature of the meteoroid to increase rapidly. The effect of this heating depends on the size of the meteoroid. For particles smaller than 0.01 mm, the drag from the atmosphere slows the meteoroid to terminal velocity and the temperature does not rise above the meteoroids melting point. For particles larger than 0.01 mm, the temperature of the meteoroid can reach approximately 2000 K. At this temperature the meteoroid begins to lose mass as the surface material sublimates and ablates, leaving a trail of hot vapourous material. This material collides with the surrounding air molecules and produces ionisation and free electrons along the path of the meteoroid. The

de-excitation of the ionised material results in the bright streak of light that is seen as a meteor. For meteor radar studies, the free electrons act as scatterers for radio waves emitted by the radar.

The ionisation associated with a meteor occurs between heights of $\sim$ 75 and 140 km. Above this range the atmosphere is not dense enough to produce enough frictional heating for the particle to ablate. Below this range particle has usually completely ablated. The ionisation typically has the shape of an elongated cone a few tens of kilometres long. This extends perhaps 10 - 15 km vertically and has a dense core of ionisation surrounded by a more diffuse ionised cloud. The initial radius of the cone is defined as the rms position of ablated ions once thermal equilibrium has been reached. This is governed by the entry speed of the meteoroid and the mean free path of the atmosphere (*Ceplecha et al.*, 1998). Due to the fact that the mean free path of the atmosphere increases with height (as density decreases), the initial radius of a given meteor trail will also increase with height. At 80 km the initial radius will be approximately 0.4 m, at 90 km it will be 0.6 m and at 100 km it will have increased to 1 m.

Meteor trails are not long-lived phenomena, their typical lifetime is less than a second, although they can last up to several minutes (*Close et al.*, 2000). Immediately after formation the electron number density starts to decrease as the trail is acted upon by ambipolar diffusion, atmospheric turbulence and as the ions and electrons start to recombine. The most important of these processes is ambipolar diffusion. Below $\sim$ 100 km the affect of the Earth's magnetic field on the trail can be ignored and the trail drifts with the winds.

2.3 Meteor Radar

Meteor radars are designed to detect radio scatter from the free electrons in the ionised meteor trail. Most meteor radars are backscatter systems, meaning that the transmitter (Tx) and receiver antenna (Rx) are based at the same site. The reflection from meteor trails is *specular* i.e. similar to a reflection from a mirrored surface. These factors means that the radar only receives a return signal if the reflection is perpendicular to the trail's axis. This can be seen in Figure 2.1.

Because of this required geometry, even all-sky meteor radars (that have low-gain antennas designed to detect echoes over all azimuths and elevation angles), only detect a small fraction of the actual population of meteors entering the 'collecting volume'. The signal returned from a meteor increases very rapidly as the advancing column of ionisation crosses the specular reflection point and the Fresnel zones form. Most of the returned signal is from the first Fresnel zone where constructive interference is greatest.
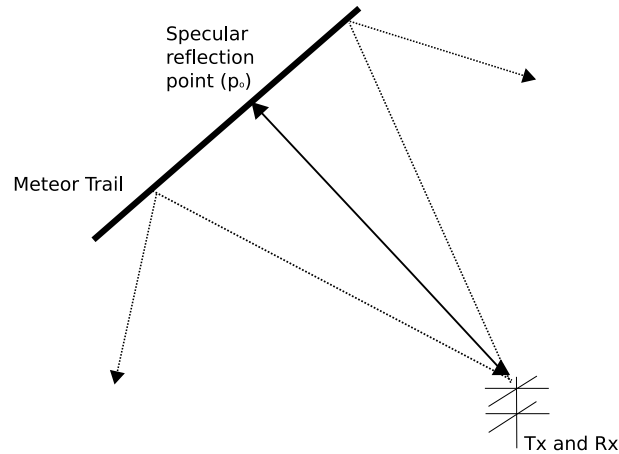
Figure 2.1: A schematic showing the geometry of meteor radar backscatter.

2.4 The Signal from a Meteor

Radio studies have revealed two main types of meteor echo – *overdense* and *underdense*. An echo that is returned from a trail which has an electron line density of less than $\sim 10^{13} \mathrm{m}^{-1}$ is termed an underdense echo. The majority of echoes are of this type. In an underdense echo the signal penetrates into the column of ionisation and the returned signal is thus a sum of the scatter from the individual electrons in the trail. The amplitude profile of a typical underdense echo is shown in Figure 2.2. The shape is very distinctive, making it relatively easy to distinguish between a meteor echo and a spurious signal. There is a sharp increase in the amplitude of the returned signal followed by an exponential decay. This decay is not the result of the dissipation of the meteor trail (recombination) but results from the expansion of the trail radius caused by ambipolar diffusion. The trail radius increases and within about 1 second it is large enough that the returning signal suffers destructive interference from waves scattered from different depths within the trail.
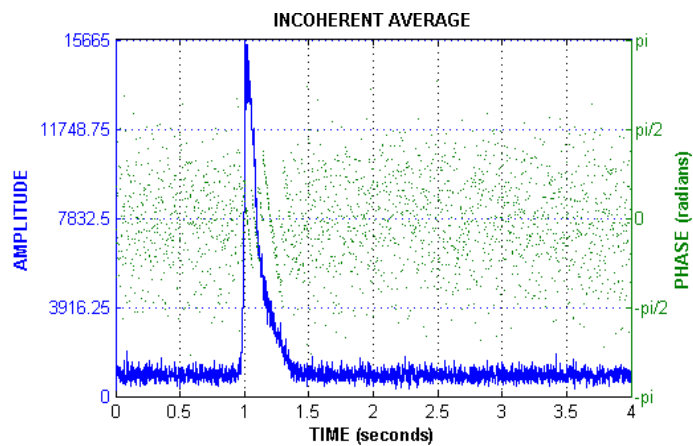
Figure 2.2: Amplitude profile of a typical underdense meteor echo.

The upper height limit for the detection of underdense echoes is called the *underdense echo*

ceiling. The height at which the ceiling occurs depends on the radio frequency used. This limiting height is a consequence of the height dependence of the initial trail radius. At the height of the echo ceiling, destructive interference is caused immediately after the trail is formed and hence the trail is not detected. Note that meteors are actually present above this height but are simply not detected by the radar. The lower limit at which meteors are detected is determined by the total destruction by ablation of the meteoroid. For typical meteoroid masses all of the material has ablated by $\sim$ 75 km and only the comparatively rare, larger meteoroids survive below this height.

If the electron line density is greater than about 10^{14} m^{-1} the meteor echo is classed as being overdense. At these electron line densities the plasma frequency of the trail becomes greater than the frequency of the radio wave and the signal cannot penetrate into the column of ionisation. The signal is instead reflected from the surface of the column and the trail reflects the signal as if it were a metal cylinder. The reflected echoes from overdense meteors last longer than those from underdense ones and can remain for several seconds.
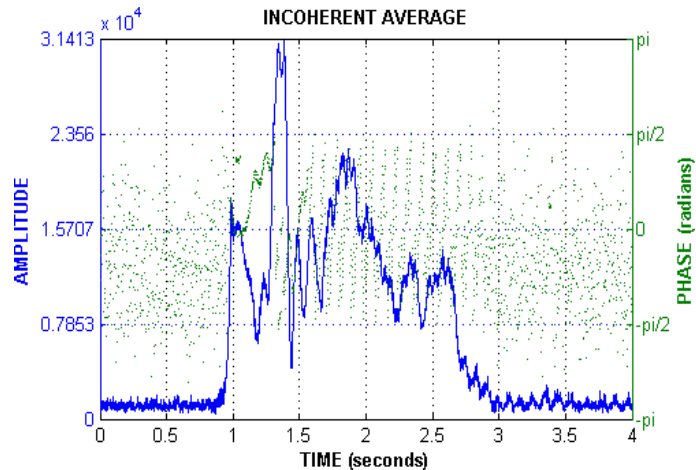
Figure 2.3: Amplitude profile of a typical overdense meteor echo.

The amplitude profile of a typical overdense meteor echo is presented in Figure 2.3. Initially there is a rapid increase in amplitude, however, following this the amplitude is variable and does not have a characteristic shape. The extended lifetime also means that the trail becomes distorted by shears in the winds and multiple specular reflection points can arise. Interference between the scatter from these multiple reflection points can cause the amplitude of the total received signal to fluctuate. Further, drift velocities measured from this type of echo may be measuring the movement of the specular reflection point rather than the motion of the trail as a whole.

Because of the possible distortion and the possibility of multiple specular reflection points arising from overdense echoes, Skiymet meteor radars only accept meteor echoes that match the signal profile of an underdense echo. This also excludes signals from other sources such as a plane passing over the radar, or from radio stars. Signals from these sources do not pass the stringent criteria used to match the returned signal to that of the characteristic shape of an underdense

echo and are discarded.

2.5   Determining Atmospheric Winds using Meteor Radar

The ionised trails created by meteors are 'frozen' into the neutral wind at the height where they form. Therefore, as they drift with the wind they can be used as a tracer for atmospheric motion. The assumption that the trails are frozen into the neutral wind is legitimate because at the height at which meteor trails form the ion-neutral collision frequency is higher than the gyro frequency of the electrons in the trail. The gyro frequency is the frequency of rotation for an electron (or other charged particle) as it spirals in a magnetic field. As this is lower than the ion-neutral collision frequency the electrons and ions recombine before the electrons in the trail drift along the magnetic field lines. This implies that the ions are carried by the flow and so the whole trail moves with the wind, not the magnetic field and can be used as a tracer of the neutral wind motion.

The drift of a trail along the line of sight of the radar is detected as a phase change in the returned signal. By measuring this phase change, it is possible to calculate the radial drift velocity of the trail. This is illustrated in Figure 2.4 where the trail is advected by the neutral wind.
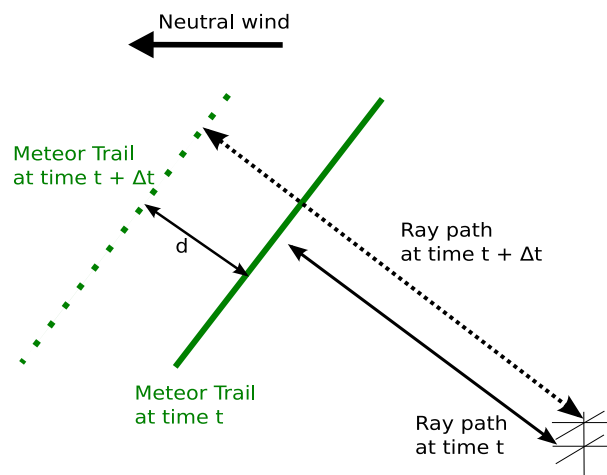
Figure 2.4: Schematic showing the geometry of the phase change method of line-of-sight velocity determination.

If the phase change of a signal from time t to $t + \Delta t$ is from ϕ_a to ϕ_b, then the phase shift is $\Delta\phi = \phi_a - \phi_b$. This can be attributed to the trial moving by a distance, d, and resulting in a lengthening of the total return path of the signal. For a drift distance of d and a signal wavelength of λ the change in phase will thus be $\frac{4\pi d}{\lambda}$. The drift velocity along the line of sight

can then be calculated using equation 2.1.

$$V_{rad} = \frac{d}{\Delta t} = \frac{(\lambda/4\pi)}{(\Delta t/\Delta \phi)} \qquad (2.1)$$

Using the assumption that flow of the neutral wind is purely horizontal i.e., that the vertical motion is negligible, we can use the line of sight velocity to estimate the horizontal motion of the atmosphere at the reflection point of the trail. This assumption can be considered, generally to be very accurate, however very large amplitude gravity waves may induce larger vertical motions. These will still be small compared to the horizontal winds. Once many such point measurements have been collected it is possible to calculate the motion of the atmosphere across the entire field of view of the radar, this will be discussed further in Section 2.8.1.

2.6 The University of Bath Meteor Radars

Data from three meteor radars are used in this study. They are based at middle, Arctic and Antarctic latitudes. The first is a system based at Castle Eaton in the UK. This radar operated nearly continuously from the 1980s to 2005 by H. G. Muller. This radar operated with no height finding capabilities (i.e., the heights of individual meteors can not be determined). However, the data from this radar is one of the longest, continuous MLT data sets. More information about this radar is detailed in Section 2.6.2. The other two systems are commercially produced Skiymet systems operating in an 'all-sky' configuration with height finding. The second radar is at Esrange, in northern Sweden and was deployed in 1999. This has provided near continuous data since then. The final system was deployed at Rothera, Antarctica in 2005 and has also provided near continuous data. These radars are identical systems, situated at conjugate latitudes, making them ideal for comparative studies between the Arctic and Antarctic atmospheres.

The positions of these radars are illustrated in Figure 2.5. The highest latitude station is Esrange in Sweden (68° N, 21° E), followed by the radar based in the UK, (51° N, 2° W) and finally the radar at Rothera in Antarctica, (68° S, 68° W).

2.6.1 The Rothera and Esrange Skiymet Meteor Wind Radars

The Esrange meteor radar was deployed in August 1999 at Esrange (68° N, 21° E) the Swedish Space Corporation rocket range located near Kiruna, Sweden. It has provided near continuous coverage since that date. A receiver antenna from the Esrange radar is shown in Figure 2.6

The Rothera radar (68° S, 68° W) was deployed in February 2005 at Rothera Point, Antarctica. A radar antenna from this system is shown in Figure 2.7.
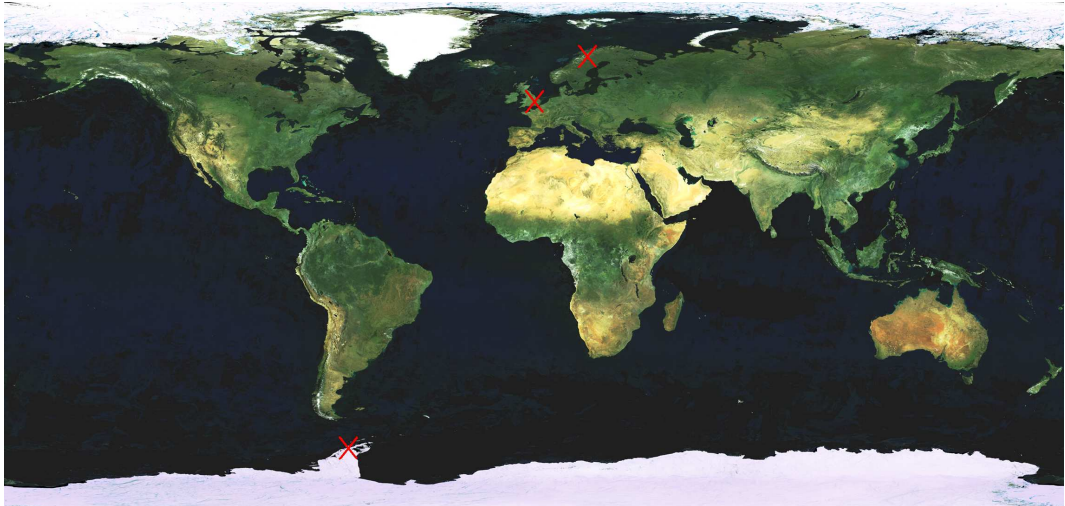
Figure 2.5: Map of the Earth showing the locations of the radars based at Esrange (68° N, 21° E), Castle Eaton (51° N, 2° W) and Rothera (68° S, 68° W) as red crosses.

Figure 2.6: A Receiver antenna at Esrange

Both the Rothera and Esrange radars are commercially produced VHF systems, made by Genesis Software Ltd., based in Adelaide, Australia and Modular Radar Designs of Canada Inc. (MAR-DOC Inc.) based in Ontario, Canada. The operational parameters of these systems are shown in Table 2.1.

The high pulse-repetition frequency is necessary to determine the entry speeds of meteors as they enter the atmosphere. Entry speeds can currently calculated for approximately 5% of meteors.

These radars operate under an 'all-sky' configuration where the radiated power is largely inde-

Figure 2.7: Antenna at Rothera Point during installation in February 2005

Table 2.1: Operational parameters of the Rothera and Esrange Skiymet meteor radar

Parameter	Value
Radio Frequency	32.5 MHz
PRF	2144 Hz
Power	6 kW
Duty Cycle	15%

pendent of azimuth. Due to the arrangement and number of receiver antenna, the radars are able to use interferometric techniques to determine the height of individual meteor echoes. The Rothera and Esrange radars are made up of six crossed-element Yagi antennas: one transmitting and five receiving. The arrangement of antennas is shown in Figure 2.8.
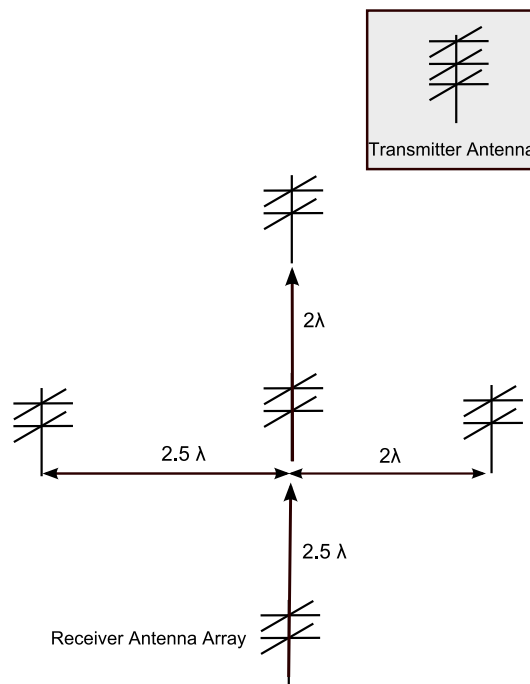
Figure 2.8: Ground plan of SKiYMET radars (λ is the radar wavelength).

These radars do not use pulse coding. As a result a returned signal cannot be identified un-

ambiguously as any of the previously transmitted pulses. This, in combination with the high pulse repetition frequency of 2144 Hz, means that the radar has a range ambiguity of 70 km. For any echo with a measured range of x km, the actual range could be 70 $\pm x$ km, 140 $\pm x$ km or 210 $\pm x$ km etc. However, the correct range can be determined with the use of *a priori* knowledge. We know that meteors only occur in a certain part of the atmosphere – the meteor region (between 70 and 140 km) and the radar can only detect meteors between heights of 70 and 110 km (see Section 2.4). Therefore, it is normally possible to reject solutions corresponding to heights outside this zone and so determine the correct range to the meteor.

The real-time analysis of echoes, identification and post-analysis is performed by an on-site PC (*Hocking et al.*, 2001). The parameters stored daily are summarised in Table 2.2. A full description of the workings of the Skiymet radars is given by *Hocking et al.* (2001).

Table 2.2: Parameters stored in an mpd file

Parameter	Description
Date	The date of detection relative to Coordinate Universal Time (UTC)
Time	The time of detection in UTC (millisecond accuracy)
Rge	The range of the echo in km
Ht	The height above ground of the detected echo, including a correction for the curvature of the Earth
Vrad	The observed radial drift velocity of the meteor
Delvr	The error associated with the radial velocity from the 5 antenna pairs in the receiver array. Observations with delVr > 5.5 ms-1 are rejected.
Theta	The zenith angle of the meteor in degrees
Phi 0	The azimuth angle of the meteor in degrees
Ambig	Due to the use of uncoded radio pulses and an interferometric method to deduce the meteor trail location, the system can calculate several possible locations for a detection. The ambig records the number of possible locations the echo could have
Tau	The half-life decay time of the meteor (in seconds)
Vmet	Entry speed of the meteor, this parameter is only available in < 5% of echoes
File	The extension of the filename storing the data on the echo
Delphase	The worst possible error between antennas assuming azimuth and zenith are correct, measured in degrees
Ant Pair	The antenna pair that have the worst error
Irex	The receive channel used in the analysis for certain single-channel data quality tests. This is always '1' during normal operation
Amax	Peak amplitude of the meteor in digitiser units

2.6.2 The UK Radar

The radar based in Castle Eaton UK, (52° N, 2° W) has produced a dataset spanning nearly 17 years from 1988 to 2005. These data span a solar cycle and may be important for studying long term changes and solar influences on the atmosphere. A picture of one of the transmission

antennas is shown in Figure 2.9.

Figure 2.9: Transmission antenna from the radar based at Castle Eaton

Table 2.3: Operational parameters of the UK radar

Parameter	Value
Radio Frequency	36.75 MHz (1988-1995), 41 MHz (1995-2005)
PRF	300 Hz
Power	12 kW (1988-1995), 18 kW (single-beam 1995-1996), additional 8 kW antenna (1996-2005)

The basic operational parameters of this radar are listed in Table 2.3. The UK system was operated using a two orthogonal beam configuration, different from the other systems used in this work (see Section 2.6.1). The beams were elevated at an angle of $\sim 30°$ above the horizon and had an effective beam width of $\sim 30°$. Where each beam intersected the meteor region it formed a broad 'footprint', so there were two collection volumes defined by the beams. The radar measures line-of-sight velocities for meteors in each beam and these were assumed to be the component of the horizontal wind in direction of the azimuth of the beam. There was no height information recorded for the echoes, so the radial velocities were converted to horizontal velocities using the range of the meteor echo and the mean height of the meteor region, under the assumption of negligible vertical winds. Hourly mean winds in the beam directions were calculated using a two-hour mean of the horizontal velocities, incremented in one hour steps. These hourly values were then combined using vector addition to give the zonal and meridional components of the wind. Therefore, the resultant velocities represent spatially *and* temporally averaged winds and can be taken to represent the prevailing wind in the broad atmospheric volume between the two 'footprints' formed by the intersection of the radar beam with the meteor region.

In the absence of height information the horizontal winds from this radar were assumed to be representative of winds near the peak in the height distribution of meteors i.e. approximately 90 to 95 km. This results in a time series of winds from one representative height only. A height of $\sim$ 90 km has been frequently assumed for such measurements. However, for this study the heights were confirmed by an analysis of the 12-hour tide using the UK data and data predicted by the Global Scale Wave Model (GSWM) model. The GSWM model has been shown to predict reliable estimates of tidal amplitude and phases at mid-latitudes on a monthly timescale (e.g., *Manson et al.*, 2002a). Monthly-mean values of phase were calculated for the 12-hour tide for all years of the UK dataset and compared to model data for the phase of the 12-hour tide at heights from 78 to 104 km at a latitude of 51° and longitude of 0°. The model was thus, in effect, used to calibrate the representative height of the winds measured by the radar. Figure 2.10 presents the rms of the differences between the phase of the 12-hour tide determined by the meteor wind radar and the value predicted by the GSWM model at several different heights.
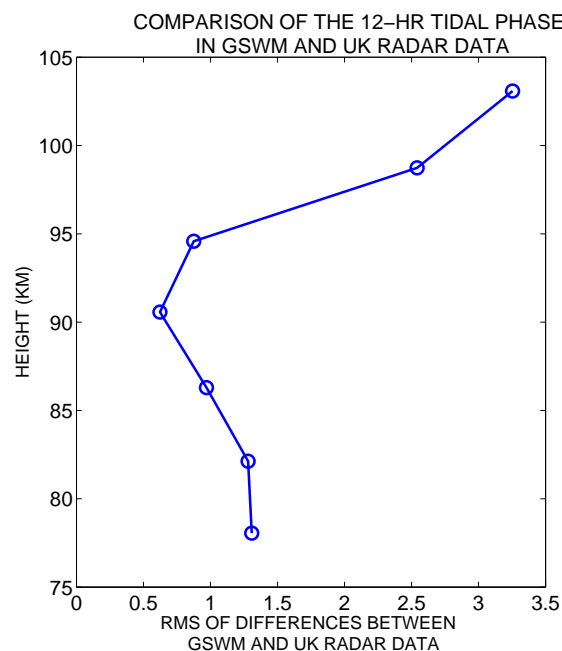
Figure 2.10: Root mean square difference between 12-hour tidal phases from the UK radar and phase predicted at different heights by the GSWM model for a latitude of approximately 52°.

The closest match for the phase of the 12-hour tide in the figure is at 90 km. This suggests that the previously assumed height of approximately 90 km for the UK meteor radar is reasonable.

The radar was operated in the same configuration from 1998 at Castle Eaton, UK (52.6° N, 2.2° W). Although there were several changes to the radars location and hardware it always remained near 52° N. More detailed descriptions of the radar in various stages of development can be found in *Muller* (1970) and *Muller et al.* (1995).

2.7 The Distribution of Meteors Echoes Observed by the Skiymet Radars

2.7.1 Height Distribution

Unlike the UK radar, the Rothera and Esrange radars are capable of measuring the height of the meteor echoes. Figure 2.11 shows the height distribution of meteor echoes detected during 2005 over Rothera. The distribution of meteors in height is almost identical over both sites. The heights of meteor echoes are calculated using the elevation angle and range measured by the radar for each meteor echo and include a correction for the curvature of the Earth. The heights can be determined to an accuracy of ~ 1 km.
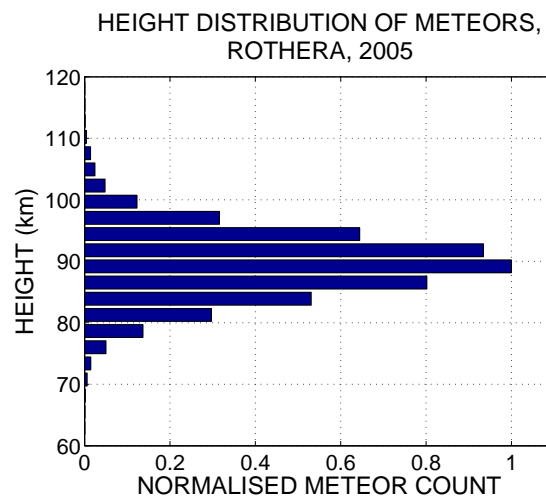
Figure 2.11: The height distribution of meteors over Rothera in 2005.

The height distribution for meteors detected by both the Rothera and Esrange radars follows an approximately Gaussian distribution centred on ~ 90 km with a standard deviation of about 5 km. Most of the meteors ($\sim 90\%$) are detected at heights between 80 and 100 km.

2.7.2 Meteor Azimuth Distributions

The all-sky configuration of the Rothera and Esrange radars allows the detection of meteor echoes from all azimuth angles around the radar. This gives an approximately even distribution of echoes in azimuth and elevation angle. Figures 2.12 and 2.13 present the distribution of meteors in azimuth and horizontal range over Rothera and Esrange respectively. These plots show data from May 5th, 2008, and are representative of the distribution of meteors at these two stations.

Figure 2.12: The distribution of 5658 individual meteors in azimuth and horizontal range for May 5th, 2008, overlaid on a map of Rothera.
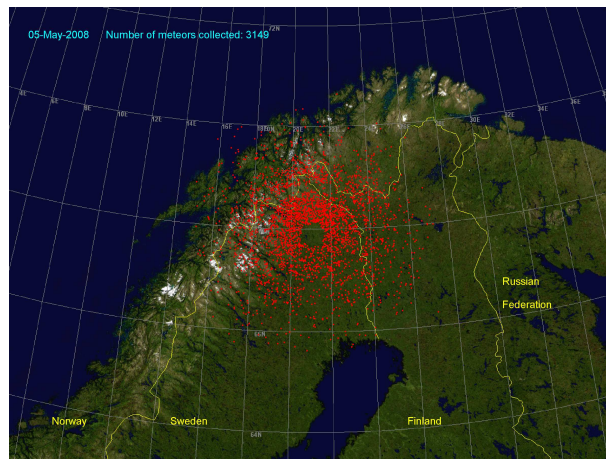
Figure 2.13: The distribution of 3149 individual meteors in azimuth and horizontal distance for May 5th, 2008, overlaid on a map of Esrange.

2.7.3 Meteor Range Distributions

The normalised distribution of meteors in range detected by the Esrange radar is shown in Figure 2.14. The range distributions for Rothera and Esrange are nearly identical. This Figure reveals several interesting characteristics of the distribution of meteors in range.

Firstly, there are very few meteors detected with ranges of less than 100 km. This corresponds to relatively few meteors being detected near to the zenith. This is in part due to the necessity of having specular reflection of radio waves from the meteor trail. For a meteor to form a specular reflection point near to the zenith it must be travelling almost parallel to the ground. This requires a long slant path through the atmosphere and most meteoroids will have completely ablated before reaching the zenith. It is for this reason that the Skiymet radars radiate peak power at an elevation angle of $\sim 30°$, rather than towards the zenith. Secondly, the number of meteors falls with increasing range. This is due the inverse square law reducing the echo power

RANGE DISTRIBUTION OF METEORS, ROTHERA
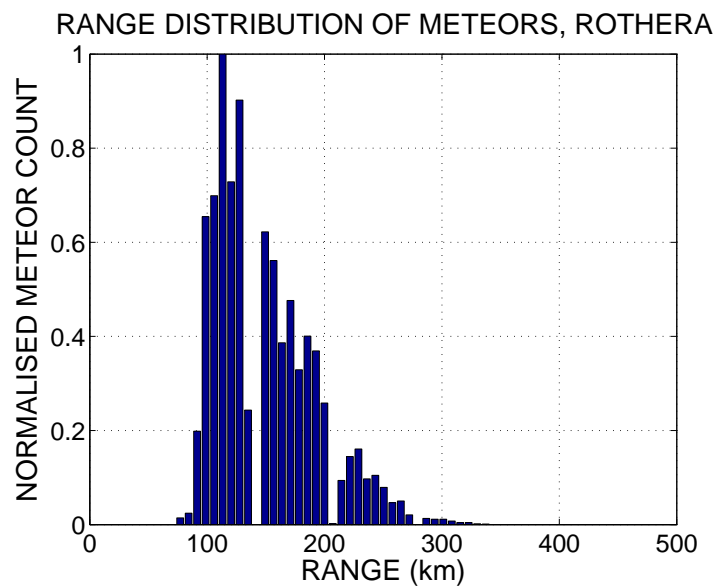
Figure 2.14: The distribution of meteors in range for all meteors recorded between 2005 and 2008 over Rothera.

from more distant echoes. Thirdly, there are very distinctive gaps in the distribution. These gaps occur at ranges of $\sim$ 140, 210 and 280 km. These gaps are formed because the transmitter and receiver array are on the same site. To avoid the receiver being saturated by the direct ground wave, the receiver is switched off whenever a pulse is transmitted. The gaps mark successive times when the receivers were disabled during the transmission of successive radar pulses.

2.7.4 Diurnal Variation in Meteor Count Rates

There is a distinct variation in the number of meteors detected during over the course of a day. Figure 2.15 presents a normalised histogram of the number of meteors in each hour of the day over Rothera. The highest count rates are in the morning and the lowest count rates are observed in the late afternoon and evening.

This diurnal cycle in count rates is due, in part, to the fact that more meteors are 'swept up' by the leading hemisphere of the Earth in its orbit around the sun. The increased count rates in the morning correspond to the radar site being on the leading hemisphere of the Earth. As the Earth rotates the radar site moves onto the trailing hemisphere by late afternoon/evening and sporadic meteors are effectively blocked from the radars view. The amplitude of this diurnal cycle is dependant of the observer's latitude. The ratio of morning to evening count rates over both Rothera and Esrange is approximately 2:1. However, at Castle Eaton this effect is more pronounced and the morning to evening count rate is approximately 11:1.

The low count rates can lead to more gaps in the derived winds in the afternoon. This is because very low meteor counts can not be used to calculate a reliable value of the wind. As a
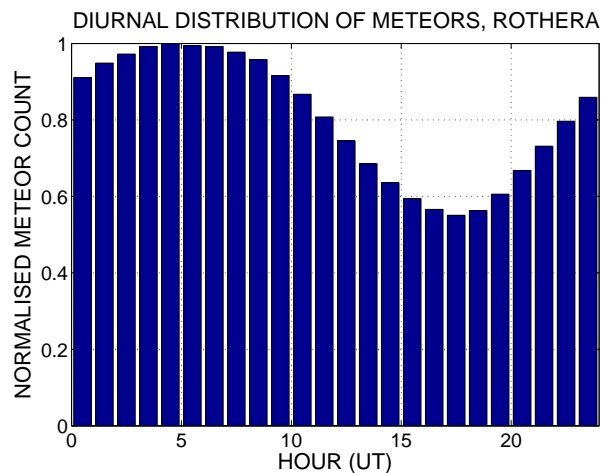
Figure 2.15: Normalised histogram showing the diurnal cycle in meteor counts for all data recorded over Rothera.

result spectral analysis techniques that do not require evenly spaced data, such as Lomb-Scargle periodograms, must be used instead of Fourier analysis. Care must also be taken in interpreting 24-hour periodicities in the meteor radar radar.

2.7.5 Annual Variation in Meteor Count Rates

As well as the diurnal cycle in meteor count rates already discussed, there is also an annual cycle in meteor counts. The daily meteor counts for Esrange for 2000 to 2002 are shown Figure 2.16. The annual cycle is astronomical in origin and is the result of the rising and setting of apparent sources of sporadic meteors on the sky. This effect is similar to the midnight sun effect experienced in the polar regions. There are also several short-lived peaks in the count rates, for example at days ~ 5, ~ 321. These increases occur as the result of meteor showers, (quadrantids and geminids respectively) when the number of shower meteors add to the usual number of sporadic meteors. Not all the showers are obvious in this composite year for example the perseids, a long lived shower that occurs between days ~ 196 and ~ 237 and leonids that occur around day 321. This is due to the considerable year-to-year variability in the strength of the showers. A weak shower will not enhance the meteor count rates enough to produce a distinct peak in the figure.

2.8 Determining Hourly-Mean Zonal and Meridional Winds

The calculation of the zonal and meridional hourly-mean winds depends on a series of simplifying assumptions. These are:
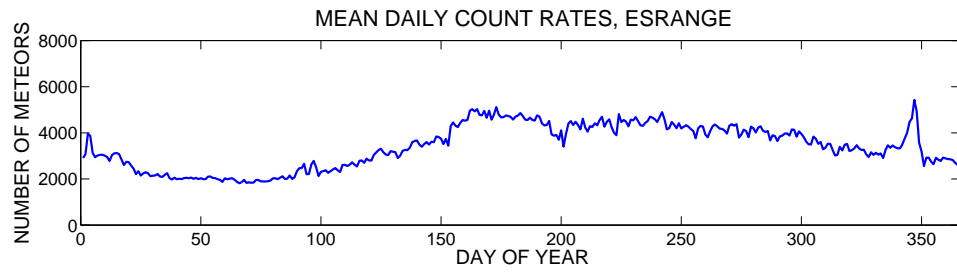
Figure 2.16: Superposed epoch of daily meteor counts over Esrange for 2000 to 2008.

1. Vertical velocities in the MLT are negligible when compared to the horizontal velocities. This allows the measured radial velocities to be unambiguously converted into horizontal velocities. This assumption is justified as the vertical winds are known to be at least an order of magnitude smaller than the horizontal winds (e.g., *Mitchell and Howells*, 1998).

2. The atmosphere moves as a uniform slab, in each height gate, across the field of view of the radar. This assumption is justified for motions that are uniform across the horizontal extent of the radar's collection volume, e.g., tides, planetary waves and the mean winds.

Hourly-mean winds can be calculated, based on these assumptions, by combining the measurements from individual meteors scattered throughout the collecting volume. All the radars discussed here use a two-hour window incremented by one hour to produce hourly-mean zonal and meridional winds.

2.8.1 Deriving Winds from the Rothera and Esrange Radars

The first step in the analysis of the radar data is the rejection of any spurious echoes. Any meteor echoes that *do not* meet the following criteria are rejected.

- *No* ambiguity in position (ambig of 1). A definition of ambig is given in Table 2.2, page 39.

- An echo decay time (TAU in Table 2.2) of greater than 0.015 s. This eliminates any short lived noise spikes.

The measured *radial* velocity, V_{rad}, for each echo is converted into a *horizontal* velocity, (V_h), using equation 2.2. This includes a correction for the curvature of the Earth.

$$V_h = \frac{V_{rad}}{sin(\alpha)}.$$

(2.2)

Where α is defined as:

$$\alpha = cos^{-1}\left(\frac{(r_E + h)^2 + r^2 - r_E^2}{2r(r_E + h)}\right) \tag{2.3}$$

and h is the true height of the meteor, r_E is the radius of the Earth, r is the range to the meteor. The relationship between these parameters is illustrated in Figure 2.17.
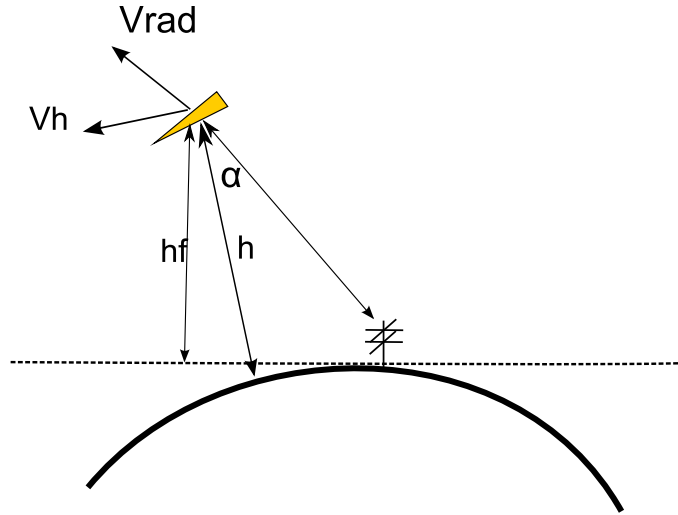
Figure 2.17: Geometry of the curved Earth correction and wind calculation. Note V_{rad} is the measured radial velocity, V_H is the calculate horizontal velocity, R is the range of the echo, R_E is the radius of the Earth, h is the calculated height, and h_f is the height uncorrected for the Earth's curvature.

Once the horizontal velocity has been determined, echoes with very high velocities (> 150 ms^{-1}) are rejected. This value was chosen as very few meteors velocities are this large and they can be defined as outliers. These very high horizontal velocities are usually associated with the small values of α that occur when the range is small. These can occur at small zenith angles and to eliminate these spurious velocities, meteors with zenith angles of less than 15° are not included in the analysis.

Within each height gate and two-hour interval the meteors are distributed approximately evenly in azimuth around the radar. Positive horizontal velocities are directed towards the radar, negative horizontal velocities away from the radar. Following the assumption that the atmosphere is moving as a slab across the field of view of the radar, the horizontal velocities will follow a sine wave in azimuth. Small-scale motions that are unresolved by the radar result in a scatter of the horizontal velocities away from a perfect sine wave. A new technique using the scatter introduced by these small-scale motions as a proxy for high-frequency gravity-wave activity is discussed in Chapter 3. An example of data of this type can be seen in Figure 2.18 which shows a typical example of a sine-wave fit to two hours worth of data from all available heights over Rothera.

The height-finding capability of the Skiymet radars allows the calculation of vertical profiles of the wind. To do this the meteor echoes are grouped in to six height gates which are analysed separately using the method described above. The height gates used are $(78 - 83)$, $(83 - 86)$,
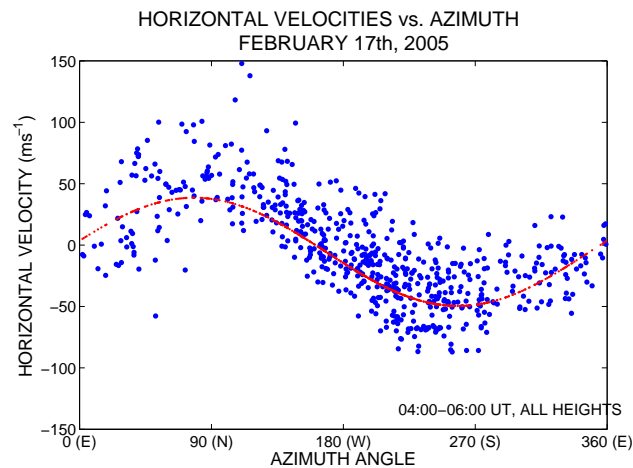
Figure 2.18: A plot of azimuth angle against horizontal velocity for individual meteors recorded between 04:00 and 06:00 UT on February 17th, 2005 over Rothera. The red line represents a least squares fit of a sine wave to the distribution of horizontal velocities in azimuth.

$(86 - 89)$, $(89 - 92)$, $(92 - 95)$, $(95 - 100)$ km. The height gates thus have depths of 5, 3, 3, 3, and 5 km. The upper and lower gates are slightly wider so that enough meteors are detected within these gates for a reliable wind estimate to be made. A representative height for each gate is defined as the mean height of echoes detected within each gate. This differs from the centre of the height gate because the distribution of meteors varies strongly with height. Thus, winds at six heights between 80 and 100 km are calculated with representative heights of 81.1, 84.6, 87.5, 90.4, 93.3 and 96.8 km.

Once a sine-wave has been fitted to all the meteors in a time-height window, a Student's T-test is performed to test the 'goodness of fit'. Bad fits can be produced when there are too few meteors collected or if there is a very uneven azimuthal distribution. The amplitude and phase of the fitted sine wave are used to calculate the velocity of the wind in zonal and meridional directions. This gives a representative wind velocity for the two-hour interval within the height gate considered. This two-hour window is incremented through the data in steps of one hour to provide an hourly spaced time-series of winds.

Once the time series has been compiled, an outlier rejection filter is applied. A window of 24 hours is incremented through the time-series of winds in steps of one hour. Any data points that are found to be more than two standard deviations away from the mean are rejected as outliers.

2.9   Summary

This Chapter has provided a brief introduction to the operation and physics behind meteor radar wind observations. Meteor radars are an excellent tool for studying the large-scale dynamics of the mesopause region. The three radars used in this study have been introduced and the

distribution of meteor echoes has been described. The representative height assigned to the UK system was also discussed and clarified. The calculation of zonal and meridional horizontal winds from meteor data was also presented.

Chapter 3

A New Technique for Studying Gravity Waves with Meteor Radar

3.1 Introduction

Gravity-wave studies have been conducted using a wide range of techniques including airglow-imagers, Medium Frequency (MF) radar, Incoherent Scatter (IS) radar, Mesosphere-Stratosphere-Troposphere (MST) radar, rockets, lidar, riometers and satellites. Each of these techniques is sensitive to waves with different parts of the gravity-wave spectrum. For example, lidars are most sensitive to gravity-waves with vertical wavelengths less than 10 km, relatively long periods and slow vertical phase progression (*Taylor*, 2002). Airglow imagers are ideal for studying short-period waves (periods less than 1 hour) with horizontal wavelengths between 5 and 200 km and vertical wavelengths greater than 8 km (*Taylor*, 2002). The resolution of gravity-wave observations with radar are limited by the size of the collecting volume and integration time (in the case of MF radars) which can vary between systems and analysis techniques. Generally MF radars can observe gravity waves with periods between 10 minutes and the inertial period, although the observations are frequently separated into period bands of 10 minutes to 6 or 8 hours and 8 to 24 hours.

Satellite measurements of gravity waves can be made using several different techniques. A common technique is to use satellite occultation. For example, *Baumgaerter and McDonald* (2007) measure the refractivity of radio occultation profiles between the CHAMP (Challenging Minisatellite Payload) and GPS (Global Positioning System) to determine gravity-wave potential energy. A similar technique using the temperature profiles measured by CHAMP/GPS was used by *Ratnam et al.* (2004) to examine gravity-wave activity during a sudden stratospheric warming. For this type of measurement the sensitivity depends on the satellites resolution along the Line Of Sight (LOS) and the viewing geometry to the phase fronts of the wave. For CHAMP/GPS a typically resolution is ∼300 km for a transparent path limb sounding. For a scan that is 90°from

the satellite path the resolvable wavelength can be smaller than 300 km.

Direct observations can also be made using satellites. *Alexander and Teitelbaum* (2007) uses measurements from the AIRS (Atmospheric Infrared Sounder) on the AQUA satellite to observe the 3-D structure of gravity waves. These measurements estimate the temperature amplitude of waves from fluctuations in the radiance received by the infrared channels on the satellite. Radiance/temperature measurements of this type are sensitive to perturbations with horizontal wavelengths over 100 km, and vertical wavelengths longer than 10 km (*Wu et al.*, 2006)

AURA, MLS (Microwave Limb Sounder) has also been used to study gravity wave temperature fluctuations. These limb radiances are sensitive to waves with horizontal wavelengths over 30 km and vertical wavelengths longer than 30 km.

Other spaced based but not satellite observations have also been made (e.g., *Fritts et al.*, 1989). *Ern et al.* (2004) use temperature fluctuations obtained by CRISTA (Cryogenic Infrared Spectrometers and Telescopes for the Atmosphere). This is a limb scanning instrument flow on shuttle missions in 1994 and 1997. It recorded temperature profiles in the stratosphere to a high resolution. This technique can extract gravity wavs with horizontal wavelengths of over 100 km and a vertical wavelengths between 5 and 25 km for the first mission and 6 and 30 km for the second mission.

However, few studies have used meteor wind radar because of the limitations on their spacial and temporal resolution (discussed in Chapter 2).

This Chapter describes a new technique for observing gravity-waves with meteor radar. The technique uses the variance of the horizontal velocities of individual meteor echoes as a proxy for high-frequency gravity-wave activity. This technique is applied to data recorded by the polar Skiymet radars at Esrange and Rothera.

The reasoning behind the new technique and the part of the gravity-wave field which are accessible, is described in Section 3.2. It is demonstrated that this method primarily measures high-frequency gravity waves (periods of ~ 20 minutes to ~ 2 hours) and gravity waves with short horizontal wavelengths ($\lambda_x \leq 400$ km). The implementation of this technique is described in Section 3.3, in which the technique's ability to observe gravity waves is illustrated. The new technique is used in Section 3.4.1 to look at short-term gravity-wave variability. The application of the technique to the calculation of monthly-mean variances is presented in Section 3.4.4. Section 3.4.4 also considers the relationship to the underlying zonal wind field and Section 3.4.5 presents inter-hemispheric comparisons of the Antarctic and Arctic drawn between Rothera and Esrange. Section 3.4.6 presents gravity-wave interactions with tides and planetary waves.

3.2   The Variance Technique

This is a new technique that uses the variance of the horizontal wind velocities of individual meteor echoes as a proxy for gravity-wave activity. For reasons of clarity this will be referred to as the *variance technique* from this point onwards. This section describes how the technique can be applied to calculate gravity-wave variance on a two hourly basis in 6 height gates between approximately 80 and 100 km for any all-sky meteor radar similar to a Skiymet radar.

The reasoning behind the technique is as follows:

1. We assume that there is a 'homogeneous wind' field across the field of view of the radar. This is composed of elements that do not vary significantly over the horizontal scale of the meteor collecting volume. Tides, planetary waves and mean winds all satisfy this condition. This 'homogeneous' motion is a part of the horizontal velocity measured for each individual meteor echo, and can be calculated using an ensemble of meteors. This was discussed in detail in Chapter 2.

2. As well as the 'homogeneous' wind, tide and planetary wave field described above, there are also many waves of a scale size smaller than that of the collecting volume of the radar. These are mostly gravity waves with periods less than $\sim$ 2 hours. Gravity waves in this frequency range generally have horizontal wavelengths which are smaller than the collecting volume of the radar. An example of such waves can be seen in Figure 3.1a, taken from *Nielsen et al.* (2006) where meteor-radar wind measurements and airglow images were used to study gravity waves over Esrange. The figure shows the collecting volumes of the meteor radars at Esrange and Andennes overlaid on a map (the smaller circles centred on these locations). A larger circle representing the field of view of the airglow imager at Esrange is also shown. Representations of the phase fronts of gravity waves observed on one night can also be seen. The horizontal wavelengths and periods for the waves shown were $\sim$ 27 km and $\sim$ 10 minutes respectively for the wave that occurred at 16:37 UT and $\sim$ 40 km and $\sim$ 11 minutes for the wave at 17:47 UT. Figure 3.1b shows the position of meteors detected at the same time as the gravity-waves were observed (in Figure 3.1a). From this it can be seen that gravity waves with horizontal wavelengths short enough that several wavelengths fall within the collecting volume of the radar and will contribute to the horizontal velocity measured by individual meteors. As a consequence of their small horizontal scales, the radar cannot resolve these waves. Nevertheless, they can be measured through the scatter they introduce in the horizontal velocities of individual meteor echoes.

3. A measure of the activity of these small-scale waves can be made as follows. The 'homogeneous' part of the atmospheric motion in the collecting volume can be removed from the horizontal velocity measured for each individual echo. This leaves only the contributions to the horizontal velocity from these small-scale waves which can then assumed to be due
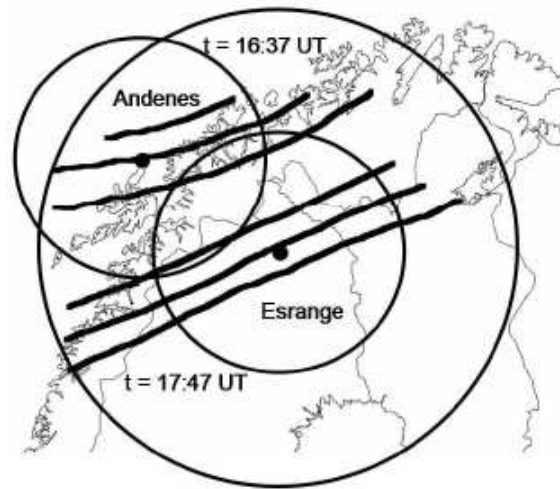
(a)
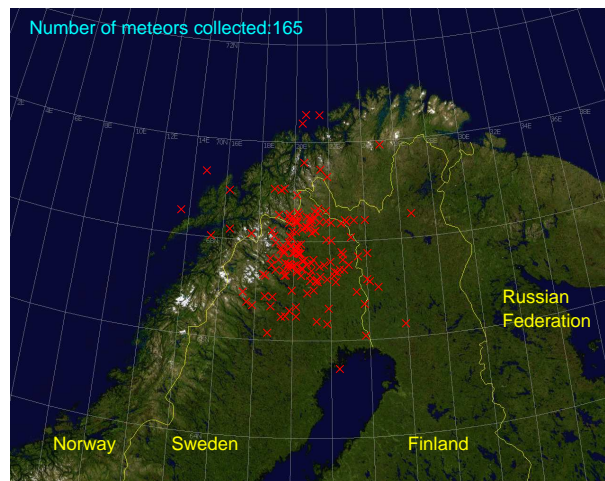
(b)

Figure 3.1: (a) A schematic diagram showing phase fronts of gravity waves over Esrange and Andennes for gravity waves detected on January 27th 16:37 and 17:47 UT. The small circles represent the field of view of the meteor radars at Esrange an Andennes, the larger circle represents the field of view of the airglow imager at Esrange. (b) A map of Scandinavia overlaid with the positions of 165 individual meteors detected on January 28th, 2003 between 15:00 and 18:00

to gravity waves. The variance of the remaining horizontal velocities of the meteor echoes can be used as a measure of the activity of the high-frequency gravity-wave field.

The small-scale waves within the collecting volume of the radar also have smaller temporal scales than tides, planetary waves and the mean wind. As a routine data product the meteor radars calculate two-hourly wind values. The small-scale waves that are the focus of this chapter have periods that are less than this and as such they cannot be resolved temporally or spatially by the meteor radar.

Both the 'homogeneous' and 'inhomogeneous' parts of the wind field can be seen in a plot of the horizontal velocities of meteors collected during one day. As an example, Figure 3.2 presents the horizontal velocities at all azimuth angles between 04:00 and 06:00 UT on February 17th, 2005 over Rothera. The homogeneous part of the flow (the background motion composed of mean winds, planetary waves and tides) is represented by the sine wave fit to all meteors, plotted on the figure as the smooth red line. The inhomogeneous component of the wind field can be seen in the scatter of the meteors away from this homogeneous background motion.
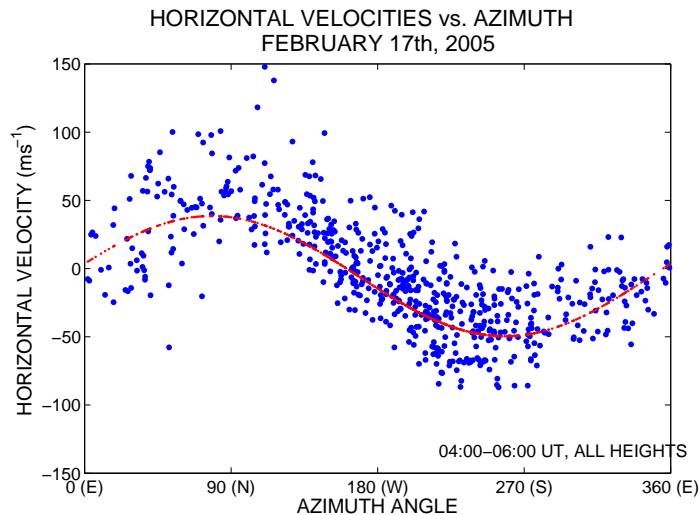
Figure 3.2: A plot of azimuth angle against horizontal velocity for individual meteors recorded between 04:00 and 06:00 UT on February 17th, 2005 over Rothera. The red line represents a least squares fit of a sine wave to the distribution of horizontal velocities in azimuth. This corresponds to the homogeneous flow across across the collecting volume resulting from a superposition of mean winds, tides and planetary waves.

The scatter of the horizontal velocities, measured by the variance, can then be used as a proxy for gravity-wave activity. The use of the variance of vertical or horizontal winds as a proxy for gravity-wave activity is, in fact, already well established. However, previous studies have used volume averages to determine winds rather than the ensemble of point measurements used here (e.g., *Vincent and Fritts*, 1987; *Isler and Fritts*, 1996; *Manson et al.*, 1998b; *Mitchell and Howells*, 1998; *Williams et al.*, 2006; *Dowdy et al.*, 2007).

This method differs from other variance measures in two very significant ways. Firstly, previous studies have used the variance of the wind measurements made as an average over a certain time interval. For example, *Mitchell and Howells* (1998) determined vertical wind speeds integrated over five minutes intervals, using the EISCAT VHF radar. *Manson et al.* (1998b) also used five minute samples obtained with an MF radar at Saskatoon, and a shorter two minute resolution was used by *Tsuda et al.* (1994) with the MU radar. This is in contrast to the collection of essentially instantaneous, localised individual measurements made in a time interval by the meteor radar.

Secondly, meteor echoes are detected within a large volume of atmosphere. An indication of

the collecting volume of the radar can be seen in Figures 2.12 and 3.1b which show the meteor echoes detected over the course of one day and over an interval of three hours respectively. Although studies made using the spaced antenna, Full Correlation Analysis (FCA) for MF radars also rely on a collecting volume with a large horizontal extent, IS radar, lidar and MST radar have much smaller collecting volumes. For example, the EISCAT VHF radar has an effective beam width of 2×3 km at a height of approximately 100 km.

Like most techniques, the method described in this chapter is sensitive to only a part of the gravity-wave spectrum. To illustrate this, consider that in order to calculate the variance from horizontal velocities, the horizontal velocity due to the background wind is removed. This removes any oscillations that are homogeneous across the field of view of the radar if they have a period significantly longer than the observation time. So, as well as removing the bulk motion (mean wind, planetary waves and tides), the analysis also removes any gravity waves with a period of more than ~ 2 hours and with horizontal scales long enough to become part of the background flow.

Note that gravity waves with periods very close to the Brunt-Väisälä period will not contribute strongly to the measured variance. This is for two reasons. Firstly, for these gravity waves, the associated air-parcel motion is almost entirely vertical. The analysis uses only meteors more than 15° from the zenith, the radial velocity for these echoes is dominated by the horizontal motion. As a result they contribute little to the horizontal variance considered here. Secondly, the vertical velocities associated with these waves is known to be small, ≤ 2 ms^{-2} (e.g., *Fritts and Yuan*, 1989; *Mitchell and Howells*, 1998). The small vertical motion compared to the much larger horizontal motion means the horizontal scatter introduced by these waves will therefore make a small contribution to the horizontal variance.

In summary, the variance technique described here is capable of observing gravity waves with periods from near to the Brunt-Väisälä period to ~ 2 hours. The basic data product of this analysis is variances associated with these high-frequency/short-horizontal wavelength gravity waves, estimated for particular height ranges and intervals of time.

3.3   Data Analysis - Applying the Variance Technique

This section discusses the accurate removal of the homogeneous part of the wind field from the measured horizontal velocities and considers the contribution of measurement uncertainties to the variance.

Figure 3.3 presents a plot of the horizontal velocity against azimuth angle for all of the meteors detected by the Rothera radar on February 19th, 2005. This data has a variance of 1377 m^{2}s^{-2}. A sine wave fit to the data is also shown (as the red line) and represents the homogeneous motion

across the field of view of the radar during the day. The scatter of the horizontal velocities around this line is the result of inhomogeneous part of the wind field. On the timescale of one day this includes a contribution from tidal winds and vertical shear in the horizontal wind as well as smaller-scale gravity waves.
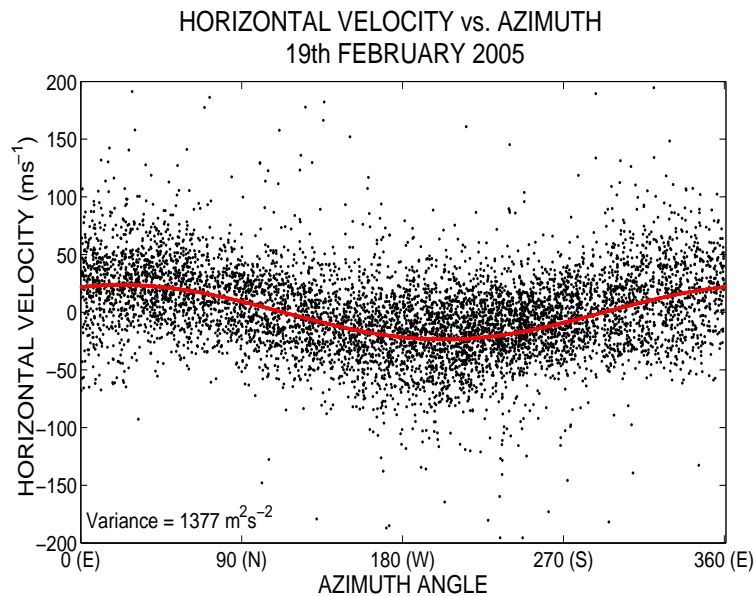
Figure 3.3: Horizontal velocity vs. azimuth for meteors detected on 19th February 2005. This includes meteors from all heights and times. The superimposed red line indicates a sine-wave fit to the distribution representing the background motion of the atmosphere.

To illustrate the magnitude of the change in the homogeneous wind field over the course of a day, Figure 3.4 presents the zonal winds for January 6th, 2007. The winds are plotted as coloured contours and overlaid with a scatter plot of the time and height of each meteor detected during this day. This date was chosen because it clearly shows the winds associated with the 12-hour tide (peaking at $\sim$ 02:00 and 15:00 UT) as well as the summer time shear in the zonal winds (a change from westwards to eastward winds from 80 to 100 km). Considering the height and time of individual meteor echoes, it can be seen that the background wind can differ greatly over 1 - 2 hours as well as over 2 - 3 km. This type of variation will cause a significant part of the scatter seen in Figure 3.3 and must be effectively removed to leave only the contribution from gravity waves.

Due to the rapid changes in background wind, calculating an average value of the background wind will not provide a reliable estimate for all of the meteors. The use of very short time intervals is also not possible due to the reduced number of meteors that are available. Therefore, to effectively remove the background motion, an accurate value of the wind field must be calculated for the height and time of each individual meteor. To do this, the hourly spaced winds recorded in the routine operation of the meteor radar (as described in Chapter 2) are used as a basis to interpolate a value of the zonal and meridional wind for each meteor echo individually. The interpolation method uses a Delauney triangulation based cubic interpolation (for further information on this and other relevant interpolation schemes see e.g. *Foster and*
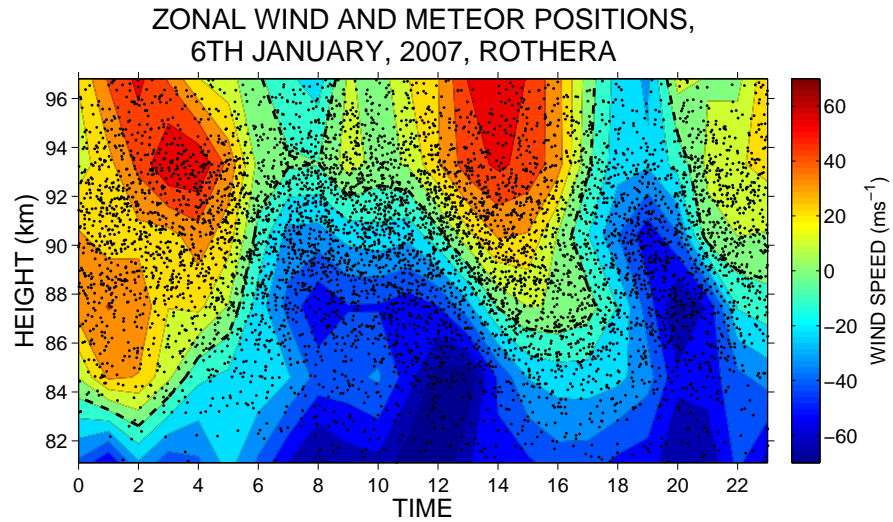
Figure 3.4: Contours of the zonal wind speed for the 6th January, 2007 over Rothera. Overlaid is a scatter plot showing the position in height and time of all the meteors detected on this day.

Evans (2008)).

The wind field used as a basis for the interpolation is made up of hourly spaced values of wind (calculated using a 2-hour window incremented by 1 hour), at six height gates representative of 81.1, 84.6, 87.5, 90.5, 93.3 and 96.8 km. Even though the meteors from 80 to 100 km have been used in the calculation of the winds any interpolation above 81.1 or below 96.8 km would be unconstrained and may have large errors. As a result meteors beyond this height range were excluded from the analysis.

For each echo, the value of the interpolated background wind is removed from the measured horizontal velocity. The remaining horizontal velocity is then assumed to be due to the inhomogeneous part of the wind field. Figure 3.5 shows the same day of data as Figure 3.3, but with the background motion removed using the interpolation method described above. The removal of the homogeneous part of the wind field decreases the amount of scatter within the horizontal velocities leaving only the contribution assumed to be from gravity waves. The data have a smaller variance of 470 m^2s^{-2} compared to the 1377 m^2s^{-2} of Figure 3.3.

As the homogeneous part of the wind has been removed the only remaining components are the short-period, small horizontal wavelength gravity waves. Before the variance is calculated, meteors with zenith angles larger than 75° and smaller than 15° are removed. Those meteors near to the zenith (less than 15°) are excluded because the error on the horizontal velocities inferred from these measurements can be very high. Those meteors detected at zenith angles greater than 75° correspond to meteors with very long ranges ($\sim$ 700 km) and can also have very high errors. The remaining meteors are then separated into six height gates of $81.1 \leq z < 83$, $83 \leq z < 86$, $86 \leq z < 89$, $89 \leq z < 92$, $92 \leq z < 95$, $95 \leq z < 96.8$. Within these height gates the meteors can be binned into a chosen time interval.

HORIZONTAL VELOCITY vs. AZIMUTH,
BACKGROUND REMOVED, 19th FEBRUARY, 2005
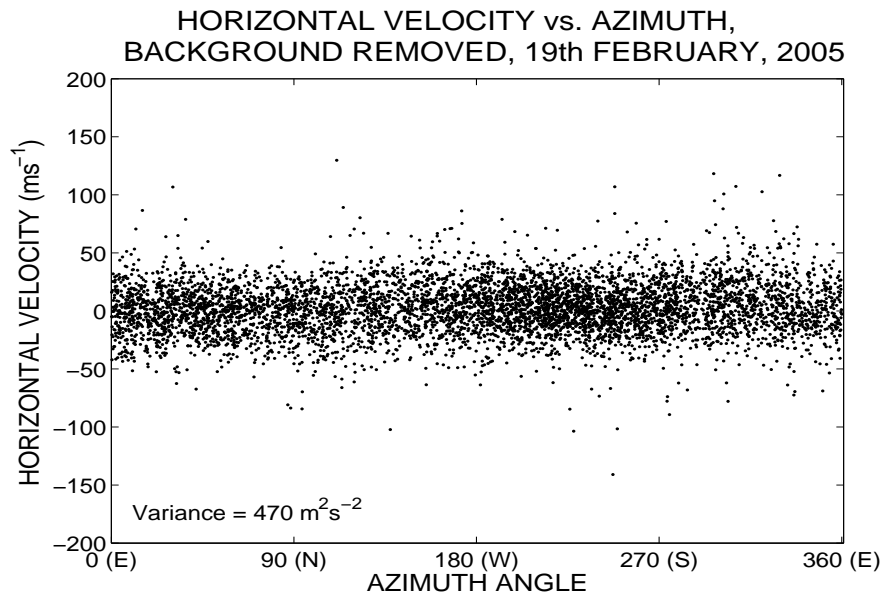
Figure 3.5: Horizontal velocity with azimuth angle for all meteors detected on 19th February, 2005 with the background motion removed.

Figure 3.6 shows meteor echoes over Rothera from 06:00 to 12:00 UT on February 19th, 2005 from two different height gates. Figure 3.6b shows the meteors from 83 to 86 km and Figure 3.6a shows meteors from the same interval of time, but in a height range of 92 to 95 km. The difference between the variances in these two height gates is clear, with values of 334 m^2s^{-2} in the lower height gate and 490 m^2s^{-2} in the higher height gate.

Separating the meteors into time and height bins allows a time series of variance to be calculated. The time bins used can be varied to produce datasets with varying time steps allowing different scales of variability to be investigated. To calculate daily and monthly-mean values, a window of 6-hours incremented through the data set by 3 hours was used. This was applied independently to each height gate. A relatively long window of 6 hours was chosen to maximise the number of meteors available in each time-height bin. This is particularly important for the top and bottom height gates where meteor count rates are lower. A variance was only calculated if at least 30 meteors were detected in the 6-hourly bin. This dataset shall be referred to as *6-hourly variances*.

To examine short-term variability of the wave field, variances were calculated using a window of 2 hours incremented in 1 hour steps. Although this provides finer time resolution, the number of meteors in the top and bottom height ranges is reduced relative to the longer time window. The minimum number of meteors needed to calculated a variance in each time-height bin was set at 30. This was chosen because it allows reliable determination of variance without creating too many gaps in the data. These hourly values are useful for investigating the effect of tidal winds on the gravity-wave field and will be referred to as *2-hourly variances*.

Another way to investigate tidal effects and to produce a dataset of higher time resolution is

HORIZ. VELOCITY vs. AZIMUTH,BACKGROUND REMOVED,
19th FEBRUARY 2005, 92–95 km, 6:00 – 12:00 UT

(a)

HORIZ. VELOCITY vs. AZIMUTH, BACKGROUND REMOVED,
19th, FEBRUARY 2005, 83 – 86 km, 6:00 – 12:00 UT

(b)
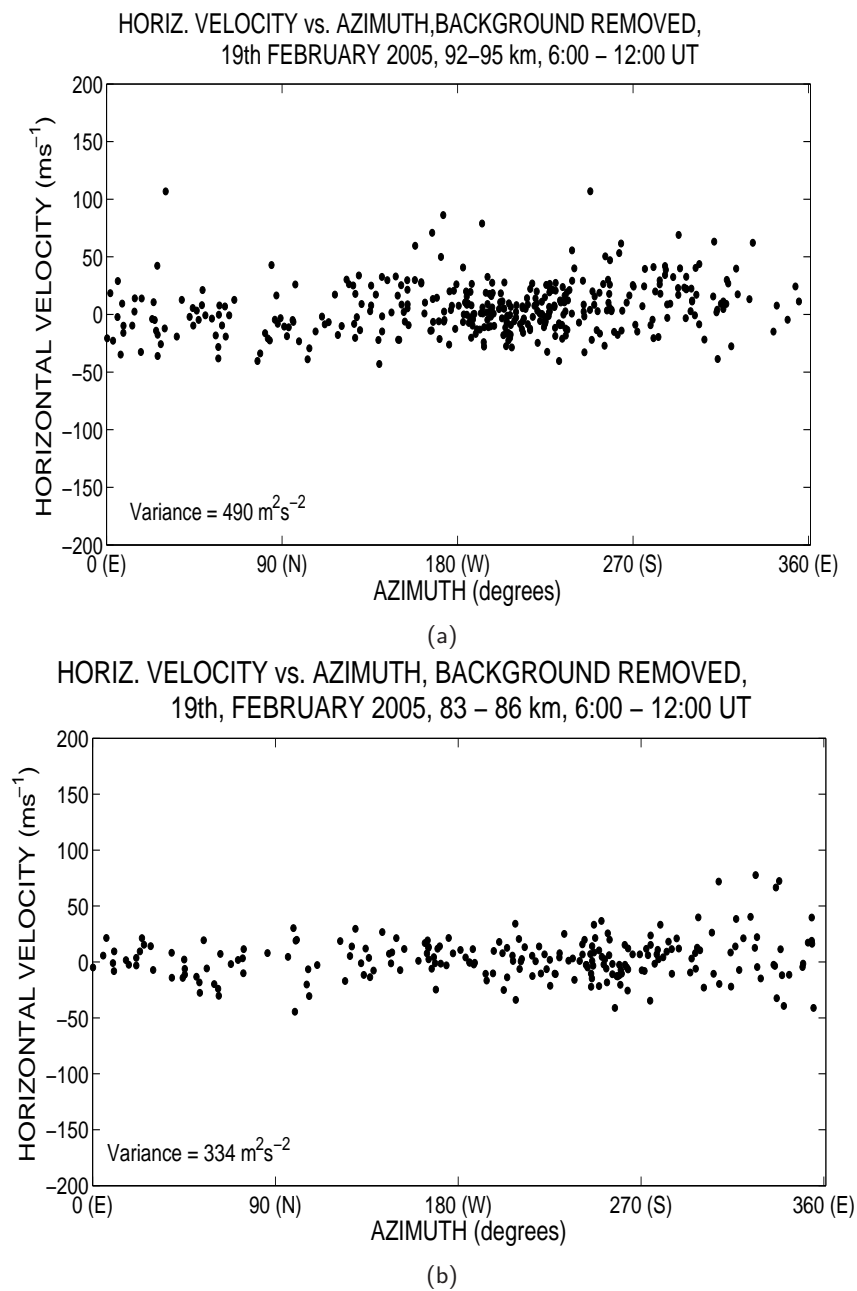
Figure 3.6: Examples of horizontal velocity as a function of azimuth for 19th February, 2005 over Rothera. Meteors from 06:00 to 12:00 UT are used in both plots, (a) meteors in the height range 83 - 86 km and (b) 92 to 95 km.

to construct a *composite day* of all the meteors detected within a month. Variances can then be calculated for each time interval independently and used to construct a day representative of that month. Note that this analysis assumes that the features of interest are repeated in each successive day. It sacrifices the ability to detect day-to-day variability in order to attain better time resolution within the composite day. In the work presented here, the composite day analysis used a 1-hour time step.

In order to remove out-lying data points in the variance time series, a window of 48 hours was

incremented through the dataset in steps of 24 hours. Within this window any values that were more than 3 standard deviations away from the mean were removed. The number of outliers is not high and only $\sim 3\%$ percent of the data were so removed. This preserves the vast majority of day-to-day variability but removes the extreme values identified as outliers that may be the result of interference. The fact that 3% of the data were thus removed indicates that the distribution of variances is not Gaussian. Further investigation revealed that the variances follow a log-normal distribution.

Figure 3.3 shows the distribution of variances for all data over Rothera at $\sim$90 km. For a lognormal distribution of variances, taking the arthimetic mean of the data may give a slightly higher mean than using the geometric average. A geometric mean based on the lognormal distribution will give a more reliable mean (*Baumgaerter and McDonald*, 2007). In order to quantify the differences between assuming a Gaussian and lognormal distribution, the data was reanalysed and monthly-mean data were calculated using the geometric average for a lognormal distribution. The improvement in the averages is minimal, and always below 10%. The seasonal cycle, monthly-mean values, behaviour with height and daily averages are essentially identical using the two averaging techniques. This is because, although the variances follow a lognormal distribution, the shape is close to Gaussian and the skew of the data is low. As a result of this the Gaussian mean is used as very little improvement is gained by using the geometric mean.
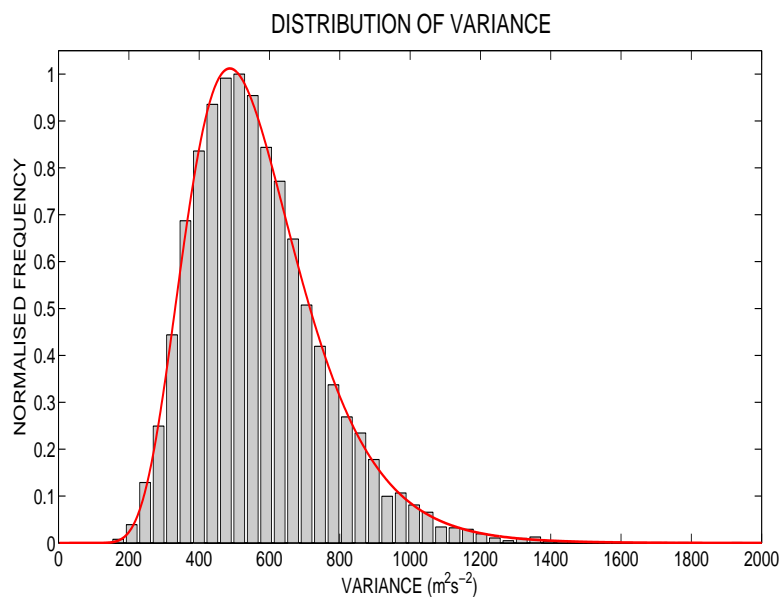
Figure 3.7: Normalised histogram showing the distribution of 6-hourly variances for all data collected over Rothera at a height of about 90 km.

3.3.1 Is there a Contribution to Variance from Measurement Uncertainty?

An important consideration for the variance technique is how much contribution the uncertainties on the individual velocity measurements make to the calculated variance. A measure of the uncertainty on the individual radial velocities is given by the standard deviation of the radial velocity, as measured by each antenna pair. This uncertainty is recorded for each individual radial velocity calculated. This uncertainty is generally small and, in fact, any echo that has an uncertainty larger than 5.5 ms^{-1} is not recorded. This raises the question of how much this uncertainty will contribute to the variance calculated from the horizontal velocities.

Figure 3.8 presents an example of the typical distribution of the uncertainties on the *horizontal* velocities for meteors detected from all height gates on February 19th, 2005. Considering the figure, it can be seen that most of the meteors have uncertainties that are below 5 ms^{-1}, and all have uncertainties below 20 ms^{-1}.
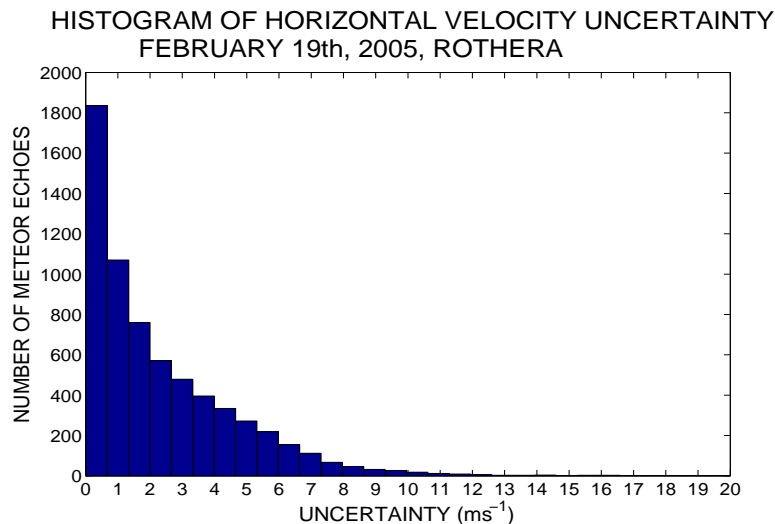
Figure 3.8: Histogram of uncertainty on horizontal velocities for February 19th, 2005.

This day was chosen to be the same day as the examples used in Figures 3.3, 3.5 and 3.6, so that direct comparisons between the horizontal velocities and their uncertainties can be made. Figure 3.9 shows the same uncertainty data plotted as a function of azimuth, using the same format and on the same scale as Figure 3.3 to make these comparable. Note that uncertainties are always positive unlike the horizontal velocities.

Figures 3.8 and 3.9 give an insight into the contribution that the uncertainties make to the calculated variances, attributed to gravity waves. For all the meteors collected on this day the uncertainties contributed 5.3 m^{2}s^{-2} to the total variance of 470 m^{2}s^{-2} (see Figure 3.5). This represents only 1.1% of the total. It can therefore be concluded that the variance calculated and assumed to be due to gravity waves is dominated by geophysical variability and overall the contribution made by measurement uncertainties is small.
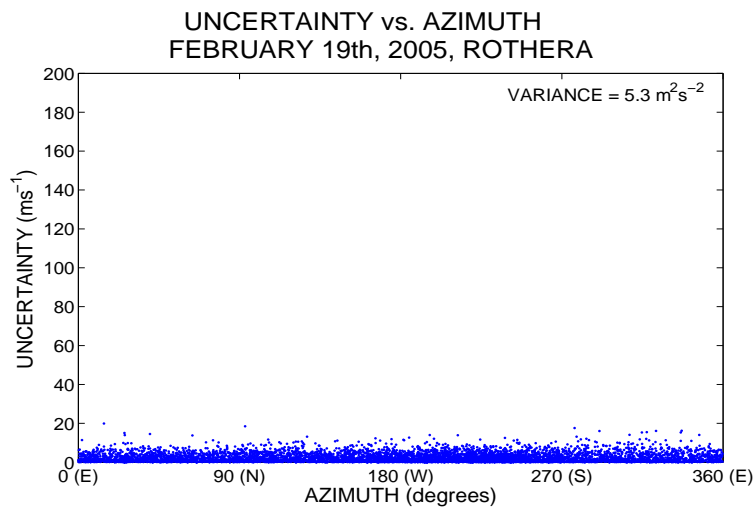
Figure 3.9: Uncertainty on horizontal velocity vs. azimuth angle for all meteors detected on February 19th, 2005.

Because of the poorer signal to noise ratio for echoes detected at very long ranges, an increase in the uncertainty on individual meteor echoes might be expected to with increasing height. Figure 3.10 presents the mean and mode of the uncertainty on the horizontal velocities of all meteors detected a typical day, February 19th, 2005.

Considering Figure 3.10, there is very little variation of the uncertainty on the horizontal velocity with height. Both the mean and mode of the uncertainty are low for all height gates and do not increase significantly with height. This indicates there is no significant increase in uncertainty with meteor height.

3.3.2 Examples of the Variance Data

To demonstrate the quality and type of data produced from the variance technique, Figure 3.11 presents 6-hourly height profiles of variance for (a) February 17th and (b) February 18th, 2005. Each height gate and 6-hour time interval is calculated independently. These days were selected because they display behaviour typical throughout the dataset.

Considering the complete profiles, it can be seen that there is a clear tendency for increasing variance with increasing height, particularly above ~ 90 km. This is consistent with a growth in the amplitudes of waves as they propagate vertically upwards (e.g., *Mitchell and Howells*, 1998; *Fritts and Alexander*, 2003; *Dowdy et al.*, 2007).

Another feature that can be seen in this example data is a similarity in the shape of profiles throughout a day. This can be clearly seen for the 17th, when the variance exhibits limited growth below ~ 90 km and then rapid growth above in all the available profiles. This behaviour

(a)

(b)
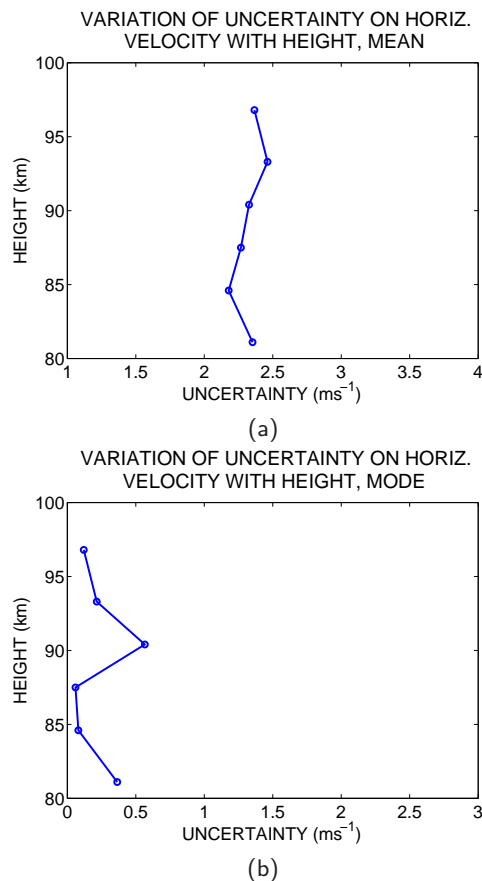
Figure 3.10: Uncertainty-height profiles for (a) the mean and (b) the mode of all horizontal velocities determined on February 19th, 2005.

will be discussed further in Section 3.4.1.

Although the profiles show a consistent shape throughout the day there is also some variability. For example in (b), on the 18th the profile calculated for 00:00 to 06:00 shows a decrease in variance below $\sim$ 90 km and limited growth above. Also noticeable is the behaviour on the 18th, (b), between 12:00 and 18:00. This profile differs from the profile at the same time on the preceding day as well as from those during the same day. It is unlikely to be the result of a tidal interaction as it is not repeated at the same time in the two days presented. This behaviour may be the result of a duct present in either the winds or temperature profile of the MLT region at this time. However, it is also possible some of the variability on these time scales is the result of noise and uncertainty inherent in the calculation of variance.

The profile of the time interval 18:00 to 24:00 UT on the 17th is one example of the data gaps than occur in the dataset. These gaps can occur for several reasons. Usually this is because the background winds could not be calculated, or because not enough meteors were detected in the time-height bin to reliably calculate a variance, or the variance itself was rejected as an outlier.

In order to more clearly demonstrate the day-to-day variability, Figure 3.12 presents daily vari-
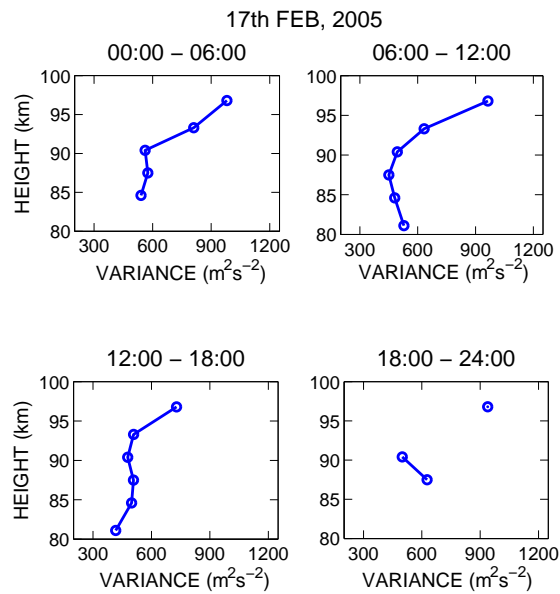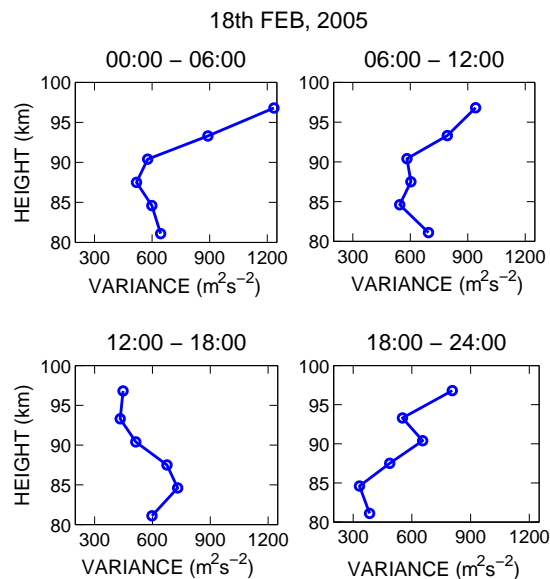
Figure 3.11: Variance-height profiles based on 6-hourly variance calculated over Rothera for (a) February 17th, 2005 and (b) February 18th, 2005.

ances over Rothera for heights from 81.1 to 96.8 km over the interval from February 14th, 2005 to November 28th, 2007. Each plotted value is a measure of the high-frequency gravity-wave field over one day. The red line plotted represents a 30-day smoothing applied to the data. This is provided to highlight any seasonal variation that may be present.
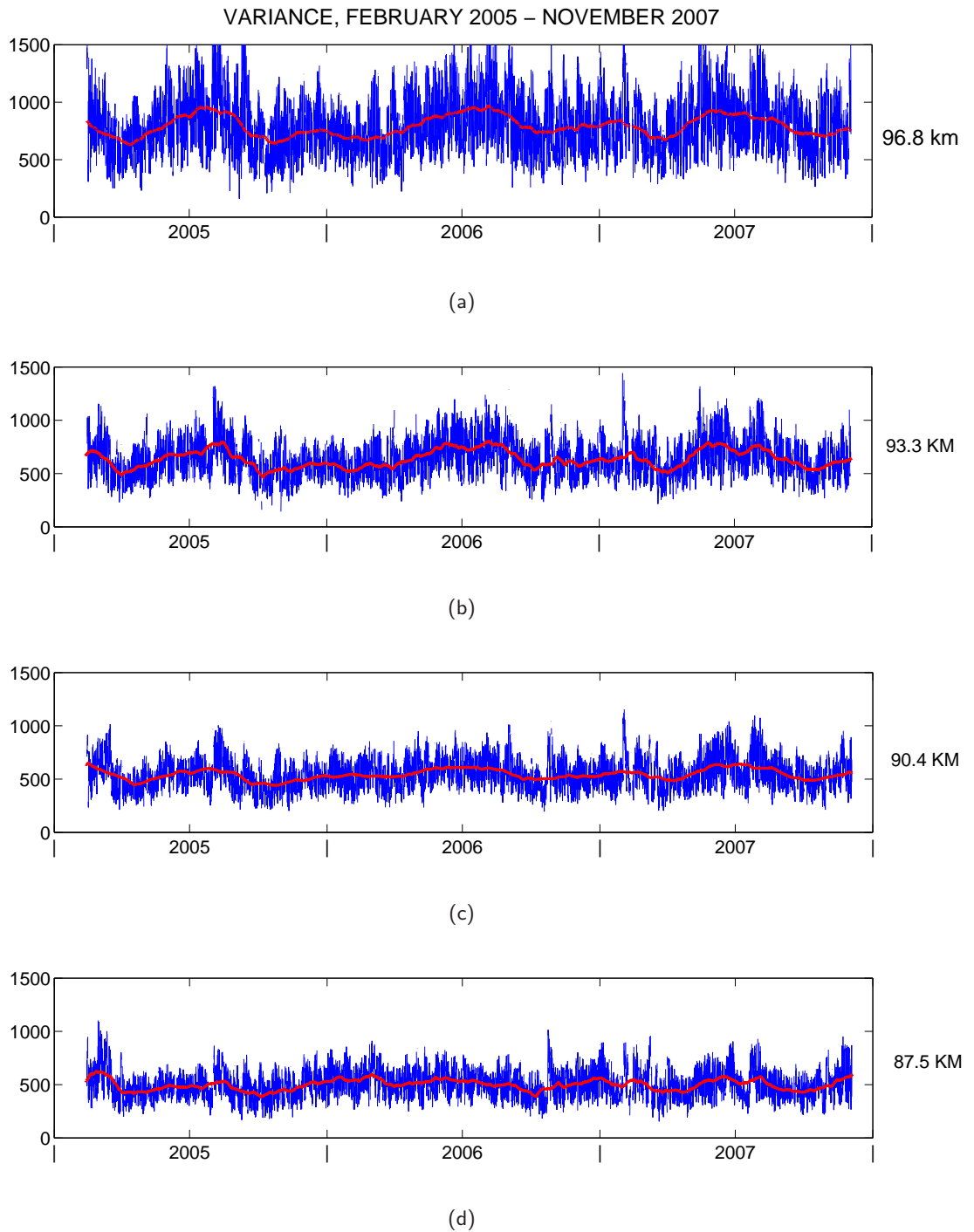
Figure 3.12: Continued on next page

Note that southern hemisphere summer is in December - February and so is at the end of the years in the plot. The Figure reveals several interesting gross properties of the gravity-wave field.

1. There is large day-to-day variability. This is shown in the large scatter of daily values around the 30-day smoothed line.

2. Variance increases with increasing height. This is most evident during the winter (June -
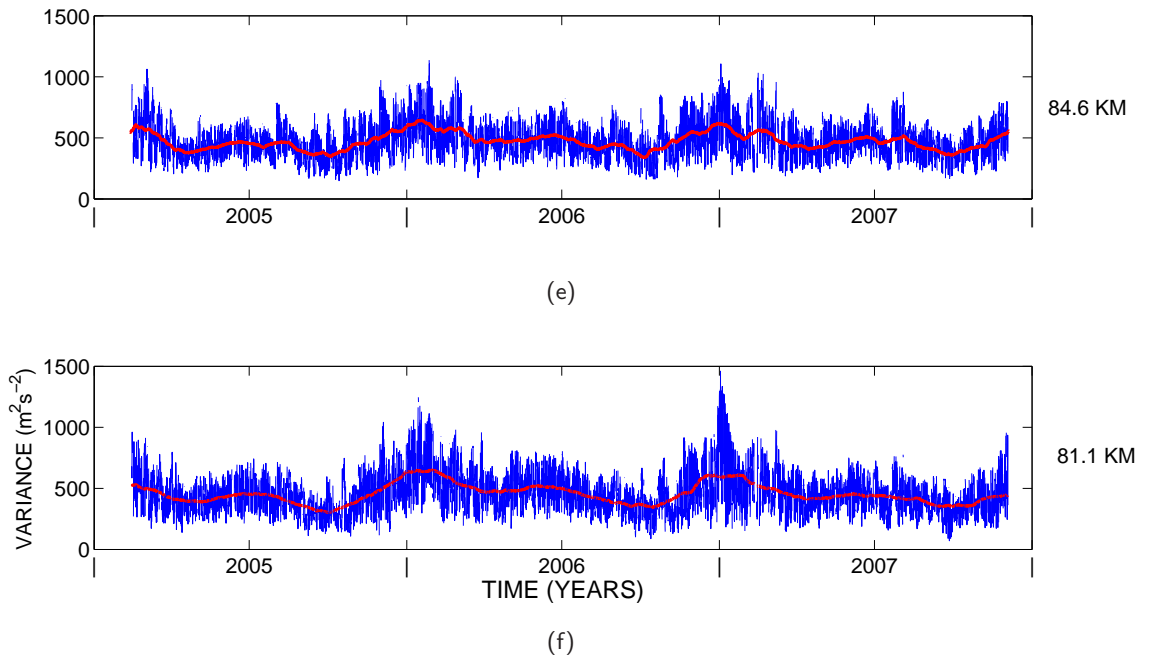
Figure 3.12: 6-hourly variances at Rothera for (a) 81-83 km (b) 83-86 km (c) 86-89 km (d) 89-92 km (e) 92-95 km and (f) 95-96.8 km. The red line indicates a 30-day smoothing of the data to reveal seasonal trends.

August) when the smoothed 30 day values increase from ~ 500 m^2s^{-2} at 81.1 km to ~ 800 m^2s^{-2} at 96.8 km, an increase of approximately 38 %.

3. A seasonal pattern is evident in all height gates. At the lower height gates the cycle is semi-annual in nature, with a strong peak in activity in summer and a smaller peak in winter. At the upper height gate the cycle becomes more annual, with a larger peak in winter.

In summary, Figures 3.11 and 3.12 both show examples of the gravity-wave variances that can be calculated using this technique. There are strong reasons to conclude that the calculated variances can be used as a proxy for gravity-wave activity. These are:

1. The magnitude of variances calculated using the new variance technique are similar to those of previous studies made at polar latitudes (e.g., *Vincent and Fritts*, 1987; *Vincent*, 1994; *Manson et al.*, 2004; *Dowdy et al.*, 2007).

2. The 6-hourly height profiles of variance vary smoothly with height, as can be seen in Figure 3.11. This would not be expected if the signal were dominated by noise.

3. The elimination of other sources of variance within the data, such as tides, planetary waves and the mean winds, support the conclusion that the remaining variance is due to gravity waves, as this is the only remaining known significant source of variance in the Mesosphere

and Lower Thermosphere (MLT) region.

4. The contribution to variance from measurement uncertainty has been shown to be very small ($\sim$1.5% compared to the horizontal variance attributed to gravity waves (Section 3.3.1).

The variance of the gravity-wave field is proportional to its kinetic energy per unit mass within the period and wavelength ranges accessible. Therefore, the variance technique can be used to calculate gravity-wave variances that can be used as a proxy for gravity-wave activity, or as a proxy for the kinetic energy per unit mass of high-frequency gravity waves.

3.4   Results

This section presents the results from the application of the variance technique to data collected by the meteor radars based at Rothera and Esrange. As already noted, this technique is sensitive to gravity waves in the period range from the Brunt-Väisälä period to about 2 hours.

Section 3.4.1 considers day-to-day variability in gravity-wave activity, the seasonal behaviour with height is considered in Section 3.4.2. The inter-annual variability of gravity-wave activity is considered in Section 3.4.4 and Section 3.4.5 considers inter-hemispheric differences between the Antarctic and the Arctic. Section 3.4.6 considers gravity wave-tidal interactions and the results are discussed in Section 3.5.

3.4.1   Short-Term (Day-to-Day) Variability of the Gravity-Wave Field

Figure 3.12 showed that there is considerable day-to-day variability in the activity of the high-frequency gravity-wave field. To examine this behaviour in more detail, the daily profiles of variance as a function of height were examined.

Figure 3.13 presents profiles from an almost complete month of data over Rothera during summer (December 2nd to the 31st, 2005) and Figure 3.14 presents daily variance profiles over Rothera for spring (September 1st to the 30th, 2005).

Considering Figures 3.13 and 3.14, several properties of the daily variances are immediately apparent. These include:

1. There is significant day-to-day variability. For example, the profiles for December 12th and 31st show distinctly different shapes. To characterise this variability, the standard

DAILY VARIANCES FOR DECEMBER 2005, ROTHERA
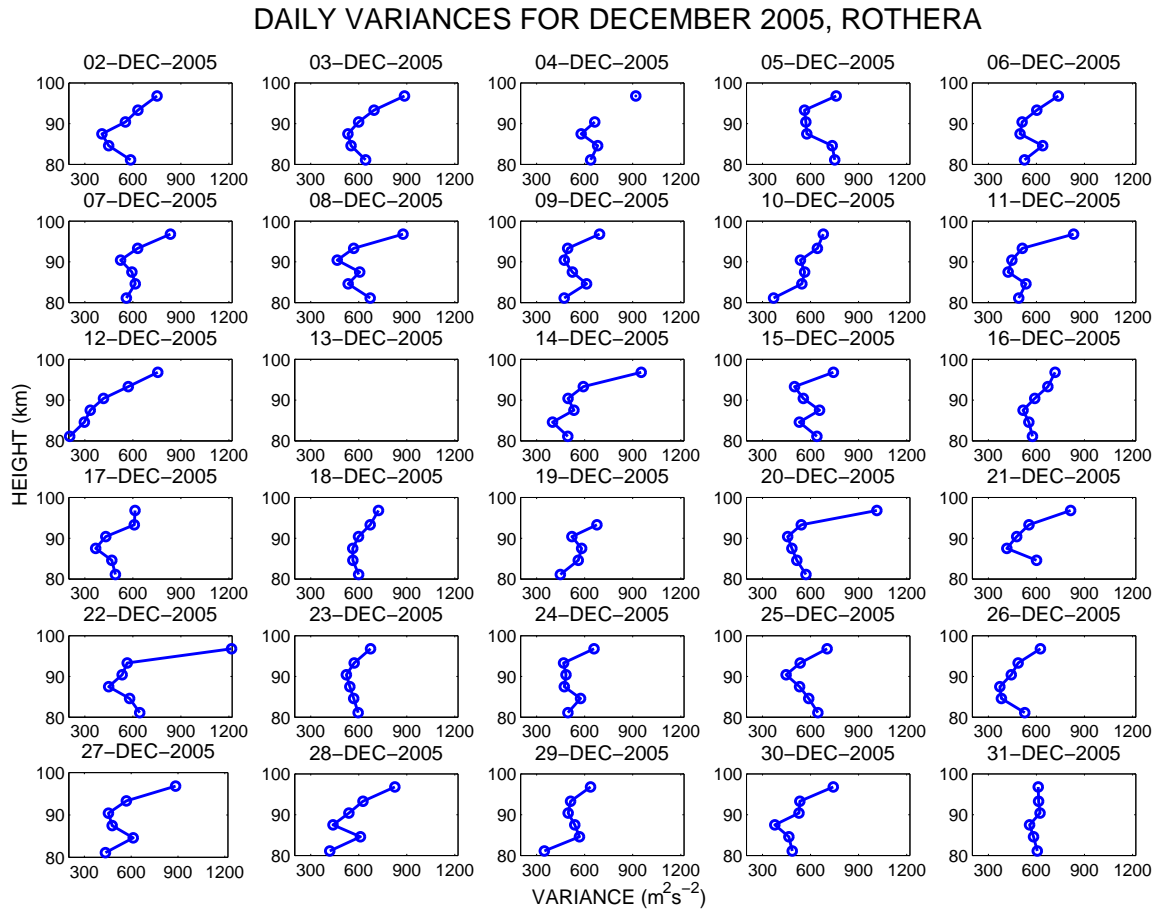
Figure 3.13: Daily profiles of variance against height over Rothera for December 2nd to the 31st, 2005.

deviation of the daily values in each height gate was calculated and taken as a percentage of the monthly mean. As an average across all 6 height gates the standard deviation is 25% of the monthly mean, indicating substantial day-to-day variability.

2. There is also an underlying structure to the profiles that can be seen in many of the profiles within a month. For example, in December 2005 the dominant behaviour is for the variance to remain constant or decrease below ~ 90 km and then to increase above. In contrast in September the dominant behaviour is increasing variance with height across the height range.

3. The growth of variance with height is less than the exponential increase $(e^{\frac{z}{H}})$ expected for free wave growth (i.e. vertical propagation without dissipation). Note that the growth of wave amplitude with height, z, scales as $e^{\frac{z}{2H}}$, in contrast to the variance which scales as $e^{\frac{z}{H}}$. The scale height, H, $(= \frac{kT}{mg})$ can be calculated, either from a reference atmosphere or using observations of temperatures made by rocket and falling sphere experiments (Section 3.4.3).

DAILY VARIANCE FOR SEPTEMBER 2005
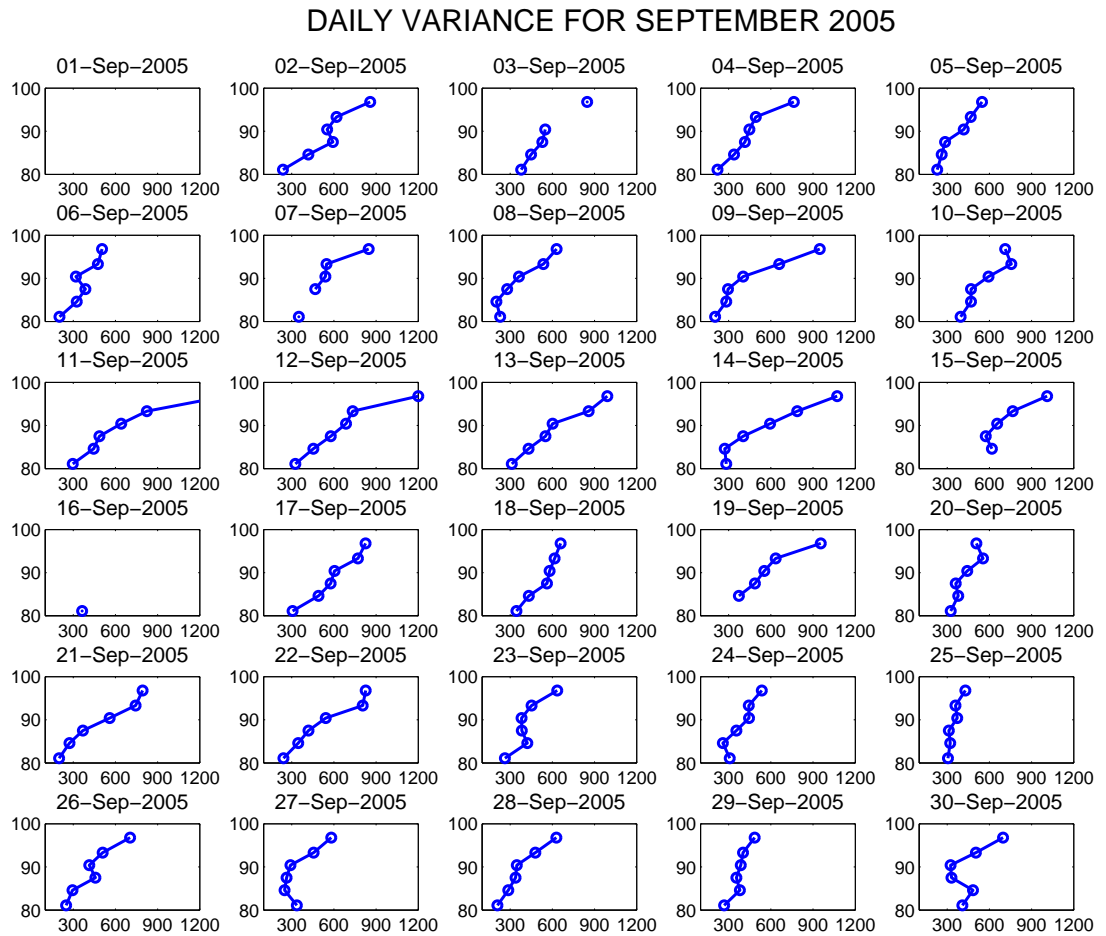
Figure 3.14: Daily profiles of variance against height over Rothera for September 1st to the 30th, 2005. The y-axis is height (km) and the x-axis is variance (m^2s^{-2}).

4. In many days during December there is little or no growth of variance with height below 90 km, and rapid growth above. For example, this occurs on the 2nd and 30th. An explanation for this striking phenomenon is proposed in Section 3.4.3.

On day-to-day time-scales the growth of waves with height can be prohibited or limited by several factors. Critical-level filtering (see Chapter 1, Section 1.3.1) can prevent gravity waves from propagating upwards. When a wave encounters a level in the atmosphere where the phase speed of the wave is equal to the background wind in the direction of propagation of the wave, the wave is absorbed. Wave saturation and/or breaking results in the removal of energy from the gravity-wave field, constraining or reducing wave growth. Both these processes are affected by the local background conditions including the background winds, tides, planetary waves and temperature. Day-to-day changes in the amplitude of tides and planetary waves will thus affect the propagation conditions for gravity waves, and can cause day-to-day changes in the gravity-wave activity. For examples see observations of wave/tide interactions presented in Section 3.4.6.

It is also possible for the waves to become trapped in a duct formed by the background winds or temperature. A ducted gravity wave is evanescent either side of the duct (i.e. its amplitude decays exponentially away from the duct in the regions in which the wave cannot propagate). A ducted wave can travel large horizontal distances while trapped. This process could result in the wave amplitude having an approximately Gaussian profile in height. This idea is consistent with the shape of some of the profiles observed here. However, this behaviour is unlikely to be solely due to ducting as a very long-lived, stationary duct would be needed to account for the duration of the events observed here. Further, a major cause of ducting is likely to be the tidal winds (e.g., *Snively et al.*, 2007). These winds cause ducts that move on timescales shorter than a day and so would not be resolved in the daily means presented in Figures 3.13 or Figure 3.14.

This type of behaviour has been noted in other investigations. For example, *Mitchell and Howells* (1998) noticed day-to-day similarities in daily profiles of variances calculated from vertical velocities measured by the EISCAT Very High Frequency (VHF) radar. They suggested interactions with the 12-hour tide as a possible cause.

The high day-to-day variability seen in Figure 3.12 is also present in the daily height profiles of Figure 3.13. However, as well as variability in the day-to-day variances there is also a consistency in the behaviour of the gravity-wave field as a function of height. To further investigate the vertical profiles of variance, Section 3.4.2 considers the monthly-mean variance profiles.

3.4.2 Seasonal Variability of the Gravity-Wave Field

To investigate the seasonal variability of the high-frequency gravity-wave field, the 6-hourly results within a month were averaged to produce monthly-mean variance profiles. The same analysis was performed on data from Rothera and Esrange. The results from all months of data available over Rothera are presented in Figure 3.15 and those from all months of data over Esrange are presented in Figure 3.16. The additional red lines indicate the growth of variance with height that would be expected for an exponential increase in gravity-wave amplitude in the case of free growth. The expected growth of variance is calculated using the variance value at a chosen height, V_0, as a starting value and the variance is then predicted at increasing heights, $V(z)$, using equation 3.1. The predicted exponential growth may be calculated using any height as the base height, in this case the lowest height and a height of ~ 90 km were chosen. These heights mark the beginning of the two different growth regimes described below.

$$V(z) = V_0 e^{\frac{z}{H}}, \tag{3.1}$$

Where H is the density scale height ($= \frac{kT}{mg}$). The value of H is taken to be 5 km, based on an average July conditions over Esrange (*Lübken*, 1999). Although this value will vary slightly with latitude and season, here it is only used for qualitative comparison and is of sufficient accuracy.
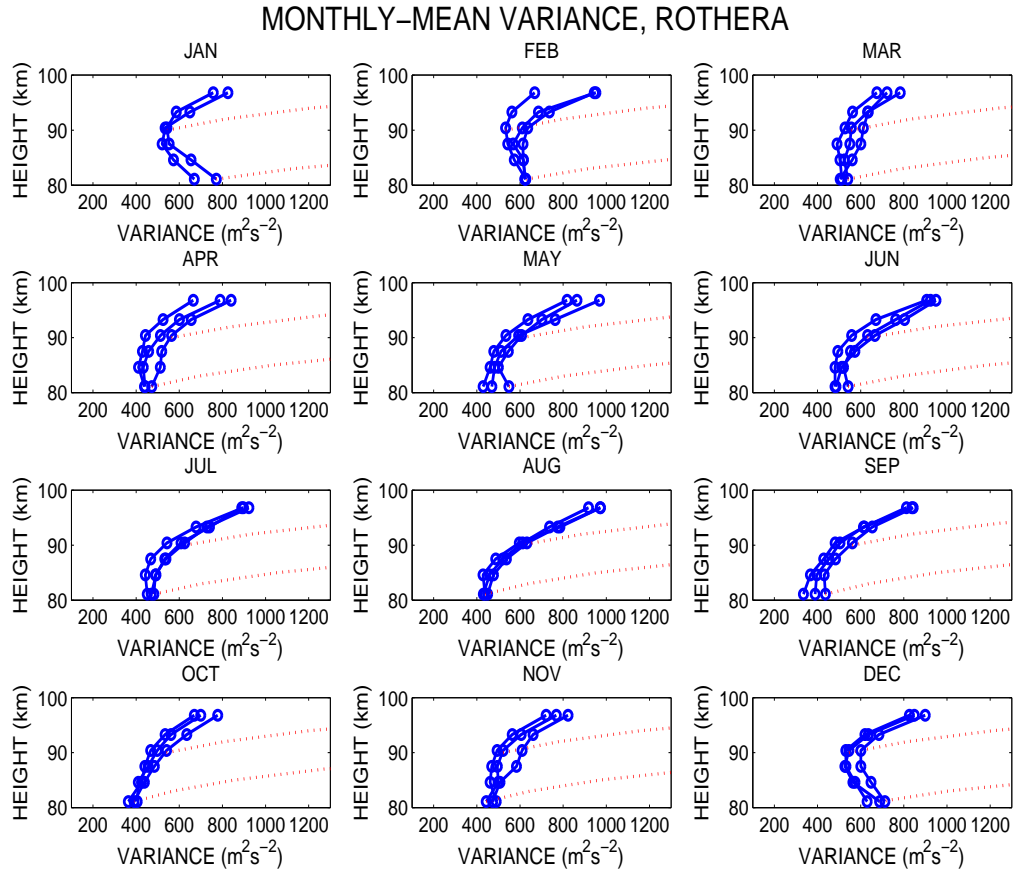
Figure 3.15: Monthly-mean variance profiles with height over Rothera for 2005 to 2007. Each panel represents a month, variance profiles are plotted as blue lines and unrestricted growth as a red dotted line based on values at 81.1 and 90 km.

The variances for all months are in the range $300 - 1000$ m^2s^{-2}, maximum values occur at the upper height gate reaching values as large as $\sim 700 - 1000$ m^2s^{-2}. The largest variances at the upper heights are present in winter (August). In contrast, in the lower height gate the largest variances are in summer (December and January).

Over Rothera, the growth rate is strongest in winter e.g., in August when the variance increases from $400 - 1000$ m^2s^{-2} from $\sim 80 - 100$ km.

The most striking feature of the monthly-mean profiles is the difference in behaviour seen between summer and the other seasons. For example, considering Rothera, in the months from March to October the variance increases with increasing height. This is consistent with the growth of waves as they propagate upwards, discussed further in Section 3.4.3. However, in summer the behaviour is somewhat different. Below ~ 90 km, the variance remains constant with height or
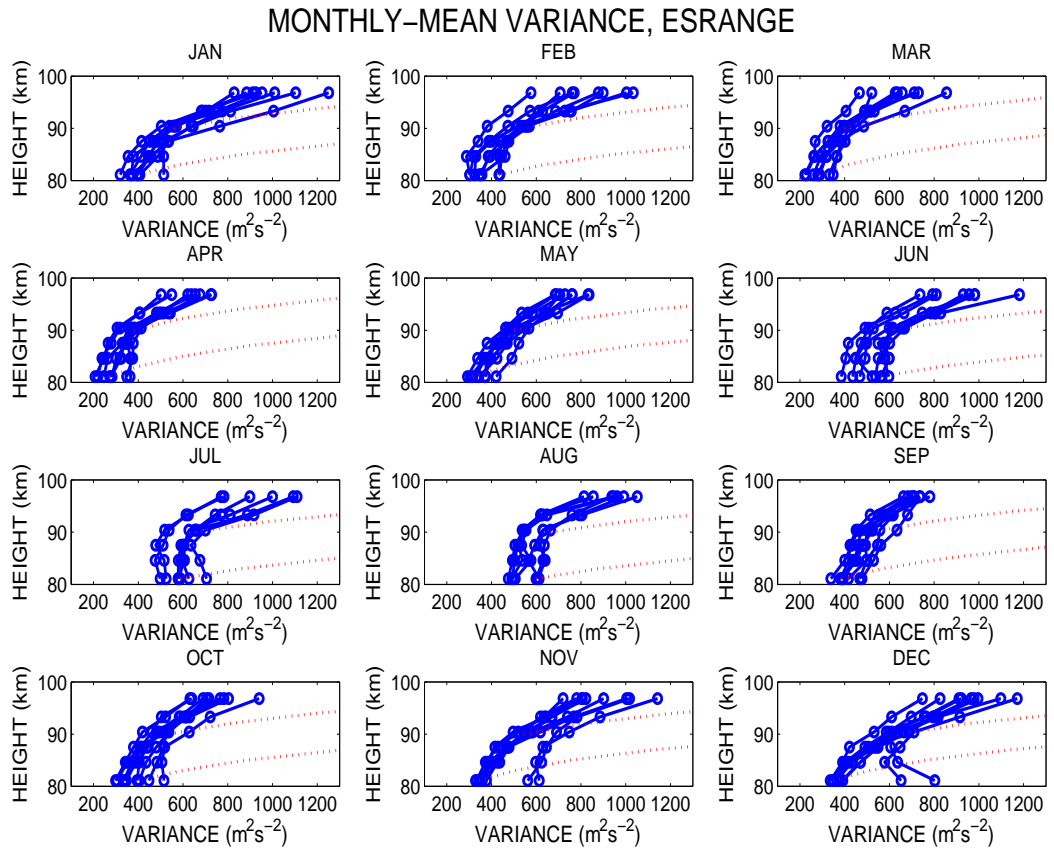
Figure 3.16: Monthly-mean variance profiles with height over Esrange for 1999 to 2007. The blue lines represent consecutive years and the red dotted line represents unrestricted, exponential growth based on the variance in the lowest height gate and at 90 km in 2006.

even *decreases* with increasing height. Above this height the variance then increases rapidly. For example, the profiles for January over Rothera show a marked decreasing variance with height below $\sim$ 90 km and a rapid increase above.

Considering Esrange, all the variances are in the range $\sim 200 - 1200$ m^{2}s^{-2}, maximum values occur in the upper height gate reaching values as large as $\sim 400 - 1000$ m^{2}s^{-2}. The largest variances at the upper height gates are present in winter (January).

The growth rate over Esrange is strongest during winter, matching the behaviour over Rothera. For example, in January the variances increase from ~ 400 to over 1000 m^{2}s^{-2} from $\sim 80 - 100$ km.

Over Esrange, there is also a difference between the behaviour in summer and the other seasons.

In the months from September to May the variance increases as height increases. In summer, below $\sim$ 90 km, the variance remains constant with increasing height and then increases above this height. For example, for August over Esrange the variance does not increase below $\sim$ 90 km and shows rapid growth above this height.

Although the variance profiles show different shapes and growth rates throughout the year (over both Rothera and Esrange), for all months the growth rate is significantly less than that predicted for the unconstrained growth represented by the red, dotted lines. However, above 90 km the growth rate is closer to, but still does not reach the unrestricted growth rate.

Within each month there is a noticeable similarity between the curves for all the years of available data, $2 - 3$ in the case of Rothera, $8 - 9$ in the case of Esrange. This is particularly evident in the case of May over Esrange and July over Rothera. In other words there is a high degree of repeatability in the shape of the profiles from year to year. However, there is also clear inter-annual variability particularly over Esrange. In particular over Esrange in November and December there are two years (2002 and 2007) that display significantly higher gravity-wave activity below $\sim$ 90 km but have values similar to other years above this height. This inter-annual variability will be considered in Section 3.4.4.

3.4.3 Explaining the Behaviour of Gravity-Wave Activity as a Function of Height

Over both Rothera and Esrange, all months show an increase of variance with height. However, in the summer months, this occurs only above $\sim$ 90 km. Below this height, the variance is approximately constant, or even decreases. This suggests that energy is being dissipated from the gravity-wave field.

A possible explanation for the behaviour seen in all months where variance increases with height, but not at the free-growth exponential rate, is that only part of the gravity-wave spectrum is saturated. Consider a spectrum of gravity-waves made up of a part that is saturated (and therefore not increasing in amplitude), and a part that is not saturated (and therefore increasing in amplitude). This combination would result in gravity-wave variances that increased with increasing height, but at a rate less than that predicted solely for free growth. This suggests that the gravity-wave field contains waves with both long and short vertical wavelengths, because saturation depends in part on the vertical wavelength. It has been suggested by *Tsuda et al.* (1994) that at mesospheric heights gravity waves with vertical scales smaller than about 10 km are saturated. Because the proposal of a mixed gravity-wave field of saturated and unsaturated waves would result in the observed variance behaviour, this is advanced as a possible explanation for the observations.

One possible mechanism that could result in a decrease in gravity-wave activity with height during the summer is critical-level filtering. Gravity waves encounter critical levels in background winds equal to their horizontal phase speed. Waves encountering such a level in the atmosphere are absorbed and removed from the spectrum of gravity waves. This would have the effect of decreasing the energy density of the gravity-wave field. To investigate when such critical levels are present the mean zonal winds were considered. Figure 3.17 presents monthly-mean zonal winds from the UARS Reference Atmosphere Project (URAP) model for both Rothera and Esrange.
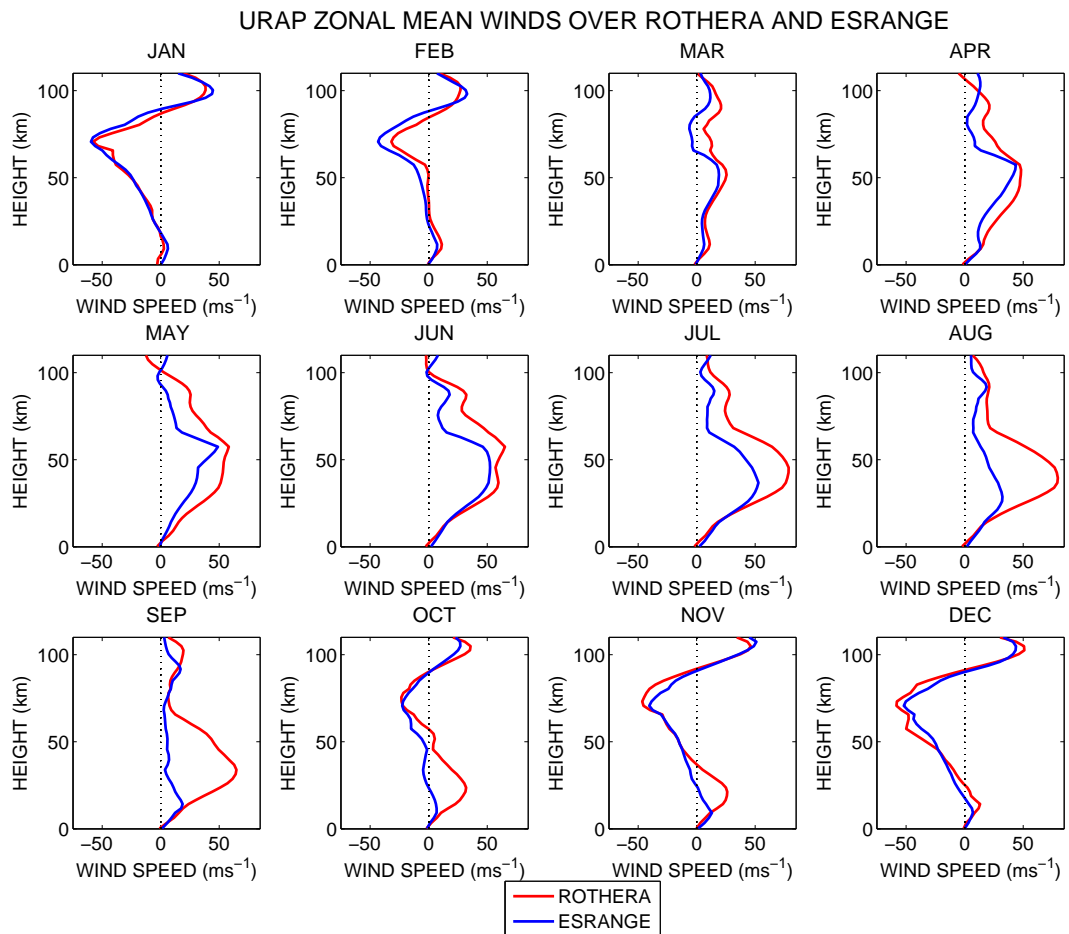
Figure 3.17: Monthly-mean zonal winds over Rothera and Esrange taken from the URAP model. The data for Esrange has been displaced by 6 months to allow seasonal comparison.

Critical level filtering below 80 km shapes the characteristics of the gravity-wave field reaching the observed region. Considering the zonal winds shown in Figure 3.17 for all months, but particularly the summer months, a large part of the gravity-wave spectrum will have encountered critical layers below 80 km. For example, in December over Rothera, the wind reaches ~ 15 ms^{-1} at about 17 km and then becomes steadily more westward until it reaches $\sim$ -55 ms^{-1} at about 70 km. Thus, waves with phase speeds of between $\sim$ -50 and 15 ms^{-1} will encounter critical levels below 80 km and so not reach the MLT region. At 80 km there will therefore only be waves with very high westward phase speeds (larger than -50 ms^{-1}) or high eastward phase speeds (over $\sim$ 15 ms^{-1}). Little or no filtering will therefore occur between 80 and 90 km and so this cannot

be the mechanism responsible for the decreasing in gravity-wave variance seen in the summer.

This can be better understood using equation 3.2 which defines the condition needed for critical-level filtering to occur in different wind speeds.

$$c - \overline{u(z)} \cos \phi = 0 \tag{3.2}$$

Where ϕ is the angle between the propagation direction of the wave and the direction of the wind, $\overline{u(z)}$ is the background wind speed at a height z and c is the phase speed of the wave with reference to the ground. As ϕ changes, values of c that satisfy equation 3.2 trace out an *exclusion circle*. This represents the phase speeds of waves that will encounter critical levels in the background wind $\overline{u(z)}$ (e.g., *Taylor et al.*, 1993).

In order to calculate the exclusion circles at the latitude of Rothera and Esrange, zonal winds from approximately $20 - 80$ km, in steps of 10 km were taken from the URAP model. These winds were averaged over all summer months at each height. Only the zonal component of the wind is included below 80 km as the mean meridional wind is small compared to the mean zonal wind in this height range and does not impose significant filtering on the wave field.
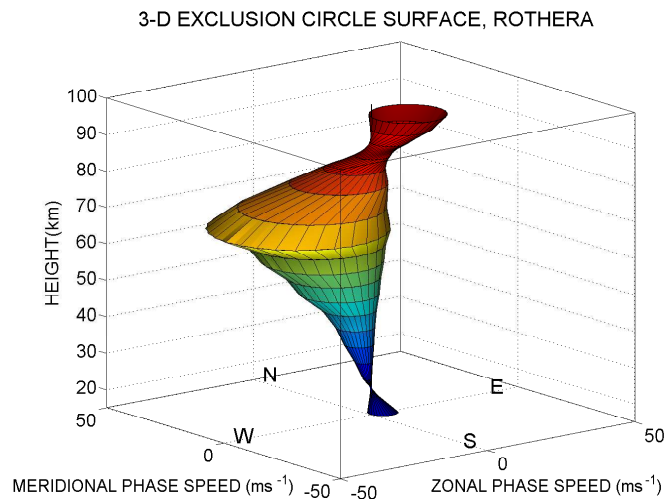
Figure 3.18: Surface showing which wave phase speeds will encounter critical levels in the winds between 20 and 100 km in summer over Rothera.

Figure 3.18 shows a surface representing the range of prohibited phase speeds for waves as they propagate upwards through the average summer zonal mean winds at the latitude of Rothera. The exclusion circles shown assume that the waves are generated below 20 km and that critical-level filtering is the dominant mechanism for removing waves as they propagate through the mean wind.

Considering Figure 3.18, it can be seen that the range of wave phase speeds of waves that will encounter critical levels increases up to approximately 70 km as the zonal winds become more westward. A large proportion of waves with westward phase speeds will be removed in the winds between 20 and 70 km. Above 70 km, the zonal mean wind weakens and the exclusion circles formed at heights of 80, 81.1, 84.6 km are contained within exclusion circle from 70 km. As a result, little or no filtering will occur from ~ 80 to ~ 85 km as the waves that would have encounter critical levels in these winds have already been removed from the wave field.

Above about 85 km, there is a more significant contribution from the mean meridional wind. The combination of zonal and meridional wind forms exclusion circles which block out some eastward and some southward phase speeds. At ~ 90 km waves with eastward phase speeds up to about 7 ms^{-1} and southward phase speeds up to about 10 ms^{-1} will be excluded. From about 90 to 100 km additional filtering will occur and waves with low eastward and southward phase speeds will encounter critical levels.

The critical-level filtering described here can not reproduce the behaviour of the variance during the summer months observed over Rothera or Esrange. In order to prevent the growth of variance below ~ 90 km the filtering would need to occur between heights of 80 and 90 km, not above this. However, the exclusion circles presented in Figure 3.18 show that little or no filtering is occurring between 80 and 90 km. It is only as the zonal wind becomes eastward above 90 km that critical-level filtering will again occur. From this we conclude that critical-level filtering is not primarily responsible for the observed variance profiles, particularly in summer.

Note, there are other mechanisms that can cause dissipation of wave energy. Wave reflections and/or ducting could result in a decreasing variance with increasing height. However, the observations presented here are unlikely to be caused by these mechanisms as very long lived, stationary ducts would be needed to cause the seasonal effects seen here.

The height of ~ 90 km is both the height where the zonal winds reach zero and the approximate height of the summer mesopause. The presence of zero wind and changing background zonal wind suggests that critical-level filtering could be occurring here. However, as already discussed, this is unlikely to cause a substantial decrease in gravity-wave activity at heights below 90 km as a majority of waves that would be filtered by the winds at these heights will have already encountered critical levels below 80 km, see the winds in Figure 3.17.

The presence of the summer mesopause at this height will have an effect on the propagation of the gravity waves in this region. Wave amplitudes can be limited or reduced by the breaking of saturated waves. Wave breaking occurs when the amplitude of a wave becomes large enough that it forces areas of local convective or dynamical instability, see Section 1.3.1, Chapter 1.

The most common types of instability that can be created are dynamical and convective instability. Dynamical instability occurs as the result of large wind shears. As shown in Figure

3.17, for high latitudes there is a strong wind shear with height in summer. The wind shear produced by the mean wind alone will not produce dynamic instability, but the mean wind in combination with tides, planetary waves and gravity waves could produce local areas of dynamic instability. However, if this were a significant factor in reducing gravity-wave activity, the larger wave amplitudes found at the top of the height range considered would produce stronger wind shears. Therefore, most breaking through this process would occur at the upper height gates resulting in a variance-height profile that decreased towards the top of the height range. This does not match the observations where the gravity-wave activity is limited below 90 km and then increases rapidly above.

High-frequency gravity-waves are believed to preferentially break through convective instability (e.g., *Dunkerton*, 1984; *Fritts and Alexander*, 2003). Convective instability occurs when the environmental lapse rate becomes greater than the adiabatic lapse rate ($\sim$ 9.5 Kkm^1 in the MLT region). The onset of instability is dependent on the combinations of background lapse rate and the wave induced perturbations.

The observed temperature structure of the mesopause over Esrange, measured using data from rocket and falling-sphere experiments is presented in Figure 3.19. This temperature profile is an average of four profiles measured in July, presented by *Lübken* (1999). In summer, at polar latitudes, the mesopause has been measured to be at a height of 86 $\pm$ 3 km (*von Zahn and Höffner*, 1996).
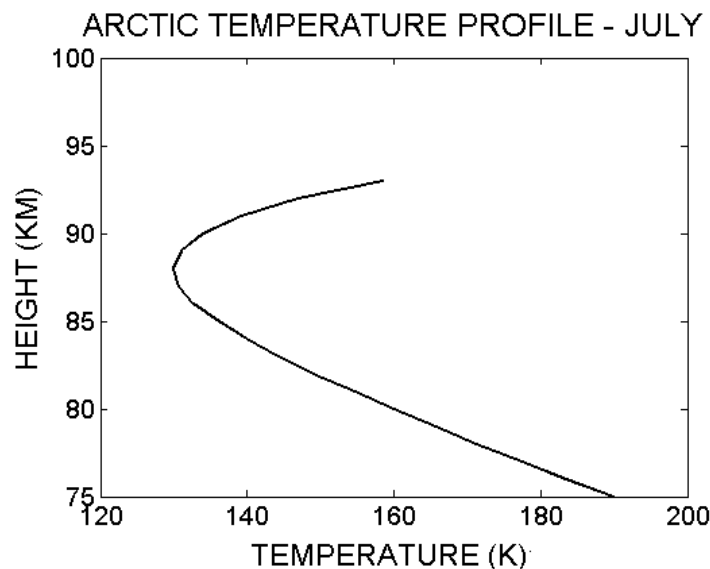
Figure 3.19: Average Arctic temperature profile over Esrange for July using data from rocket soundings and falling sphere experiments. Results are taken from *Lübken* (1999).

The height and cold temperature of the summer mesopause, result in a steep temperature gradient above and below about 87 km. Using the temperatures shown in Figure 3.19, the temperature gradient was calculated to be $\sim$ -5 Kkm^{-1} below the mesopause and $\sim$ 8 Kkm^{-1} above. The temperature gradient below the mesopause is relatively close to the adiabatic lapse

rate of 9.5 Kkm^{-1}. Although this indicates that the atmosphere is stable as a monthly average, the presence of tides, planetary waves and gravity waves themselves could all result in localised unstable regions as observed by for example, *Hecht et al.* (1997); *Williams et al.* (2002, 2006). In order for a wave, in combination with the background temperature profile, to be convectively unstable the wave would need to induce a temperature gradient of only $\sim$ 5 Kkm^{-1} such that the combined temperature gradient is convectively unstable. This limits the amplitudes that gravity waves can reach before breaking.

In these conditions strong gravity-wave breaking will occur below $\sim$ 87 km and so limit the gravity-wave activity below this height. Above the mesopause, the temperature gradient reverses and the atmosphere is much more stable. A gravity wave would need to induce a temperature gradient of $\sim$ 18 Kkm^{-1} for breaking to occur, that is, the wave would have to overcome a much more stable atmosphere. This is complicated by the change in the Brunt-Väisälä caused by the change in temperature gradient from below to above the mesopause. In a rough approximation, the Brunt-Väisälä period doubles from about 3 minutes below the mesopause to about 6 minutes above the mesopause. For gravity waves the vertical wavenumber, m, depends upon the phase speed of a wave, c_x,

$$c_x \sim \frac{N}{m}. \tag{3.3}$$

If the wave's horizontal phase velocity remains constant, then halving the Brunt-Väisälä frequency will double the wavenumber and so halve the vertical wavelength. This smaller vertical wavelength will result in steeper temperature gradients being induced by the wave for a given amplitude and so the maximum amplitude the wave can reach before saturating will actually be smaller. This will to some extent counteract the effects of the lapse rate on breaking wave amplitudes discussed above.

We will illustrate the combined effect of these two processes by considering a gravity wave with a vertical wavelength of 15 km propagating across the mesopause temperature structure. In order for this wave to be convectively unstable below the mesopause, the wave would need to induce a temperature gradient perturbation of only $\sim$ 5 Kkm^{-1}. This corresponds to the wave being limited to an amplitude of $\sim$ 10.7 K. As this wave crosses the mesopause, its vertical wavelength will shrink to $\sim$ 7.5 km. However, in the more stable background temperature gradient above the mesopause this wave would still be able to grow to an amplitude of $\sim$ 20.9 K before inducing super-adiabatic temperature gradients and so breaking. The overall effect is that the wave can roughly double in amplitude as it crosses from below to above the summer polar mesopause.

This mechanism would act to constrain the amplitude of high-frequency gravity waves below the mesopause, but would allow amplitude growth above - as observed over both Rothera and Esrange. This mechanism appears to provide a plausible, qualitative explanation of the observations presented in Figures 3.15 and 3.16.

Note that this mechanism is less effective at other times of the year because of the difference in the background temperature profile throughout the year. The summer temperature profile has much steeper gradients than the winter profile, both above and below the mesopause. The steeper gradients mean smaller wave amplitudes are reached before the wave breaks. The winter temperature profile is not steep enough below the mesopause to induce breaking, and so the wave amplitudes keep growing from 80 to 100 km. *Lübken et al.* (1999) have shown that the temperature profile changes rapidly away from a sharp summer mesopause at high latitudes and all but disappears in the winter months. The sharp summer mesopause persists into February, agreeing well with the timing of the changes seen in the variance profile with height over both Esrange and Rothera.

Increased gravity-wave breaking below the summer mesopause will transfer energy and momentum from the gravity-wave field to the background flow. This deposition of energy and momentum acts to decelerate and then reverse the zonal-mean flow, resulting in the summertime zonal wind shear. It also results in an equatorward, meridional flow which is observed at these heights in summer. This equatorward flow should be strongest when and where deposition is occurring, and decrease as the gravity waves begin to propagate more freely. Therefore, the height of maximum of the meridional winds should correspond, approximately, to the height of the mesopause and the height above which the variance starts to increase. Note that this assumes that the background flow is driven primarily by the momentum deposited by the high-frequency gravity waves observed by the variance technique.
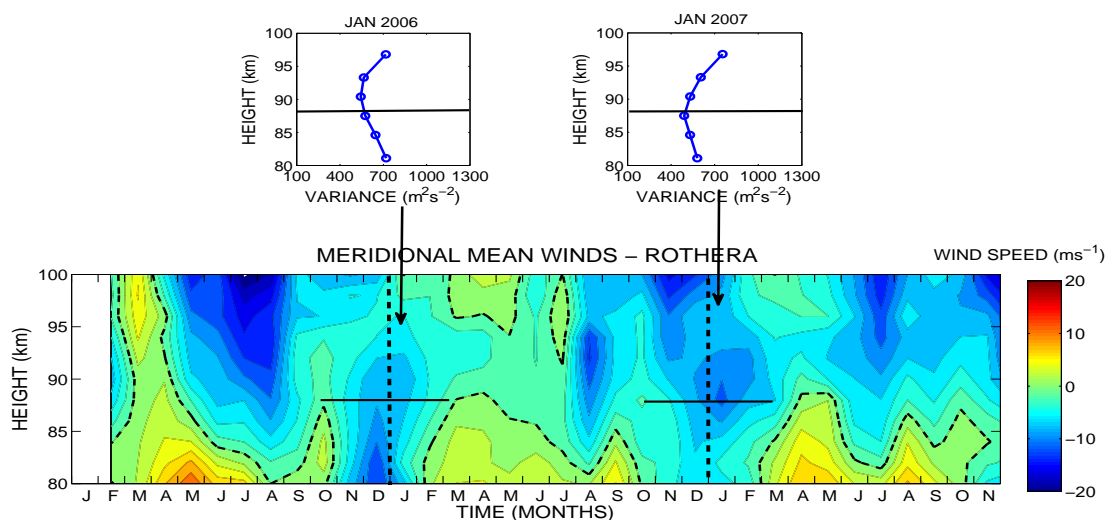
Figure 3.20: Meridional mean winds over Rothera (2005 - 2007), with variance profiles for January as separate plots. Horizontal lines on both the variance profiles and mean winds indicate the approximate height of the summer mesopause.

Figures 3.20 and 3.21 show contour plots of the monthly-mean meridional winds over the entire datasets of Rothera and Esrange. Above each plot are the corresponding monthly-mean *variance* profiles calculated for each January (July) over Rothera (Esrange). These are taken from Figures

3.15 and 3.16. The black horizontal lines correspond to the approximate height of the mesopause from observations *Lübken* (1999). For Figure 3.20, over Rothera the meridional winds have been adjusted so that negative values correspond to equatorward winds. This is to allow comparisons between the two hemispheres.

By considering Figure 3.20, it can be seen that the period of equatorward flow corresponds to summer months when gravity-wave activity does not increase with height. This suggests that the energy from the gravity-wave field is being deposited into the mean flow and results in an equatorward flow at this time of year. However, there are only two years worth of data available over Rothera, and the meridional winds are significantly different in each year.

Considering Figure 3.21 a similar period of equatorward flow can be seen in summer. Contrasting with the behaviour over Rothera, the equatorward winds are more regular from year to year and are more confined in height. It can be seen from the figure that the height marked of the summer mesopause is the same height as the beginning of the increase in variance, as well as the height of maximum equatorward flow. This agrees well with the prediction that the strongest equatorward flow should correspond to the maximum deposition of energy by the gravity-wave field.

In summary, the lack of growth or decrease in variance observed in the summer variance profiles cannot be explained by gravity-wave filtering alone. There is a clear relationship between the change in the growth of gravity-wave variance, the height of the summer mesopause and the summertime meridional equatorward jet. This is strong evidence that the lack of growth below ~ 87 km is due to enhanced gravity-wave breaking below the summer mesopause where the atmosphere is close to being unstable.
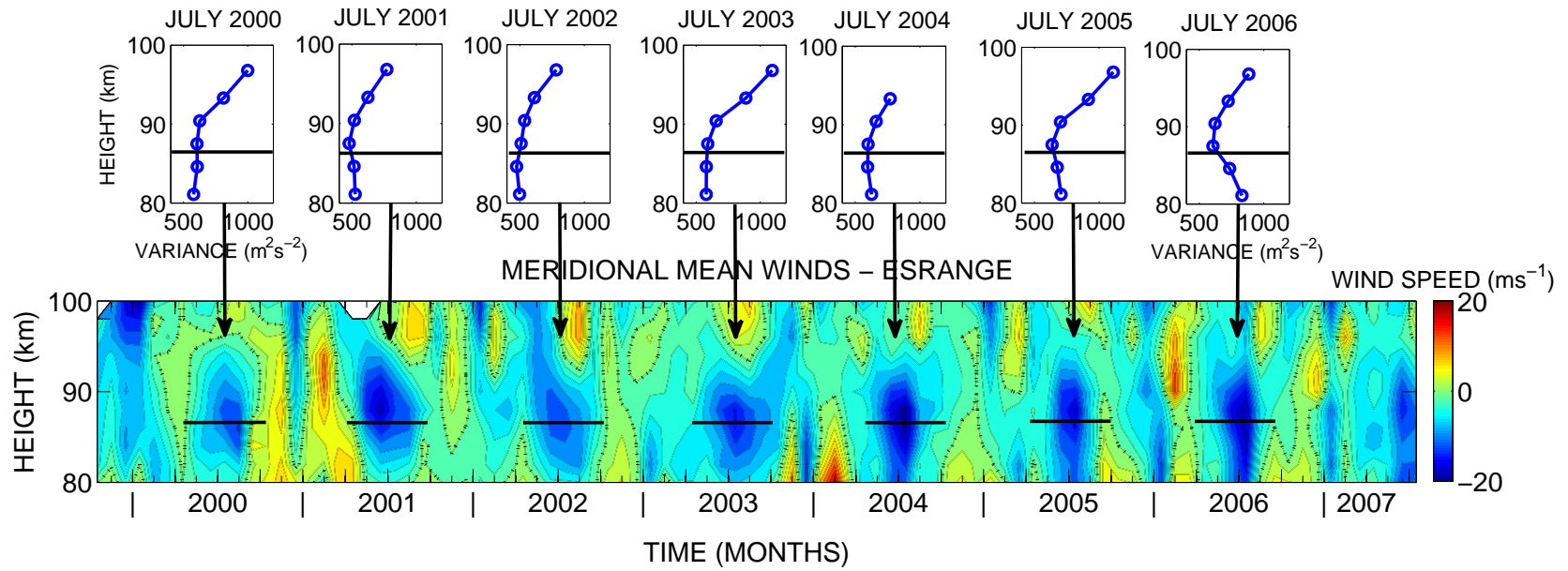
Figure 3.21: Meridional mean winds over Esrange (1999 - 2007), with variance profiles for July as separate plots. Horizontal lines on both the variance profiles and mean winds indicate the approximate height of the summer mesopause.

3.4.4 Inter-Annual Variability of the Gravity-Wave Field

The use of the variance technique to provide an insight into the vertical behaviour of the gravity-wave field on daily and monthly timescales has been discussed above. This section will focus on the seasonal variation of gravity-wave variances over Rothera and Esrange as revealed by this technique. Figures 3.22a and 3.22b present monthly-mean values of variance for all height gates for Rothera and Esrange respectively.

One of the most obvious features of both datasets is that the variance increases with height at nearly all heights and times. There is also a clear semi-annual cycle in gravity-wave activity. However, over Rothera, the maxima in variance in summer and winter are not of equal magnitude. At the bottom of the height range, 81.1 km, the summer peak exceeds the winter peak by nearly 30%, and at 90 km the peaks are approximately equal. However, at the top of the height range, 96.8 km, the maxima is largest in winter. This suggests a combination of both annual, dominant at $\sim$ 100 km, and semi-annual, dominant at $\sim$ 80 km.

Over Esrange, (Figure 3.22b), the behaviour is slightly different than that seen for Rothera. The distinct semi-annual pattern is generally the same, with summer maxima larger than the winter maxima below $\sim$ 90 km. However, at the top of the height range, $\sim$ 96.8 km, the summer and winter peaks have more similar magnitudes. Although for some years the winter peak is larger than the summer one (e.g. 2002 and 2006), in most of the years the summer and winter variances in the top height gates are of similar size.

In summary, the general seasonal cycle over both Rothera and Esrange, is repeated from year-to-year. The variances generally increase with height and a semi-annual cycle is observed in all height gates over both Rothera and Esrange.

However, there is also evidence of inter-annual variability. For instance, over Esrange 2001, 2002 and 2006 show behaviour distinct from other years. Considering the the behaviour during 2002 in particular, this year is different from other years because of the lack of a semi-annual cycle (summer maximum is missing) below 93 km. This is present in all other years at these heights. This year was noted in Section 3.4.2 as being one of two years that displayed enhanced gravity-wave activity below 90 km in November and December. These enhanced variances can be seen in Figure 3.22b. Considering the gravity-wave activity at about 92 km, the variance starts to increase in summer and remains elevated throughout autumn and winter. Above $\sim$ 92 km a separate summer maxima can be seen with smaller variances than the winter. Also the winter of 2002 / 2003 is marked by very high variances — the highest found over all 6 years across the height range. Note that a major stratospheric warming took place in the southern hemisphere during the summer of 2002. Similar behaviour can be seen in 2007, was the summer maxima is extended, but not greater than, other years.

MONTHLY MEAN VARIANCE, ROTHERA

(a)

MONTHLY MEAN VARIANCE, ESRANGE

(b)
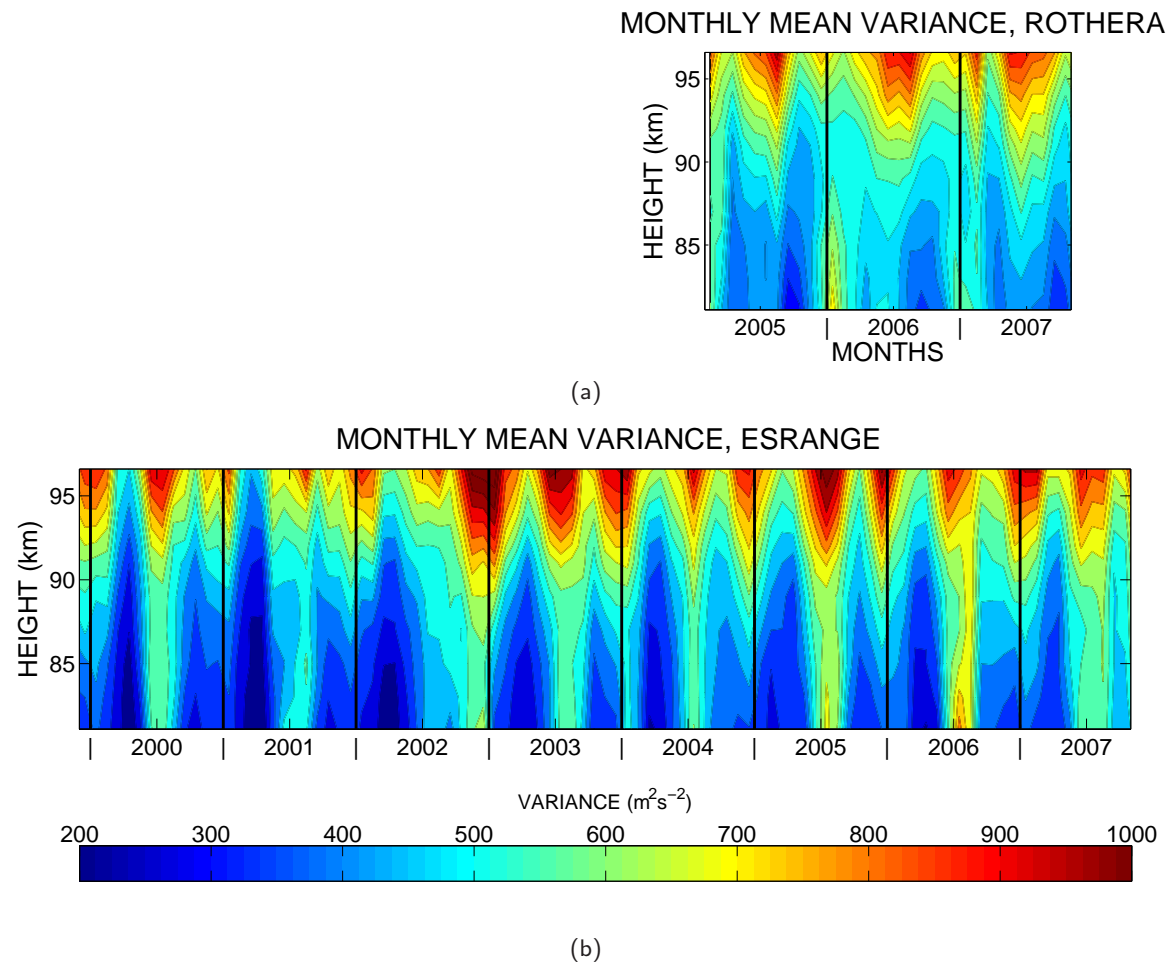
Figure 3.22: Monthly-mean variances over (a) Rothera and (b) Esrange, the vertical lines denote the beginning of each year.

Although there is clear inter-annual variability, particularly over Esrange, the seasonal behaviour of gravity-wave activity is generally the same from year-to-year. The spectrum of gravity-waves that reaches the MLT is shaped by the winds in underlying atmosphere. To understand the seasonal cycle in gravity-wave activity the seasonal cycle of winds from the ground to 100 km must be considered.

Figures 3.23 and 3.24 show climatologies of variances over Rothera and Esrange plotted as the filled contour plot in the upper parts of the figures (using an average year based on all available data). On top of this are plotted the zonal mean winds as measured by the radars. The lower part of the figure shows the zonal mean winds taken from the empirical URAP model. The combination of radar data and model values from URAP gives a representative picture of the structure of the zonal mean wind from the ground to 100 km.
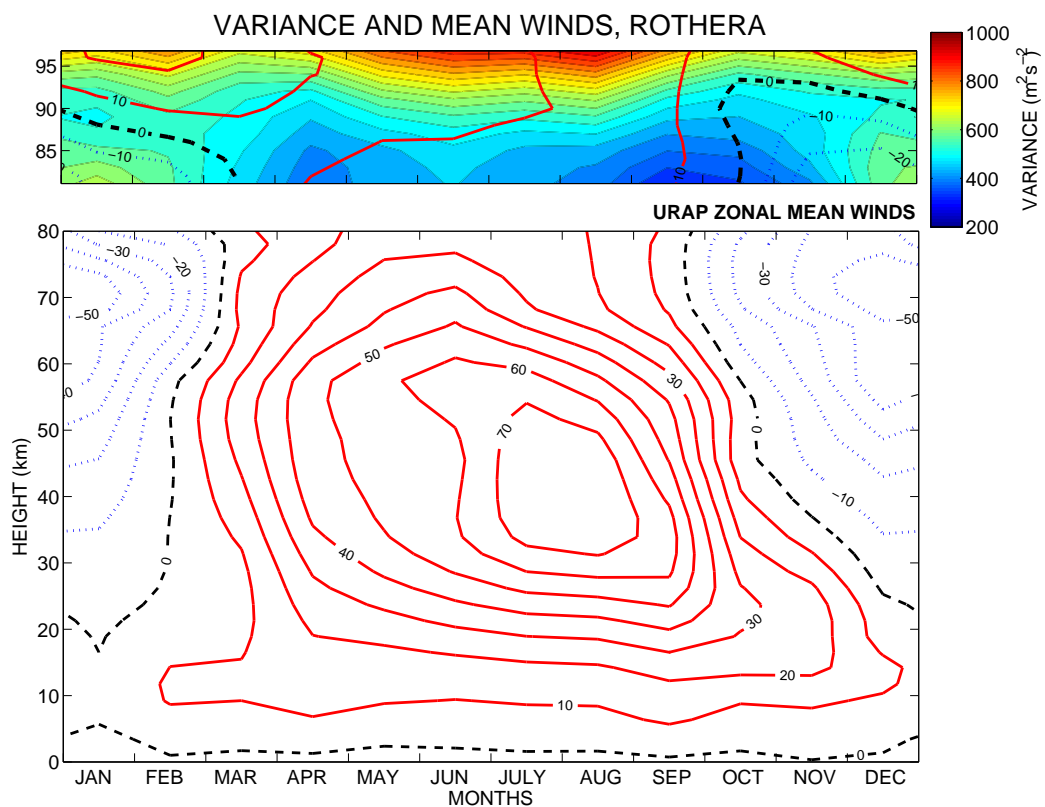
Figure 3.23: Climatology of variances over Rothera using data from February 2005 to December 2007. Variances are shown as filled contours, overlaid is a climatology of zonal mean winds measured by the Rothera radar during the same time interval. The lower panel shows the zonal mean winds predicted by the URAP model at the latitude of Rothera.

The spectrum of gravity waves that propagates into the MLT is shaped by the conditions in the underlying atmosphere. Processes such as critical-level filtering and wave breaking remove or modify different parts of the gravity wave spectrum before these waves reach the MLT. These processes are themselves influenced by changes in the winds and temperature structure of the atmosphere. To understand the seasonal cycle of variances in the MLT, the seasonal cycle of
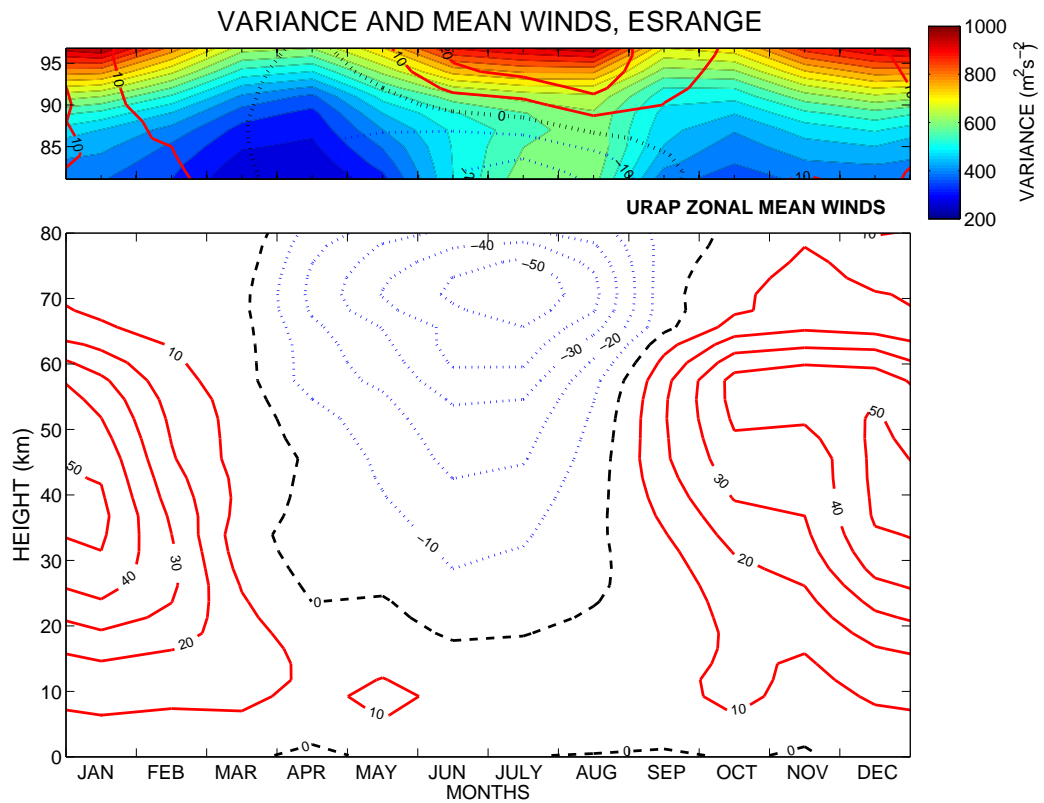
Figure 3.24: Climatology of variances over Esrange using data from October 1999 to December 2007. Variances are shown as filled contours, overlaid is a climatology of zonal mean winds measured by the Esrange radar during the same time interval. The lower panel shows the zonal mean winds predicted by the URAP model at the latitude of Esrange.

winds lower in the atmosphere must be considered.

The zonal mean winds will be considered because they have a clearer seasonal cycle and more extreme values, in both positive and negative flow speeds, than the meridional winds. The large seasonal variations have a stronger influence on the spectrum of gravity waves through critical-level filtering than the weaker meridional winds. It can be seen from Figures 3.23 and 3.24 that there is a relationship between the zonal mean winds below 80 km and the gravity-wave variance in the MLT. The largest variances in the MLT correspond to times when there are large positive or negative winds occurring from 20 to 80 km (i.e. summer and winter). The lowest variances correspond to the time when the zonal winds are near zero, i.e. at the equinoxes.

This pattern can be explained by considering the propagation of gravity waves from their source regions, through these winds and the distribution of the phase speeds of launched gravity waves. The spectrum of gravity-wave phase speeds is composed of gravity waves from many different sources. Steady flow of winds over topography will excite gravity-waves with zero phase speeds. Convective activity, such as thunderstorms, will excite waves with a broader range of phase speeds matching the speed of the tropospheric winds. There is also evidence for waves with a range of phase speeds, and low-frequencies, excited by spontaneous geostrophic adjustment and

frontal collapse (*Fritts and Alexander*, 2003). The results of *Fritts and Nastron* (1992) indicate that topographic generation plays a major role in gravity-wave excitation, and jet-stream shears, convection and frontal activity all make significant contributions. *In situ* generation of high-frequency gravity waves in the MLT by wind shears has also been suggested (e.g., *Nakamura et al.*, 1999).

The spectrum of launched gravity-wave phase speeds is often assumed to have a Gaussian distribution centred on zero, with a half-width of a few 10s of ms^{-1} (e.g., *Thorsen and Franke*, 1998; *Fritts and Alexander*, 2003; *England et al.*, 2006). This spectrum of gravity-waves will be influenced by the winds at different heights. As the waves propagate vertically, the winds form critical levels, successively removing waves from the gravity-wave field that have the same phase speed as the wind speed at that particular height. At the equinoxes, the winds below 80 km are close to 0 ms^{-1} and range from small negative winds to small positive winds. These winds will remove those waves with low phase speeds. Because the energy in the gravity-wave spectrum is greatest around zero phase velocity this will remove a large part of the spectrum of gravity-waves before they reach 80 km. This is supported by observations made with airglow imagers that suggest that near the equinoxes gravity-waves with small phase speeds are not as common as near the solstices (*Nakamura et al.*, 1999). This suggests that waves with small phase speeds are more effectively removed near the equinoxes, corresponding to the minima in observed gravity-wave activity.

At the solstices, the zonal winds have large speeds, but are either positive (eastward) or negative (westwards) throughout the height range. These winds will remove either eastward-propagating waves in winter, or westward-propagating waves in summer. This will not remove as many gravity waves as the equinoctial conditions. Therefore, the solstitial winds yield the maxima observed in gravity-wave activity in the MLT.

The result of this critical-level filtering occurring below 80 km is that there is more gravity-wave activity in the mesosphere and lower thermosphere around the solstices and less gravity-wave activity activity near the equinoxes.

An illustration of this can be seen in Figure 3.25. This shows that under equinox conditions, a larger part of the energy in the gravity-wave spectrum is removed as those waves with low phase speeds are filtered out. Under solstitial conditions, although many gravity waves with either eastwards (winter) or all westward (summer) phase speeds are removed, less energy is removed overall as the Gaussian distribution is narrow and there is less energy in the high phase speed part of the spectrum.

Although the Gaussian distribution of gravity waves illustrated in Figure 3.25 can explain the general seasonal cycle of gravity-wave activity in the mesosphere, there are some inconsistencies when the data are considered on a month to month basis. To consider this in more detail Figure 3.26 shows the zonal mean winds from the URAP model plotted from $0 - 80$ km.
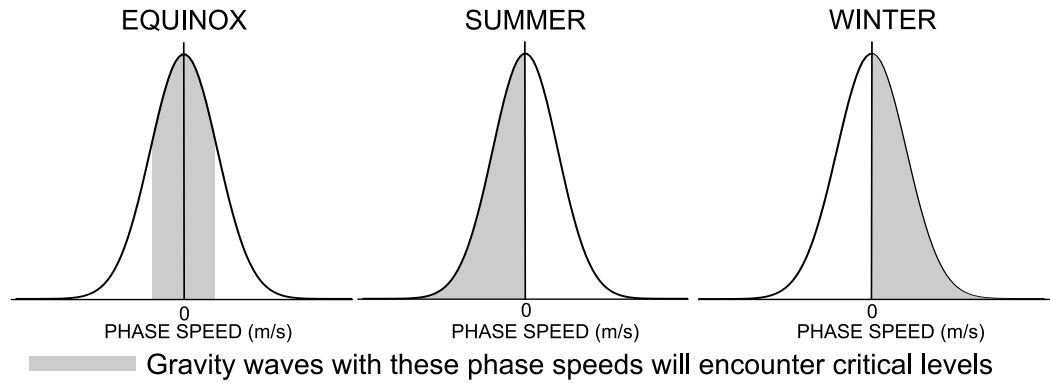
Figure 3.25: A schematic diagram showing phase speed distributions near the equinox, in summer and winter. Shaded areas represent the range of phase speeds of waves that will encounter critical levels below ~ 80 km.
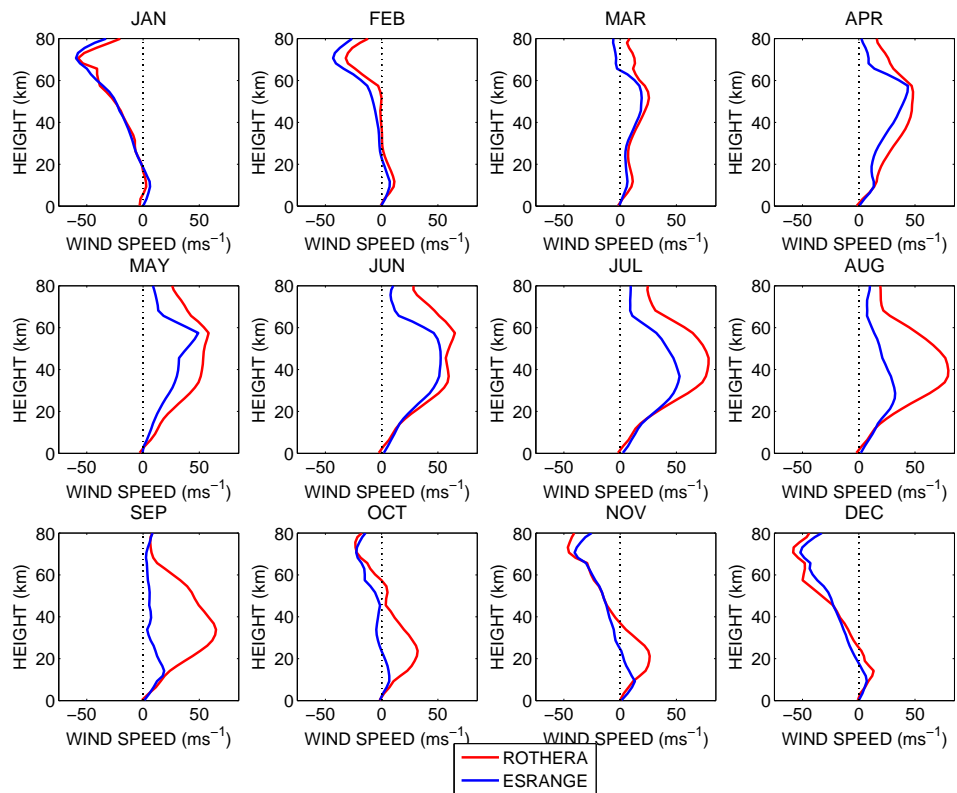
Figure 3.26: Zonal mean winds from 0 to 80 km from the URAP model. Month labels correspond to Rothera, the data over Esrange is shifted by 6 months to make the seasons comparable.

Considering Figures 3.23 and 3.26, over Rothera, the zonal winds which might be expected to provide the most effective filtering in autumn, occur in February and March. However, the autumnal minima in gravity-wave activity is observed in *April* when the zonal winds below 80 km are weakly eastwards. If the distribution of phase speeds follows a Gaussian centred on zero, then the most effective filtering should occur when the winds are near zero below 80 km. Therefore, the minima in gravity-wave activity would be expected to occur in February and March. It can also be seen in Figure 3.23 that the spring minima over Rothera is centred on September.

However, Figure 3.26 shows that the small and zero winds below 80 km mostly occur in October and November again when the winds are weakly eastwards.

The same behaviour can be seen over Esrange in Figure 3.24. In autumn the zonal winds below 80 km are zero in August and September. However, the minima in gravity-wave activity occurs in October when the zonal winds below 80 km mostly have small eastward values. Note that this corresponds to February, March and April in Figure 3.26. During spring over Esrange, the minima in gravity-wave activity is more extended and occurs in March and April. This corresponds to the zero and small winds, both eastwards and westwards, below 80 km and agrees with the results expected for a distribution of gravity waves centred on zero.

During both spring and autumn over Rothera, and autumn over Esrange, the minima in gravity-wave activity is observed when the winds below 80 km are small and eastwards, *not* when the winds are only near zero. The exception to this is the behaviour is spring over Esrange. These observations suggest that the narrow Gaussian distribution of gravity-wave phase speeds may not be centred on zero during these times of year. If the distribution of phase speeds were a narrow Gaussian centred on small eastwards phase speeds the critical level filtering would be most effective at removing energy from the gravity-wave field when the zonal winds below 80 km were near zero but slightly eastward.

Such a distribution of phase speeds was suggested by *Thorsen and Franke* (1998) to explain a similar difference in timing between the minima in gravity-wave activity and the wind reversal below 80 km as observed using an MF radar in Urbana, Illinois (40° N, 88° W). *Thorsen and Franke* (1998) used a Gaussian distribution of phase speeds centred on 15 ms^{-1} with a standard deviation of 10 ms^{-1} in a modelling study to examine the effects of critical level filtering. The model was able to accurately reproduce their observations for spring, but was less accurate during autumn. They suggested the differences may be due to filtering by the meridional winds which were not considered in the model.

When considering a possible explanation for a distribution of gravity-waves centred on weak eastward phase speeds, the sources of these waves must be considered. *Tsuda et al.* (1994) observed a strong correlation between the intensity of the jet stream and gravity-wave activity at 15.5 – 17 km. This suggests that the peak of the jet stream is a important source for gravity-waves with periods of 5 minutes to 2 hour. The jet stream is embedded in the tropospheric eastward winds and can be found between latitudes of 30 and 70° depending on the time of year. Gravity-waves generated by either shear instabilities or geostrophic adjustment associated with the jet stream could have eastward phase speeds and possibly account for more eastward waves in the high-frequency part of the gravity-wave spectrum *Ern et al.* (2004). However, the jet stream would not provide a consistent source throughout the year as the it varies in latitude and is often located at lower latitudes than those of the radar sites.

3.4.5 Differences between the Antarctic and Arctic Mesosphere

Several differences in gravity-wave behaviour between Rothera and Esrange are noticeable from Figures 3.22a and 3.22b. To investigate these differences in more detail, annual climatologies over both stations were calculated to reduce any contribution to the differences that could be the result of inter-annual variability. Figures 3.27a and 3.27b present these climatologies of gravity-wave activity over Rothera and Esrange.

(a)

(b)
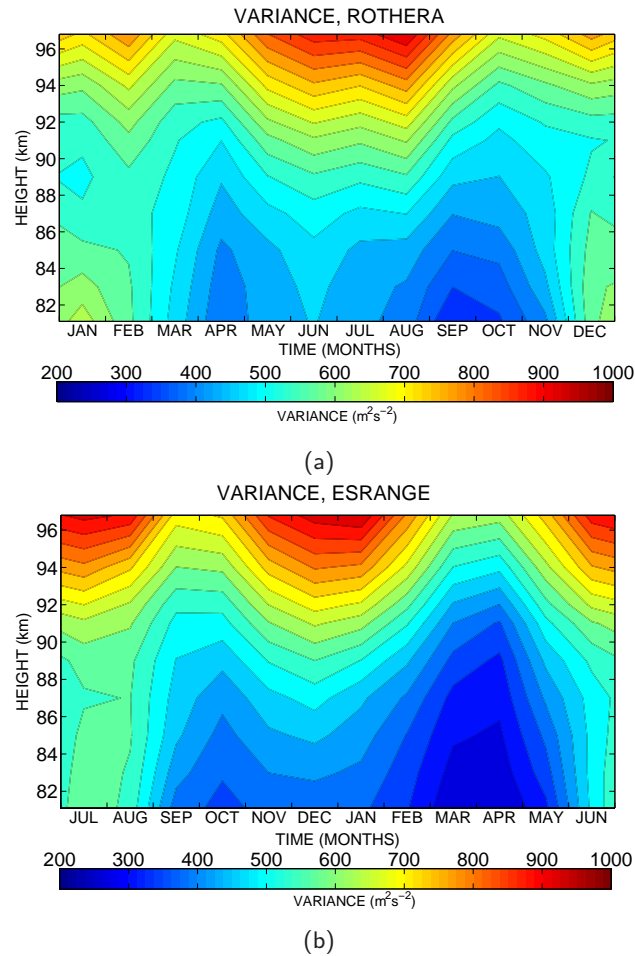
Figure 3.27: Climatologies of variance over (a) Rothera using data from February, 2005 to November 2007 and (b) Esrange using data from October 1999 to November 2007. The results for Esrange have been plotted displaced by six months to make the seasons comparable.

Figures 3.27a and 3.27b both show obvious similarities in the behaviour of the gravity-wave field in the two polar regions. Over both Rothera and Esrange, wave activity increases with height and has a semi-annual cycle with maxima in winter and summer. However, a number of differences are also apparent. These differences include a weak summertime maximum over Rothera at the upper heights compared to the approximately equal summer/winter activity over Esrange. For example, over Rothera the variance during summer reaches ~ 730 m^{2}s^{-2} while over Esrange the summer variances reach ~ 920 m^{2}s^{-2}.

To see the differences between the two stations more clearly, Figures 3.28a and 3.28b present the *difference* and *ratio* between the two climatologies. For Figure 3.28a, the Esrange variances were subtracted from the Rothera variances, with the Esrange data displaced by 6 months to make the seasons comparable. For Figure 3.28b the Rothera variances are divided by the Esrange variances. Again the data over Esrange is displaced by 6 months to make the seasons comparable.

(a)

(b)
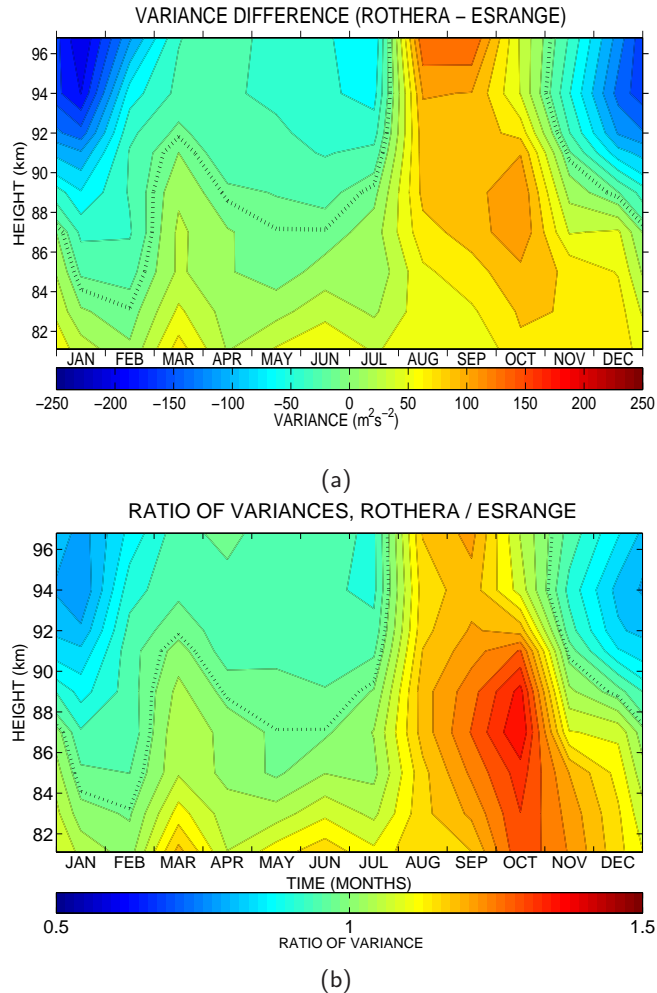
Figure 3.28: (a) Difference between climatological variances over Rothera and Esrange (Rothera - Esrange). (b) Ratio between climatological variances over Rothera and Esrange, (Rothera/Esrange). Values larger than 1 indicate higher variances over Rothera, values less than 1 indicate higher variances over Esrange. Months are labelled relative to the months at Rothera and Esrange data is shifted by 6 months to make seasonal comparisons possible.

Considering Figures 3.28a and 3.28b, it can be seen that the magnitude of the variances over Rothera and Esrange are approximately similar, i.e. the values are close to 1 in most of Figure 3.28b. However, there are several significant differences apparent. The gravity-wave activity over Esrange is larger at the upper height gates in most months. This can be seen as the negative values in the top part of Figure 3.28a. The exceptions are during the spring (August, September and October), when the variances are larger at all heights over Rothera.

In the middle and lower height gates during the summer, the variances are very similar over both stations. However, above ~ 90 km the activity over Esrange is greater and the largest difference

(~ 250 m^{2}s^{-2}) is observed near the top of the height range. During autumn and winter the variances over the two stations are similar but follow a trend of slightly larger variances over Rothera at the bottom of the height range and slightly larger variances over Esrange at the top. The most striking difference is the difference in the wave activity in spring. Variances over Rothera are consistently higher compared to those over Esrange.

Figure 3.28 is useful for investigating the seasonal pattern in the differences between the two stations. However, to examine the difference in the height structure in more detail, Figure 3.29 presents the averaged monthly profiles for both Rothera and Esrange. These profiles are an average of monthly-means calculated from February 2005 to November 2007 over Rothera, and October 1999 to November 2007. Note that the error bars are calculated as the standard deviation of the individual monthly means that were used to calculate the representative value. These are intended only to provide an idea of the level of inter-annual variability within the data set.
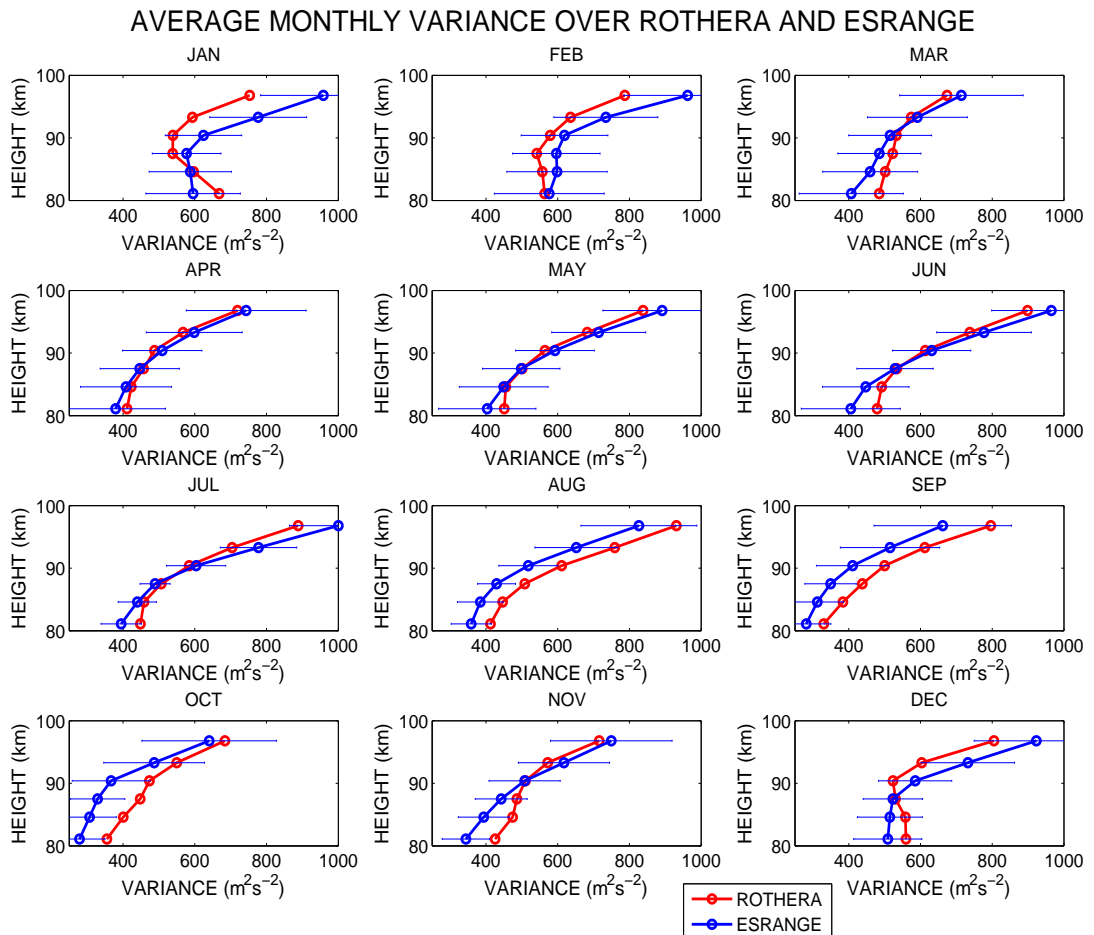
Figure 3.29: Average monthly gravity-wave variances as a function of height over Rothera and Esrange. The standard deviation of the individual monthly-means over Esrange are plotted as error bars. No error bars are shown for Rothera as there is only 2 to 3 years of data available. The data for Esrange has been shifted by 6 months and the months are labelled for Rothera.

Considering Figure 3.29, it can be seen that the largest differences between Rothera and Esrange occur in late winter and spring, that is August, September and October in the figure. The difference between the variances over the two stations is approximately the same at all heights observed and amounts to approximately $100 - 150$ m^{2}s^{-2}. During summer, (December and January) the gravity-wave activity below ~ 90 km over Rothera shows a larger decrease with height than over Esrange. However, above ~ 90 km the rate of the increase of variance is similar between the two stations.

An explanation for the differences occurring in spring is proposed as follows. Consider the differences in the critical-level filtering occurring between the two stations, Figure 3.30 presents the zonal winds calculated by the URAP model for July to October over Rothera. The zonal winds for Esrange, displaced by 6 months, are also shown.
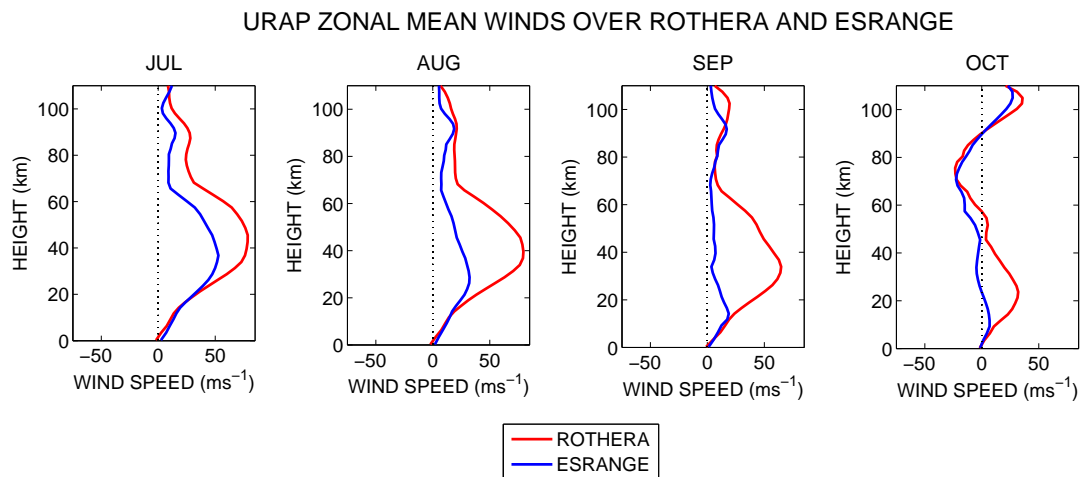
Figure 3.30: Zonal mean winds from the URAP model for Autumn (July - October). Data over Esrange is shifted by 6 months to make comparisons possible.

Considering Figure 3.30, a clear difference in the zonal winds between ~ 20 and ~ 75 km can be seen. Over Rothera, there are much stronger eastwards winds peaking at 30 km and reaching ~ 70 ms^{-1}. Over Esrange, the winds are much weaker and are closer to zero from $0 - 80$ km. The stronger eastward flow observed over Rothera is due to the more intense stratospheric polar vortex present in the Southern hemisphere. In the Southern Hemisphere the polar vortex forms more rapidly, is stronger and lasts longer than the in the Northern Hemisphere. It is the extended lifetime of the Antarctic vortex that results in differences in the spring zonal winds between the two hemispheres. As well as difference in strength, the Southern Hemisphere polar vortex shows much less year-to-year variability, a consequence of the stronger winds and lower planetary-wave activity in the Southern Hemisphere.

It is during the months when there is a large difference in the eastward winds forming the polar vortices that the largest differences in the gravity-wave variance occur. These different winds will impose different levels of filtering on the field of ascending gravity waves.

The effect of different wind field can be explored by assuming that the distribution of gravity-wave phase speeds, when launched, is a Gaussian centred on, or near zero. The energy in the gravity-wave field is then concentrated at, or close to, zero phase velocity. As a consequence, the weaker winds over Esrange will remove more energy from the gravity-wave field through the process of critical level filtering. It should be noted that the URAP data presented here is a climatology based on 5 years of data and therefore is representative only of an average behaviour. Short-term and inter-annual variations in winds will cause deviation from the average behaviour. In the case of Esrange this means the winds will vary from small positive to small negative variances and will more effectively filter the gravity-wave field.

In summary, differences in the stratospheric polar vortex between the Antarctic and Arctic result in significant differences in the zonal winds below 80 km in the late winter and early spring. Assuming a Gaussian distribution of phase speeds centred on or near zero, the small wind speeds present over Esrange filter more of the gravity-wave spectrum as the waves propagate upwards. This results in weaker gravity-wave variances at 80 km over Esrange in winter/spring as observed in Figure 3.29.

3.4.6   Gravity-Wave Modulation by Tides and Planetary Waves

The tides are a significant feature of the dynamics in the MLT. At the latitudes observed here, the tide with largest amplitude is the 12-hour tide, which can reach instantaneous amplitudes in excess of 50 m^2s^{-2} (e.g., *Mitchell et al.*, 2002). Also present are tides with periods of 24, 8 and 6 hours (see Chapter 5).

A strong tidal wind will combine with the mean winds and can result in a rapidly changing propagation environment for gravity waves. As such, the tides, particularly the 12-hour tide in this case, might be expected to have a noticeable effect on the gravity-wave field. As the amplitudes of both the tides and gravity waves increase with height, interactions might be expected to have the most noticeable effect *in situ* in the MLT where the waves and tides, reach large amplitudes.

In order to investigate any interactions between the high-frequency gravity-wave field and the tides, a superposed epoch analysis was performed to examine variability of the gravity-wave field on time-scales of less than day. For this analysis, all the meteors detected in a particular hour of the day, for a particular month, regardless of year, were used to calculate the gravity-wave variance. This allows the calculation of variance for a representative or 'composite' day for each month of the year. The results represent a composite day derived from all years observed. In the case of Rothera, this comprises data from February 2005 to December 2007. Because of the large number of meteors used the variance can be calculated with a time resolution of one hour.

COMPOSITE DAYS OF VARIANCE, ROTHERA
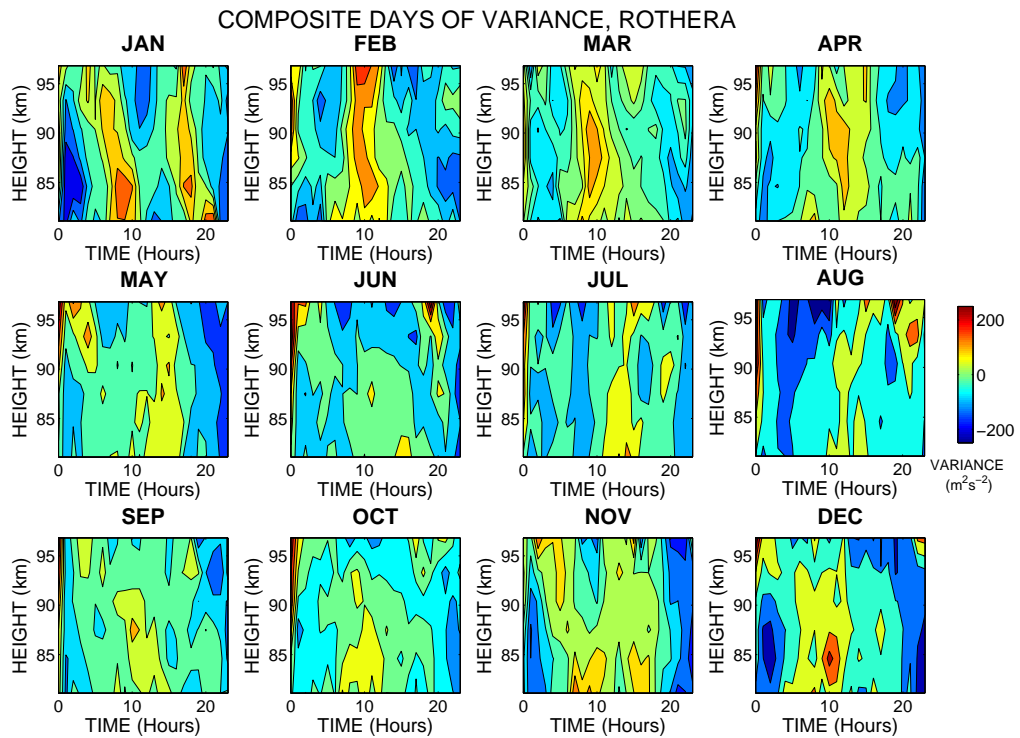
Figure 3.31: Superposed epoch analysis of variances over Rothera using data from February 2005 to November 2007. The mean value of variance in each height gate has been removed so that the figure is not dominated by the increasing variance with height.

Figure 3.31 shows the composite days calculated for Rothera. In each height gate the mean variance, calculated for that height gate, has been subtracted. This removes the trend of increasing variance with increasing height and allows any variation within the day to be more clearly seen.

Considering Figure 3.31 it can be seen that in January, there is a clear 12-hour modulation in the variance. Maxima occur at approximately 09:00 and 20:00 UT at $\sim$ 80 km and $\sim$ 07:00 and 18:00 UT at 100 km. This shows a tendency for the maxima in variance to have a 12-hour periodicity and to move downwards with time. A tidal origin for this modulation is strongly suggested by the regular maxima across the height range and downward phase progression throughout the composite day. The vertical wavelength of the 12-hour tide over Esrange (at a conjugate geographical latitude to Rothera) has been shown to be $\sim$ 115 km in summer *Mitchell et al.* (2002). Assuming that the vertical wavelength of the 12-hour tide is similar over Rothera and Esrange, it is consistent with phase change with height seen in Figure 3.31.

A possible 12-hour modulation is also present in other months. For example, in February, there are maxima in variance at $\sim$ 00:00 and $\sim$ 11:00 UT, and again in November there are maxima in variance at 06:00 and 18:00 UT.

As well as 12-hour variations, there are also some months that display variation with a period

of approximately 24 hours. For example, in June, below $\sim$ 90 km, the variance only peaks at $\sim$ 16:00 UT, and considering October, the variance maximises at 10:00 UT.

These results suggest the presence of tidal/gravity-wave interactions. To examine this behaviour in more detail, a time series of variances was calculated using a 2-hour window, incremented in 1-hour steps. This allows a spectral analysis of the whole dataset to be performed to examine modulations on tidal or planetary wave periods. Due to the presence of gaps in the time series, a Lomb-Scargle periodogram was used instead of a Fourier analysis to determine the frequency content of the variance time series.
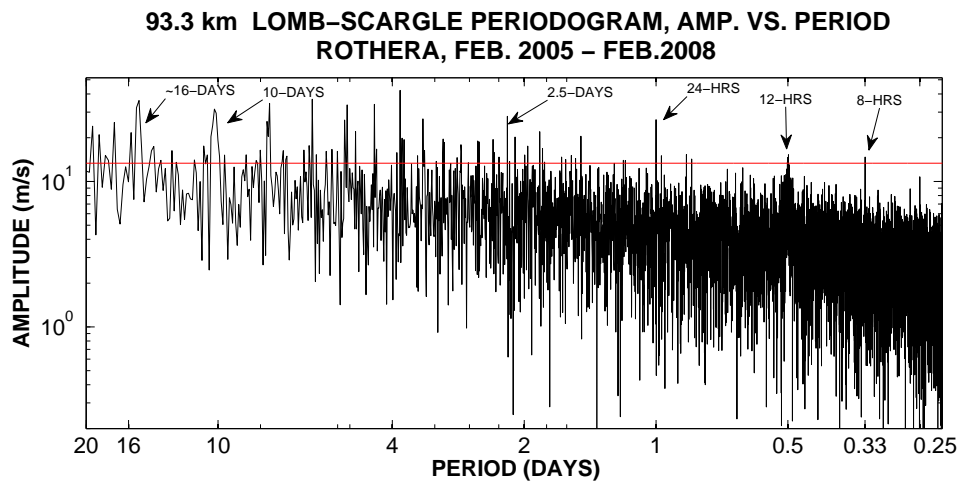
Figure 3.32: A Lomb-Scargle periodogram of 2-hourly gravity-wave variances for the Rothera dataset (February 2005 - February 2008), from 93 to 96 km. A 95% significance level is plotted as the red horizontal line.

As an example of this analysis, Figure 3.32 presents a Lomb-Scargle periodogram of the 2-hourly variances at a height of $\sim$ 93.3 km for all data over Rothera (February 2005 - February 2008). Note that the significance level is calculated using the amplitude of the highest peak and under the assumption that the dataset has a white noise spectrum. This makes this significance level pessimistic for the tidal peaks seen in this data. Several peaks can be seen in the spectra. Clear peaks are present at both 12 and 24 hours, reaching $\sim$ 30 m^{2}s^{-2}, indicating a modulation of the gravity-wave activity at these periods. There is also a smaller, but significant, peak present at 8 hours. Several peaks at planetary-wave periods are also present, in particular at periods close to 2.5, 10 and 16 days.

Although this analysis reveals the presence of peaks at tidal and planetary-wave periods in the gravity-wave activity over Rothera, it gives no indication of any seasonal dependence of the occurrence of the modulation. To look at the seasonal variation in these modulations more closely, a running-window Lomb-Scargle was applied to both the Rothera and Esrange datasets. In this analysis, a Lomb-Scargle periodogram was applied to the data within a 30-day window. This window was then incremented in 10-day steps through the dataset. Some typical results of the running Lomb-Scargle analyses are presented in Figure 3.33. Only features over a 90%

confidence limit are plotted.
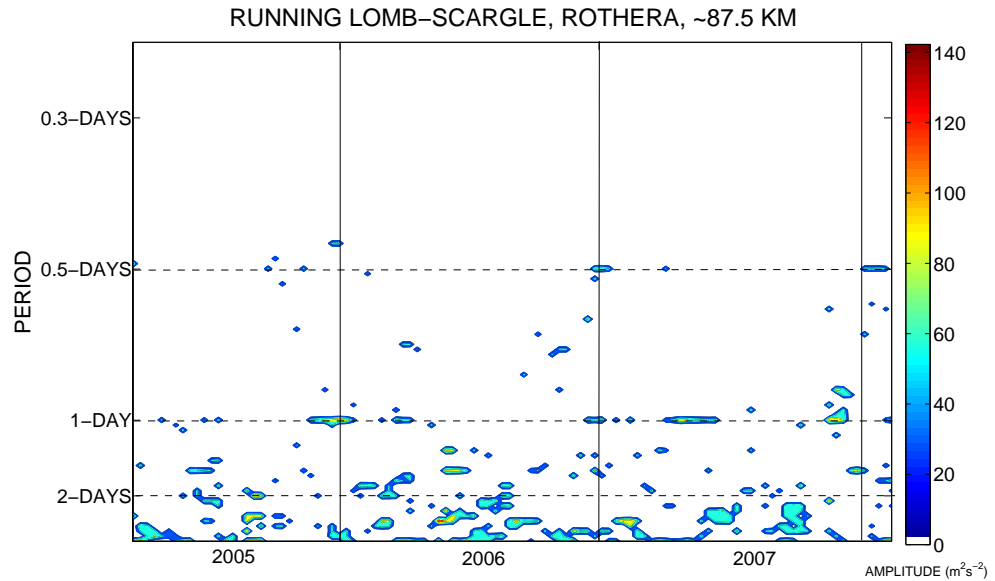
Figure 3.33: A running Lomb-Scargle analysis of the gravity-wave variances over Rothera, March 2005 to December 2007, at ~ 87 km. Points are only plotted when the amplitude of the signal is above a 90% confidence limit.

There are several significant features revealed in this running Lomb-Scargle analysis. These include:

1. There are collections of peaks in the periodograms at periods of 12 hours, 24 hours and at planetary-wave periods (e.g. 2 days).

2. The peaks at $\sim$12 hours are a mostly summer-time occurrence. The maxima in the periodogram at this period only occur in the months of October to April over Rothera.

3. The 24-hour peaks are present most strongly in summer but also occur intermittently throughout the year.

4. The modulation at all periods is intermittent, occurring in bursts throughout the dataset.

It is worth noting that there may be a contribution to the 24-hour modulations from the diurnal cycle in the uncertainty of the horizontal velocities, or the diurnal cycle in the number of meteors detected during a day. Less meteors are detected in the afternoon and evening and this may introduce a diurnal cycle to the variances. However, this is likely to be small as a minimum of 30 meteors is needed in a time-height bin for a variance to be calculated. There is also a diurnal cycle in the uncertainty on horizontal velocities, although the uncertainties have been shown to be small for all times of day. Due to these spurious diurnal variations, care must be taken when interpreting any diurnal variation in the gravity-wave variances. Over Esrange a dominant 24-hour modulation is present with a smaller 12-hour modulation, due to the risk of

contamination of the 24-hour signal the results over Esrange are not presented here.

Figure 3.34 presents an alternative analysis. Here, a running Lomb-Scargle is again applied a 30-day window of data, incremented in 10-day steps through the dataset. However, in this case a dot is plotted for each signal over a 90% significance level at a particular frequency. Data from the entire Rothera dataset, regardless of year is included in the Figure. This analysis more clearly shows any seasonal pattern that may be present and could indicate tidal/gravity-wave interactions. This analysis follows that of *Manson et al.* (1998b).
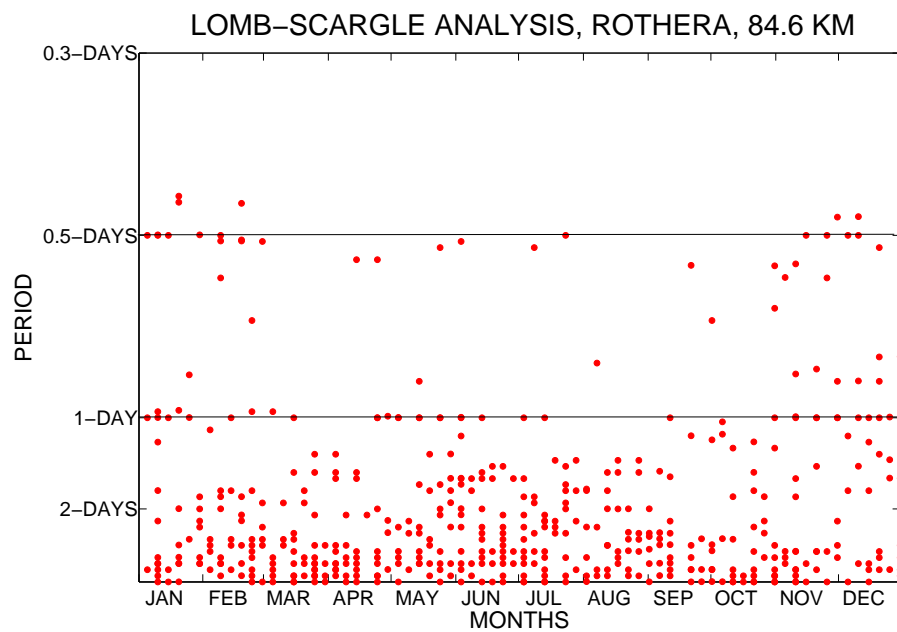
Figure 3.34: Lomb-Scargle analysis of 2-hourly gravity-wave variances over Rothera at ~ 84.6 km. A point is plotted for each frequency found above the 90% confidence limit.

The signals at tidal and planetary wave frequencies are once again obvious in Figures 3.34. Over Rothera, the modulation at a period of 12 hours is largely confined to the summer months, (December to February). The modulation at a period of 24 hours has a rather different seasonal cycle and is present in both summer and winter. However, it is less evident around the equinoxes.

These Lomb-Scargle analyses over Rothera indicate that there are periodicities in gravity-wave activity at 12, 24 hours and planetary-wave periods. This strongly suggests that interactions are occurring between the 12- and 24-hour tides, planetary waves and the gravity-wave field. It is interesting to note that the seasonal behaviour of the modulations seems unconnected to the seasonal changes in tidal amplitudes. For example, the 12-hour tide is known to maximise in winter and autumn, but not during the summer at these latitudes (*Mitchell et al.*, 2002).

A possible explanation for the modulation of the gravity-wave field at tidal frequencies has been proposed by some authors including *Walterscheid* (1981) *Thayaparan et al.* (1995) and *Manson et al.* (1998b). The proposed explanation relies on understanding the critical level filtering that

occurs below 80 km as well as the action of the tide.
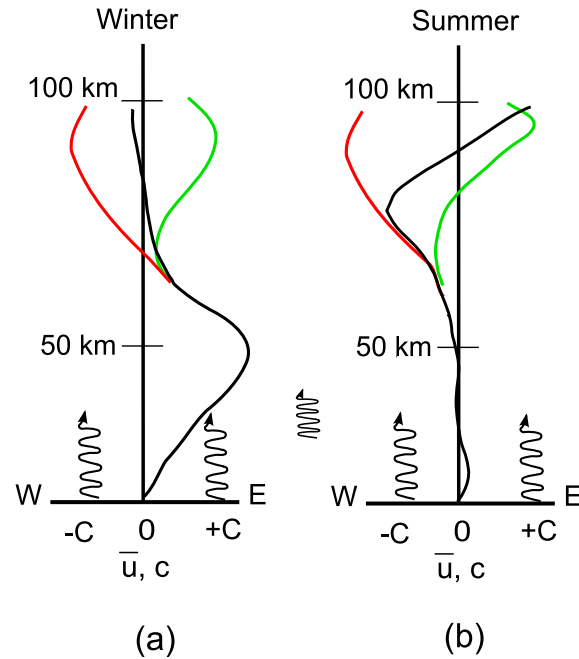
Figure 3.35: Schematic diagram showing proposed mechanisms for tidal/gravity-wave interactions. The black line shows mean zonal winds alone, the red line shows a perturbation caused by a diurnal tidal wind, the same tide 12 hours later is shown by the red line, (a) shows winter conditions, (b) shows summer conditions.

Figure 3.35 shows a schematic diagram illustrating a combination of the mean zonal wind and a tidal wind. Figure 3.35a shows a typical height profile of zonal mean wind in winter at the latitudes of Rothera or Esrange, as a black line. A combination of the mean wind and a diurnal tide at two times, separated by 12 hours, are also shown as the red and green lines. The green line in Figure 3.35a shows the result of a combination of a diurnal tide and the mean zonal wind, when the tidal winds at ~ 80 km are eastward. The red line shows the same combination of tide and mean wind, but 12 hours later when the tidal winds are westward. Figure 3.35b shows the mean zonal winds for summer conditions as the black line. As in 3.35a, the green line represents the combination of the mean wind and diurnal tide when the tidal wind is westwards in the mesosphere and the red line represents the tidal wind blowing eastward in the mesosphere, 12 hours later.

Considering the winter conditions, Figure 3.35a, waves with eastward phase speeds $(+c)$ will encounter critical levels in the eastward winds up to about 50 km. In a typical winter this will remove any waves with eastward phase speeds of $0 - 60$ ms^{-1} (the value of the eastward wind maximum at about 50 km). As a result, the wave field reaching the mesosphere will be made up predominantly of waves with *westward* phase speeds $(-c)$. Waves with high eastward phase speeds will also reach these heights, but as previously discussed, an assumed Gaussian distribution of gravity-wave phase speeds means that most of the energy is contained in the small phase speed part of the gravity-wave spectrum, see Section 3.4.5.

When the mesospheric tidal winds are blowing eastward, (shown by the green line) further critical-level filtering will not occur, as the eastward waves have already encountered critical levels below about 50 km.

However, half a cycle later, when the mesospheric tidal wind blows westward, (red line) it causes the overall mesospheric winds to blow *westward*. Waves with small westward phase speeds will now encounter critical levels in the mesosphere where they were previously free to propagate. This will result in a reduction of the gravity-wave activity and will result in a modulation of gravity-wave activity at the period of the tide, i.e. there will be less gravity-wave activity at meteor heights when the tidal winds in the mesosphere are westward.

In summer conditions a similar argument can be used to produce a modulation at the period of the tide. Critical-level filtering below $\sim$ 70 km removes a large proportion of the waves with eastward phase speeds leaving a wave field dominated by waves with westward phase speeds. Using the mechanism illustrated in Figure 3.35b, a reduction of gravity-wave activity will result when when the tidal wind is eastward and critical levels are formed for the eastward propagating waves.

This means that in summer most filtering will occur when the tidal winds are *eastward*, but in winter there will be most filtering when the tidal winds are *westward*.

This mechanism also applies under equinox conditions. However, during equinox the gravity-wave field reaching the mesosphere is much more isotropic (assuming an isotropic phase-speed distribution when the waves are generated). Therefore, critical levels will be reached when the tidal winds are maximum in both the eastward and the westward directions and a modulation of gravity-wave activity will occur at *half* the period of the tide. However, as shown in Figure 3.34 the modulation at both 24 and 12 hours, is less frequent near the equinoxes. This corresponds to the time when overall, the gravity-wave activity is lower and much of the field has already been filtered out before reaching 80 km.

The mechanism described above predicts a relationship between the phase of the tide and the maxima and minima in gravity-wave activity. The maxima in gravity-wave activity will occur when the tidal wind pushes the background wind to be at a maximum *westward* during summer and an maximum *eastward* during winter.

To determine if this relationship is present, the composite days of variance were considered for each month of the Rothera dataset and compared to composite days of the zonal winds for each month. As an example of this, Figures 3.36 and 3.37 show the composite days of variance and zonal winds for January 2007 (summer), and May 2006 (autumn) over Rothera. These were selected as being clear examples of the phenomena of interest.

Considering Figure 3.36, in summer, the maxima in variance (see Figure 3.36a) occur through-

(a)

(b)
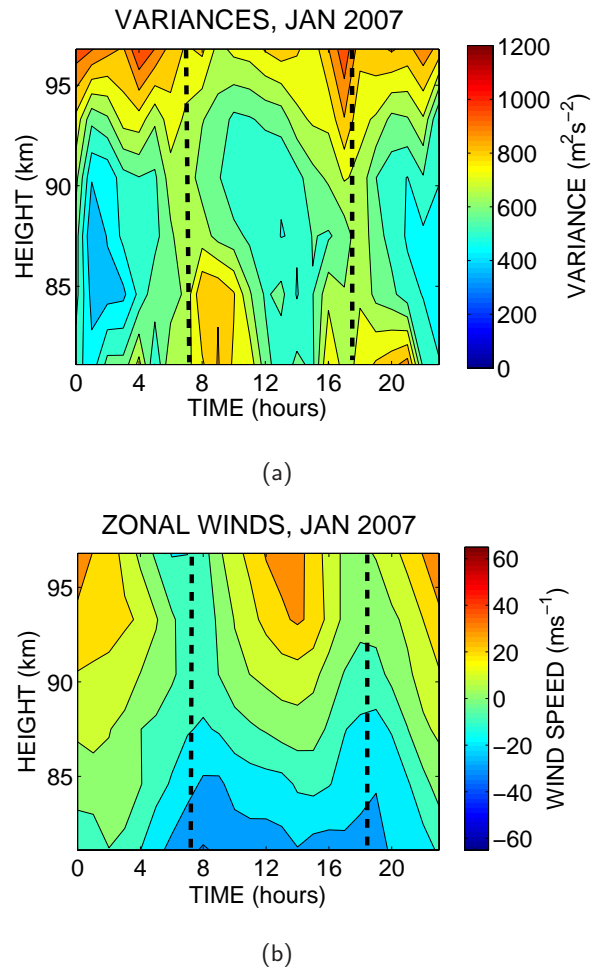
Figure 3.36: Composite days of (a) variance and (b) zonal winds for January 2007 over Rothera.

out the height range at approximately 07:00 and 18:00 UT, corresponding to the *westward* background winds forced by the 12-hour tide. The summer gravity-wave field is dominated by waves with eastward phase speeds at these heights and the maxima correspond to the time when little or no *in situ* filtering is occurring and gravity waves with eastward phase speeds are not encountering critical levels. This is as predicted by the theory described above.

Considering Figure 3.37, in autumn (or winter), the maxima in variance occur at approximately 04:00 and 14:00 UT, corresponding to the maximum *eastward* zonal winds. The winter gravity-wave field is dominated by waves with westward phase speeds at these heights and the maxima correspond to the time when little or no *in situ* filtering is occurring and gravity-waves with westward phase speeds are not encountering critical levels. Again, this matches the predicted relationship between the phase of the tide and the variation in gravity-wave activity and strongly supports the proposed mechanism.

It is interesting to note that in Figure 3.37 the maxima in variance at 04:00 UT is only evident above ~ 90 km, whilst the maxima at 14:00 UT is present throughout the height range. This maybe due to the difference in strength of the eastward winds at these times. At 14:00 UT the

(a)

(b)
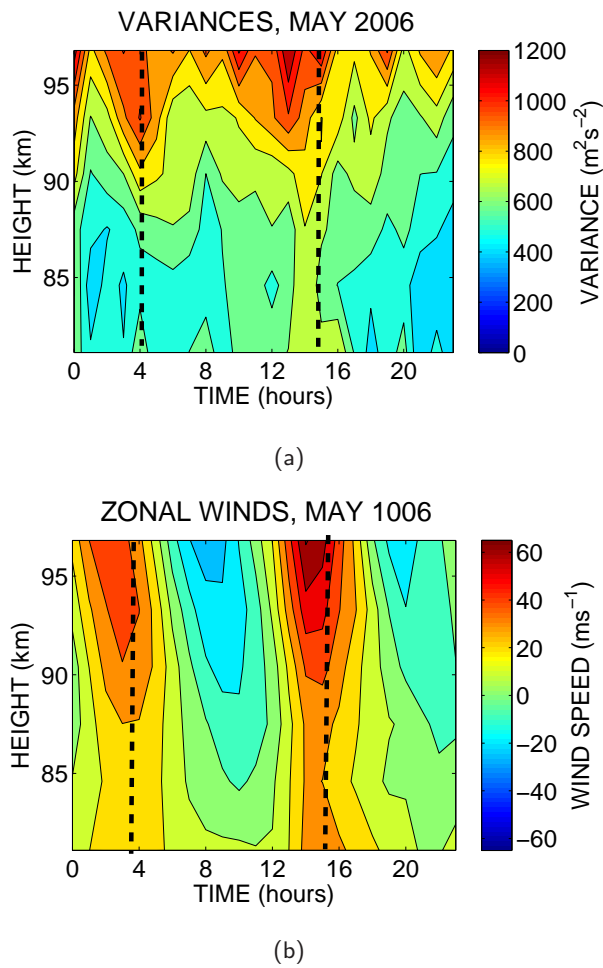
Figure 3.37: Composite days of (a) variance and (b) zonal winds for May 2006 over Rothera.

zonal winds are ~ 30 ms^{-1} or above throughout the height range, and the maxima in variance also extends through the height range. At 04:00 UT the maxima in variance can be seen above ~ 90 km when the zonal winds reach ~ 30 ms^{-1}. This may suggest that a large proportion of the modulation is occurring *in situ* in the upper mesosphere and requires relatively strong zonal winds in order to form critical levels for the mesospheric gravity-wave field.

3.5 Discussion

The new technique described in this chapter is capable of calculating the variance of high-frequency gravity-waves over a range of time scales and in 6 height gates between about 80 and 100 km. The advantages of using this variance technique with meteor radar to study gravity waves are fourfold.

1. They have 24-hour coverage all year round. This allows detailed climatologies to be established including data from all seasons, weather conditions and times of day.

2. A large back catalogue of data exists from multiple meteor radars. This technique can be applied retrospectively to these data sets.

3. The number and position of available datasets will allow a global network of gravity-wave measurements to be made.

4. This method works well above $\sim$ 90 km. It is above this height that MF radars have been reported to underestimate winds and as a consequence may also underestimate gravity-wave variance (e.g., *Manson et al.*, 2004).

There are also several disadvantages to consider.

1. Meteor radar can not resolve individual waves.

2. The observations are limited to horizontal variance and cannot provide estimates of momentum flux.

3. The meteor radar observes a relatively narrow height range compared to the depth of the atmosphere.

4. The frequency/wavenumber range detected by this technique can only be defined approximately.

Several climatological studies of gravity-wave activity have been conducted at polar latitudes. The semi-annual cycle in activity at mesospheric heights is already well established. (e.g., *Vincent and Fritts*, 1987; *Nakamura et al.*, 1993; *Tsuda et al.*, 1994; *Vincent*, 1994; *Connor and Avery*, 1996; *Thorsen and Franke*, 1998; *Dowdy et al.*, 2007). The presence of a semi-annual cycle in the results from the variance technique over Rothera and Esrange agrees well with previous observations made with differing techniques. This provides additional confidence in the technique.

Climatological observations of gravity-wave variance using 6 years of MF radar data from Mawson, Antarctica (67° S, 63° E), are presented by *Vincent* (1994). The total variance was calculated for gravity waves with periods of 1 to 24 hours. The variances observed over Mawson are of similar magnitude to those observed over Rothera and Esrange and presented here. There is a semi-annual cycle present over Mawson below $\sim$ 95 km with peaks in summer and winter. This is consistent with the behaviour observed over Rothera although an additional peak observed at the upper height gates in December over Rothera is not evident in the Mawson data.

The vertical behaviour of variance over Mawson during summer also shows similarities to the results presented here for Rothera and Esrange. Over Mawson, below $\sim$ 90 km, the variances during January and February show decreasing variance with increasing height below about 90 km,

then, increasing variance with increasing height above 90 km. This is similar to the behaviour seen in summer over both Rothera and Esrange. As previously discussed, a possible explanation for this behaviour is the breaking of gravity waves below the summer mesopause acting to remove energy from the gravity-wave field.

A more recent study using an MF radar based at Rothera was presented by *Hibbins et al.* (2007). This radar is co-located with the meteor wind radar at Rothera and so observed differences are likely to be the result of differences between the techniques. The magnitude of variances over Rothera are similar when observed with the meteor or MF radar. Both zonal and meridional components of gravity wave variances presented from the MF radar show an obvious seasonal cycle. However, the MF radar observes a wintertime maximum at all heights and no summertime maximum. This is different to observations at other polar latitudes using MF radars which show the semi-annual behaviour seen in the results from both the Rothera and Esrange meteor radar (e.g., *Vincent and Fritts*, 1987; *Tsuda et al.*, 1994; *Vincent*, 1994).

Dowdy et al. (2007) used MF radars (Davis 69° S, Syowa 69° S, Poker Flat 65° N and Andennes 69° N), in a recent study to compare gravity-wave climatologies from the Arctic and Antarctic. All four stations used the activity from gravity waves with periods between 20 minutes and 2 hours. The variances exhibit a strong semi-annual behaviour below $\sim$ 90 km, and a more annual behaviour above. *Dowdy et al.* (2007) noted several differences between the gravity-wave activity at the northern and southern hemisphere sites. In particular the growth of activity with height was reported to be stronger over the two southern hemisphere radars during both summer and winter. Such a difference is not evident in the variances presented here for Rothera and Esrange. However, that the MF radars used by *Dowdy et al.* (2007) were similar but not identical instruments and differences between the radars could account for some of the differences in the results.

Manson et al. (1997) presented gravity-wave activity from periods from $10 - 100$ mins and 1.5 to 6 hours using MF radars in the Canadian Prairies (49°N, - 52°N) and at Tromsø,(69°N). Tromsø is located very close to the Esrange meteor radar. *Manson et al.* (1997) presented substantially higher activity over Tromsø ,for both frequency ranges, than over the other, lower latitude stations. A strong semi-annual cycle is also present at heights between 76 and 88 km over Tromsø with maxima in summer and winter. The results presented over Tromsø agree favourably with those presented here for both Rothera and Esrange.

In general, the results from MF radars show some differences, especially above $90 - 95$ km, with the results from the variance technique presented here. The results from the studies using MF radars discussed here show the semi-annual behaviour above $90 - 95$ km becoming more annual (e.g., *Vincent*, 1994; *Dowdy et al.*, 2007). Although the behaviour over Rothera exhibits a tendency for the maxima in variance in winter to become stronger than the summer maxima at these heights, the behaviour is semi-annual above 95 km. Over Esrange the semi-annual behaviour is more variable but is strong throughout the height range. Differences between

MF and meteor radar winds are well documented and there is a tendency for MF radar to underestimate the mean winds above 95 km when compared to meteor radar winds (e.g., *Manson et al.*, 2004; *Hall et al.*, 2005). These differences in winds derived from the MF and meteor-radar techniques must also be taken into account when comparing the gravity-wave variances. It is likely that the difference in the two techniques plays a part in the differences in variances observed above 95 km. There are also some differences in the part of the gravity-wave spectrum observed. *Vincent* (1994) observed waves with periods between 1 and 24 hours, and *Dowdy et al.* (2007) observed waves with periods between 20 minutes and 8 hours. Both of these studies include much longer-period waves than those observed here with the variance technique.

There are relatively few observations of gravity-wave interaction with tides or planetary waves. In fact, opinion is divided about the effects of such interactions on tidal amplitudes (e.g., *Fritts and Alexander*, 2003; *Norton and Thuburn*, 1999). One study of the modulation of gravity wave variances by *Isler and Fritts* (1996) showed variance enhancements correlated with times of strong diurnal tidal, 2-day wave and mean wind. *Isler and Fritts* (1996) proposed that a diurnal tide would produce a semidiurnal modulation of the gravity-wave variance. As discussed in Section 3.4.6, this occurs for an isotropic distribution of gravity-wave phase speeds. The gravity-wave phase-speed spectrum is not isotropic in summer and winter due to the critical-level filtering imposed by the underlying winds. During these times a modulation at the period of the tide is produced, as se t tidal periods were observed by *Manson et al.* (1998a) in a long term study using the MF radar based in Saskatoon. *Manson et al.* (1998a) found that the modulation was strongest in summer, agreeing with the results over Rothera where more modulation is observed in the summer. However, over Rothera there is also strong modulation of gravity-wave variance observed during the winter.

A modulation of gravity-wave momentum fluxes was presented by *Espy et al.* (2004b). A marked 12-hour oscillation was observed using 18 hours of airglow imager and IDI data from Halley, Antarctica (76° S). These results indicate that the modulation of momentum flux by tides may be significant at Antarctic latitudes.

A study by *Thayaparan et al.* (1995) using the MF radar at London, Canada (43° N, 81° W) presented evidence of modulation of gravity-wave activity at a 24-hour period. These results suggested that in winter the maximum gravity-wave variance corresponded to eastward tidal winds, and in summer the maximum in gravity-wave variance corresponded to westward tidal winds. This is in excellent agreement with the results presented over Rothera in Section 3.4.6. However, *Thayaparan et al.* (1995) found no evidence of a semidiurnal modulation of the gravity-wave field. They attribute this to the smaller amplitude of the 12-hour tide compared to the 24-hour tide.

Espy et al. (2004b) presented evidence of gravity wave / tidal interaction using momentum fluxes measured by a combination airglow imagers and Imaging Doppler Interferometer (IDI) radar over Halley, Antarctica (76° S). A marked 12-hour oscillation and a smaller 24-hour oscillation

were observed. The oscillations were strong in the zonal component, although there was some evidence of modulation of the meridional momentum fluxes. The sense of oscillation was out of phase with the tidal winds, as expected from the mechanism described here and predicted by (*Walterscheid*, 1981).

3.5.1 Conclusions

- A new technique has been developed to study high-frequency gravity waves with meteor radar.

- This new technique can detect gravity-waves with periods from $\sim$ 20 minutes to $\sim$ 2 hours.

- A semi-annual seasonal cycle has been observed with solstitial maxima and equinoctial minima.

- There is clear evidence of interactions between the underlying mean winds and high-frequency gravity-wave field. These interactions are proposed as a source of the observed seasonal cycle.

- Possible interactions between high-frequency gravity waves and the temperature field in the summer months can explain the observed growth rates of gravity-wave activity.

- Gravity-wave activity exhibits evidence of modulation at tidal and planetary-wave periods, particularly evident in summer and winter.

- The modulation at tidal and planetary-wave periods may be the result of *in situ* filtering as the tide or planetary wave drives the background winds to form critical levels in the MLT.

Chapter 4

Gravity-Wave Variance and Momentum Flux Measured with Meteor Radar

4.1 Introduction

Chapter 3 introduced the variance technique, a novel technique using meteor-radar data to determine the gravity-wave variance. This technique can measure variance from waves with periods of between $\sim$ 20 minutes and 2 hours and at heights between 80 and 100 km. Although this provides a useful proxy for high-frequency gravity-wave activity, the variance technique can only determine a *total variance* and cannot give any information about wave propagation direction or the momentum flux associated with the observed waves.

This chapter applies a different technique for studying gravity waves using meteor radar. This technique is based on that developed by *Hocking* (2005) and hereafter will be referred to as the *matrix technique*. The matrix technique uses the variance of the radial velocities of individual meteor echoes to determine gravity-wave parameters. Unlike the variance technique, the matrix technique can be used to determine both zonal and meridional variances separately. The matrix technique can also be used to determine the vertical flux of horizontal momentum, or more specifically the horizontal and vertical wind covariance, not possible with the variance technique.

Measurements of momentum flux is an important tool in understanding the dynamics and energetics of the atmosphere. The divergence of zonal momentum flux can give an indication of the strength of the driving of the zonal mean winds through the breaking of gravity waves.

Throughout this work the covariance of the horizontal and vertical winds ($u'w'$ and $v'w'$) or momentum flux per unit density shall be referred to as momentum flux for simplicity. Momentum flux is a second-order statistic of the gravity-wave field. It is also a vector quantity so that if,

for example, the eastward and westward momentum flux are equal, then the resultant zonal momentum flux is zero. Therefore, the momentum flux is also a measure of the anisotropy of the gravity-wave field. The more positive, i.e., eastward, the zonal momentum flux, the more eastward propagating waves there are. Similarly, the more positive the meridional momentum flux the more northward propagating waves there are. It is believed that the deposition of momentum in the Mesosphere and Lower Thermosphere (MLT) is responsible for the slowing and reversal of the mesospheric jets. In summer a decrease in zonal momentum flux is expected across the observed height range. This decreasing momentum flux with height indicates that eastward momentum flux is being deposited which acts to slow and reverse the westward zonal winds present in summer. The opposite is true in winter.

Momentum fluxes are notoriously difficult to measure. Very accurate, high temporal resolution measurements of both vertical winds, which are small at these heights, and horizontal winds are needed. As a result time averages on the order of days are needed to determine statistically significant fluxes. Some previous studies of momentum flux have used VHF and MF radar with oppositely directed beams (e.g., *Reid and Vincent*, 1987; *Murphy and Vincent*, 1993). This type of beam system can be simulated by all-sky meteor radars by selecting azimuth dependent subsets of meteors. However, in practice, this severely limits the number of meteors available in each height-time window and can lead to high numbers of gaps and large errors in the data. This makes simulated beams impractical for determining gravity-wave activity or momentum flux. The technique developed by *Hocking* (2005) uses a generalised formulation of this two-beam method for use with radar systems operating *without* narrow beams but where the position of each of the scatters, in this case meteors, is known to a good accuracy. *Hocking* (2005) demonstrated the technique on the all-sky meteor radars at Resolute Bay, Canada and Socorro, New Mexico. In this Chapter the technique is adapted and applied to the all-sky meteor radars at Rothera and Esrange.

It should be noted that this technique is different to that described in Chapter 3 in several ways. The most important of these is that the variance technique uses the variance of the horizontal velocities of meteors to determine the activity within the high-frequency gravity-wave field. In contrast, the matrix technique uses the radial velocities of meteors to determine zonal and meridional components of variance and momentum flux.

A description of the data analysis for the matrix technique used in this chapter is given in Section 4.3. The variances calculated from this technique are presented in Section 4.4 and discussed in Section 4.5. The short-term variability, seasonal cycle, inter-annual variability and inter-hemispheric differences of the *zonal* momentum fluxes are presented in Section 4.6. The short-term variability, seasonal cycle, inter-annual variability and inter-hemispheric differences of the *meridional* momentum fluxes are presented in Section 4.7. These zonal and meridional momentum flux are discussed in Section 4.8.

4.2   The Matrix Technique

The reasoning behind this technique is similar to that already described in Chapter 3 for the variance technique. That is:

1. We assume that there is a 'homogeneous' wind-field across the field of view of the radar. This is composed of elements that do not vary significantly over the horizontal scale of the meteor collecting volume such as tides, planetary waves and mean winds. This 'homogeneous' motion is one part of the horizontal velocity measured for each individual meteor echo, and can be calculated using an ensemble of meteors from all azimuth angles. This was discussed in detail in Chapter 2.

2. As well as this 'homogeneous' wind described above, there are also many waves with scale sizes smaller than the collecting volume of the radar. These are mostly gravity waves with periods less than $\sim$ 2 hours and with horizontal wavelengths less $\sim$ 400 km. As a consequence of their small horizontal scales, the radar cannot individually resolve these waves. They can nevertheless be measured through the scatter they introduce in the horizontal velocities of individual meteor echoes.

3. A measure of the activity of these small-scale waves can be made once the 'homogeneous' part of the atmospheric motion in the collecting volume has been removed from the horizontal velocity measured for each echo.

Like the variance technique described in Chapter 3, the matrix technique uses a collection of individual, essentially instantaneous and localised measurements. These are made throughout a time interval and over the large horizontal extent of the radar's collecting volume. The matrix technique can be used to determine momentum flux and variances from gravity waves with periods from near to the Brunt-Väisälä period to $\sim$ 2 hours and with horizontal wavelengths less than $\sim$ 400 km.

It should be noted that although the reasoning behind the matrix technique is the same as for the variance technique, the sensitivity of these techniques is slightly different. Only meteors detected between 15° and 45° from the zenith are used in the matrix technique (compared to 15° and 75° for the variance technique). The lower limit on zenith angle of 15° is common to all meteor radar data analysis and is imposed because the horizontal velocities inferred for meteors close to the zenith can have large errors. The upper limit of 45° is imposed because meteors detected with zenith angles larger than 45° have a smaller vertical component to their radial velocities. Ideally the analysis would be limited to meteors even closer to the zenith. However, the radars at Rothera and Esrange detect peak meteor counts at $\sim$ 60° from the zenith so too few meteors are detected at zenith angles less than 45° to determine reliable wind, variance or momentum fluxes. For the meteors included in the matrix technique that are closer to the zenith, the vertical

motion contributes a more significant portion of the radial velocity. So the matrix technique is more sensitive to the vertical motions associated with high-frequency gravity-waves. However, this difference is not large and the wave period ranges accessible to both techniques are near the Brunt-Väisälä period to ~ 2 hours.

4.3 Data Analysis

The routine calculation of hourly winds by meteor radar is described in in Section 2.5. In summary, a least-squares fit to the horizontal velocities over all azimuths is performed for all meteors echoes detected in a 2 hour window and within each height gate. In the routine calculation of winds the vertical component of velocity is assumed to be negligible compared to that of the the horizontal velocity.

For an individual meteor echo detected with a zenith angle of θ and an azimuth of ϕ, the radial velocity which is a component of the homogeneous part of the wind field, can be defined as:

$$v_{radm} = U \sin\theta \cos\phi + V \sin\theta \sin\phi + W \cos\theta, \tag{4.1}$$

where v_{radm} is the radial velocity of an assumed uniform slab of atmosphere in Cartesian co-ordinates moving with speeds in the zonal, meridional and vertical directions of U, V and W. This represents the part of the wind field that is resolved by the radar, both temporally and spatially, and is composed of tides, planetary waves, the mean wind and gravity waves of large scale size.

The 'in-homogeneous' part of the motion can be determined by removing the calculated 'homogeneous' motion (v_{radm}) from the radial velocity of each individual meteor (v_{rad}) as was done in Chapter 3. Section 4.3.1 describes two alternative methods of removing this 'homogeneous' part of the wind field and compares their accuracies.

Once the 'homogeneous' part of the wind field has been removed from the measured radial velocity, v_{rad}, we can assume that the remaining radial velocity, v'_{rad} ($= v_{rad} - v_{radm}$), is primarily due to the motion of gravity waves not resolved by the radar. Again in similar manner to the analysis presented in Chapter 3.

Unlike the variance method of Chapter 3, the *Hocking* (2005) method attempts to use these data to determine the gravity-wave variance and momentum fluxes. A least-squares fit to the remaining radial velocities is performed. This minimises equation 4.2 and is equivalent to maximising the similarity between the measured and model *variances* of radial velocity as a function

of time and position (*Hocking*, 2005).

$$\Delta = \sum ((v'_{rad})^2 - (v'_{radm})^2)^2 \tag{4.2}$$

To minimise this equation we must express v'_{radm} in terms of the perturbations of the wind components (u', v' and w') as shown in equation 4.3.

$$v'_{radm} = u' \sin\theta \cos\phi + v' \sin\theta \sin\phi + w' \cos\theta \tag{4.3}$$

This equation can then be squared and substituted back into equation 4.2. The result is equation 4.4, which can be minimised over all detected meteor positions within a chosen height and time interval.

$$\begin{aligned}\Lambda = \quad & \sum [(v')^2 - (u'^2 \sin^2\theta \cos^2\phi + v'^2 \sin^2\theta \sin^2\phi + w'^2 \cos^2\theta + \\ & 2u'v' sin^2\theta \cos\phi \sin\phi + 2u'w' \sin\theta \cos\theta \cos\phi + \\ & 2v'w' \sin\theta \cos\theta \sin\phi)]^2\end{aligned} \tag{4.4}$$

In order to minimise Λ we take the partial derivatives with respect to all the parameters within equation 4.4 (u'^2, v'^2, w'^2, $u'v'$, $u'w'$ and $v'w'$) and set them equal to zero.

The result of this can be put into a matrix equation of the form shown in equation 4.5 and 4.6. Note that this assumes that the parameters u'^2, v'^2, w'^2, $u'v'$, $u'w'$ and $v'w'$ are all uniform across the field of view of the radar.

$$A \times \begin{bmatrix} u'^2 \\ v'^2 \\ w'^2 \\ u'v' \\ u'w' \\ v'w' \end{bmatrix} = \begin{bmatrix} \sum v'^2_{rad} \sin^2\theta \cos^2\phi \\ \sum v'^2_{rad} \sin^2\theta \sin^2\phi \\ \sum v'^2_{rad} \cos^2\theta \\ \sum 2v'^2_{rad} \sin^2\theta \cos\phi \sin\phi \\ \sum 2v'^2_{rad} \sin\theta \cos\theta \cos\phi \\ \sum 2v'^2_{rad} \sin\theta \cos\theta \sin\phi \end{bmatrix} \tag{4.5}$$

Where A is defined as :

$$A = \begin{bmatrix} \sum \dfrac{\sin^4\theta}{\cos^4\phi} & \sum \dfrac{\sin^4\theta}{\cos^2\phi\sin^2\phi} & \sum \dfrac{\sin^2\theta}{\cos^2\theta\cos^2\phi} & \sum \dfrac{2\sin^4\theta}{\cos^3\phi\sin\phi} & \sum \dfrac{2\sin^3\theta}{\cos\theta\cos^3\phi} & \sum \dfrac{\sin^3\theta\cos\theta}{\cos^2\phi\sin\phi} \\[1em] \sum \dfrac{\sin^4\theta}{\cos^2\phi\sin^2\phi} & \sum \dfrac{\sin^4\theta}{\sin^4\phi} & \sum \dfrac{\sin^2\theta}{\cos^2\theta\sin^2\phi} & \sum \dfrac{2\sin^4\theta}{\sin^3\phi\cos\phi} & \sum \dfrac{2\sin^3\theta}{\cos\theta\sin^2\phi\cos\phi} & \sum \dfrac{2\sin^3\theta}{\cos\theta\sin^3\phi} \\[1em] \sum \dfrac{\sin^2\theta}{\cos\theta^2\cos^2\phi} & \sum \dfrac{\sin^2\theta}{\cos^2\theta\sin^2\phi} & \sum \cos^4\theta & \sum \dfrac{2\sin^2\theta}{\cos^2\theta\sin\phi\cos\phi} & \sum \dfrac{2\cos^3\theta}{\sin\theta\cos\phi} & \sum \dfrac{2\cos^3\theta}{\sin\theta\sin\phi} \\[1em] \sum \dfrac{2\sin^4\theta}{\cos^3\phi\sin\phi} & \sum \dfrac{2\sin^4\theta}{\sin^3\phi\cos\phi} & \sum \dfrac{2\sin^2\theta}{\cos^2\theta\sin\phi\cos\phi} & \sum \dfrac{4\sin^4\theta\sin^2\phi}{\cos^2\phi} & \sum \dfrac{4\sin^3\theta\cos\theta}{\sin\phi\cos^2\phi} & \sum \dfrac{4\sin^3\theta\cos\theta}{\sin^2\phi\cos\phi} \\[1em] \sum \dfrac{2\sin^3\theta}{\cos^3\phi\cos\theta} & \sum \dfrac{2\sin^3\theta\cos\theta}{\sin^2\phi\cos\phi} & \sum \dfrac{2\cos^3\theta}{\sin\theta\cos\phi} & \sum \dfrac{4\sin^3\theta\cos\theta}{\cos^2\phi\sin\phi} & \sum \dfrac{4\sin^2\theta}{\cos^2\theta\cos^2\phi} & \sum \dfrac{4\sin^2\theta\cos^2\theta}{\sin\phi\cos\phi} \\[1em] \sum \dfrac{2\sin^3\theta\cos\theta}{\cos^2\phi\sin\phi} & \sum \dfrac{2\sin^3\theta\cos\theta}{\sin^3\phi} & \sum \dfrac{2\cos^3\theta}{\sin\theta\sin\phi} & \sum \dfrac{4\sin^3\theta\cos\theta}{\sin^2\phi\cos\phi} & \sum \dfrac{4\sin^2\theta\cos^2\theta}{\cos\phi\sin\phi} & \sum \dfrac{4\sin^2\theta\cos^2\theta}{\sin^2\phi} \end{bmatrix} . \quad (4.6)$$

For reasons of space the expressions in A are split over two lines. The matrix expression in equation 4.5 can now be inverted to solve for $u'^2, v'^2, w'^2, u'v', u'w'$ and $v'w'$. An outlier rejection filter is then applied to the data using a sliding 48-hour window to remove any values which are more than 3 standard deviations away from the mean.

The final data product from the matrix technique are three-hourly values of $u'^2, v'^2, w'^2, u'w', v'w'$ and $u'v'$, calculated within the range of heights considered. This work will focus on using the variances (u'^2, v'^2) and vertical flux of horizontal momentum $(u'w', v'w')$. The variances and momentum fluxes can be used to investigate the behaviour of the gravity-wave field as well as the deposition of momentum by high-frequency gravity waves.

4.3.1 Removal of the Homogeneous Motion

Gravity-wave variances and momentum fluxes can only be calculated once the homogeneous part of the measured motion has been removed. This Section describes two different methods of removing this homogeneous motion. The first, as described in *Hocking* (2005), calculates the homogeneous component of motion from the sine-wave fit to the *radial* velocities of meteors for all azimuths. This represents the removal of a time and height average of the homogeneous component, where the time interval and height intervals are user defined. The second, as used in Chapter 3, uses an interpolated wind field to calculate the horizontal velocity due to the homogeneous motion at the height and time of each individual meteor so that the homogeneous motion removed is unique to each meteor.

The first method for removing the homogeneous motion calculates a time-height average over

a three hour window and a 3 or 5 km height gate as used by *Hocking* (2005). A sine-wave fit to the radial velocities in this window can then be used to determine a radial velocity for the azimuth angle of each meteor. This value is then removed from the radial velocity measured for each meteor echo to leave, in principle, only the radial velocity due the in-homogeneous part of the wind field.

The length and height of window used can be varied as long as enough meteors are collected within each window to accurately determine variance and momentum flux values. Although relatively few meteors are needed in each window to determine an accurate wind velocity, a minimum of about 30 meteors is necessary to calculate reliable variance and momentum flux measurements (*Hocking*, 2005). Because this technique only uses meteors detected between 15° and 45° from the zenith, the number of available meteors is greatly limited. On average, only $\sim 40\%$ of the total number of meteors detected over Rothera and Esrange are within this range.

In the analysis performed here, a three-hour time window is used so that over 30 meteors are present in a significant fraction of the time-height windows. However, the use of a three-hour window means that the wind velocity determined from the sine-wave fit will be an average over this three-hour, 3 km, time-height interval. This relatively long time-average does not fully take account of the variation in the tidal winds occurring over the three hours. At these heights and the latitudes of Rothera and Esrange, the 12-hour tide has very large amplitude and higher frequency tides, specifically the 8-hour, tide also reach significant amplitudes. Over 3 hours, the phase of the 12-hour tide progresses through 90°, thus causing a rotation of the direction of the wind by 90°. The effect of this on the azimuth-radial velocity plot is a phase shift in the sine wave. Figure 4.1 shows the effect of a three hour time difference on a simplified wind field composed only of a wind vector rotating with a period of 12 hours. Meteors at given time, for example hour 0, will lay on the blue sine wave. Meteors detected three hours later will lay on the second, red, sine wave.
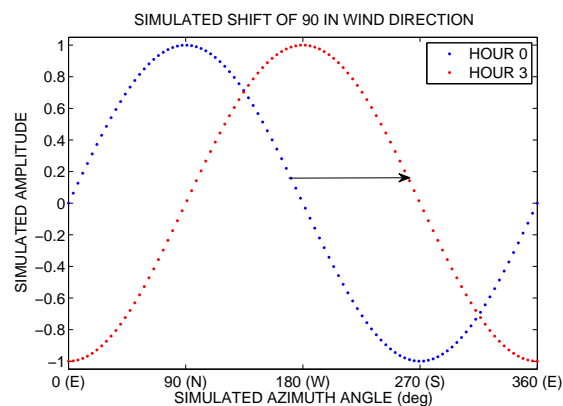
Figure 4.1: Schematic diagram showing the shift between sine waves resulting from a 90°rotation of the prevailing wind.

The radial velocity calculated as the homogeneous motion for the meteors detected at the

beginning and end of the time interval will not represent the true wind speed and direction at those times. The result of this will be that the radial velocities used in the further analysis will contain a contribution from the tides and the calculated variance and momentum flux will also be contaminated. This may cause spurious modulations at tidal periods in the data that are so solely due to the incorrect removal of the homogeneous part of the motion.

In addition to the tidal variations, at polar latitudes in summer there is a large wind shear in the horizontal winds across the height range observed. From 80 to 100 km the mean winds can change from $\sim$ -40ms^{-1} to $\sim$ +30 ms^{-1} (e.g., *Mitchell et al.*, 2002). This rapid change in the background winds with height can result in a difference of up to 70 ms^{-1} between the top and bottom of the height range and could potentially contaminate the gravity-wave variance if not correctly removed. Both of these factors mean that the removal of the homogeneous flow using the time-average method may leave a contribution to the variance and momentum flux from the incomplete removal of tides and wind shear leading to an overestimate of the gravity-wave activity.

An alternative method for removing the background motion was developed in this thesis and discussed in Chapter 3. Instead of using a time-height average, the hourly horizontal winds calculated as a routine product of the radar analysis are used as a basis to interpolated a *unique* value of the homogeneous zonal and meridional wind for the exact time and height of each meteor.

The zonal and meridional wind for the time and height of each meteor combine to give a wind vector that is the homogeneous wind at the time and height of each meteor. Once this has been calculated, its contribution to the meteors measured horizontal velocity is also be determined. This is then the part of the measured horizontal velocity for each meteor that is due to the homogeneous motion alone. This is then removed from the measured horizontal velocity for each meteor to leave only the horizontal velocity from the in-homogeneous part of the wind motion and converted back into a radial velocity. This process is repeated for each meteor individually.

The advantage of this method over the time-height average is that there is no assumption that the average homogeneous wind is constant throughout the time-height interval considered. As a result the homogeneous part of the wind field will be removed more effectively, resulting in a more accurate calculation of gravity-wave variance and momentum flux .

4.3.2 Comparing Removal Methods

To illustrate the relative performance of the two techniques described above, data from a typical day (July 24th, 2005) was taken from the Rothera dataset. Gravity-wave variances were

calculated in 3-hourly bins, first without the background motion removed, secondly with the homogeneous motion removed using the height-time average method and lastly with the homogeneous motion removed using the interpolation method.
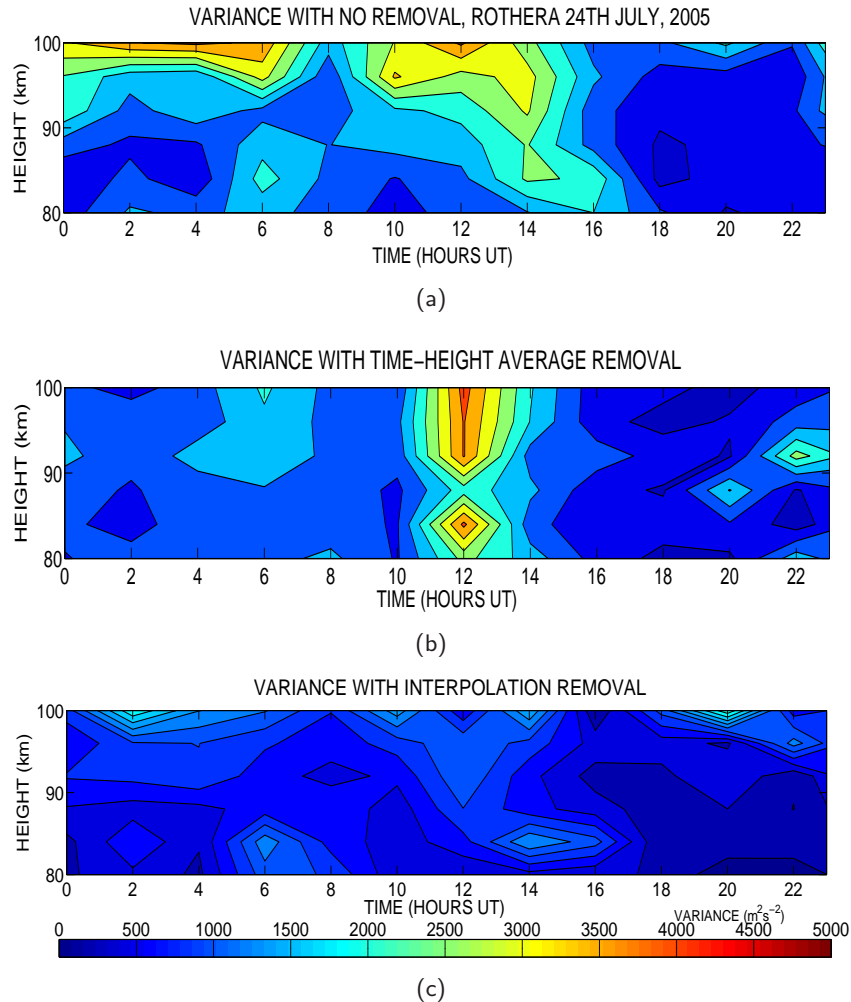
Figure 4.2: Variances calculated before and after removal of the homogeneous motion using time-average and interpolation methods for July 24th, 2005 over Rothera.

Figure 4.2 shows height-time contour plots of the variances calculated by each of three methods. Figure 4.2(a) presents no removal of the homogeneous motion, Figure 4.2(b) present a time-average removal and Figure 4.2(c) presents an interpolation removal of the homogeneous motion. The top panel, showing no removal, has very large variances, particularly at the top of the height range, where tidal amplitudes are large. A large proportion of this variance is due to the contribution of the tides, mean winds and planetary waves. While both the time-average and interpolation methods successfully remove a large quantity of this spurious variance, the interpolation removal removes more in total (up to 50%) and removes more of the structures seen in the top panel, particularly the peak at $\sim$ 12 UT.

This can be demonstrated for a longer term average by calculating composite days of variance using the different removal techniques. Figure 4.3 shows composite days determined over Rothera
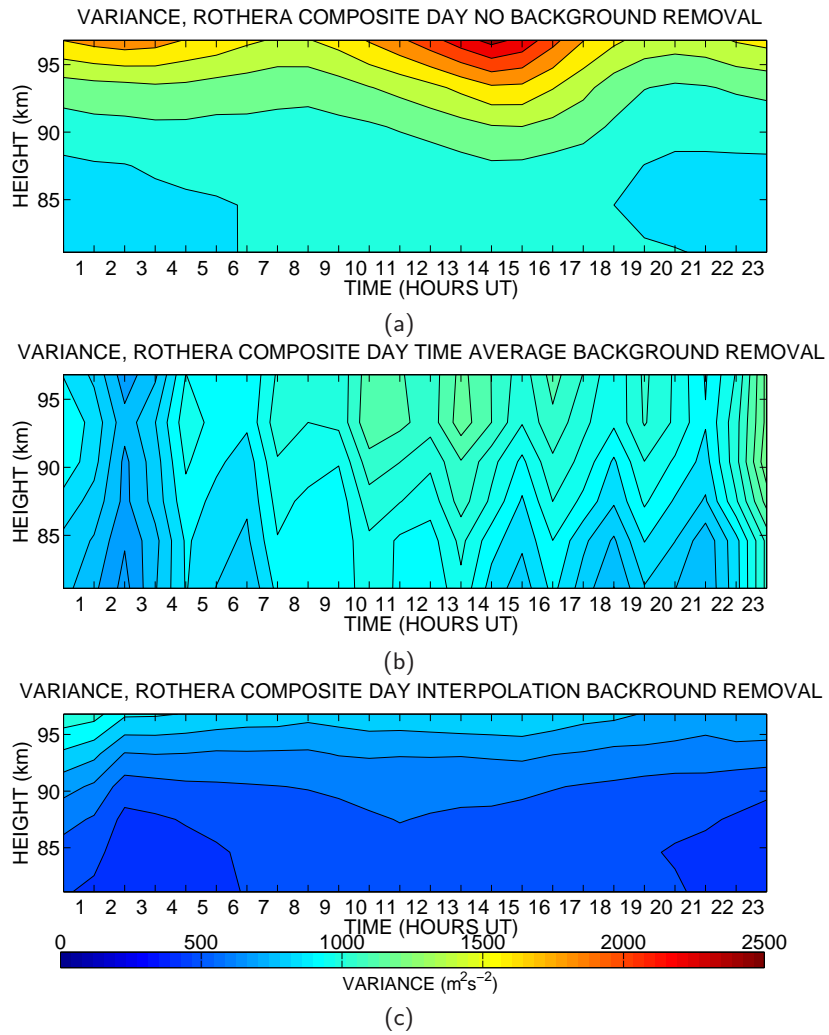
Figure 4.3: Composite-day of variances with (a) no background motion removal, (b) a height-time average removal technique and (c) an interpolation removal technique.

using data from February 2005 to December 2006. Figure 4.3a presents the composite day of variance with no removal of the homogeneous motion. This shows clear peaks up to ~ 2400 m^{2}s^{-2}, evident in the upper half of the figure, separated by ~ 12 hours. These are the result of contamination by the 12-hour tide. Figure 4.3b shows the composite day from the results using the height-time average removal method. The variances are in general lower than those in Figure 4.3b by about 50%, but still larger than those in Figure 4.3c by $\sim 60\%$. There is also a high degree of noise in Figure 4.3b, not evident for the interpolation removal method. It also appears that the peak in variance at ~ 12 UT has not been fully removed by the time-average method, which may result in a spurious modulation of the variance or momentum flux if they were calculated using this method.

In conclusion, the method of removing the homogeneous motion using interpolation is the most effective. In order to remove the homogeneous motion in the most accurate way, the interpolation method will therefore be used for all further analysis presented in this thesis.

4.4 Results - Zonal and Meridional Gravity-Wave Variance

This section presents the variances over Rothera and Esrange determined using the matrix technique. In contrast to the result presented in Chapter 3, the matrix technique allows zonal and meridional components of the variances to be estimated. As already noted, this technique is sensitive to gravity-waves with periods from about $\sim$ 20 minutes to 2 hours and with horizontal wavelengths less than $\sim$ 400 km.

The variances calculated from the matrix technique are 3-hour estimates in six height gates between 80 and 100 km. However, due to the low meteor counts in the top and bottom of the height range, it was found that high-quality data are only available in the height gates centred on $\sim$ 87.4, 90.4 and 93.3 km. Because of this, only data from these height gates are used in the analysis presented here. There is also considerable variability in the 3-hourly variances as well as a few remaining outliers, even after an outlier rejection filter has been applied. To minimise the effect of these outliers, daily averages were calculated by taking the median of all the 3-hourly variances in a particular day. The median was chosen instead of the mean as this is less sensitive to the effects of outliers.

Section 4.4.1 presents daily averages of zonal and meridional variances and considers their short-term behaviour, Section 4.4.2 presents monthly-mean variances over Rothera and Esrange and Section 4.4.3 considers the seasonal behaviour of the variances and inter-hemispheric differences.

4.4.1 Short-Term Variability of Gravity-Wave Variance

To provide an idea of the character and quality of the data, Figure 4.4 presents a time series of daily zonal variances for Rothera from February 2005 to July 2008 at $\sim$ 93 km, (Figure 4.4a), $\sim$ 90 km (Figure 4.4b) and $\sim$ 87 km (Figure 4.4c). Overlaid are lines representing a 30-day smoothing filter applied to the data. The zonal and meridional components show very similar short-term behaviour thus only zonal variances are presented here for reasons of space.

Several features are noticeable from the figure:

1. The daily values at all heights show a large level of day-to-day variability with values between 100 and 1000 m^2s^{-2} .

2. There is a clear seasonal cycle with peaks at the solstices and minima at the equinoxes revealed by the smoothed data.

3. The variance generally increases with increasing height. For example, the variance in the winter of 2002 increases from $\sim$ 370 m^2s^{-2} at $\sim$ 87 km to $\sim$ 475 m^2s^{-2} at $\sim$ 93 km.
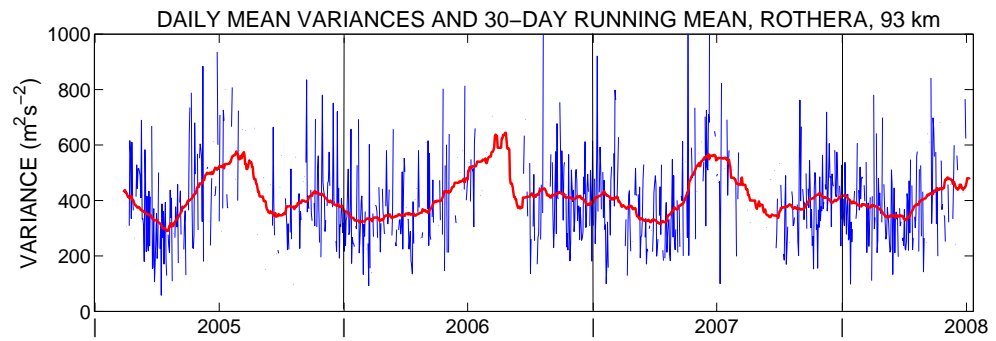
(a)
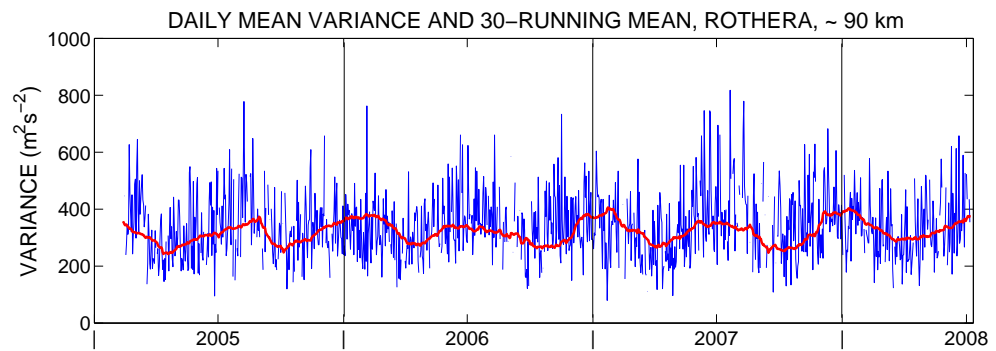
(b)
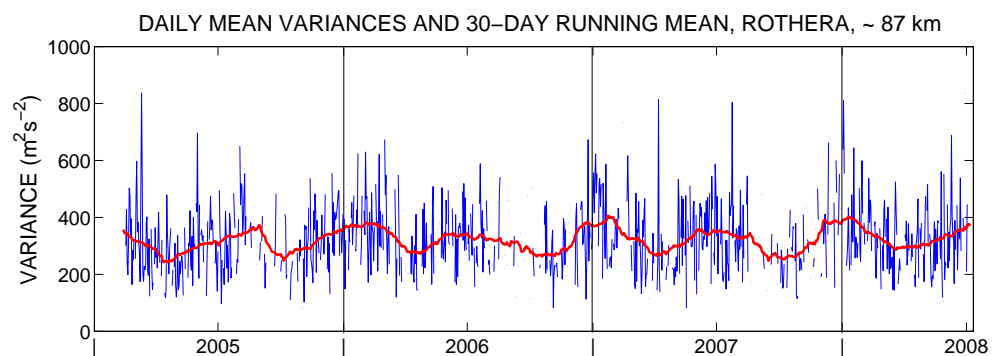
(c)

Figure 4.4: Daily values of variance over Rothera at (a) $\sim$ 93 km, (b) $\sim$ 90 km and (c) $\sim$ 87 km for February 2005 to July 2008. The smooth red line represents the 30-day running average.

4. The number of data gaps in the daily time series is largest in the lower and upper height gates shown.

Figure 4.5 presents the daily averages calculated over Esrange for January 2000 to July 2008. This data shows the same general features as the data over Rothera shown in Figure 4.4. However, Figures 4.5a and 4.5c illustrate the high number of data gaps occurring in the dataset over Esrange where lower count rates are received.

Some of the features are similar to those seen over Rothera. There is a high level of short-term
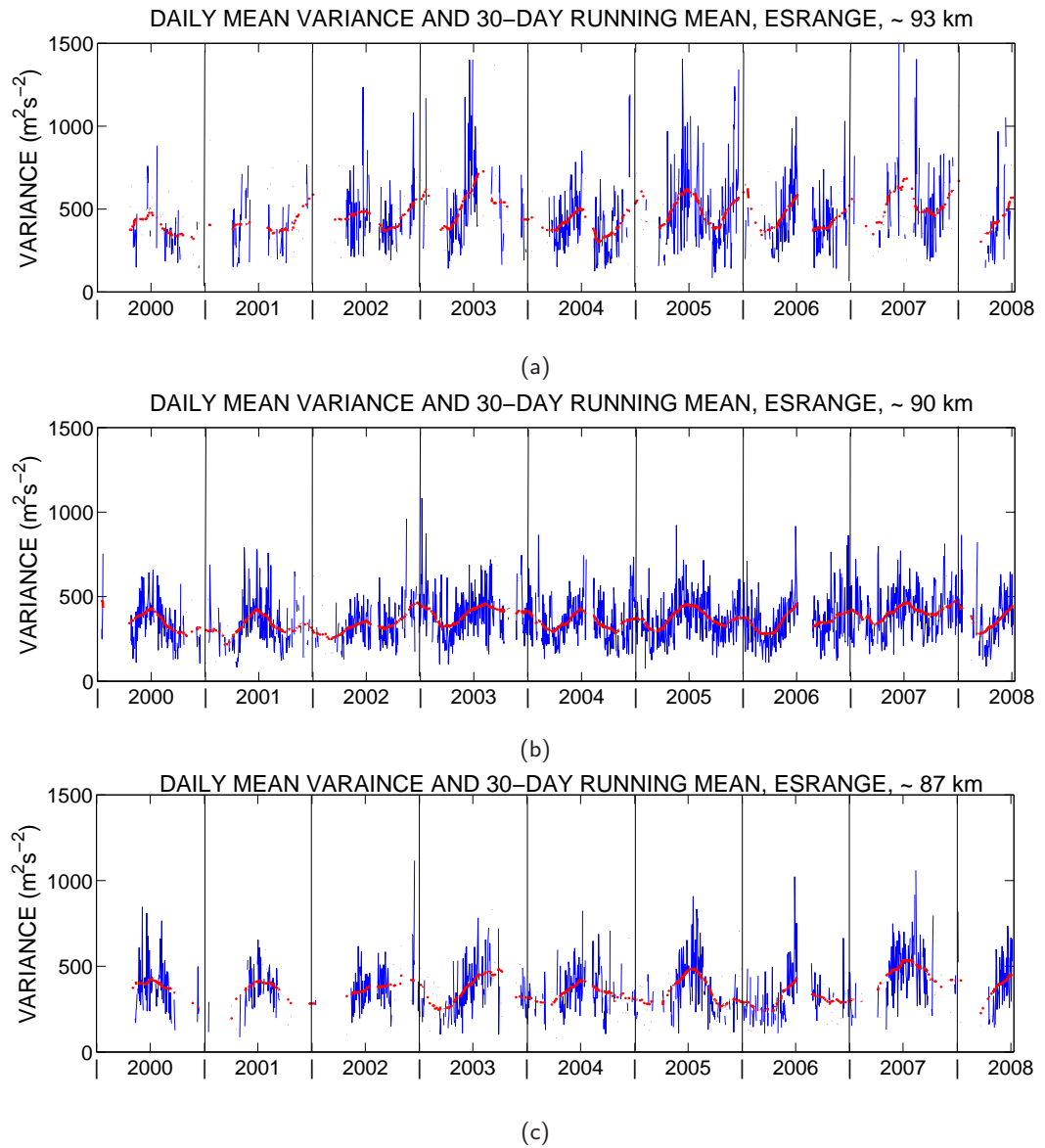
Figure 4.5: Daily values of variance over Esrange at (a) $\sim$ 93 km, (b) $\sim$ 93 km and (c) $\sim$ 87 km for February 2005 to July 2008. The smooth red line represents the 30-day running mean.

variability with daily values in the upper height gate reaching 1000 m^2s^{-2} on occasion. The semi-annual seasonal cycle of zonal variances is evident in the 30-day smoothing. The variances also show an increase with increasing height in both the daily and smoothed values.

4.4.2 Seasonal and Inter-Annual Behaviour of Gravity-Wave Variance

To investigate the seasonal pattern over both stations in more detail, monthly-means of the zonal and meridional variances were calculated. A monthly-mean was only calculated if there were at least 10 days worth of data available in a particular month. Figure 4.6 presents the monthly-mean values of zonal and meridional variance over Rothera at at (a) $\sim$ 93 km, (b) $\sim$

90 km and (c) $\sim$ 87 km calculated using data from February 2005 to July 2008. The beginning and end of each year is delineated by a vertical black line. The error bars denote the standard error on the mean.
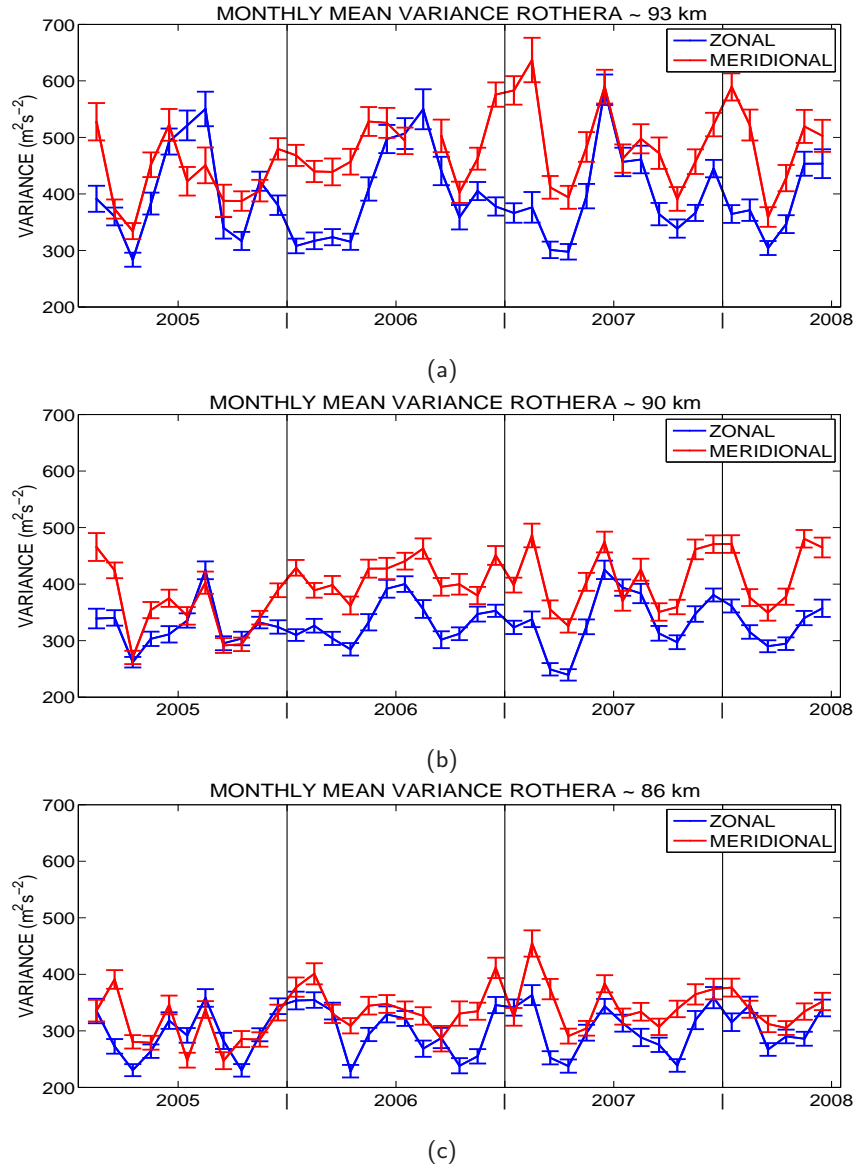
Figure 4.6: Zonal and meridional monthly-mean gravity-wave variances over Rothera at heights of (a) 93 km, (b) 90 km (c) 87 km for February 2005 to July 2008.

The semi-annual seasonal cycle with peaks in summer and winter is clear in both zonal and meridional variances. This behaviour persists in all years and across all three height gates. The largest values of variance are in summer (December / January) of 2006 / 2007 at the upper height gate where the meridional variances reach $\sim$ 650 m^{2}s^{-2}. There is also a systematic difference between the zonal and meridional variances. In nearly all months and in all height gates, the meridional variances are larger than the zonal. The difference between the two components also becomes larger as height increases.

As well as similarities between the years observed, there is also significant inter-annual variability.

For example, at ~ 87 km variances in the summer of 2006 / 2007 are larger than the other years. Figure 4.7 presents a similar analysis of the zonal and meridional monthly-means over Esrange at (a) ~ 93 km, (b) ~ 90 km and (c) ~ 93 km. Over Esrange the data extends from January 2000 to July 2008, again the end of each year is shown as a vertical black line.
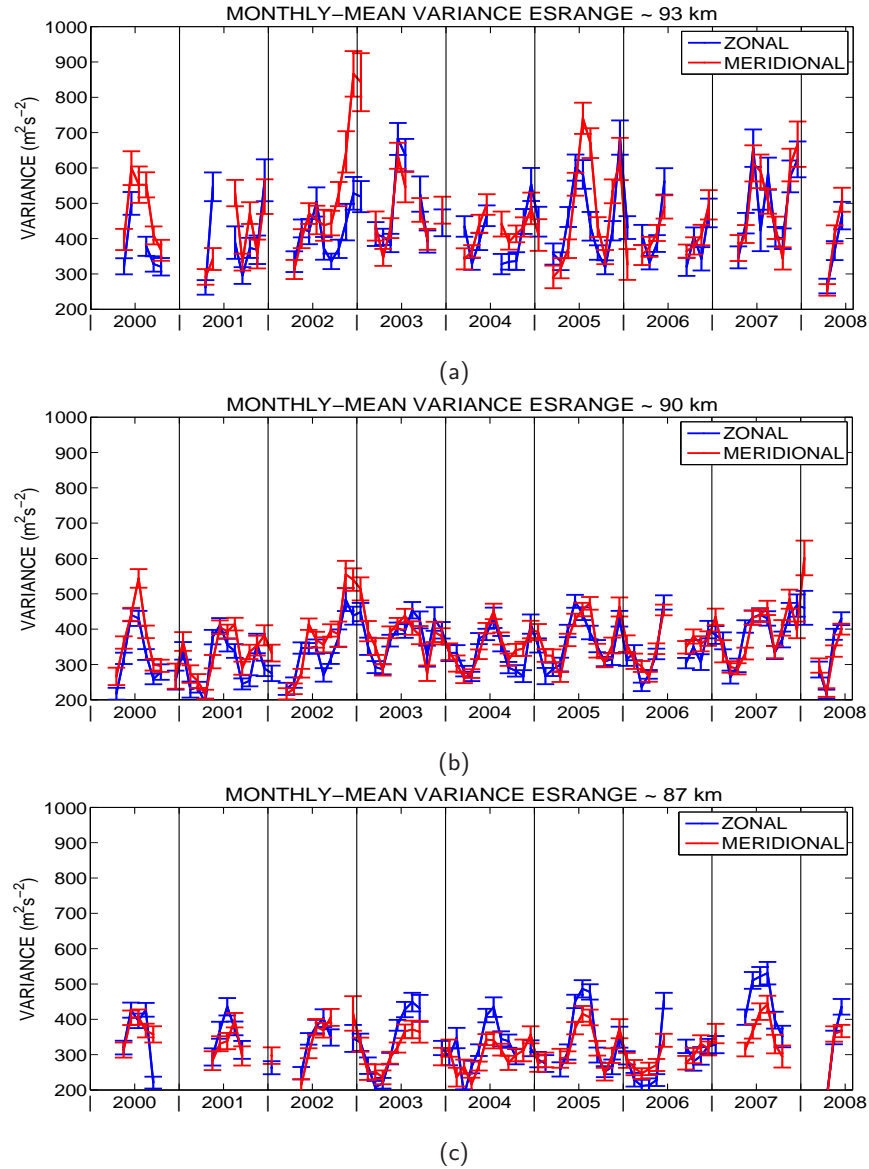
Figure 4.7: Zonal and Meridional monthly-mean gravity-wave variances over Esrange, (a) 93 km, (b) 90 km (c) 87 km for February 2005 to July 2008.

Once again there is a clear semi-annual seasonal cycle which persists in all years and in all three height gates with solstitial peaks and equinoctial minima. A growth of variance with height can also be seen in most months. The largest variances are found at ~ 93 km in the summer of 2005, where the meridional variance reaches ~ 700 m^{2}s^{-2}. Note that this is larger than the variances at this height over Rothera by ~ 50 m^{2}s^{-2}.

The difference between the zonal and meridional variances seen over Rothera is not evident over Esrange. There is a slight tendency for meridional variances to be larger than the zonal in the

upper part of the height range, but a tendency for the zonal variance to be larger in the lower part of the height range.

Inter-annual variability is also evident over Esrange. For example at $\sim$ 90 km both zonal and meridional variances are unusually high in the summer of 2000 and the winter of 2002 / 2003. It was noted in Chapter 3 that the gravity-wave activity over Esrange in 2002 had a different seasonal behaviour, with elevated values of variance in the winter and that this may have been related to the major stratospheric warming that occurred over Antarctica in September 2002.

4.4.3 Polar Inter-Hemispheric Differences in Gravity-Wave Activity

To investigate further the seasonal cycle and to compare results from Rothera and Esrange, climatologies of zonal and meridional gravity-wave variances were calculated. These were calculated as a mean of all variances within a given month, regardless of the year. A value was only calculated if at least 10 days worth of data were available. The length of the datasets over both stations allows the construction of reliable climatologies as they are based on data from 2005 to 2008 over Rothera and 2000 to 2008 over Esrange.

Figure 4.8 presents climatologies of zonal and meridional variance over Rothera and Esrange at $\sim$ 87 km. The error bars denote the standard error on the mean. The equivalent data for Rothera and Esrange at $\sim$ 90 km is presented in Figure 4.9 and for $\sim$ 93 km in Figure 4.10. Note that the data over Esrange has been shifted by six months to make the seasons comparable.

Considering Figure 4.8, several features are noticeable in the data for $\sim$ 87 km. The variances over Rothera and Esrange are on the same order of magnitude throughout the year. Over both stations and in both the zonal and meridional components there is a clear semi-annual cycle with peaks in both summer and winter. However, over Esrange, the summer maxima is larger than the winter maxima in the zonal component whereas over Rothera peaks are of similar magnitude. The difference between the stations in the summer is most evident in December and January when the zonal variances reach $\sim$ 475 m^2s^{-2} over Esrange, but only reach $\sim$ 400 m^2s^{-2} over Rothera (Figure 4.8a).

An interesting inter-hemispheric difference occurs in both zonal and meridional variances in the late summer and spring (August to November). The gravity-wave activity is consistently lower over Esrange during this time.

Considering Figure 4.9, several of the same features that were evident at $\sim$ 87 km are also seen at $\sim$ 90 km. The semi-annual cycle is present over both stations but the zonal variances in summer are still smaller than those over Esrange. The most interesting feature is that the lower activity over Esrange is also present at this height.
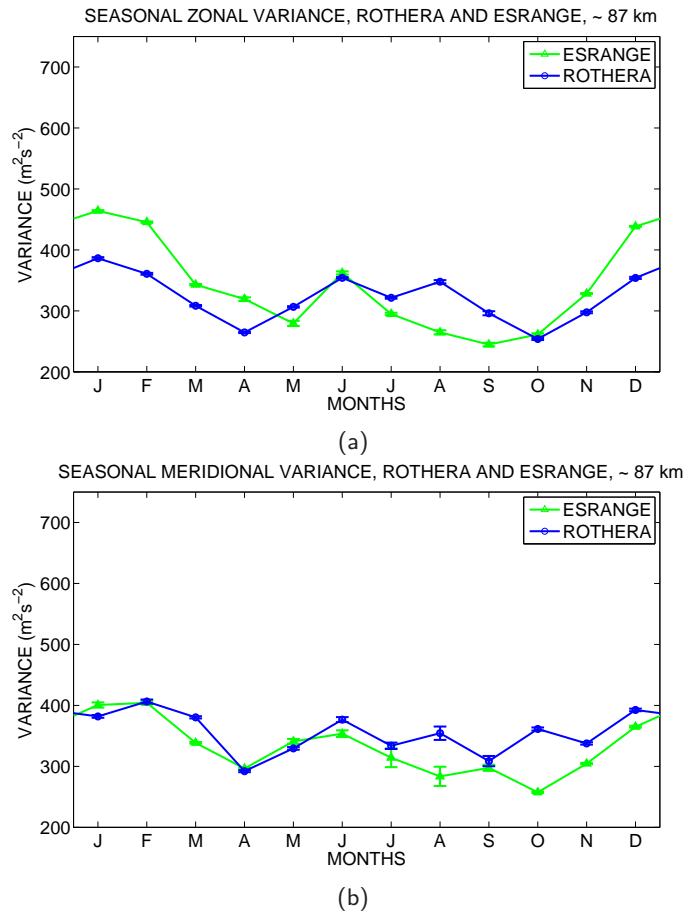
Figure 4.8: Climatology of (a) zonal and (b) meridional gravity-wave variance over Rothera (February 2005 - June 2008) and Esrange (October 1999 - June 2008) for $\sim$ 87 km. Data from Esrange has been displaced by 6 months to make the seasons comparable.

Considering Figure 4.10, while the seasonal cycle is still present at $\sim$ 93 km, the behaviour over Rothera is slightly different than that seen in the lower height gates. For the zonal component over Rothera the summer maximum is reduced compared to the winter maximum. Over Esrange the summer and winter peaks are of approximately equal magnitude. In the meridional component the peaks are again approximately equal. The difference in late winter / spring is still evident but only in the meridional component.

In summary, considering all the height gates:

1. There is a growth of variance with height, but this is not as rapid as would be expected for the exponential growth of uninhibited gravity waves.

2. A clear semi-annual cycle is present in all height gates. However, the cycle shows some variation with height as well as between the zonal and meridional components.

3. Variances over Esrange are generally higher than those over Rothera in summer in the zonal component.
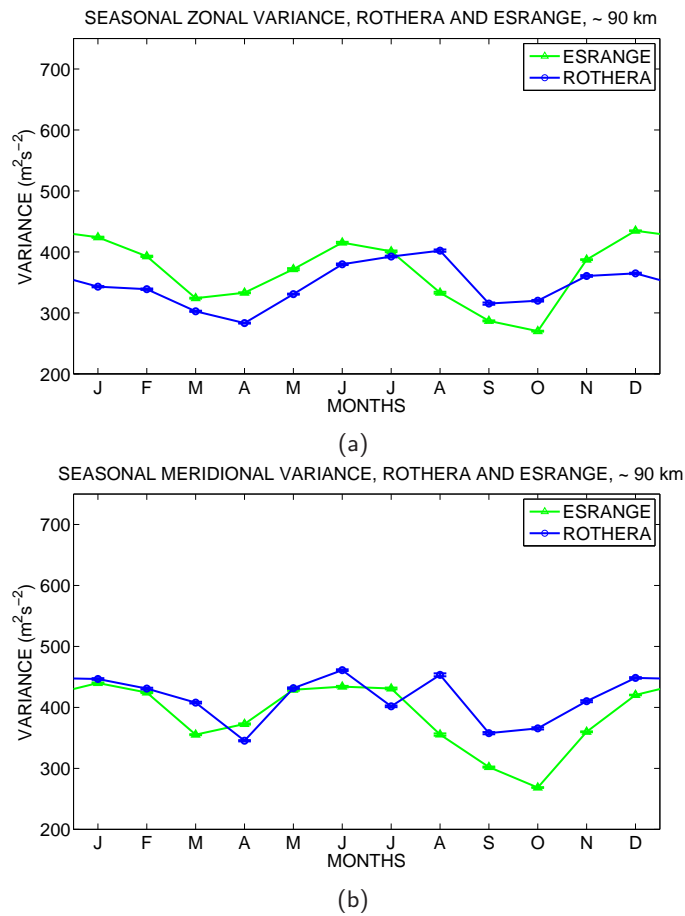
Figure 4.9: Climatology of (a) zonal and (b) meridional gravity-wave variance over Rothera (February 2005 - June 2008) and Esrange (October 1999 - June 2008) for $\sim$ 90 km. Data from Esrange has been displaced by 6 months to make the seasons comparable.

4. A strong inter-hemispheric difference is obvious in late winter and spring, where variances are higher over Rothera.

5. There are differences between the behaviour of the zonal and meridional components at both stations within a height gate. This implies a degree of polarisation within the gravity-wave field. This may be as the result of an anisotropy in the generation source, or imposed by anisotropic filtering in the underlying atmosphere.

4.5 Discussion

The daily averages of zonal and meridional variances (Figures 4.4, 4.5) show considerable short-term variability in the high-frequency gravity wave field over both Rothera and Esrange. This type of short-term variability can arise either from changes in the source characteristics or changes in the propagation conditions for the gravity-waves either *in situ* or in the underlying atmosphere. However, an underlying seasonal variability is also present. There are peaks in both the zonal

SEASONAL ZONAL VARIANCE, ROTHERA AND ESRANGE, ~ 93 km

(a)

SEASONAL MERIDIONAL VARIANCE, ROTHERA AND ESRANGE, ~ 93 km

(b)
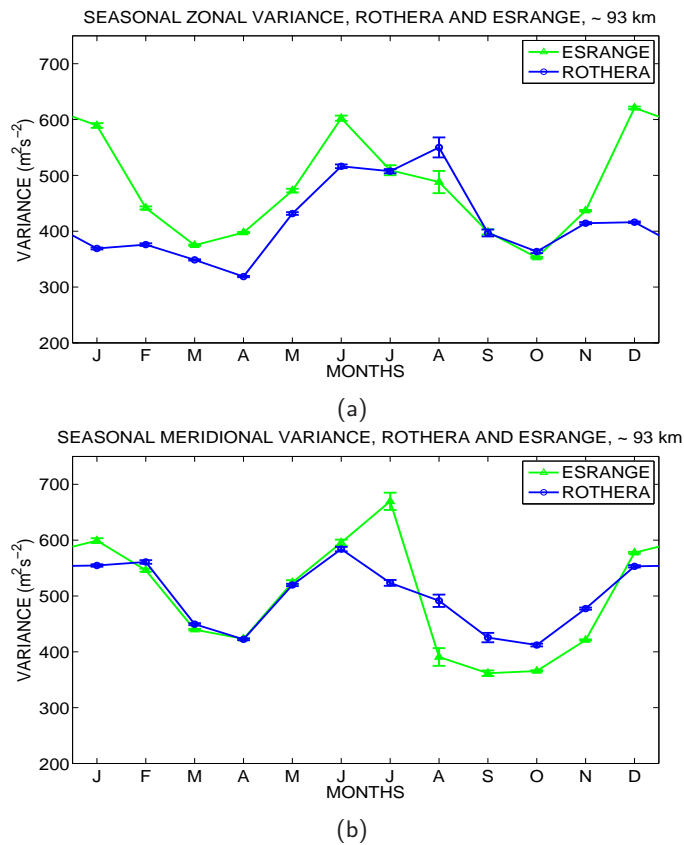
Figure 4.10: Climatology of (a) zonal and (b) meridional gravity-wave variance over Rothera (February 2005 - June 2008) and Esrange (October 1999 - June 2008) for ~ 93 km. Data from Esrange has been displaced by 6 months to make the seasons comparable.

and meridional variances in summer and winter with minima at the equinoxes. This behaviour is consistent both with the results presented in Chapter 3 and with previous observations of high-frequency gravity-wave activity (e.g., *Manson et al.*, 2004; *Manson and Meek*, 1993; *Mitchell and Howells*, 1998; *Vincent and Fritts*, 1987; *Taylor et al.*, 1993).

The magnitude of the monthly-mean amplitudes of both the zonal and meridional variances are similar to those measured by Medium Frequency (MF) radar in Adelaide. *Vincent and Fritts* (1987) present daily values of the zonal and meridional variances from gravity waves with periods between 1 and 24 hours (note this is different to the ~ 5 minutes to ~ 2 hours observed using the matrix technique). A least-squares fit to a mean, an annual and a semi-annual cycle indicated winter values of variance to be between ~ 350 and 450 m^2s^{-2} at ~ 86 km. This agrees very well with the monthly-mean averages over both Rothera and Esrange at ~ 87 km. Observations of high-frequency gravity-waves in the northern hemisphere also agree well with the magnitude of the zonal and meridional variances presented for Rothera and Esrange, (e.g., *Manson et al.*, 1997; *Dowdy et al.*, 2007).

A marked difference between the zonal and meridional components of gravity-wave activity was seen over Rothera. Meridional variances are consistently higher than the zonal, particularly in summer and at ~ 93 km. Such a difference has been seen in previous observations in the

southern hemisphere (e.g., *Vincent and Fritts*, 1987; *Vincent*, 1994). It has been suggested that this represents anisotropy in the gravity-wave field. The higher variance in one direction represents a polarisation of the gravity-wave field, with the fluctuations in one direction being larger than those in the other. For high-frequency gravity waves the dominant direction of propagation was generally found to be meridional at high and middle latitudes (e.g., *Ebel et al.*, 1987; *Vincent and Fritts*, 1987; *Vincent*, 1994; *Manson et al.*, 1997; *Thorsen and Franke*, 1998).

Chapter 3 suggested that critical-level filtering in the lower and middle atmosphere has a profound effect on the gravity-wave field in the MLT. Therefore we will consider this filtering as a possible cause of the observed anisotropy of the gravity-wave field. The larger positive and negative values of zonal winds will filter out more zonally propagating waves than meridionally propagating waves. The zonal winds below ∼ 80 km have larger values than the meridional in most months. There are strong eastward winds in winter and strong westward winds in summer. Winds with extreme values will remove a large proportion of either the eastward or westward propagating waves depending on season and thus create an anisotropy within the wave field. The meridional winds do not reach the same large positive or negative values and so do not impose a strong anisotropy on the gravity-wave field. This may result an anisotropy in the gravity-wave field and thus a higher meridional gravity-wave variance compared to zonal.

In contrast to the behaviour over Rothera, over Esrange the two components are approximately equal at ∼ 90 and ∼ 93 km, whilst at ∼ 87 km the zonal component is larger than the meridional. The UARS Reference Atmosphere Project (URAP) data presented in 3.17, Chapter 3 indicate that there are significant inter-hemispheric differences in the stratospheric winds. The larger values of zonal winds over Rothera from May to November may explain why a greater level of anisotropy is seen over Rothera. It has also been suggested that the anisotropy of the gravity-wave field is due to a combination of seasonally varying source characteristics *and* critical-level filtering (*Ebel et al.*, 1987) and thus differences in the source characteristics between Rothera and Esrange may also explain some of the differences.

The climatological data presented in Figures 4.8, 4.9 and 4.10, indicated two main inter-hemispheric differences. The first is that the zonal variance is higher over Esrange during the summer months, particularly at ∼ 93 km. This is consistent with the differences observed using the variance technique described in Chapter 3 where above ∼ 86 km the variances are higher over Esrange. What is interesting is that the matrix technique reveals that this difference is mainly due to the difference in the zonal variance rather than the meridional.

The second is that during spring the zonal and meridional variances are larger over Rothera than Esrange. This behaviour was also observed using the variance technique in Chapter 3 and was explained as the result of the different filtering imposed by the northern and southern polar stratospheric vortices.

4.6 Results - Zonal Momentum Fluxes

This Section presents the zonal momentum fluxes determined using the matrix technique over Rothera and Esrange. Section 4.6.1 presents the short-term behaviour, Section 4.6.2 considers the inter-annual variability and Section 4.6.3 presents the climatological behaviour and inter-hemispheric differences in zonal momentum flux between Rothera and Esrange.The 3-hourly dataset was found to be too noisy to give a reliable estimate of short-term variability. Therefore, only the daily-mean momentum fluxes will be considered.

4.6.1 Short-Term Variability
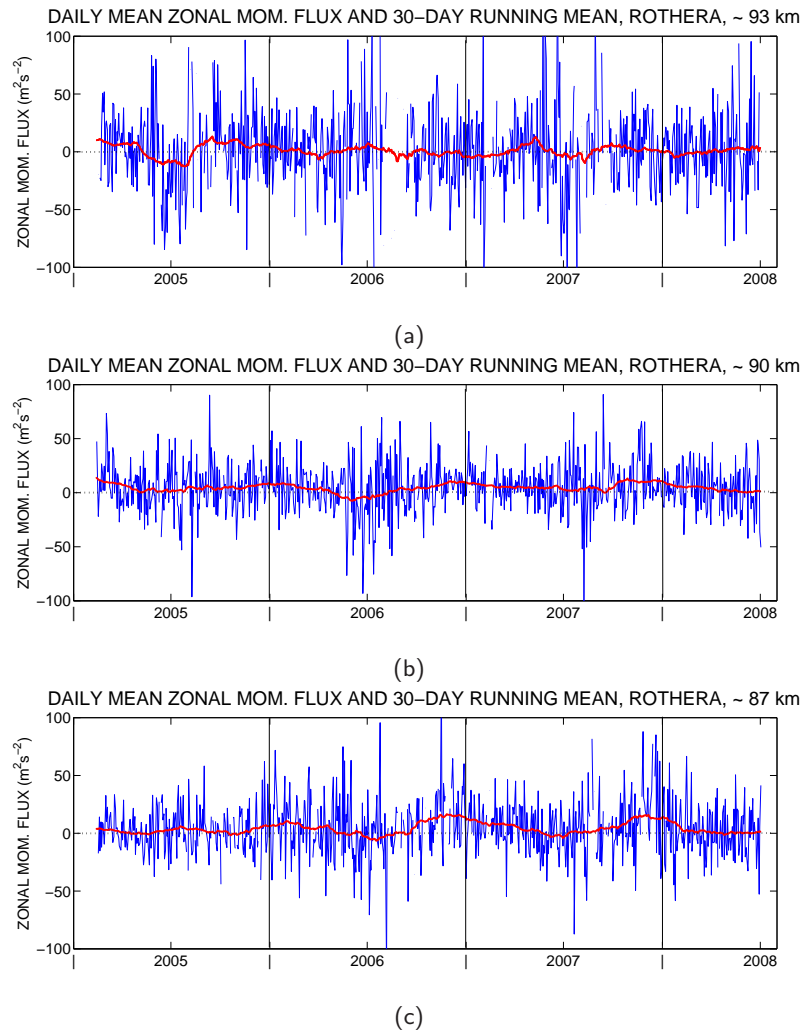
Figure 4.11: Daily values of zonal momentum flux over Rothera at (a) $\sim$ 93 km, (b) $\sim$ 90 km and (c) $\sim$ 87 km for February 2005 to July 2008.

Figure 4.11 presents the daily averaged values of the zonal momentum flux ($u'w'$), from February 2005 to July 2008 over Rothera. Considering the figure, a very high level of short-term variability is obvious. Daily averages of momentum flux can reach $\pm$ 100 m^{2}s^{-2}. However, the 30-day

smoothing reveals that there is also a seasonal cycle present. Although the smoothed line indicates that the zonal momentum fluxes remain small in a 30-day average, there is a tendency for the zonal momentum flux to be negative in the winters (June - August) and positive in summer (December - February). This can be seen most clearly at $\sim$ 87 km in 2006 and 2007, 90 km in 2006 and at $\sim$ 93 km in 2005 and 2007.

Figure 4.12 presents the daily-average zonal momentum fluxes over Esrange at (a) $\sim$ 93, (b) $\sim$ 90 and (c) 87 km. Considering Figure 4.12, the zonal momentum flux shows considerable short-term variability with values reaching $\sim$ +150 and $\sim$ −150 m^2s^{-2} in the upper height gate. However, the 30-day smoothing reveals that on these time scales the momentum flux usually remains below $\pm$ 40 m^2s^{-2}. The seasonal cycle seen over Rothera is also evident over Esrange. For most years the momentum flux in winter is smaller than in summer. At $\sim$ 90 km it is actually negative in 5 of the 8 winters of available data. There are also two unusual events in the data at $\sim$ 90 km. The first is a positive peak in the zonal momentum flux in the early winter of 2002/2003, the second is another positive peak in the winter of 2007/2008. These are discussed in Section 4.8.

(a)

(b)

(c)
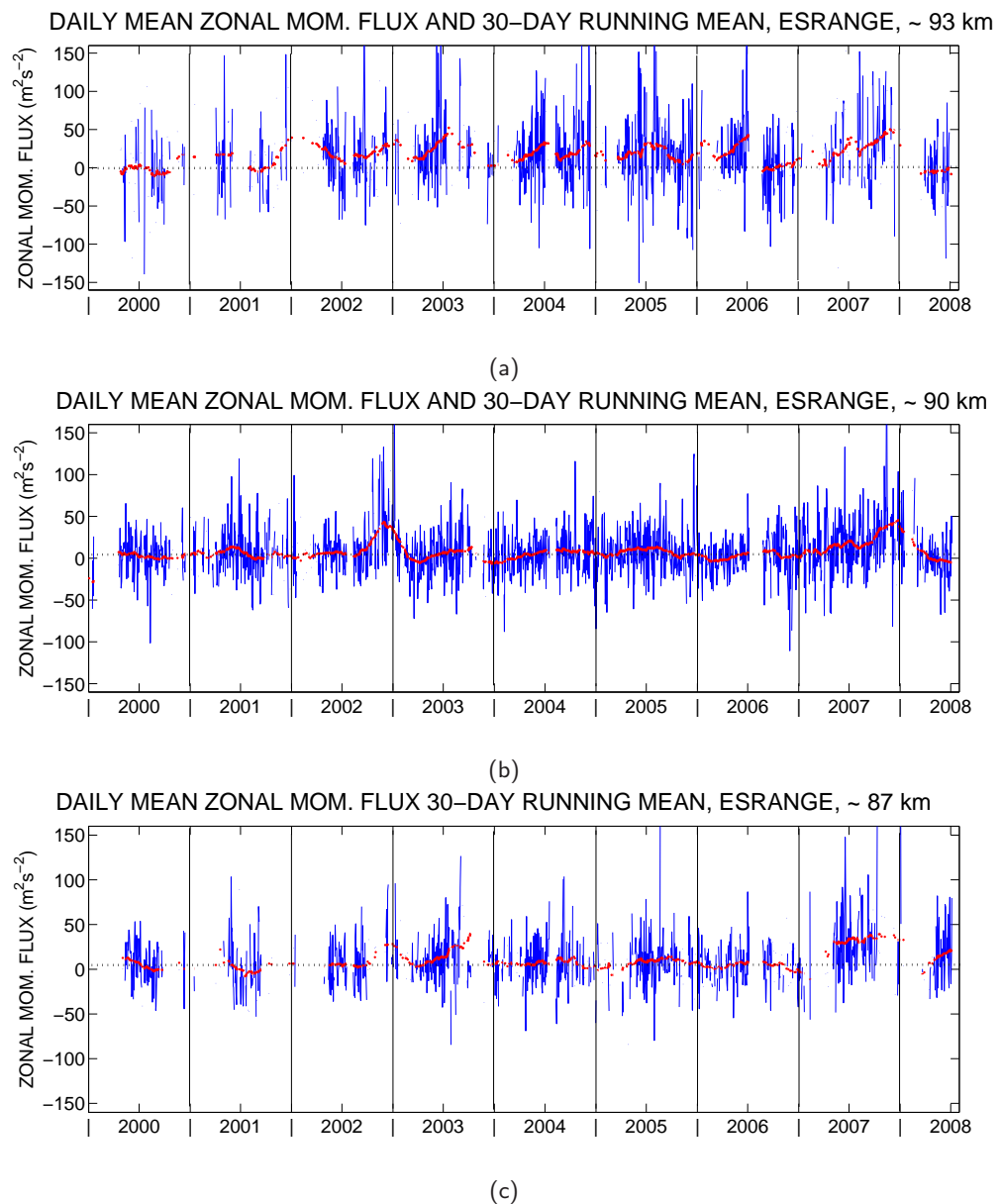
Figure 4.12: Daily values of zonal momentum flux over Esrange at (a) ~ 93 km, (b) ~ 90 km and (c) ~ 87 km for January 2000 to July 2008.

4.6.2 Inter-Annual Variability of Zonal Momentum Flux

To further characterise the seasonal variability and to investigate the inter-annual variability of the zonal momentum flux, monthly-mean momentum fluxes were calculated as the median of all the days of data available within each month. Figure 4.13 presents the monthly-mean zonal momentum fluxes at ~ 87, ~ 90 and ~ 93 km over Rothera. The vertical black line marks the beginning and end of each year and the error bars represent the error on the mean.

Considering Figure 4.13, the monthly-mean zonal momentum fluxes show a clear seasonal cycle at ~ 87 and ~ 90 km. However, this is less clear at ~ 93 km. The zonal momentum fluxes
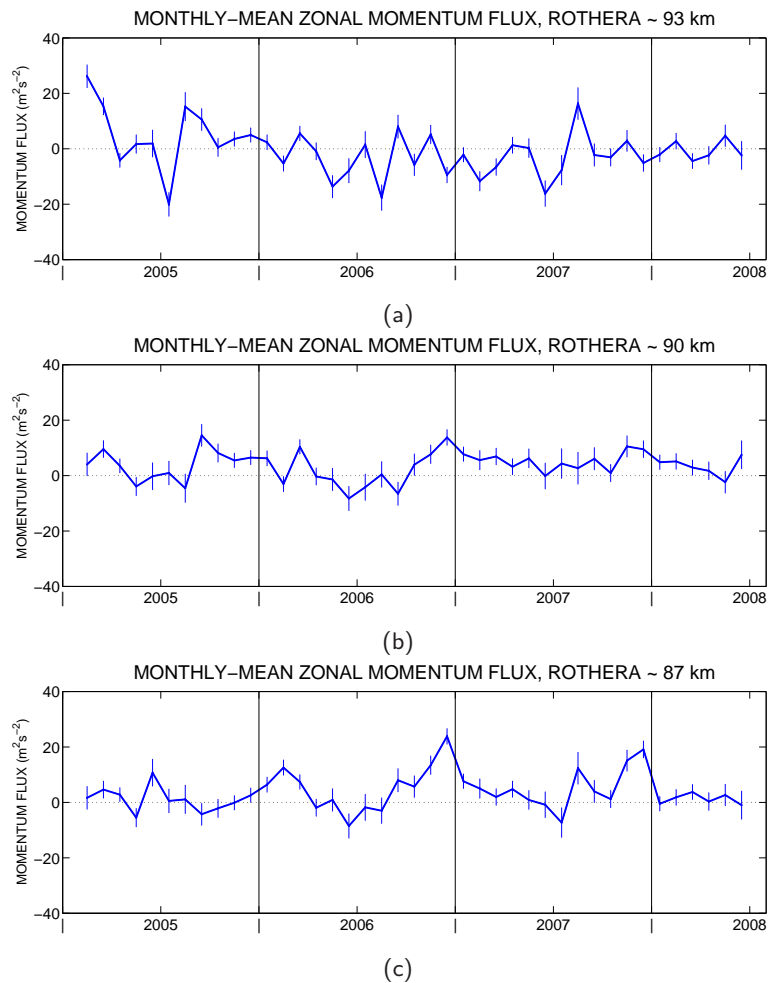
Figure 4.13: Monthly-mean zonal momentum fluxes at (a) $\sim$ 93 km, (b) $\sim$ 90 km and (c) $\sim$ 87 km over Rothera (February 2005 - July 2008).

tend to be negative in winter, reaching $\sim$ -10 m^{2}s^{-2}, and positive in summer, reaching $\sim$ 20 m^{2}s^{-2}. It is interesting to note that although the winter values are similar at all height gates, the monthly-means in summer *decrease* with height by $\sim$ 5 m^{2}s^{-2} over the observed height range. This decrease in zonal momentum fluxes with height indicates that momentum is being deposited in this region by breaking gravity-waves.

Substantial inter-annual variability is evident in all height gates. For example, at $\sim$ 87 km the peak in the summer of 2005 occurs later than the peak in the summer of 2006. In the upper height gate monthly-mean values differ by up to $\sim$ 20 m^{2}s^{-2}. Consider, for example, successive Februarys at $\sim$ 93 km.

Figure 4.14 presents the monthly-mean zonal momentum fluxes over Esrange. The number of gaps in the monthly-mean averages at the top and bottom height gates make a seasonal cycle at $\sim$ 87 or $\sim$ 93 km difficult to determine. Error bars are calculated as the standard error on the mean of the 6-hourly values and are presented only to provide an idea of the variability in the data.
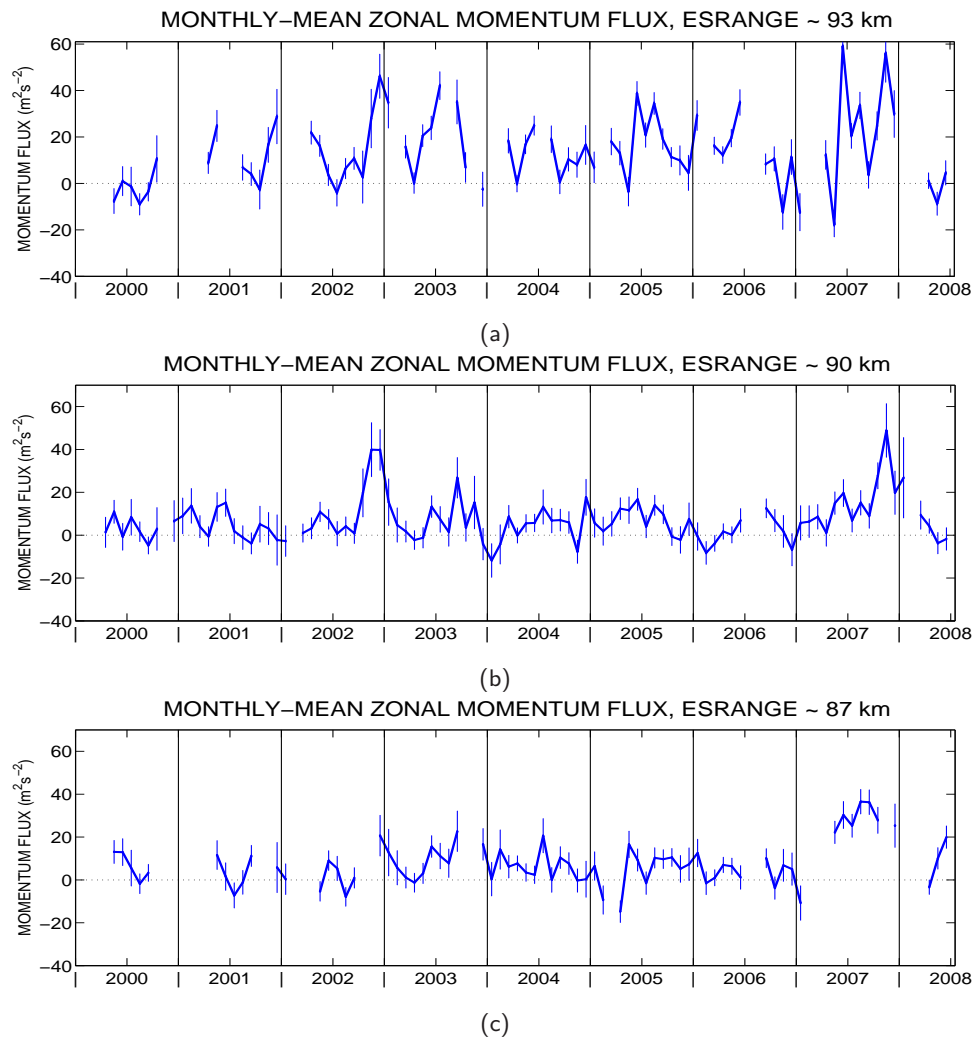
Figure 4.14: Monthly-mean zonal momentum fluxes at (a) $\sim$ 93 km, (b) $\sim$ 90 km and (c) $\sim$ 87 km over Esrange (January 2000 - July 2008).

A higher level of variability is evident over Esrange, particularly in the upper height gate where values are higher in general reaching $+60$ m^{2}s^{-2}, compared to $+30$ m^{2}s^{-2} over Rothera. At $\sim$ 90 km a seasonal cycle is apparent in most years (note that there is missing data in 2000). There is a tendency for the zonal momentum flux to be negative in winter and positive in summer, similar to the behaviour seen over Rothera.

The high levels of inter-annual variability seen over Rothera can also be seen over Esrange. For example, at $\sim$ 90 km in the late summer of 2002 and 2007 the zonal momentum fluxes are larger by $\sim$ 20 m^{2}s^{-2} than in other years. These two years are distinctly different in behaviour from all the other years observed. These positive zonal momentum fluxes indicate a bias towards eastward propagating waves during these months, compared to the negative zonal momentum flux in most other years.

4.6.3 Polar Inter-Hemispheric Differences in Zonal Momentum Fluxes

This Section presents representative years of zonal momentum flux for all height gates over Rothera and Esrange. These are constructed by taking the mean of all available days of data within a month, regardless of year. The error bars plotted represent the error on the mean. For most months this error is small, however, for months where fewer days of data were available, the error bars are larger. Note that the data over Esrange has been shifted by six months to make the seasons comparable.

Figure 4.15 presents climatologies of zonal momentum flux over Rothera and Esrange at (a) $\sim$ 93, (b) $\sim$ 90 and (c) $\sim$ 87 km. Considering the figure, the weak seasonal cycle over Rothera and Esrange is obvious, particularly in the middle and lower height gates. Over Rothera the zonal momentum flux are near zero in most months, reaching a maximum of nearly $\sim$ 20 m^2s^{-2} in December at $\sim$ 87 km. The zonal momentum flux are negative in winter at all heights, reaching the lowest values at $\sim$ 93 km. The summer values of momentum flux decrease with height, particularly in December, and drop below zero (-4 m^2s^{-2} in December) at $\sim$ 93 km. This behaviour results in reduced zonal momentum flux at $\sim$ 93 in the summer. This, in turn, creates an approximately semi-annual pattern with peaks occurring in March (autumn) and November (spring), and minima in summer and winter.

Over Esrange, the seasonal cycle is not as obvious, however, there is a tendency for lower values to occur in winter / spring in all height gates. Unlike the behaviour over Rothera, the momentum flux in winter becomes *more positive* with height from $\sim$ 10 m^2s^{-2} at $\sim$ 87 km to $\sim$ 25 m^2s^{-2} at $\sim$ 93 km. In summer the momentum fluxes also become more positive with increasing height, varying from approximately 10 m^2s^{-2} at $\sim$ 87 and $\sim$ 90 km to approximately 25 m^2s^{-2} at $\sim$ 93 km.

There are several similarities obvious from Figure 4.15. These are:

1. The seasonal behaviour shows a similar structure over both stations.

2. A semi-annual behaviour is present in the upper height gate which is not apparent in either of the lower height gates.

There are also a number of differences apparent:

1. At $\sim$ 93 km there is a semi-annual behaviour over both stations. However, the equinoxes mark the minima over Esrange and maxima over Rothera.

2. The summer momentum flux decreases with increasing height over Rothera, whereas over Esrange the summer values show little change between $\sim$ 87 and $\sim$ 90 km and increase
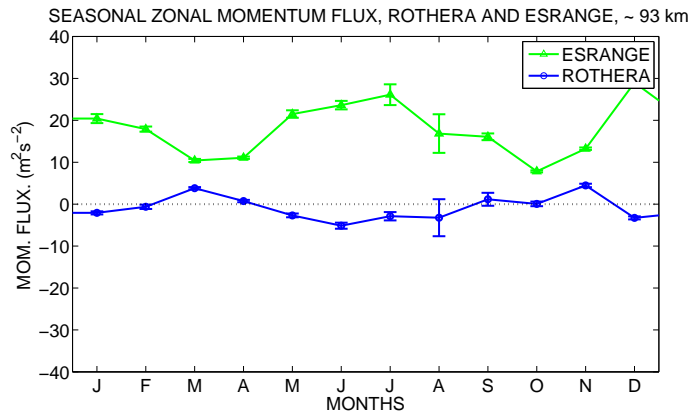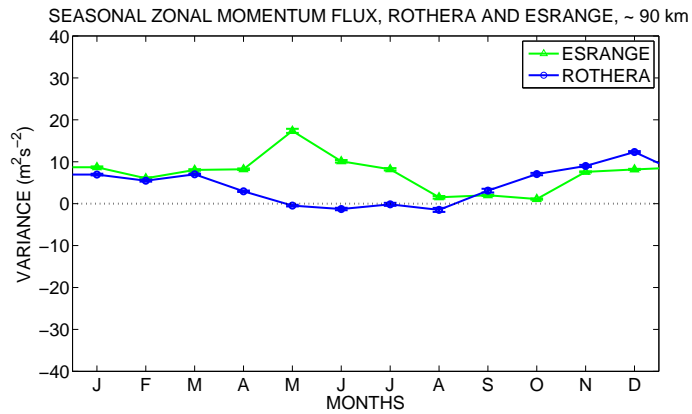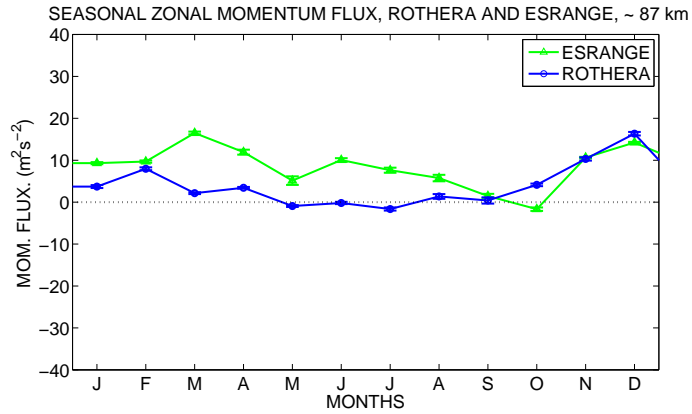
Figure 4.15: Climatology of zonal gravity-wave momentum flux over Rothera and Esrange at (a) $\sim$ 93 km, (b) $\sim$ 90 km and (c) $\sim$ 87 km.

between $\sim$ 90 and $\sim$ 93 km.

3. The data over Esrange has more extreme values of momentum flux particularly in the upper height gate where the momentum flux reaches a maximum of 30 m^2s^{-2} in December.

The differences in the behaviour with height in summer between these two stations may indicate differences in the amount of momentum deposition for the two polar regions. However, it should

be noted that the lower count rates over Esrange may mean that the climatology over Esrange is less reliable.

4.6.4 Zonal Momentum Flux Behaviour with Height

The high data quality over Rothera allows some investigation of the vertical structure of the zonal momentum fluxes. Figure 4.16 presents height profiles of zonal momentum flux over Rothera. The representative months were calculated using all available data over Rothera (February 2005 to June 2008). Note that there are only data from three height gates because of the low meteor count rates in the other height gates.
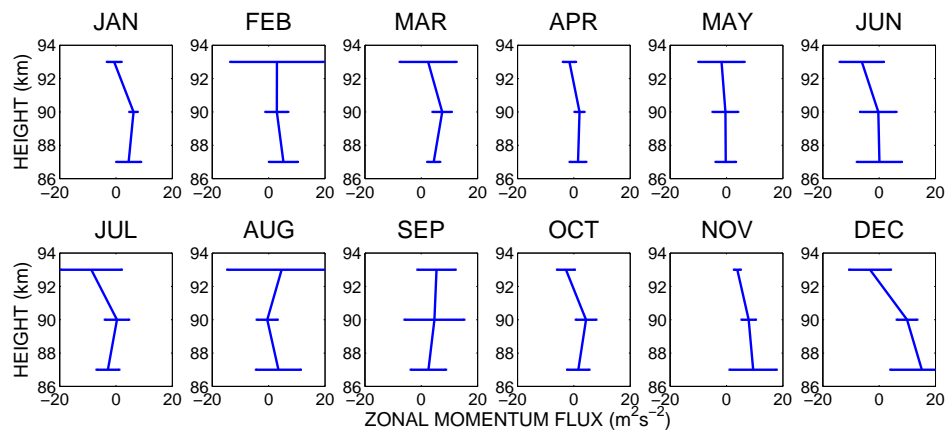
Figure 4.16: Height profiles of the climatological zonal momentum fluxes over Rothera. Data is included from February 2005 to June 2008.

Considering Figure 4.16, there is a relatively small change in momentum flux with height across the observed height range. There is an overall decrease in zonal momentum flux in all months except August and September (winter). All other months show either no significant change of momentum flux with height e.g., February, March and April, or a decrease of zonal momentum flux with height e.g., November, December and January (summer). The significance of these profiles will be discussed in Section 4.8. However, it should be noted that because of the high variability shown in the error bars and the fact that there are only three height gates of available data the conclusions drawn from this data should be regarded with caution.

4.7   Results - Meridional Momentum Fluxes

This section presents the meridional momentum fluxes over Rothera and Esrange. Section 4.7.1 presents the short-term behaviour and Section 4.7.2 presents the inter-annual variability. Section 4.7.3 presents the climatological behaviour and inter-hemispheric differences between Rothera

and Esrange. As before the three-hourly dataset was found to be very noisy and so only the daily-mean momentum fluxes will be considered.

4.7.1 Short-Term Behaviour

Figure 4.17 presents the daily-average meridional momentum flux over Rothera at $\sim$ 87, 90 and 93 km with a 30-day smoothing filter applied to these data.

(a)

(b)

(c)
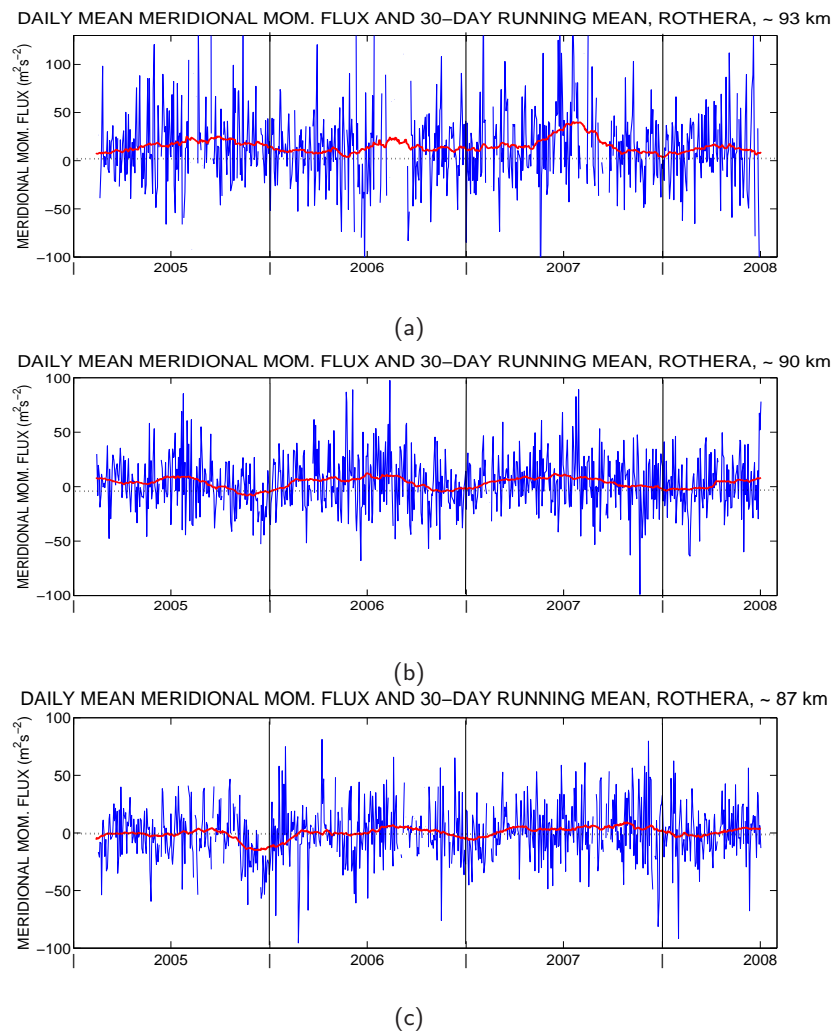
Figure 4.17: Daily values of meridional momentum flux over Rothera at (a) $\sim$ 93 km, (b) $\sim$ 90 km and (c) $\sim$ 87 km for February 2005 to July 2008.

Considering the figure, a high level of short-term variability exists within the daily averages. Daily values can reach up to $\pm$ 150 m^{2}s^{-2}, although most of the are smaller. The 30-day smoothing, shown by the red line, reveals that there is also a seasonal cycle in the meridional momentum flux. There is a tendency to be near zero during the winter and have small negative values in summer. This is true for all the observed height gates.

Figure 4.18 presents the daily averages for ∼ 87, 90 and 93 km over Esrange from 2000 to 2008. Black vertical lines indicate the start and end on each year and the 30-day smoothing applied to the data is shown as a red line. Considering Figure 4.18, the meridional momentum fluxes over Esrange also show high levels of short-term variability. The seasonal cycle that is evident over Rothera is not as clear over Esrange. However, it is interesting to note two bursts of negative meridional momentum flux in the winters of 2002/2003 and 2007/2008. These coincide with the two positive peaks in *zonal* momentum flux seen in Figure 4.12. This indicates that at these times the high-frequency gravity-wave field is dominated waves propagating in eastward and southward directions. Whereas in other years at this time, the dominant propagation direction is north-west.

(a)

(b)

(c)
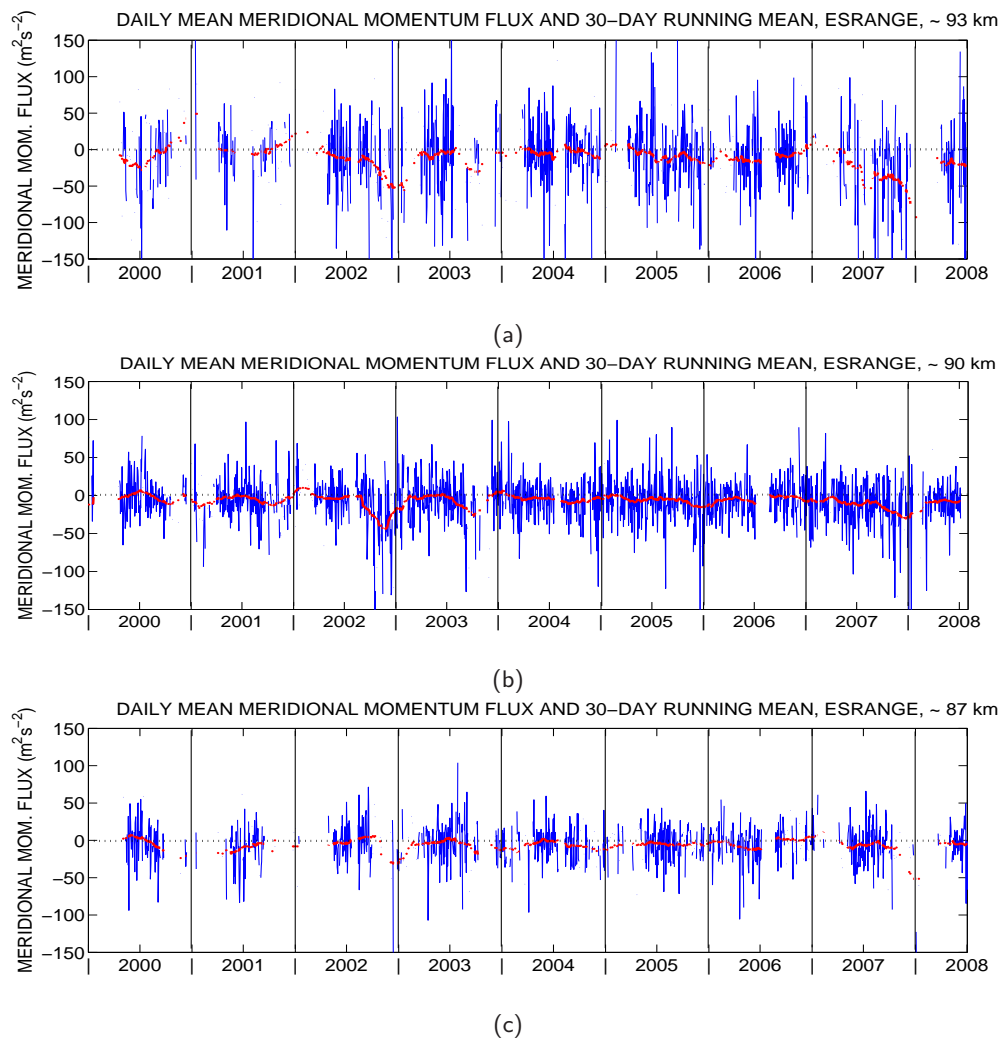
Figure 4.18: Daily values of meridional momentum flux over Esrange at (a) ∼ 93 km, (b) ∼ 90 km and (c) ∼ 87 km for January 2000 to July 2008.

4.7.2 Inter-Annual Variability of Meridional Momentum Flux

Figure 4.19 presents the monthly-mean averages of meridional momentum fluxes over Rothera from February 2005 to July 2008. A seasonal cycle is present in the lower two height gates with small positive meridional momentum fluxes during the winter and small negative momentum fluxes in the summer. For example at ~ 87 km, in 2005/2006 momentum fluxes are negative in October to February and positive in March to September.

(a)

(b)

(c)
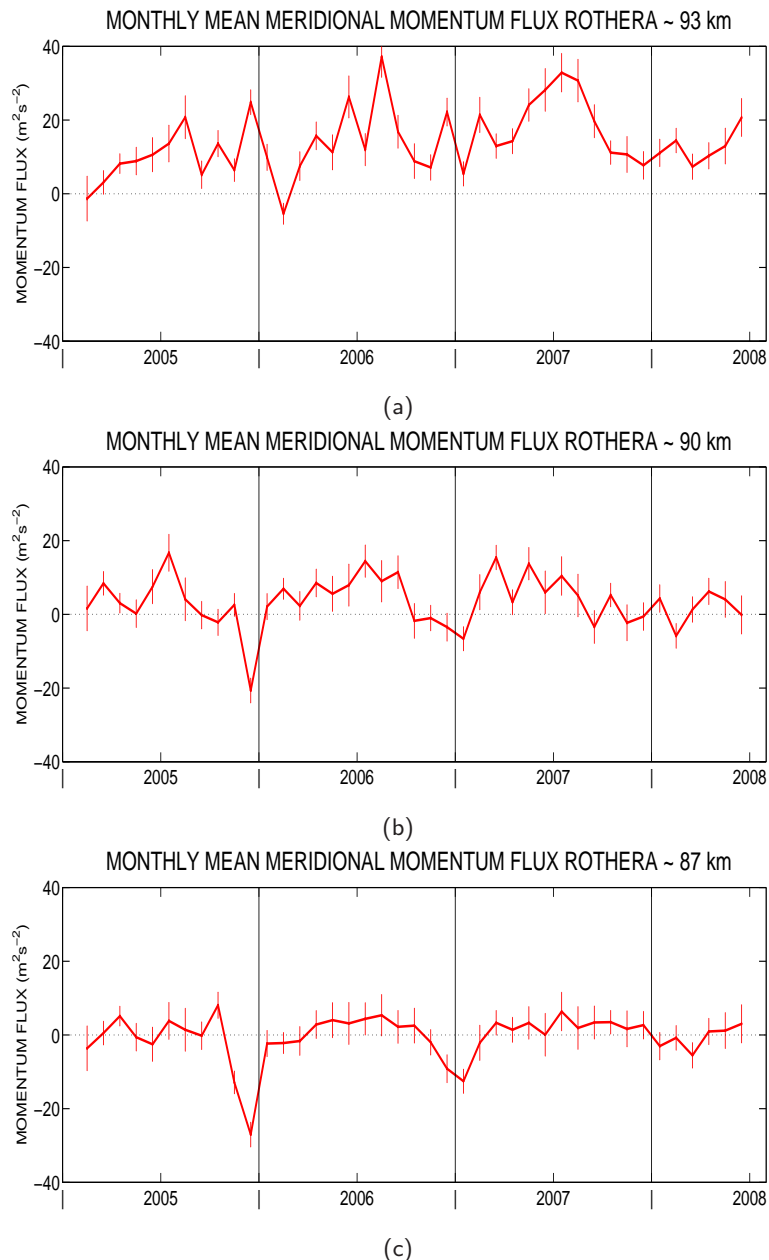
Figure 4.19: Monthly-mean meridional momentum fluxes at (a) ~ 93 km, (b) ~ 90 km and (c) ~ 87 km over Rothera (February 2005 - July 2008).

Considering all three height gates, the meridional momentum flux increases with height in most months and most years so that at ~ 93 km the monthly means are generally no longer negative

in summer. In fact, at $\sim$ 93 km the only negative momentum fluxes are in February 2005 and January 2006.

Substantial inter-annual variability is also evident in the meridional momentum fluxes over Rothera. For example, the summer of 2005 / 2006 shows a much more negative momentum flux than other years. This persists throughout all three height gates. Once again the variability is largest in the upper height even though the error bars are no larger in this height gate than at $\sim$ 87 or $\sim$ 90 km.

Figure 4.20 presents the meridional momentum fluxes at (a) $\sim$ 93 km, (b) $\sim$ 90 km and (c) $\sim$ 87 km over Esrange from January 2000 to July 2008. Once again the vertical black lines indicate the beginning and end of each year.

(a)

(b)

(c)
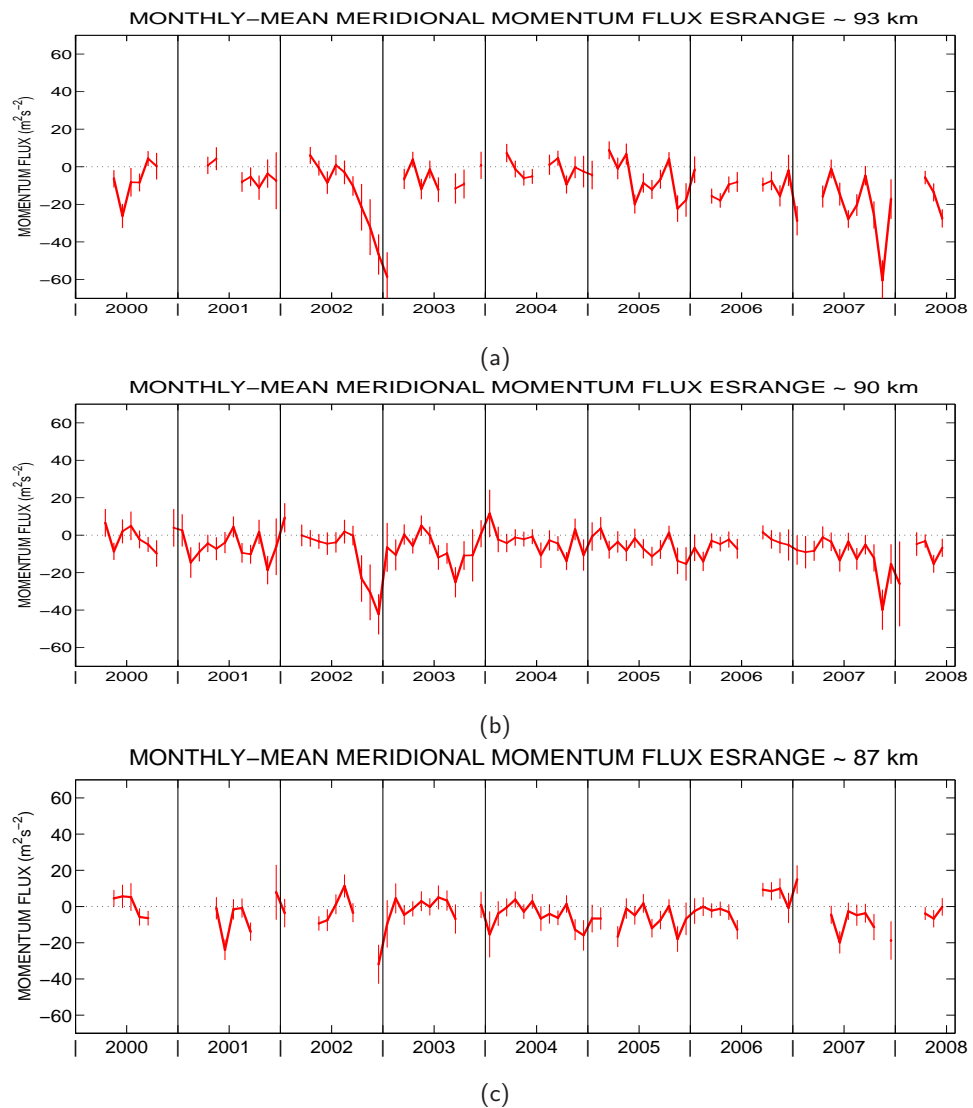
Figure 4.20: Monthly-mean meridional momentum fluxes at (a) $\sim$ 93 km, (b) $\sim$ 90 km and (c) $\sim$ 87 km over Esrange (January 2000 - July 2008).

A seasonal cycle is difficult to see in the meridional component as the intra- and inter-annual

variability is very high. Momentum flux values remain around 0 to -20 m^2s^{-2} for most months in all height gates. However, there are negative values of meridional momentum flux evident in most winters at ~ 87 and ~ 90 km and values closer to zero in the summer months.

There were anomalously low momentum fluxes recorded in the autumn/winters of 2002 and 2007. In 2002 the negative peak in meridional momentum flux is very prominent at ~ 93 km, where there is a steady decrease in the monthly-mean values from June 2002 to January 2003. These peaks in negative (southward) meridional momentum flux correspond to the two positive (eastward) peaks seen in the zonal momentum flux over the same site.

4.7.3 Polar Inter-Hemispheric Differences in the Meridional Momentum Flux

Figure 4.21 presents climatologies constructed from all available data over Rothera and Esrange at (a) ~ 93 km , (b) ~ 90 km and (c) ~ 87 km. The data over Esrange has again been shifted by six months to make the seasons comparable and the scale is consistent throughout the height gates to aid comparison. It should be noted that because of the vector nature of momentum flux, a positive value over Rothera corresponds to a northward or *equatorward* direction. However, over Esrange, a positive momentum flux also corresponds to a northward direction, but this is *poleward* over Esrange. Therefore, if the behaviour is the same in the two hemispheres then the meridional momentum flux over Rothera and Esrange should be anti-correlated, that is a poleward direction is *negative* over Rothera and *positive* over Esrange.

Firstly, considering the seasonal behaviour of meridional momentum fluxes over Rothera. The seasonal cycle of more positive values in winter (June - August) and more negative values in summer (December - February) is present in the lower two height gates. At ~ 93 km the cycle is similar but a general increase in momentum flux with height has displaced the curve upwards so the values are positive throughout the year.

The seasonal behaviour of meridional momentum flux over Esrange is less clear. At ~ 87 and ~ 90 km there is a tendency for the momentum fluxes to be more negative in winter (June - August) and closer to zero in summer (December - February). At ~ 93 km the momentum flux are negative in all months except August. However, this month has a large error bar which extends into negative values indicating fewer points were used in the calculation of this value.

There are several similarities apparent between the meridional momentum fluxes over Rothera and Esrange. These include:

1. The values are similar over both stations reaching maximum values of ± 30 m^2s^{-2}.

2. At ~ 87 and ~ 90 km there is a tendency for values to be equatorward in winter and
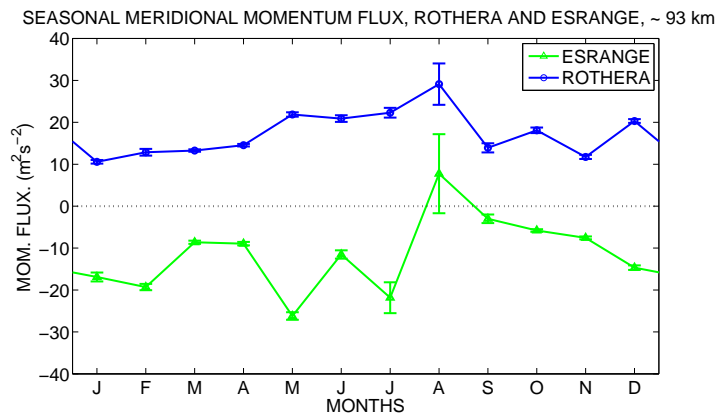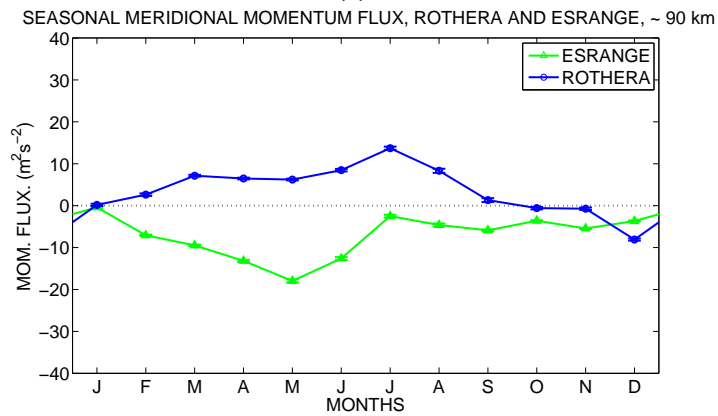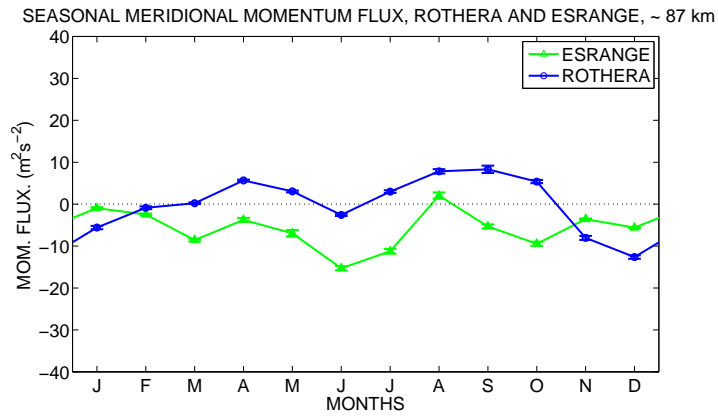
Figure 4.21: Climatology of meridional gravity-wave momentum flux over Rothera and Esrange at (a) $\sim$ 87 km, (b) $\sim$ 90 km and (c) $\sim$ 93 km.

more poleward in summer. This is shown by the more positive momentum flux in winter over Rothera and more negative flux over Esrange.

3. At $\sim$ 93 km the momentum fluxes are more equatorward than at other heights throughout the year over both Rothera and Esrange.

4. The seasonal cycle is less clear at $\sim$ 93 km than at the lower height gates. This occurs

over both stations and not at ~ 87 km, suggesting that this is not an effect of lower data quality in this height gate.

There are also two obvious differences apparent from Figure 4.21. These are:

1. That the maximum equatorward flow over Rothera occurs around late summer in all three height gates (August/September at ~ 87 km, July at ~ 90 km and August at ~ 93 km). Whereas over Esrange, the peak equatorward flow occurs slightly earlier in the year (June at ~ 87 km, March at ~ 90 and ~ 93 km - note that the months are correct for the axis shown).

2. The summer momentum flux is slightly negative (poleward) over Rothera in the lower two height gates. However, over Esrange the momentum fluxes are close to zero. This probably indicates that there are equal numbers of northward and southward propagating waves in summer.

4.8 Discussion

The daily averages of zonal and meridional momentum flux presented in Figures 4.11, 4.12, 4.17 and 4.18 show very high levels of short-term variability in both the zonal and meridional momentum fluxes. The range of daily values observed over Rothera and Esrange is quite large, reaching ± 150 m^{2}s^{-2}. This level of variability is similar to, if smaller than, than the results presented by *Hocking* (2005) over Socorro (34° N, 107° W) where three hourly zonal momentum fluxes reached over ± 200 m^{2}s^{-2}.

It is interesting to note that, in contrast daily momentum fluxes measured over Trivandrum (8.5° N, 76.9° E) using this technique by *Antontia et al.* (2008) reached only ± 40 m^{2}s^{-2}, somewhat smaller than the values presented here. These studies suggest that there are large latitudinal differences in momentum fluxes , as might be expected given the geographical variations in gravity-wave sources and differences in propagation conditions (e.g., *Fröhlich et al.*, 2007).

Momentum fluxes measured using other techniques at polar latitudes also show high levels of variability. For example, hourly-average values as large as 160 m^{2}s^{-2} were observed over Adelaide using MF radar (*Murphy and Vincent*, 1998) (although most of the values were below 50 m^{2}s^{-2}). Three-day averages were presented by *Fritts and Vincent* (1987) which showed values of 30 m^{2}s^{-2}. Measurements made using a combination of airglow and MF radar results over Rothera found daily averages of zonal momentum flux reaching nearly -150 m^{2}s^{-2} in winter (*Espy et al.*, 2006). However, the daily values presented by *Espy et al.* (2006) are nearly always negative, whereas the results presented here, over Rothera and Esrange show both positive and

negative daily averages in all seasons. It is only in longer term averages (monthly-mean) that the seasonal behaviour is revealed.

The large range of daily-average momentum fluxes measured using the matrix technique, as well as the fact that both positive and negative values are recorded in all seasons, indicate that the daily averages are quite noisy. As a consequence of this large variability, care should be taken when considering individual daily values.

Despite the high short-term variability, the monthly-mean averages show a repeating seasonal behaviour in both zonal and meridional momentum fluxes . The zonal momentum fluxes shown in Figures 4.13 and 4.14 show a tendency for zonal momentum flux to be positive in winter and negative in summer, at least in the lower two height gates observed. The values of the monthly-mean zonal momentum fluxes range between ± 30 m^2s^{-2} but are mostly less than 20 m^2s^{-2}. These values are consistent with the magnitudes observed in some previous studies at polar latitudes (e.g., *Espy et al.*, 2004a, 2006; *Tang et al.*, 2002).

The monthly-mean meridional momentum fluxes over Rothera and Esrange shown in Figures 4.19 and 4.20 are similar in magnitude. Over Esrange the zonal component is slightly larger than the meridional component. Over Rothera the reverse is true. The values tend to be below ± 10 m^2s^{-2} in the lower two height gates over both stations, with larger momentum fluxes in the upper height gate.

There is considerable year-to-year variability present in both zonal and meridional momentum fluxes. This may be the result of variations in the propagation conditions for the waves (such as the temperature structure or the strength of the background winds) or the result of variations in the characteristics of the gravity-wave sources or the strength of excitation.

There are two particular features of interest in the momentum fluxes measured over Esrange. In the autumn/winter of 2002 and 2007 there are prominent increases in eastward (positive) zonal momentum flux (Figure 4.14) which coincides with prominent increases in southward (negative) meridional momentum flux (Figure 4.20). The event in 2002 is more prolonged and corresponds to a burst of gravity-wave activity measured by both the matrix (Figure 4.7) and variance techniques (Chapter 3, Figure 3.22b). This may be related to the Antarctic sudden stratospheric warming that occurred in September of 2002.

4.8.1 The Seasonal Behaviour of Zonal Momentum Flux

Some investigation of the seasonal behaviour as well as inter-hemispheric differences can be made using the climatologies shown in Figures 4.15. This figure reveals a clear seasonal structure in the zonal momentum fluxes which is most distinct in the bottom two height gates.

Over Rothera the momentum fluxes tend to be negative in winter and positive in summer. In the upper height gate the behaviour is similar but the zonal momentum flux decreases with height in the summer resulting in smaller momentum fluxes in summer at $\sim$ 93 km.

Over Esrange, the seasonal behaviour is similar in the lower height gates, but the values tend to be close to zero in winter and spring and more positive in winter. However, a distinct semi-annual behaviour is present at $\sim$ 93 km, with increased momentum fluxes in summer and winter.

The difference between the seasonal behaviour observed over Rothera and Esrange may be the result of the higher inter-annual variability seen over Esrange and the larger number of gaps present in the data over Esrange. The variability and number of data gaps is worst in the upper height gate where the agreement with Rothera is also worst.

A seasonal cycle similar to that seen over Rothera and Esrange, with negative zonal momentum fluxes in winter and more positive values in summer is also seen in other observations of the MLT gravity-wave field at polar latitudes (e.g., *Espy et al.*, 2006, 2004a; *Tang et al.*, 2002; *Murphy and Vincent*, 1993; *Fritts and Alexander*, 2003). It has been suggested that this cycle in zonal momentum flux is the result of critical-level filtering acting on the waves as they propagate to these heights (e.g., *Fritts and Alexander*, 2003). This can be explained as follows.

In summer, below $\sim$ 80 km, the zonal winds are predominantly westward and reach a maximum velocity of $\sim$ -60 ms^{-1} at a height of $\sim$ 70 km. These strongly westward winds will form critical levels for westward propagating gravity waves and thus create an anisotropy in the gravity-wave field reaching the MLT. As the westward propagating waves are filtered out, there is less and less westward (negative) momentum in the gravity-wave field. The eastward-travelling waves do not encounter critical levels and carry eastward (positive) momentum as they ascend. Thus the anisotropy of the gravity-wave field creates an dominance of eastward (positive) momentum flux in the summer.

This reasoning also applies in the winter, when below $\sim$ 80 km the zonal winds are predominantly eastwards. The zonal winds maximise with winds of $\sim$ 75 ms^{-1} at a height of $\sim$ 40 km. These winds will also impose an anisotropy on the gravity-wave field as it ascends to the MLT and result in more westward momentum than eastward and thus westward (negative) momentum fluxes in winter.

In summary, the differences in the zonal winds below $\sim$ 80 km result in differences in the critical-level filtering occurring between summer and winter. This then causes more eastward (positive) momentum flux in winter and more westward (negative) momentum flux in summer in the MLT. As already described in Chapter 3, there are large differences in the winds below $\sim$ 80 km over Rothera and Esrange in late winter and spring. It is possible that these differences contribute to some of the differences seen in momentum fluxes measured over the two sites. However, it cannot explain the differences in summer and autumn nor the semi-annual cycle

seen over Esrange at the upper height gate.

4.8.2 Zonal Momentum Flux Deposition

The change in zonal momentum flux with height over Rothera shown in Figure 4.16 indicates that in most months there is no change, or a small decrease, in zonal momentum flux with height. However, during summer (particularly December and January), zonal momentum flux noticeably decreases with height. In contrast during winter (August and September), momentum flux increases with height.

Current modelling studies of gravity-wave breaking ascribe the reversal of the zonal mean wind at $\sim$ 90 km to the deposition of momentum flux by breaking waves (e.g., *Lindzen*, 1981; *Holton*, 1983; *Fritts and Alexander*, 2003). Considering the zonal mean winds in summer conditions, the zonal winds become gradually more and more eastward with increasing height above about 70 km. If this is being driven by gravity-wave breaking, then eastward momentum must be deposited into the mean flow from about 70 km to $\sim$ 100 km. This means that eastward momentum is being removed from the gravity-wave field and the zonal momentum flux will become more westward with increasing height. This corresponds to a decrease of zonal momentum flux with height as seen in Figure 4.16. The observations presented here thus support this interpretation, at least qualitatively.

In winter conditions, the zonal mean wind becomes more westward with height above about 50 km. This corresponds to westward momentum being lost from the gravity-wave field and deposited into the mean flow. As a result the momentum flux will become more and more eastward with increasing height in winter. This is seen in the increasing momentum fluxes in winter over Rothera (Figure 4.16). Again, the observations presented here thus support this interpretation, at least qualitatively.

4.8.3 The Seasonal Behaviour of Meridional Momentum Flux

The seasonal behaviour of the meridional momentum flux over Rothera and Esrange are shown in Figure 4.21. This reveals a distinct seasonal behaviour in the lower two height gates over Rothera. There are poleward (negative) momentum fluxes in summer (November, December and January), and positive (equatorward) momentum fluxes throughout most of the rest of the year. The upper height gate shows the same cycle but positively displaced by approximately 10 m^2s^{-2}. Over Esrange the cycle is less clear. However, in the middle height gate, the behaviour over Esrange is approximately anti-correlated with that over Rothera. Although all but one months have equatorward (negative) meridional momentum flux, the momentum fluxes at $\sim$ 90 km show the momentum flux is most equatorward (negative) in autumn and winter.

A seasonal cycle qualitatively matching that of Rothera has been observed at middle latitudes (e.g., *Manson and Meek*, 1993; *Gavrilov et al.*, 2000; *Nakamura et al.*, 2001; *Tang et al.*, 2002). However, very few studies have examined the seasonal behaviour of meridional momentum flux at polar latitudes and the nature of the polar seasonal cycle remains unclear. Studies show either no repeating seasonal cycle (e.g., *Fritts and Alexander*, 2003) or yield contradictory results (e.g., *Murphy and Vincent*, 1993).

Observations made over Rothera using a combination of MF radar and an airglow imager data suggest that, at ~ 90 km, the seasonal cycle of meridional momentum flux is equatorward (positive) from April to September and poleward (negative) in March and October (*Espy et al.*, 2006). Although observations were not made from November to February, because the imager cannot function in daylight, the results agree well in magnitude and direction with those presented here over Rothera.

Espy et al. (2004a) also measured momentum fluxes in the Antarctic using an airglow imager and an dynasonde/Imaging Doppler Interferometer (IDI) radar. Monthly-mean meridional momentum flux was poleward (positive) in winter and equatorward (positive) in summer. Again, this agrees with the results over Rothera and is not dissimilar to those over Esrange. *Espy et al.* (2004a) suggested that, like the zonal component, critical-level filtering by the meridional mean winds causes the seasonal cycle observed in the MLT.

However, observations made at mid-latitudes over Adelaide, Australia using an MF radar reveal a different seasonal cycle for the meridional momentum flux (*Murphy and Vincent*, 1993). For short-period gravity waves (periods between 8 minutes and 1 hour), *Murphy and Vincent* (1993) observed poleward (negative) momentum flux in late summer to autumn and equatorward (positive) momentum flux in summer and spring. This is opposite to the cycle seen over Rothera. These differences may simply represent the difference between the polar and mid-latitude MLT.

Although the seasonal cycle over Esrange is less distinct than that over Rothera, the momentum fluxes are equatorward (negative) in winter agreeing with those over Rothera and in a number of previous studies (e.g., *Tang et al.*, 2002; *Espy et al.*, 2004a, 2006). The less distinct seasonal cycle and higher inter-annual variability over Esrange may be the result of higher variability in gravity-wave sources in the Arctic, or the result of differences in the filtering imposed by the mean-winds. It should be noted that the high-levels of planetary-wave activity over the Arctic will effect the wind structure below and in, the MLT. This may result in more variation in the amount of critical-level filtering the gravity-wave field encounters as it ascends to the MLT and thus a greater degree of variability in the gravity-wave momentum fluxes.

4.9 Conclusions

1. The technique developed by *Hocking* (2005) has been applied to data recorded by meteor radars in the Arctic and Antarctic.

2. Both the zonal and meridional variances and momentum fluxes calculated using this technique have revealed high levels of short-term and inter-annual variability.

3. Zonal and meridional variances reveal a similar seasonal cycle with solstial maxima and equinotial minima.

4. Over Rothera, the monthly-mean meridional variances are higher than the zonal, particularly in summer.

5. Momentum fluxes show a seasonal cycle tending to southwest in summer and northeast in winter over Rothera. This corresponds to waves propagating toward the summer pole in all seasons. Over Esrange the cycle is less distinct, but has a tendency for southeast momentum fluxes in summer and eastward momentum fluxes in winter.

6. The change of zonal momentum flux with height over Rothera indicates that momentum flux is being deposited across the observed height range. This may be responsible for slowing and reversing the zonal winds in summer and winter.

7. Clear evidence of interactions with the mean winds below ~ 80 km is present and can be used to explain the seasonal cycle of both variance and momentum flux.

Chapter 5

The 8-hour Tide in the MLT over the UK, 1988-2004

5.1 Introduction

The dynamics of the Mesosphere and Lower Thermosphere (MLT) are dominated by large ampli-
tude waves and tides. These transport energy and momentum from their source regions (usually
in the troposphere and stratosphere) and deposit them at greater heights where they drive the
planetary-scale circulation of the MLT. Among the most conspicuous features of the MLT are
the 12- and 24-hour tides excited by the absorption of solar radiation in the underlying atmo-
sphere. The general structure and seasonal variability of the 12- and 24-hour tides in the MLT
are now quite well established – at least at middle latitudes.

However, there also exist tides in the MLT region with periods of 8 and 6 hours (the terdiurnal
and quarterdiurnal tides). These latter tides generally have smaller amplitudes than the 12- and
24-hour tides (particularly in the case of the 6-hour tide).

Ground-based observations by meteor and MF radars have revealed that the 8-hour tide is a
persistent feature of the atmosphere at MLT heights and on occasion can reach amplitudes
comparable to or greater than those of the 24- and 12-hour tides. Studies have established the
broad characteristics of its seasonal behaviour, particularly at middle and Arctic latitudes and
have identified a high degree of short-term variability in the tide's amplitude and phase (e.g.,
Glass and Fellous, 1975; *Manson and Meek*, 1986; *Teitelbaum et al.*, 1989; *Thayaparan*, 1997;
Younger et al., 2002; *Aso*, 2003; *Wu et al.*, 2005). Passive optical measurements have also shown
a significant 8-hour tidal signature at MLT heights (e.g., *Oznovich et al.*, 1997; *Pendelton et al.*,
2000).

Satellite observations have also been used to study the large-scale structure of the 8-hour tide

in the MLT region. *Smith* (2000) used data from the High Resolution Doppler Imager (HRDI) instrument on the Upper Atmosphere Research Satellite (UARS) to investigate the tide at 95 km and at latitudes from 60° S to 60° N and identified its seasonal behaviour, concluding that maximum amplitudes are reached in autumn to mid-winter (September – January, Northern Hemisphere).

Smith and Ortland (2001) examined the 8-hour tide in a theoretical study the Research for Ozone in the Stratosphere and its Evolution (ROSE) model, a three-dimensional chemical transport model. This study suggested that (at a height of 97 km) the 8-hour tide maximises at mid-latitudes and around the winter solstice.

Note that some of these studies yield conflicting results. For instance, the mid-latitude MF- and meteor-radar study of *Teitelbaum et al.* (1989) suggest that there is a distinct Northern-Hemisphere amplitude maximum in January – March and a secondary maximum in September – November. However, the MF-radar observations of (*Thayaparan*, 1997) suggest that at similar latitudes the autumn/early-winter maximum is weak or absent. Further, the model of *Smith and Ortland* (2001) suggests that (at a height of 97 km) the mid-latitude 8-hour tide maximises around the winter solstice and has no autumnal secondary maximum.

There is some evidence that the seasonal behaviour varies with latitude. For instance, *Younger et al.* (2002) reported that the January-March maximum evident at mid-latitudes is greatly reduced in the Arctic and that the largest amplitudes are reached in September and October.

A conclusion common across the varied results described above is that the monthly-mean amplitudes of the 8-hour tide in the MLT are generally quite small – ranging from ~ 1 ms^{-1} to ~ 10 ms^{-1}.

Despite this body of observations, the excitation mechanism of the 8-hour tide is still uncertain. A number of different mechanisms have been proposed. These are:

- Excitation by direct solar heating of the lower and middle atmosphere (e.g., *Chapman and Lindzen*, 1970).

- A non-linear interaction between the 24- and 12-hour tides (e.g., *Teitelbaum et al.* (1989))

- Interaction between the 24-hour tide and gravity waves (e.g., *Miyahara and Forbes* (1991))

- A combination of some or all of the above mechanisms

Some of these proposed excitation mechanisms are testable. In particular, the non-linear excitation mechanism predicts that the 8-hour tide will have a vertical wavelength related to that of the 12- and 24-hour tides. Some of the observational studies described above have investigated

this question and concluded that, although unlikely to be the sole mechanism responsible for producing the tide, non-linear coupling may make a contribution at particular times.

In this study, a 16-year dataset is used to investigate the 8-hour tide over the UK. The analysis is used to explore three poorly understood features of the tide. Firstly, this extended dataset allows investigation of the inter-annual variability of the 8-hour tide. Secondly, the length of the dataset allows an accurate determination of the seasonal variability of the tide in a representative climatology. Thirdly, comparisons with observations made with another meteor radar at Esrange (68° N, 21° E) are used to suggest that the seasonal behaviour of the tide changes significantly from middle to Arctic latitudes. The radar instrumentation, data collection and data analysis techniques are described in Section 5.2. The basic characteristics and seasonal behaviour of the 8-hour tide are described in Section 5.3.1.

5.2 Data Collection and Analysis

The data used in this study come from a VHF meteor radar located at Castle Eaton in the UK (52.6° N, 2.2° W). It is a pulsed Doppler system operating at 36.3 MHz with a pulse repetition frequency of 300 Hz. It uses two orthogonal broad beams, elevated at $\sim 30°$ that intersect the meteor region at slant ranges of over 200 km. This creates a broad footprint on the meteor region and so it can detect echoes from a volume of several hundred kilometres across (e.g., *Mitchell et al.*, 1999). Hourly mean horizontal winds were calculated for each beam and then combined to yield hourly mean zonal and meridional winds.

For the observations used in this study, the radar operated with no routine height determination. However, the data from this and similar systems are usually taken to represent the approximate height range 90 to 95 km. In this study, a simple check of this assumption was made. The method used the phase of the 12-hour tide to calibrate the meteor-radar measurements. This tide was used because its phase behaviour has been well established in numerous studies at very similar latitudes, and particularly at Saskatoon (e.g., *Manson et al.*, 2002b) and Collm (e.g., *Jacobi et al.*, 1999). The tide is also well modelled in the Global Scale Wave Model (GSWM) at middle latitudes (e.g., *Hagan and Forbes*, 2003)). Here, the phase of the 12-hour tide was calculated for each month in the UK dataset and then vector averaged over the full 16-year interval. The large amplitude of the 12-hour tide at UK latitudes ensures a reliable estimate of its phase. Detailed comparisons with both the Saskatoon and Collm observations and the GSWM revealed the best agreement if the UK data is representative of a height of 90 to 95 km. Although this result agrees with the common assumption of many meteor-radar studies, it is nevertheless a useful confirmation. We should further note that measurements made by meteor radars equipped with interferometers (and so able to measure the heights of meteor echoes) suggest that the mean height of radio meteors varies by only ~ 1 km over the course of a year (e.g., *Mitchell et al.*, 2002; *Singer et al.*, 2004).

The data used in this study spans the interval from January 1988 to January 2004, during which the only significant gaps are July to December 1988, May 1995 to November 1996 and June to September 2003 where no usable data was recorded. The data used in the calculation of the tide had only two months with less than 10 complete days of data and the results from these two occasions were found to be consistent with other months in the dataset. Of the 157 months of data used ~99% had over 10 days of data and ~ 95% had over 15 days of data.

Two main analysis techniques were applied to the data. A superposed epoch (composite day) technique was used to investigate seasonal and climatological properties of the 8-hour tide. In this analysis, monthly-mean amplitudes and phases for the 8-hour tide were calculated using Fourier analysis from the monthly composite day of zonal and meridional winds. Following from this, a superposed epoch analysis of winds generated from the entire data set was used to calculate monthly-mean values of amplitude and phase for the full 16 years of the dataset.

The second technique was used to investigate short-term variability of the tide. In this analysis, a linear least squares fit was used to retrieve hourly-spaced values of amplitude and phase. A one-day window was incremented in one-hour steps through the zonal and meridional wind time series and the hourly winds were fitted with a superposition of a mean wind, 24-, 12-, 8- and 6- hour harmonic components. Any short breaks in the data were omitted without seriously affecting the results and a fit was only performed if there were at least 16 hours of data present in the 24-hour window.

5.3 Results

5.3.1 Basic Characteristics of the 8-Hour Tide
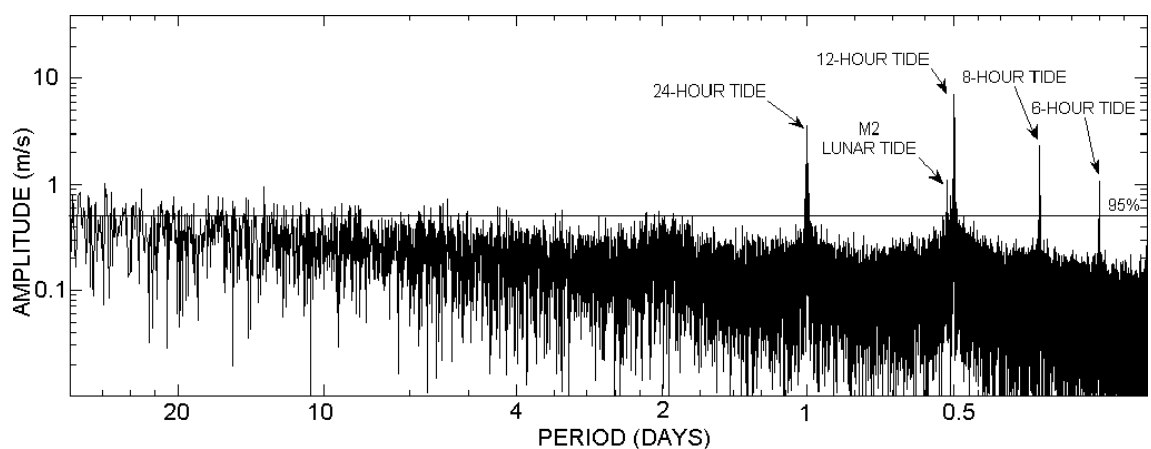
Figure 5.1: Lomb-Scargle periodogram of zonal winds from January 1988 to January 2004. Tidal signals are marked, as is the 95% confidence level.

Because the dataset contains a number of gaps of various lengths, a Lomb-Scargle periodogram

was used to investigate the spectral characteristics of the zonal and meridional winds. Figure 5.1 presents as an example a Lomb-Scargle periodogram of the raw zonal winds calculated for the interval January 1988 to January 2004. The periodogram clearly shows peaks at frequencies of 1, 2, 3 and 4 cycles per day (the 24-, 12-, 8- and 6-hour tides), as well as a number of less well-defined peaks at lower frequencies which are associated with planetary waves. Also present is a signal at a frequency of ~ 1.9 cycles per day, which is the signature of the lunar M2 gravitational tide. The peak at 3.0 cycles per day (8-hour period) will be interpreted hereafter as the signature of the 8-hour tide because, although gravity waves may occur at this frequency, the peak rises above the surrounding level which would not be the case for gravity waves in a long-term average.

To examine the general nature of the tides in more detail, a band-pass filtering of the wind time series was performed. The band-pass intervals of $0.75 - 1.5$, $1.5 - 2.5$ and $2.5 - 3.5$ cycles per day were selected to reveal oscillations of 24, 12, 8 hours. As an example, the results of this analysis for zonal winds in October 2000 are shown in Figure 5.2 The figure shows that at times the 8-hour tide is significantly smaller than the 12- and 24-hour tides, but at other times can reach amplitudes comparable to the 24- or even the 12-hour tide, see for example the instantaneous amplitudes during days $281 - 283$ (October 7th − 9th).
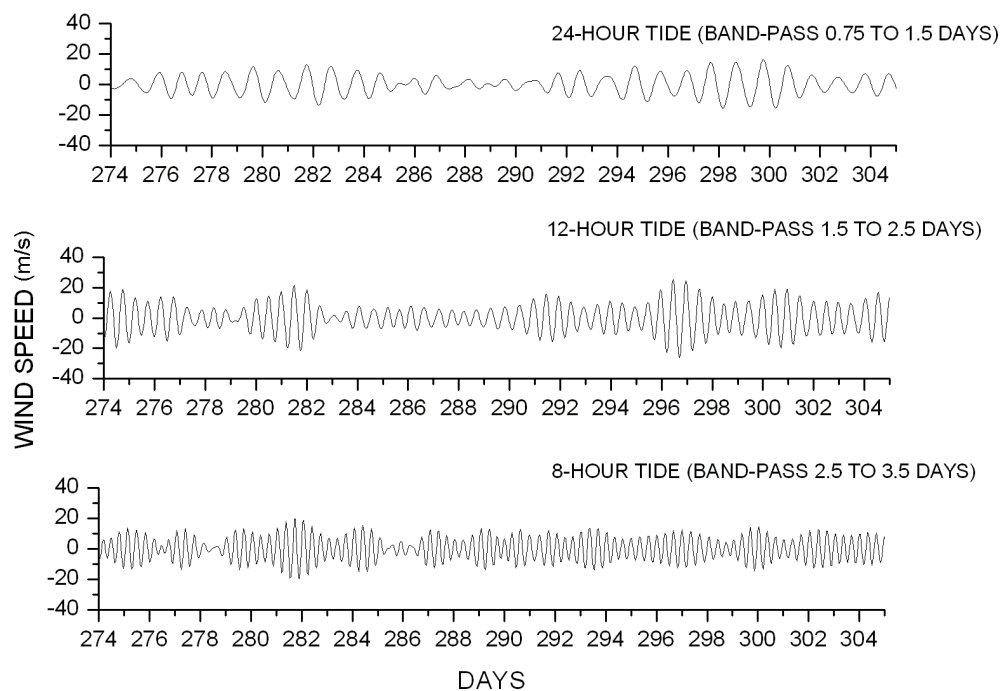
Figure 5.2: Band-pass filtered zonal winds for October 2000.

The data in Figure 5.2 also reveal a high degree of variability in the amplitude of all three tides. In the case of the 8-hour tide, the amplitude ranges from ~ 2 ms^{-1} to ~ 20 ms^{-1} from day 279 to day 282 (October 5th - 8th). This high level of day-to-day variability is typical of the observed 8-hour tide. Note that some of the variability, particularly in the first half of the month, appears to be quasi-periodic. Successive maxima occur regularly every ~ 2 to 3 days. *Younger*

et al. (2002) observed similar quasi-periodic variation in the 8-hour tide at arctic latitudes and explained this as a result of interactions between the quasi-2-day wave and the tide, possibly as a result of non-linear tidal/planetary-wave coupling (e.g., *Mitchell et al.*, 1996). In this case, only a weak 2-day wave signature was observed, suggesting that if a non-linear interaction was indeed responsible then it had occurred elsewhere in the atmosphere.

5.3.2 Seasonal Variation

To determine a representative seasonal behaviour of the 8-hour tide over the entire 16-year dataset, a superposed epoch analysis was carried out in which the composite day was produced by considering all data recorded within a particular month regardless of year (i.e., a composite day was produced from all January data from 1988 to 2004 etc). Figure 5.3 presents the seasonal behaviour of the amplitude and phase of the tide based on this analysis. The error bars in the figure represent the standard deviation of the monthly-mean values when calculated independently for each month in the dataset — the error bars are thus a measure of inter-annual variation

Considering firstly the amplitude results of Figure 5.3a, it can be seen that a distinct and similar seasonal behaviour is apparent in both wind components. Largest amplitudes of ~ 5 ms^{-1} occur during autumn (September – November), followed by a fall off to lower values in December. The amplitudes of both components decrease rapidly from March to May where the smallest values of ~ 1 ms^{-1} are observed. Following this minimum, the amplitudes increase slightly to ~ 2 ms^{-1} during the summer months (June – August). During summer the meridional amplitudes are larger than the zonal by ~ 1 ms^{-1} (some $\sim 25\%$) while during winter the zonal amplitudes are larger by about the same amount. In other seasons they have more comparable amplitudes.

The phase behaviour presented in Figure 5.3b again shows a clear seasonal pattern. For both components the winter phases are earliest and advance to later values in summer. This advance is particularly noticeable during June and July in the zonal component. There is a consistent phase difference very close to 2 hours between the two components – except in June and July where the difference increases to approximately 3.5 hours. The 2-hour phase difference observed in most months indicates phase quadrature and thus that the tide is approximately circularly polarised.

5.3.3 Hodograph Analysis

To investigate the phase difference between zonal and meridional components further, the hourly winds were band-passed filtered to reveal the 8-hour tide (using a band-pass frequency range of 2.5 to 3.5 cycles per day). The resulting winds were again subjected to a superposed epoch
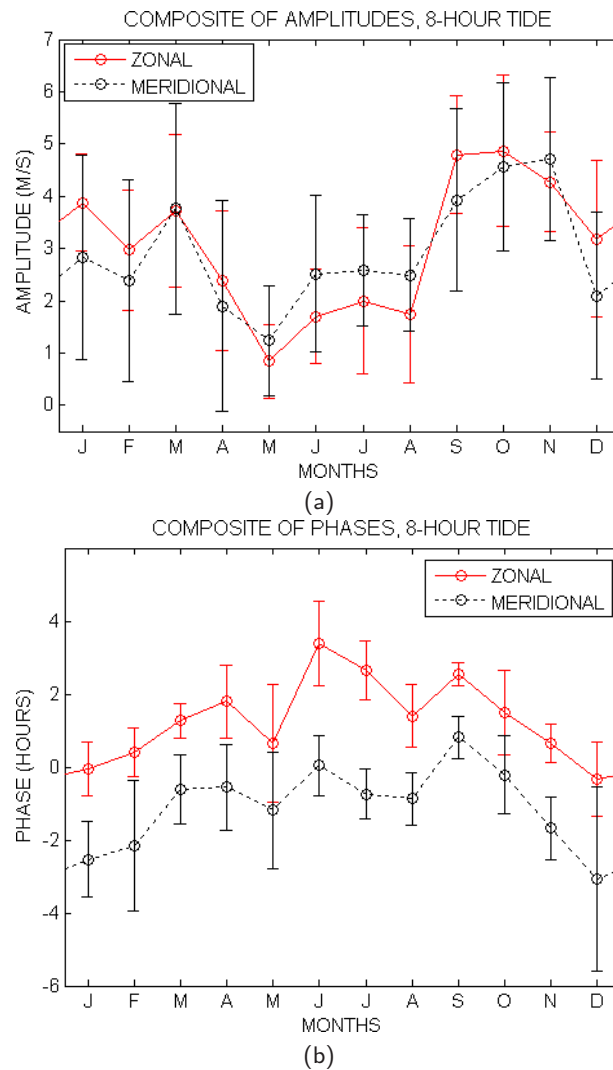
Figure 5.3: Climatology of the (a) amplitude and (b) phase of the 8-hour tide using data from 1988 to 2004. The error bars indicate the standard deviation of the individual monthly-mean values. Red solid lines indicate the zonal component, black dashed indicate the meridional component

analysis to determine a composite day for each month of the dataset. From each composite day a wind vector for each hour was calculated, the path the vector tips trace out is plotted as a hodograph which describes the change in wind velocity over the day. The zonal component is plotted on the x-axis and meridional on the y-axis and the sense of rotation is found to be clockwise in all cases.

An examination of the behaviour of the monthly-mean tide within the individual years observed is shown in Figure 5.4, which presents a hodograph for each month in each year of the dataset. No hodograph is plotted for those months where only one component of the wind was recorded or where the radar was inoperative.

The hodographs show that, in most cases, the pattern evident in Figure 5.3a is also displayed in the individual years (i.e., largest amplitudes in October etc). However, a degree of inter-annual
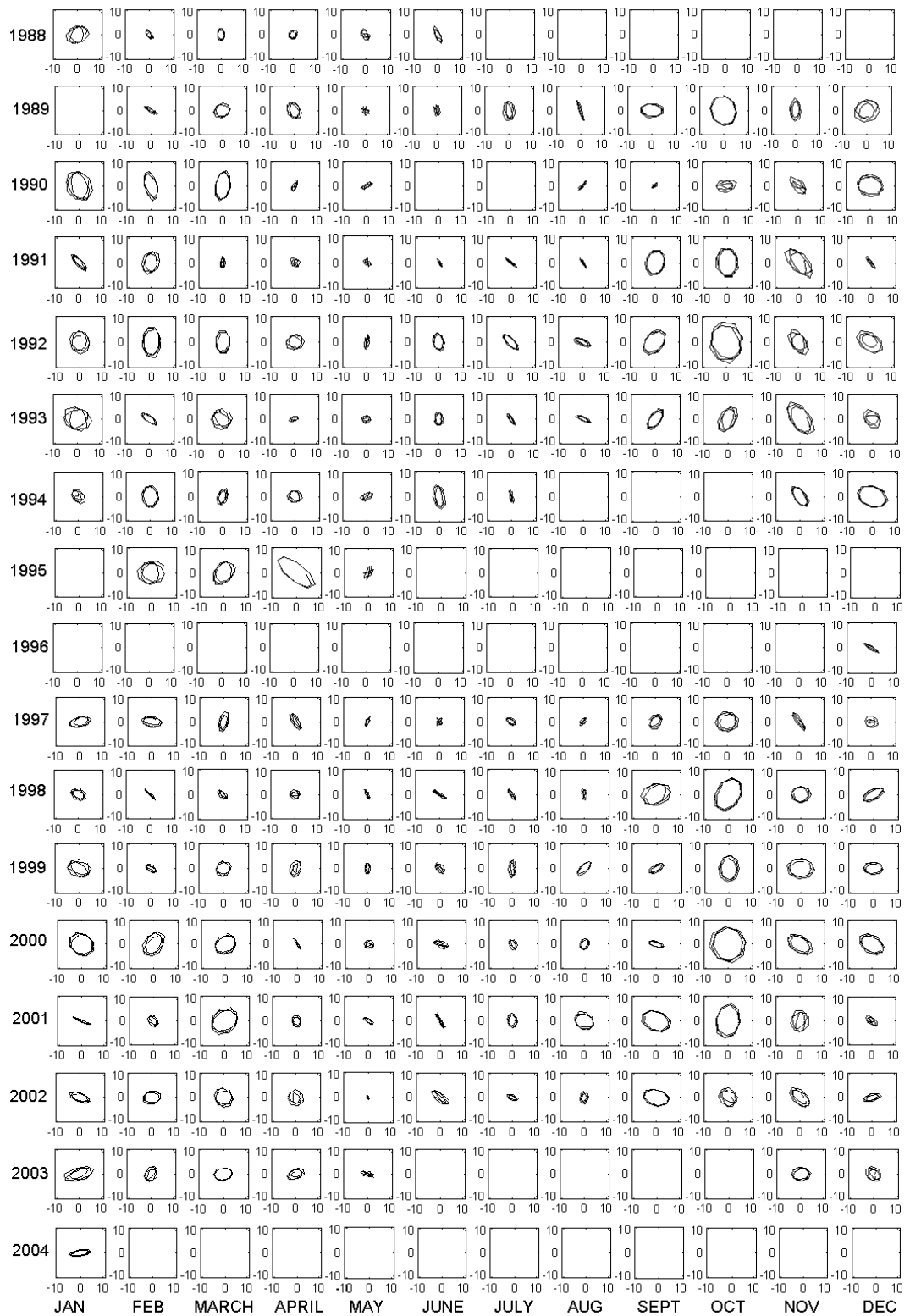
Figure 5.4: Hodographs for all months in the dataset, gaps are the result of missing data. Zonal wind is plotted on the x-axis, meridional on the y-axis.
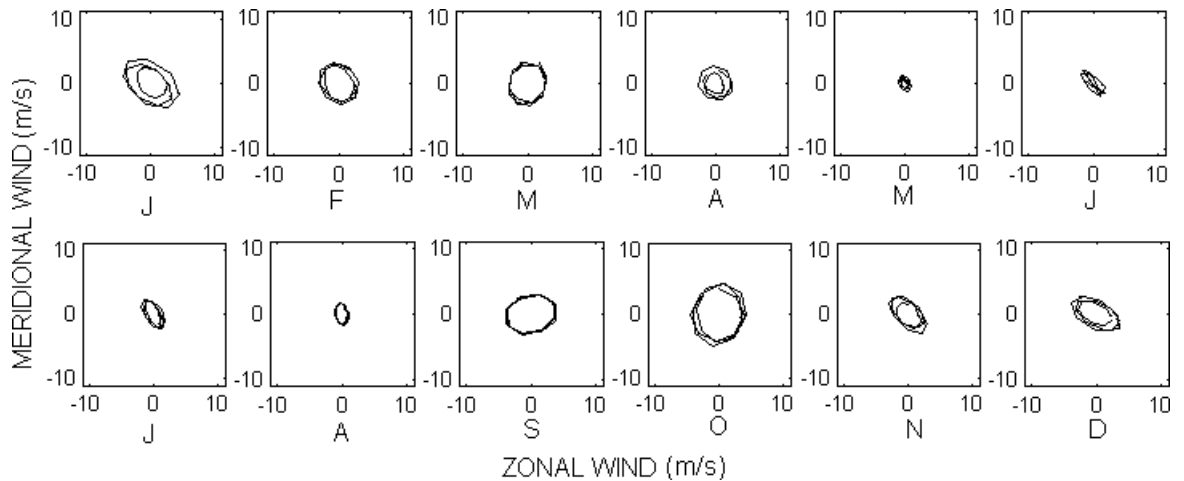
Figure 5.5: Hodographs of the monthly, composite-day 8-hour tide calculated using all data available in the interval January 1988 to January 2004.

variability is also apparent. For example, the largest tide during March occurred in 1990 when the meridional amplitudes reached ~ 7 ms^{-1} , the weakest tide during March was in 1998 when the meridional amplitudes were ~ 2ms^{-1}. In general, in the months with largest amplitudes the tide shows an approximate circular polarisation. The polarisation in other months is sometimes significantly more elliptical – e.g., during June. Note that the degree of polarisation in a particular month can change significantly from year to year (e.g., January in 2000, c.f., 2001).

Hodographs representing the average behaviour over the entire interval of time covered by the dataset are shown in Figure 5.5. The seasonal behaviour revealed by the climatology in Figure 5.3a is again evident. The largest amplitudes are observed in October and this corresponds to a time when the tide is close to being circularly polarised as a result of the two-hour phase difference and nearly identical amplitudes. More elliptical polarisations are evident in the winter months (November to January) and in summer (June to August). In both seasons the polarisation tends to be approximately aligned NW – SE.

5.3.4 Inter-Annual Variability

To examine year-to-year changes in the seasonal behaviour of the tide, individual monthly-mean values of amplitude, calculated using a superposed epoch, are presented in Figures 5.6a and 5.6b

The autumnal maximum and summer minimum can be clearly seen in each year throughout the dataset in both components. Some variation in the position of the autumnal maximum can be seen, with the maximum occurring in winter (November) in 1993 in both components. In 1994, large amplitudes occur in November and December; due to the lack of data from August to October it is not clear if this actually was the maximum or if the amplitude was larger in October. A high degree of inter-annual variability is apparent, for example the amplitudes in

(a) Monthly mean amplitudes of the 8-hour tide

(b) Meridional Amplitude of the 8-hour tide
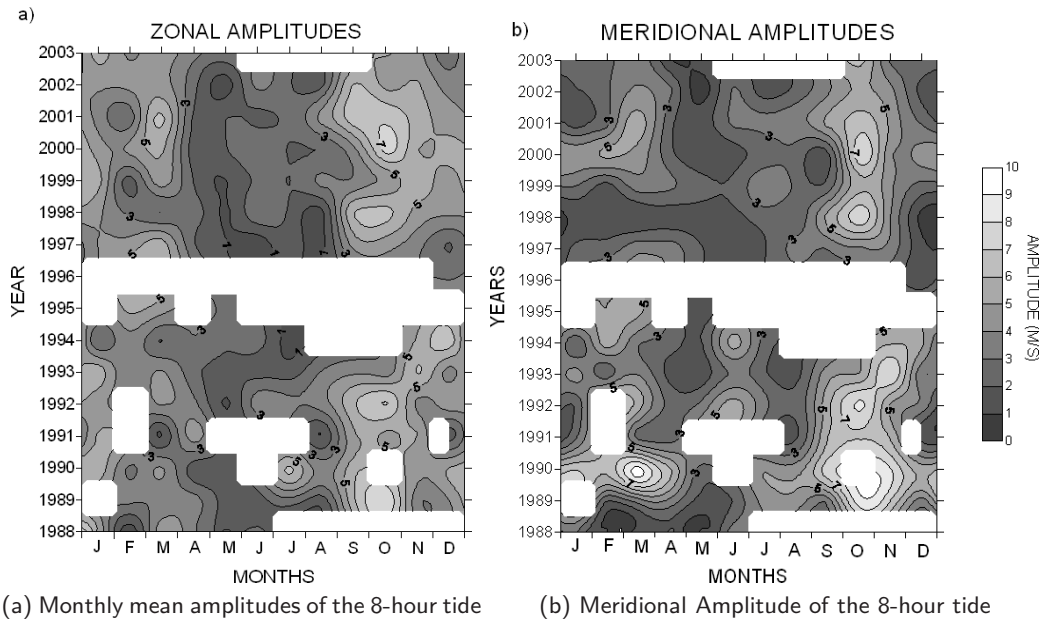
Figure 5.6: Monthly mean amplitudes for the (a) zonal and (b) meridional components of the 8-hour tide from January 1988 to January 2004. Tick marks indicate the beginning and end of each month.

March range from $\sim$ 1 to $\sim$ 9 ms^{-1}. For the zonal component the October amplitudes range from $\sim$ 3 to $\sim$ 7.5ms^{-1} with similar variations in the other autumn and winter months.

(a) Zonal phase of the 8-hour tide (1988 - 2004)

(b) Meridional phase of the 8-hour tide (1988 - 2004)
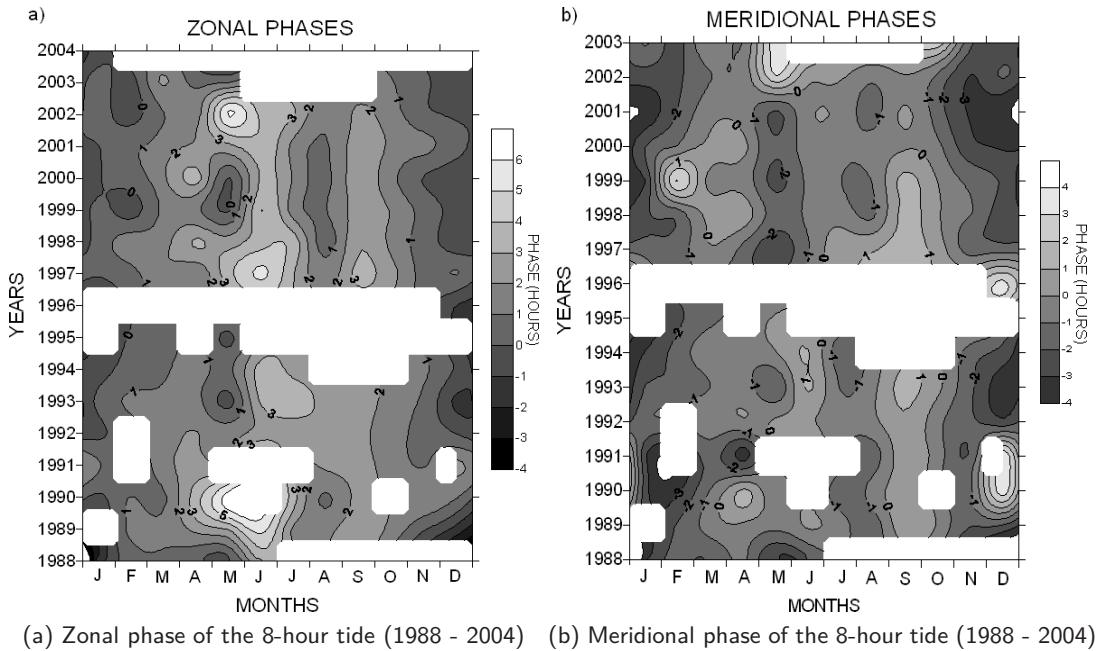
Figure 5.7: Monthly-mean phases for the (a) zonal and (b) meridional components of the 8-hour tide from January 1988 to January 2004.

The monthly-mean phases for the 8-hour tide are presented in Figures 5.7a and 5.7b. At times when the amplitudes are above approximately 2 ms^{-1} the phases remain quite constant from year to year, changing by no more than $\sim$ 2 hours and usually less than 1 hour over the period

covered by the dataset (e.g., see the relatively constant phases in October). The phases are more variable during the times of small amplitude (<2 ms^{-1}), particularly during April to June. However, this variability in phase most likely reflects less reliable phase determination at these small amplitudes and so we do not regard it as significant.

5.3.5 Short-Term Variability

The monthly-mean values confirm that the 8-hour tide is present in all months throughout the year at meteor heights. However, as well as inter-annual and seasonal variability the tide exhibits high levels of day-to-day variability (e.g., Figure 5.2). To investigate this, a sliding least-squares fit analysis was again used to calculate hourly-spaced values of tidal amplitude and phase. The analysis used a 24 hour window which was incremented through the dataset in one-hour steps.

The results of this analysis confirm the high level of day-to-day variability revealed in Figure 5.2, in which the amplitude can range from ~ 20 ms^{-1} to near zero in the space of a few days. A number of mechanisms may be responsible for tidal variability. *Vial* (1993) summarised several mechanisms, including variations in the relative amplitudes and phases of the different tidal modes, day-to-day variability caused by tidal set-up time, non-linear interactions between planetary waves and the tide and local interactions between gravity waves and the tide.

Non-linear coupling with planetary waves can result in a periodic modulation of the amplitude of the tide at the period of the planetary wave (e.g., *Teitelbaum and Vial*, 1991; *Mitchell et al.*, 1996; *Beard et al.*, 1997; *Pancheva*, 2001). A Lomb-Scargle periodogram of the hourly-spaced amplitude time series was calculated to search for periodic modulations. Here we present some results of this analysis for the summer months during which the 2-day wave reaches its largest amplitudes.

As an example of this analysis, Figure 5.3.5 presents the periodograms of the hourly meridional winds (Figure 5.8a) and tidal amplitudes (Figure 5.8b) for the summer months of 1989. The figure reveals a number of oscillations above the 95% confidence level that are presumably due to planetary waves (note that the inclusion of a strong deterministic signal — the 12-hour tide – in the time series means that these confidence levels are pessimistic). The periodogram reveals significant oscillations at periods around two days (strongest at a period of ~ 2.2 days, corresponding to the summertime 2-day wave) and also at longer periods (e.g., ~ 5 days and ~ 28 days). The cluster of peaks at periods near two days represents either the periodogram's response to a non-stationary time series (i.e., fluctuations in amplitude) or possible interactions between the 2–day wave and lower-frequency waves.

The corresponding periodogram of 8-hour tidal amplitudes is presented in Figure 5.8b. It can be seen that the tidal amplitude displays a clear 2.1-day modulation, as well as a modulations at
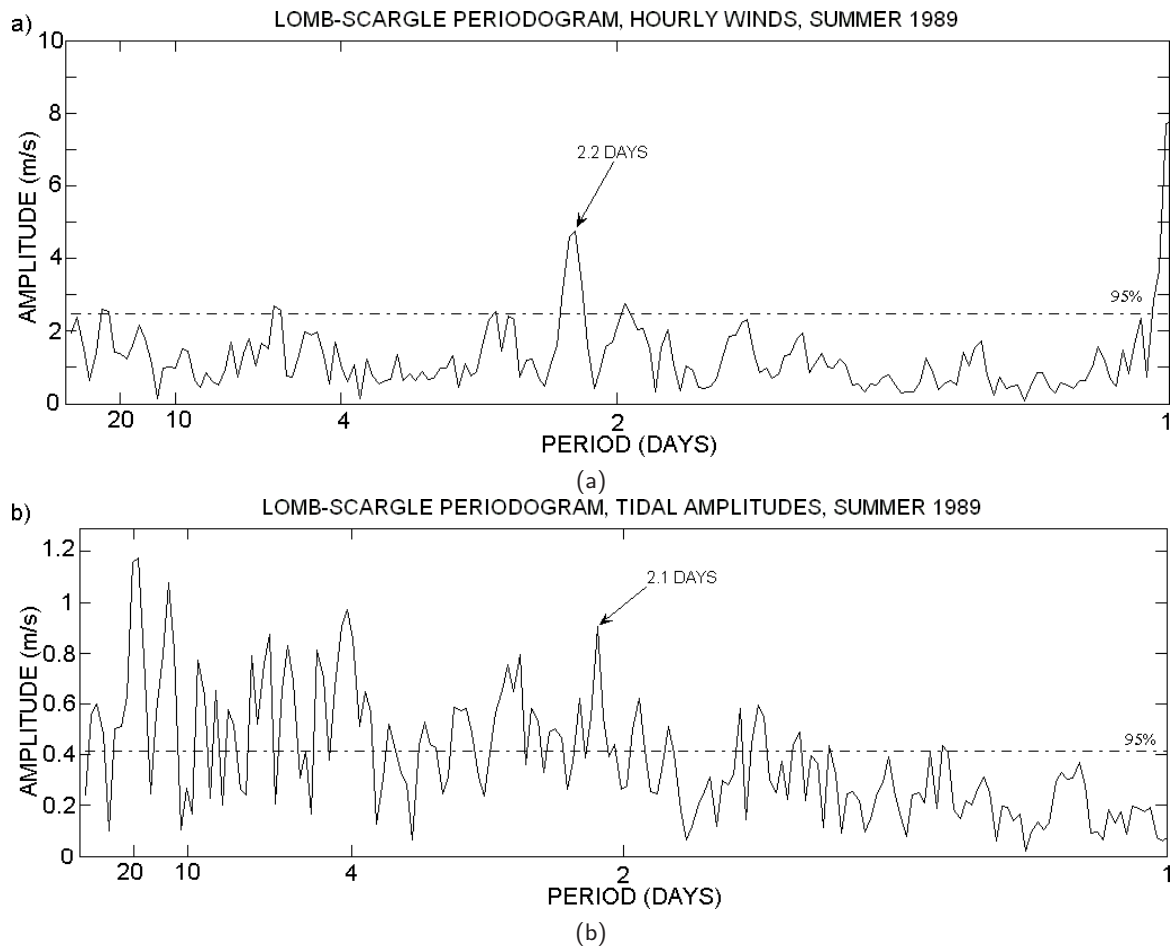
Figure 5.8: Lomb-Scargle periodogram of (a) meridional hourly winds for June – August 1989 (b) Lomb-Scargle periodogram of the corresponding amplitude-time series of the 8-hour tide. 95% confidence level is marked.

periods between $\sim$ 4 and 30 days. It may be that these modulations are caused by nonlinear interactions between the tide and the waves of these periods evident in Figure 4.8a. However, other peaks are seen in Figure 5.8b without corresponding signals being present in the periodogram of the winds. It is possible that these represent an interaction between the tide and a planetary wave occurring elsewhere in the atmosphere (e.g., at lower heights or other latitudes). However, it is also possible that these peaks represent the response of the periodogram to variations in tidal amplitude caused by other mechanisms (e.g., fluctuations in the strength of tidal excitation or variations of propagation conditions). Examination of similar data for the other years reveals no clear pattern – during some years it appears that the 8-hour tide undergoes modulation at periods associated with planetary waves and during other years no such modulation is observed. This suggests that although interactions with planetary waves may contribute to the variability of the 8-hour tide, such interactions are intermittent and only partially explain the observed variations.

5.3.6 Decadal-Scale Variability

The 16-year dataset allows some assessment of the degree of decadal-scale variability of the 8-hour tide. Two particular questions to be addressed are the possible role of solar variability in influencing the behaviour of the tide and the possible presence of any long-term trends in tidal properties.

To smooth out the month-to-month fluctuations in amplitude and phase described in Section 5.3.4, seasonal means are used. Each mean was calculated using a superposed epoch analysis of three months of data. Winter was defined as December to February, spring as March to May, summer as June to August and autumn as September to November. Corresponding seasonal means of F10.7 were used as a proxy for solar activity and the correlation of F10.7 with seasonal-mean amplitude and phase was investigated. A simple linear fit was used to investigate any dependence of seasonal-mean tidal amplitude and phase on F10.7. The Student T-test was used to identify significant relationships.

(a) Summer zonal and meridional phase   (b) Summer zonal and meridional amplitudes
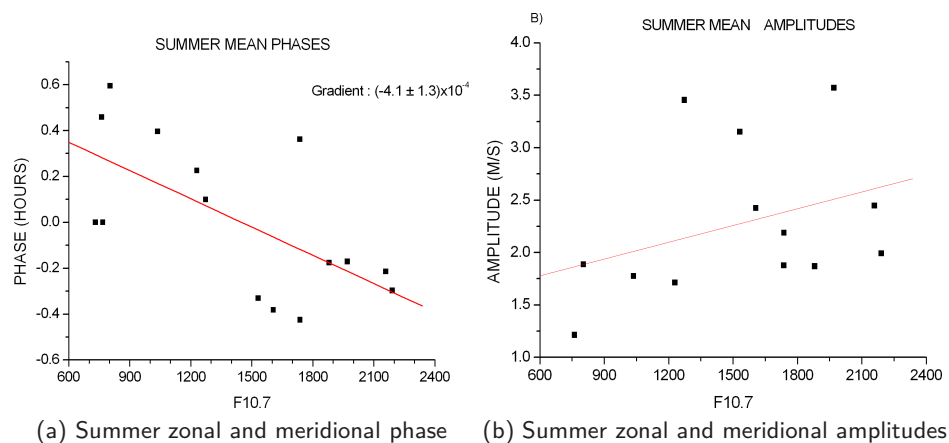
Figure 5.9: Summer zonal and meridional (a) phases and (b) amplitudes against F10.7.

Figure 5.9a presents the variation of summer phases with F10.7 for the 15 summer intervals for which data were available. The best-fit straight line is also indicated on the figure. No summer data were available for 1996.

Note that although not all summers had three complete months of data, all but one (1995) had at least two complete months and most had three. The gradient of the best-fit line is (-4.1 $\pm$ 1.3) $\times 10^{-4}$ hrs per sfu. A Student's T-test suggests this is significant above the 95% confidence level. Figure 5.9b presents the corresponding amplitudes. There is an apparent trend towards higher amplitudes at higher values of F10.7 , the gradient of the best-fit line is (5.3 $\pm$ 4.2) $\times 10^{-4}$ms^{-1} per sfu (solar flux unit). The Student's T-test suggests this is only significant at the 90% confidence level and so there is only weak evidence for a relationship. However, we should note that since the three other seasons did not show any significant relation between F10.7 and tidal amplitude or phase these relationships must, at best, be regarded with caution.

5.4 Discussion

Before we consider how the UK observations compare to those made at other locations we should recognise the specific limitations of the dataset used. A particular limitation is that no height information was available and so the calculated horizontal winds represent a sampling of the MLT weighted by the vertical distribution of meteors. This means that waves and tides may display some degree of self cancellation if their vertical wavelengths are comparable to the depth of the vertical distribution of meteor echoes (approximately Gaussian with a full width at half maximum of $\sim$ 8 km (e.g., Mitchell et al., 2002). However, we note that the mid-latitude vertical wavelengths calculated from the longer data intervals reported by Namboothiri et al.(2004) suggest that the vertical wavelengths of the 8-hour tide are very long in winter and autumn ($>$ 1000 km), shorter in spring (mean of $\sim$ 125 km) and shortest in summer ($\sim$107 km). These values would not cause significant self cancellation – although we should note that individual stations do sometimes record very short vertical wavelengths, e.g., 22 km over London, Canada (43° N, 81° W) in summer (Thayaparan, 1997). We should also note that some caution must be used in making comparisons between observations made in different years because the degree of inter-annual variability is believed to be quite high (Section 5.3.4). Additionally, the range of longitudes over which observations have been made is considerable and longitudinal variability (including contributions from non-migrating 8-hour tides) may be significant. With these caveats in mind, we will now consider how the UK observations compare to those made at other sites.

Namboothiri et al. (2004) reported observations made at heights of $\sim$ 76 − 98 km using MF radar during 1997 - 2001 over Wakkanai, Japan (45.5° N, 141.7° E). As with our observations, large day-to-day fluctuations in amplitude were observed, with the largest amplitudes being $\sim$ 20 ms^{-1}. The amplitudes at heights of 90 - 95 km revealed only a weak seasonal behaviour with a winter maximum and summer minimum. These results did not reveal the clear autumnal maximum observed over the UK. Further, the seasonal-mean amplitudes were significantly larger than over the UK, ranging from $\sim$ 6 to $\sim$ 8 ms^{-1} at these heights. However, the phase behaviour was generally similar to that observed over the UK, with a summertime advance from lower winter values.

Observations of the 8-hour tide made using an MF radar at London, Canada (43° N, 81° W) were reported by *Thayaparan* (1997). The observations span four years, from 1992 to 1996 and cover heights from 85 to 94 km. Again, large day-to-day fluctuations in amplitude were observed, with the largest amplitudes being $\sim$ 20 ms^{-1}. The largest amplitudes generally occurred in winter and the smallest in summer. There is no evidence of the autumnal maximum observed over the UK, although the phase behaviour is rather similar to our observations. Note that this study and that of *Namboothiri et al.* (2004) both reveal considerable inter-annual variability, particularly in amplitude.

Observations made by meteor radar at several mid-latitudes sites were reported by *Teitelbaum et al.* (1989). Climatologies were presented based on data from 1970 to 1980 at 94 km over Garchy (47° N) and Montpazier (44° N) in France. Also presented were MF-radar observations from Saskatoon (52° N) in Canada. On average, the monthly-mean amplitudes reported are about 50% greater than those observed over the UK. These data sets do indicate a localised autumnal amplitude maximum. However, unlike the UK data it is not larger than the winter amplitudes. Phases over Garchy and Montpazier are generally similar to those over the UK, but the Saskatoon phases advance to much higher values in the summer months (e.g., $\sim 6 - 7$ hours LT c.f. $\sim 2 - 4$ hours LT).

Observations made by meteor radar over Esrange (69° N, 21° E) in the Arctic in the interval October 1999 to April 2001 were reported by *Younger et al.* (2002). Over the height range of 81 - 97 km, monthly-mean amplitudes were found to peak strongly in a relatively short-lived maximum during September and October, where monthly-mean amplitudes reached up to ~ 7 ms^{-1}. Amplitudes throughout the rest of the year were ~ 2 ms^{-1}. Additional years of observation are now available from the Esrange meteor radar, so a similar analysis to that carried out for the UK radar was used to derive a monthly-mean climatology based on data from October 1999 to June 2005. Figure 5.4 presents monthly-mean amplitudes over Esrange for this interval. The figure shows that the Arctic 8-hour tide reaches largest amplitudes in August – October and has very low amplitudes throughout the rest of the year. This result confirms the earlier results of (*Younger et al.*, 2002) and suggests that at Arctic latitudes the winter-time secondary amplitude maximum observed over the UK is absent.
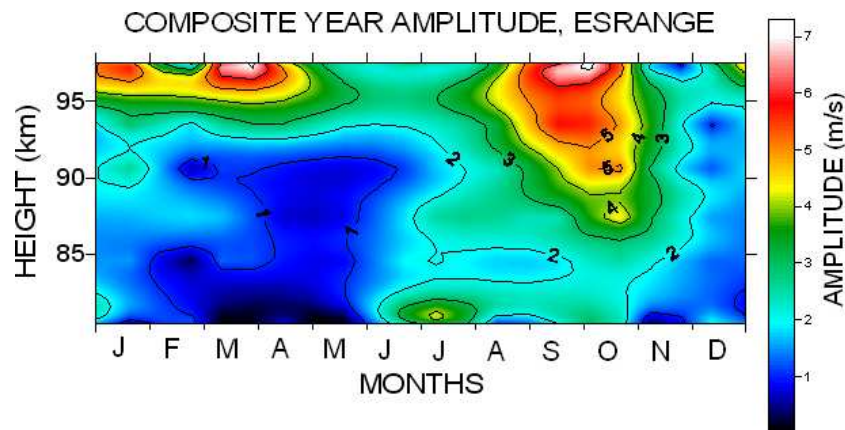
Figure 5.10: Monthly-mean amplitudes for the meridional component of the 8-hour tide from October 1999 to June 2005 at Esrange.

Global satellite observations using the HRDI, UARS instrument were reported by *Smith* (2000). At a height of 95 km at UK latitudes, tidal amplitudes were found to maximise around the autumnal equinox, with values of ~ 15 ms^{-1} for both the zonal and meridional components. However, this seasonal behaviour was investigated with time steps of ~ 2.4 months and so could not easily confirm the existence of a distinct autumnal maximum of the sort observed in the UK radar data.

In summary, comparison of the UK radar observations reported here with other published studies suggests that the 8-hour tide has a seasonal behaviour that varies with latitude. At latitudes of 43° S – 45° N the tide has a winter amplitude maximum, smaller equinoctial amplitudes and an extended summer minimum (Wakkanai and London). At slightly higher mid-latitudes of $\sim 52°$ N the winter amplitudes are somewhat reduced and amplitudes at the autumnal equinox increase to be larger than those in winter (UK, Saskatoon and Garchy) – although this behaviour is also evident at the lower latitude of Montpazier (44° N). At Arctic latitudes, Esrange (68° N), the tide has small amplitudes throughout the year except for a conspicuous maximum around the autumnal equinox. In general, all the mid-latitude observations report similar phase behaviour.

Comparisons of observed amplitudes and phases with the relatively small number of modelling studies investigating the 8-hour tide should be made with care. The models considered below exhibit steep gradients in amplitude or phase vs height and/or latitude, therefore small changes in the height of comparison can affect the strength of agreement or disagreement.

Smith and Ortland (2001) used a global, three-dimensional, non-linear model to predict the characteristics of the 8-hour tide at an altitude of 97 km. The seasonal behaviour predicted by the model indicates that maximum amplitudes of up to 9 ms^{-1} occur around midwinter and that smaller amplitudes (<2 ms^{-1}) occur throughout the spring to autumn period (April – September). Largest amplitudes are strongly localised in latitude and peak at latitudes of $\sim 55°$. The observations presented here show amplitudes that are generally smaller in winter (e.g., ~ 3 - 4 ms^{-1} c.f. up to 9 ms^{-1}) and a conspicuous autumnal amplitude maximum that is not present in the model results. We should note, however, that the results of (*Smith and Ortland*, 2001) are for a height of 97 km and the UK meteor-radar data are more representative of a height range ~ 90 - 95 km. The larger amplitudes in the model may be partially explained by the growth in amplitude with height. Further, at times when the tide has a short vertical wavelength, there will be some degree of self-cancellation in estimates of tidal amplitude because of the vertical distribution of meteors.

Akmaev (2001) presented results from a modelling study of the 8-hour tide at heights of 70 – 105 km. Akmaev separately considered excitation of the tide by: a) a combination of non-linear and direct solar excitation and b) non-linear excitation alone. Results were presented in particular for a latitude of 44°. If we consider these model results over the $\sim 90 - 95$ km "meteor height range" appropriate to the present study, we find that in the case of combined solar and non-linear excitation, the amplitudes were largest in winter, smaller at the equinoxes and smallest in summer. This does not agree with the UK meteor-radar observations of Section 5.3.1 (where amplitudes are largest at the autumnal equinox). Our UK meteor-radar observations are in reasonable agreement with Akmaev's model results for non-linear excitation alone, having maximum amplitudes at the autumnal equinox, smaller amplitudes in winter and spring and smallest amplitudes in summer. However, the amplitudes predicted by the model were smaller than those observed. This may suggest a significant role for non-linear processes in the excitation of the tide. The seasonal mean phases between $90 - 95$ km presented by *Akmaev* (2001)

generally agree very well (within 2 hours) with the radar observations. *Akmaev* (2001) also presented seasonal phases calculated for the case of combined excitation (only). Considering the model phases over the 90 - 95 km height range, there is excellent agreement with the radar observations. The model phases are usually within 1 to 1.5 hours of the observations.

5.5 Conclusions

Observations using a UK-based meteor radar over the interval January 1988 – January 2004 have revealed the 8-hour tide to be a persistent feature of the MLT at $\sim 52°$ N. Peak amplitudes can be as large as 20 ms^{-1}, comparable to the amplitudes of the 24- and 12-hour tides. Considering the average behaviour over the entire time period of the measurements a distinct seasonal cycle in amplitude and phase is apparent. The largest monthly-mean amplitudes of ~ 5 ms^{-1} are observed in autumn (September – November). Amplitudes of ~ 3 - 4 ms^{-1} are observed in winter (December – February) and the smallest amplitudes of ~ 2 ms^{-1} are observed in spring and summer. Hodographs reveal that the tide varies from being close to circularly polarised to having a major/minor axis ratio of ~ 2. Strong short-term variability is observed in the tidal amplitudes, with fluctuations occurring on a time scale of a few days. Some of the variation seen in the amplitudes appears to be quasi-periodic and occurs at periods associated with planetary waves (e.g., 2 days), suggesting that the tide may interact with planetary waves.

Considerable inter-annual variability in tidal amplitude is observed in all seasons. Comparisons with F10.7 , used as a proxy for solar activity, suggest that summer amplitudes increase with increasing F10.7 and summer phases decrease with increasing F10.7 . However, the confidence levels of these relationships are not high, being 90% and 95%, respectively. No significant relationships were found for the other seasons.

Comparisons with observations made at middle and Arctic latitudes suggest that the seasonal amplitude behaviour of the 8-hour tide may vary with latitude. At latitudes of $\sim 43°$– 45° N a winter maximum is observed with smallest amplitudes in summer. At latitudes of $\sim 52°$ N an autumnal maximum is evident, although winter amplitudes remain quite strong. At Arctic latitudes the autumnal maximum remains but the winter amplitudes are significantly smaller.

Chapter 6

Suggestions for Future Work

The studies described in this thesis have addressed only a small fraction of the scientific questions that can be answered using meteor wind radar. The following are proposed as logical continuations of the work already described.

1. *Gravity-waves over the equator.* Chapter 3 described a novel method of measuring the high-frequency gravity-wave field using meteor radar. So far this technique has only been applied to data from the two polar radars in Rothera and Esrange. However, this technique could be used to study the gravity-wave field near the equator using the University of Bath Skiymet radar based on Ascension Island (8°S, 14°W). This radar was deployed in October 2001 and has provided nearly continuous data until the end of April 2007. There are relatively few long-term studies of high-frequency gravity-waves at the equator and the variance technique can be used to investigate both the long-term climatology, as well as short-term variations in gravity-wave activity (e.g., *Kumar et al.*, 2007). This study will also be interesting as the gravity-waves over Ascension are believed to be mostly generated by deep tropospheric convection in contrast to Rothera and Esrange where the nearby topography also excites gravity-waves. The dynamics of the equatorial Mesosphere and Lower Thermosphere (MLT) is also significantly different to that at the poles. The presence of the Quasi-Biannual Oscillation (QBO), Kelvin waves and a large amplitude 24-hour tide can all interact with and influence the gravity-wave field.

2. *The effects of sudden stratospheric warmings on gravity-wave activity in the MLT.* Sudden stratospheric warmings can have a profound effect on the mesospheric gravity-wave field (e.g., *Dowdy et al.*, 2001). The variance technique described in Chapter 3 can provide gravity-wave variances with a temporal resolution high enough to investigate the effects of the rapid changes to the wind field associated with sudden stratospheric warmings on the high-frequency gravity-wave field.

3. *Solar cycle effects on gravity-wave activity in the MLT*. It has been suggested that gravity-wave activity in the MLT is affected by the solar cycle (e.g., *Gavrilov et al.*, 1995; *Jacobi et al.*, 2006). The length of data available over Esrange allows some investigation of long-term trends in gravity-wave activity which may give some insight into how solar cycle affects the dynamics of the MLT.

4. *Inter-instrument biases*. There has been considerable interest in the use of networks of instruments to monitor the atmosphere on a global scale (e.g., *Pancheva et al.*, 2002; *Manson et al.*, 2004; *Dowdy et al.*, 2001). When instruments of different types are used together, observed differences can be the result of biases inherent in the instruments used. It is therefore important to characterise and explain the biases inherent in instruments. The meteor radar based at Rothera is co-located with a Medium Frequency (MF) radar making this site ideal for investigating the differences these two techniques.

5. *Accelerations of the mean flow due to gravity-wave momentum deposition*. The breaking of gravity waves in the MLT is believed to be responsible for the slowing and reversing of the zonal mean winds at $\sim$ 90 km (e.g., *Lindzen*, 1981; *Holton*, 1983; *Fritts and Alexander*, 2003). As gravity-waves break they deposit momentum into the mean flow. Therefore, a change in the momentum flux with height should cause an acceleration of the mean flow. This can be calculated using $\left(\frac{\partial U}{\partial t}\right)_{u'w'} = -\frac{\partial \overline{u'w'}}{\partial z}$, where the acceleration is only due to the deposition of zonal momentum by the observed gravity waves (*Hocking*, 2005). The data presented in Chapter 4 indicates that the data from the current class of Skiymet, all-sky, radars is not suitable for accurate calculations of the acceleration of the mean wind. The error on the monthly-mean values of zonal momentum flux is too high, and there are only three height gates of data available. This makes any estimation of acceleration made from this data too unreliable. however, a new Skiymet radar was deployed in southern Argentina in 2008 which directs more power towards the zenith. Using this system, it may be possible to calculate more reliable momentum fluxes in a wider height range. This would allow more accurate calculation of momentum flux and the acceleration of the mean flow caused by high-frequency gravity-waves.

6. *Excitation mechanisms of the 8-hour tide*. The work in Chapter 5 presented the characteristics the 8-hour tide over the UK. The radar used in this study did not have height-finding capability and so no information about the vertical wavelength of the tide can be determined. There are several mechanisms that could be the primary source of excitation of the 8-hour tide including solar heating and non-linear coupling between the 24- and 12-hour tides. If the tide is generated through the non-linear interaction of the 24- and 12-hour tides, the vertical wavelength of the 8-hour tide will be related to the vertical wavelengths of the two primary tides. The radars over Rothera and Esrange do have height finding information and so can be used to investigate the vertical wavelength of the 24-, 12 and 8-hour tides and so can be used as a diagnostic of the generation mechanism of the 8-hour tide.

7. *Effect of the QBO on the 8-hour tide.* The decadal-scale variability investigated in Chapter 5, Section 5.3.6 illustrated that there are long term trends in the amplitude and phase of the 8-hour tide. As well as changes in solar flux, it is possible that the behaviour of the tide is influenced by the changes in phase of the QBO. The UK radar would be well suited to an investigation of this type as there are over 15 years of available data.

Bibliography

Akmaev, R. A., Seasonal variations of the terdiurnal tide in the mesosphere and lower thermosphere: a model study, *Geophysical Research Letters*, *28*(19), 3817 – 3820, 2001.

Akmaev, R. A., and V. Fomichev, Cooling of the mesosphere and lower thermosphere due to doubling of CO2, *Annales Geophysicae*, *16*, 1501–1512, 1998.

Alexander, M. J., and H. Teitelbaum, Observation and analysis of a large amplitude mountain event over the antarctic peninsula, *Journal Geophysical Research*, *112*(D21103), doi:10.1029/2006JD008368, 2007.

Andrews, D. G., J. R. Holton, and C. B. Leovy, *Middle Atmosphere Dynamics*, Academic Press, 1987.

Antontia, T. M., G. Ramkumar, K. K. Kumar, and V. Deepa, Meteor wind radar observations of gravity wave momentum fluxes and their forcing toward the Mesospheric Semiannual Oscillation, *Journal Geophysical Research*, *113*, D10,115, 2008.

Aso, T., An overview of the terdiurnal tide observed by polar radars and optics, *Advances in Polar Upper Atmosphere Research*, *17*, 167–176, 2003.

Baumgaerter, A. J. G., and A. J. McDonald, A gravity wave climatology for Antarctica complied from Challenging Minisatellite Payload/Global Positioning System (CHAMP/GPS) radio occultations, *Journal of Geophysical Research*, *112*, D05,103, doi:10.1029/2006JD007504, 2007.

Beard, A. G., N. J. Mitchell, P. J. S. Williams, and H. Muller, Mesopause-region tidal variability observed by meteor radar, *Advances in Space Research*, *20*(6), 1237–1240, 1997.

Beer, T., *Atmospheric Waves*, Wiley, 1974.

Beldon, C. L., H. G. Muller, and N. J. Mitchell, The 8-hour tide in the mesosphere and lower thermosphere over the uk, 1988-2004, *Journal of atmospheric and Solar-Terrestrial Physics*, *68*(6), 655–668, doi:10.1013/j.jastp.2005.10.004, 2006.

Ceplecha, Z., J. Borovicka, W. G. Elford, D. O. ReVelle, R. L. H. ad V. Prubcan, and M. Simek, Meteor Phenomena and Bodies, *Space Science Reviews*, *84*(3-4), 327–471, doi:10.1023/A:1005069928850, 1998.

Chapman, S., and R. S. Lindzen, *Atmospheric Tides*, D. Reidel Press, 1970.

Charney, J. G., and A. Eliassen, A numerical method for predicting the perturbations of the middle latitude westerlies, *Tellus*, *1*(2), 38–54, 1949.

Close, S., S. M. Hunt, M. J. Minardi, and F. M. McKeen, Meteor shower characterization at Kwajalein missile range, *Lincoln Laboratory Journal*, *12*, 33–44, 2000.

Connor, L. N., and S. K. Avery, A three-year gravity wave climatology of the mesosphere and lower thermosphere, *Journal of Geophysical Research*, *101*(D2), 4065–4077, 1996.

Dowdy, A., R. A. Vincent, K. Igarashi, Y. Murayama, and D. J. Murphy, A comparison of mean winds and gravity wave activity in the northern and southern polar mlt, *Geophysical Research Letters*, *28*(8), 1475–1478, 2001.

Dowdy, A. J., R. A. Vincent, M. Tsutsumi, K. Igarashi, Y. Murayama, W. Singer, and D. J. Murphy, Polar mesosphere and lower thermosphere dynamics: 1. Mean wind and gravity wave climatologies, *Journal of Geophysical Research*, *112*, D17,104, doi:10.1029/2006JD008126, 2007.

Dunkerton, T. J., Inertia-gravity waves in the stratosphere, *Journal of the Atmospheric Sciences*, *41*(23), 3396–3404, 1984.

Ebel, A., A. H. Manson, and C. E. Meek, Short period fluctuations of the horizontal wind measured in the upper middle atmosphere and possible relationships to internal gravity waves, *Journal of Atmospheric and Terrestrial Physics*, *49*, 385–401, 1987.

England, S. L., A. Dobbin, M. J. HArris, N. F. Arnold, and A. D. Aylward, A study into the effects of gravity wave activity on the diurnal tide and airglow emissions in the equatorial mesosphere and lower thermosphere using coupled middle atmosphere and thermosphere (cmat) general circulation model., *Journal of Atmospheric and Solar-Terrestrial Physics*, *68*, 293–308, 2006.

Ern, M., P. Preusse, M. J. Alexander, and C. D. Warner, Absolute values of gravity wave momentum flux derived from satellite data, *J. Geophys. Res*, *109*, 2004.

Espy, P. J., G. O. L. Jones, G. R. Swenson, J. Tang, and M. J. Taylor, Seasonal variations of the gravity wave momentum flux in the Antarctic mesosphere and lower thermosphere, *Journal of Geophysical Research*, *109*(D23), 2004a.

Espy, P. J., G. O. L. Jones, G. R. Swenson, J. Tang, and M. J. Taylor, Tidal modulation of the gravity-wave momentum flux in the Antarctic mesosphere, *Geophysical Research Letters*, *31*, 2004b.

Espy, P. J., R. E. Hibbins, G. R. Swenson, J. Tang, M. J. Taylor, D. M. Riggin, and D. C. Fritts, Regional variations of mesospheric gravity-wave momentum flux over Antarctica, *Annales Geophysicae*, *24*(1), 81–88, 2006.

Flemming, E. L., S. Chandra, and J. J. Shoeberl, M. R. Barnett, Monthly Mean Global Climatology of Temperature, Wind, Geopotential Height and Pressure for 0 – 120 km, *NASA Technical Memorandum 100697*, 1988.

Forbes, J. M., Tidal and Planetary Waves, in *The Upper Mesosphere and Lower Thermosphere: A review of Experiment and Theory, Geophysical Monograph*, vol. 87, edited by R. M. Johnson and T. L. Killeen, pp. 67–87, American Geophysical Union, 1995.

Foster, M. P., and A. N. Evans, An evaluation of Interpolation Techniques for Reconstructing Ionospheric TEC maps, *IEEE Transactions on Geosciences and Remote Sensing*, *46*(7), 2153–2164, 2008.

Fritts, D. C., and M. J. Alexander, Gravity wave dynamics and effects in the middle atmosphere, *Reviews of Geophysics*, *41*(1), 1003, 2003.

Fritts, D. C., and G. D. Nastron, Sources of Mesoscale Variability of Gravity Waves. Part ii: Frontal, Convective, and Jet Stream Exctation, *Journal of the Atmospheric Sciences*, *49*(2), 111–127, 1992.

Fritts, D. C., and P. K. Rastogi, Convective and dynamical instabilities due to gravity wave motions in the lower and middle atmosphere: Theory and observations, *Radio Science*, *20*(6), 1247–1277, 1985.

Fritts, D. C., and R. A. Vincent, Mesospheric momentum flux studies at Adelaide, Australia: Observations and a gravity wave-tidal interaction model, *Journal of the Atmospheric Sciences*, *44*(3), 605–619, 1987.

Fritts, D. C., and L. Yuan, Measurement of momentum fluxes near the summer mesospause at Poker flat, Alaska, *Journal of Atmospheric Sciences*, *46*(16), 2569 – 2579, 1989.

Fritts, D. C., R. C. Blanchard, and L. Coy, Gravity Wave Structure between 60 and 90 km Inferred from Space Shuttle Reentry Data, *Journal of Atmospheric Sciences*, *46*, 423–434, 1989.

Fröhlich, K., T. Schmidt, M. Ern, P. Preusse, A. de la Torre, J. Wickert, and C. Jacobi, The global distribution of gravity wave energy in the lower stratosphere derived from GPS data and gravity wave modelling: Attempt and challenges, *Journal Atmospheric and Solar-Terrestrial Physics*, *69*(17–18), 2238–2248, 2007.

Garcia, R. R., and S. Solomon, A numerical-model of the zonally averages dynamical and chemical-structure of the middle atmosphere, *Journal of Geophysical Research - Oceans and Atmospheres*, *88*(NC2), 1379–1400, 1983.

Gavrilov, N. M., A. H. Manson, and C. E. Meek, Climatological monthly characteristics of middle atmosphere gravity waves (10 min-10 h) during 1979-1993 at Saskatoon, *Annales Geophysicae*, *13*(3), 285–295, 1995.

Gavrilov, N. M., S. Fukao, and T. Nakamura, Gravity wave intensity and momentum fluxes in the mesosphere over Shigaraki, Japan (35°N, 136°E) during 1986-1997, *Annales Geophysicae*, *18*(7), 834–843, 2000.

Geller, M. A., Dynamics of the middle atmosphere, *Space Science Reviews*, *34*, 359–375, 1983.

Glass, M., and J. L. Fellous, The eight-hourly (ter-diurnal) component of atmospheric tides, *Space Research*, *15*, 191–197, 1975.

Hagan, M., J. Forbes, and A. Richmond, Atmospheric tides, in *Encyclopedia of Atmospheric Sciences*, vol. 1, edited by J. R. Holton, J. A. Curry, and J. A. Pyle, pp. 159–165, Academic Press, 2003.

Hagan, M. E., and J. M. Forbes, Migrating and nonmigrating semidiurnal tides in the upper atmosphere excited by tropospheric latent heat release, *Journal of Geophysical Research*, *108*(A2), 1062–1075, 2003.

Hall, C. M., T. Aso, M. Tsutsumi, S. Nozawa, A. H. Manson, and C. Meek, A comparison of mesosphere and lower thermosphere neutral winds as determined by meteor and medium-frequency radar at 70° n, *Radio Science*, *40*, RS4001, doi:10.1029/2004RS003102, 2005.

Hecht, J. H., R. L. Walterscheid, D. C. Fritts, J. R. Isler, D. C. Senft, C. S. Gardner, and S. J. Franke, Wave breaking signatures in OH airglow and sodium densities and temperatures 1. Airglow imaging, Na lidar, and MF radar observations, *Journal of Geophysical Research*, *102*(D6), 6655–6668, 1997.

Hibbins, R. E., P. J. Espy, M. J. Jarvis, D. M. Riggin, and D. C. Fritts, A climatology of tides and gravity wave variance in the MLT above Rothera, Antarctica obtained by MF radar, *Journal of Atmospheric and Solar-Terrestrial Physics*, *69*, 578–588, 2007.

Hines, C. O., Internal Atmospheric Gravity Waves at Ionospheric Heights, *Canadian Journal of Physics*, *38*, 1441–1481, 1960.

Hocking, W. K., A new approach to momentum flux determinations using SKiYMET meteor radars, *Annales Geophysicae*, *23*(7), 2433–2439, 2005.

Hocking, W. K., B. Fuller, and B. Vandepeer, Real-time determination of meteor-related parameters utilizing modern digital technology, *Journal Atmospheric and Solar-Terrestrial Physics*, *63*, 155–169, 2001.

Holton, J. R., The influence of gravity wave breaking on the general circulation of the middle atmosphere, *Journal of the Atmospheric Sciences*, *40*, 2497–2507, 1983.

Isler, J. R., and D. C. Fritts, Gravity-wave Variability and Interaction with Lower-Frequency motions in the Mesosphere and Lower Thermosphere over Hawaii, *Journal of the Atmospheric Sciences*, *53*(1), 37–48, 1996.

Jacobi, C., N. M. Gavrilov, K. D, and K. Frohlich, Gravity-wave climatology and trends in the mesosphere / lower thermosphere region deduced from low-frequency drift measurements 1984-2003 (52.1° n, 13.2° e), *Journal of Atmospheric and Solar-Terrestrial Physics*, *68*, 1913–1923, 2006.

Jacobi, C. H., et al., Climatology of the semidiurnal tide at 52 - 56°N from ground-based radar wind measurements 1985 - 1995, *Journal of Atmospheric and Solar Terrestrial Physics*, *61*, 975–991, 1999.

Jarvis, M. J., G. O. L. Jones, and B. Jenkins, Nwe initiatives in observing the antarctic mesosphere, *Advances in Space Research*, *24*(5), 611–619, 1999.

Jarvis, M. J., R. E. Hibbins, M. J. Taylor, and T. J. Rosenberg, Utilizing riometry to observe gravity waves in the sunlit mesosphere, *Geophysical Research Letters*, *30*(19), 1979–1982, 2003.

Kumar, K. K., T. M. Antonia, and S. T. Shelbi, Initial results from SKiYMET meteor radar at Thumba (8.5° n,77° e): Gravity wave observations in the MLT region., *Radio Science*, *42*, RS6009, 2007.

Lindzen, R. S., Turbulence and stress owing to gravity wave and tidal breakdown, *Journal Geophysical Research*, *86*(C10), 9707–9714, 1981.

London, J., Radiative Energy Sources and Sinks in the Stratosphere and Mesosphere, in *Proceedings of the NATO Advanced Study Institute on Atmospheric Ozone: Its Variation and Human Influences*, edited by A. A, pp. 703 – 721, 1980.

Lübken, F. J., Thermal Structure of the Artic summer meosphere, *Journal of Geophysical Research*, *104*(D8), 9135–9149, 1999.

Lübken, F. J., M. J. Jarvis, and G. O. L. Jones, First in situ temperature measurements at the antarctic summer mesopause, *Geophysical Research Letters*, *26*, 3584–3584, 1999.

Manson, A. H., and C. E. Meek, Dynamics of the middle atmsophere at Saskatoon (52°N, 107°W): a spectral study during 1981, 1982, *Journal of Atmospheric and Terrestrial Physics*, *48*(11-12), 1039–1055, 1986.

Manson, A. H., and C. E. Meek, Characteristics of gravity waves (10 min-6 hours) at Saskatoon (52°N, 107°W): observations by the phase coherent medium frequency radar, *Journal of Geophysical Research*, *98*(D11), 20,357–20,367, 1993.

Manson, A. H., C. E. Meek, and Q. Zhan, Gravity wave spectra and direction statistics for the mesosphere as observed by MF radars in the Canadian Prairies (49°N-52°N) and at Tromso (69°N), *Journal of Atmospheric and Solar-Terrestrial Physics*, *59*(9), 993–1009, 1997.

Manson, A. H., C. E. Meek, and G. E. Hall, Corrleations of gravity waves and tides in the mesophere over Saskatoon, *Journal of Atmospheric and Solar-Terrestrial Physics*, *60*, 1089–1107, 1998a.

Manson, A. H., C. E. Meek, and G. E. Hall, Correlations of gravity waves and tides in the mesosphere over Saskatoon, *Journal of Atmospheric and Solar-Terrestrial Physics*, *60*(11), 1089–1107, 1998b.

Manson, A. H., Y. Luo, and C. Meek, Global distributions of diurnal and semi-diurnal tides: observations from HRDI-UARS of the MLT region, *Annales Geophysicae*, *20*, 1877–1890, 2002a.

Manson, A. H., C. E. Meek, C. Hall, S. Nozawa, N. J. Mitchell, D. Pancheva, W. Singer, and P. Hoffmann, Mesopause dynamics from the scandinavian triangle of radars within the PSMOS-DATAR project, *Annales Geophysicae*, *22*(2), 367–386, 2004.

Manson, A. H., et al., Seasonal variations of the semi-diurnal and diurnal tides in the MLT: multi-year MF radar observations from 2-70 °N, modelled tides (GSWM, CMSM), *Annales Geophysicae*, *20*(5), 661–677, 2002b.

Mitchell, N. J., and V. S. C. Howells, Vertical velocities associated with gravity waves measured in the mesosphere and lower thermosphere with EISCAT VHF radar, *Annales Geophysicae*, *16*, 1367–1379, 1998.

Mitchell, N. J., P. J. S. Williams, A. G. Beard, G. R. Buesnel, and H. G. Muller, Non-linear Planetary/Tidal Wave Interactions in the Lower Thermosphere Observed by Meteor Radar, *Annales Geophysicae*, *14*(3), 364–366, 1996.

Mitchell, N. J., H. R. Middleton, A. G. Beard, P. J. S. Williams, and H. G. Muller, The 16-day planetary wave in the mesosphere and lower thermosphere, *Annales Geophysicae*, *17*, 1447–1456, 1999.

Mitchell, N. J., D. Pancheva, H. R. Middleton, and M. E. Hagan, Mean winds and tides in the Arctic mesosphere and lower thermosphere, *Journal of Geophysical Research*, *107*(A1), 1004, 2002.

Miyahara, S., and J. M. Forbes, Interactions between gravity waves and the diurnal tide in the mesosphere and lower thermosphere, *Journal of the Meteorological Society of Japan*, *69*, 523–531, 1991.

Moffat-Griffin, T., R. E. Hibbins, K. Nielsen, M. J. Jarvis, and M. J. Taylor, Observing mesospheric gravity waves with an imaging riometer, *Journal of Atmospheric and Solar-Terrestrial Physics*, *70*(10), 1327–1335, 2008.

Muller, H. G., The sheffield meteor wind experiment, *Quarterly Journal of the Royal Meteorological Society*, *96*, 195–213, 1970.

Muller, H. G., R. L. Havill, V. E. Comley, and P. C. J. Hill, A study of meteor radar winds from two locations in the british isles, *Journal of Atmospheric and Terrestrial Physics*, *57*(9), 979–993, 1995.

Murphy, D. J., and R. A. Vincent, Estimates of momentum flux in the Mesosphere and Lower Thermosphere over Adelaide, Austrailia, from March 1985 to February 1986, *Journal of Geophysical Research - Atmospheres*, *98*(D10), 18,617–18,638, 1993.

Murphy, D. J., and R. A. Vincent, Mesospheric momentum fluxes over Adelaide during the 2-day wave: Results and interpretation, *Journal of Geophysical Research-Atmospheres*, *103*(D22), 28,627–28,636, 1998.

Nakamura, T., T. Tsuda, S. Fukao, S. Kato, A. H. Manson, and C. E. Meek, Comparative observations of short-period gravity waves (10-100 min) in the mesosphere in 1989 by saskatoon mf radar (50° n), canada and the mu radar (35° n), japan, *Radio Science*, *28*(5), 729–746, 1993.

Nakamura, T., A. Higashikawa, and Y. Matsushita, Seasonal variations of gravity wave structures in OH airglow with a CCD imager at Shigaraki, *Earth, Planets and Space*, *51*, 897–906, 1999.

Nakamura, T., T. Tsuda, R. Maekawa, M. Tsutsumi, K. Shiokawa, and T. Ogawa, Seasonal variation of gravity waves with various temporal and horizontal scales in the MLT region observed with radar and airglow imaging, *Advances in Space Research*, *27*(10), 1737–1742, 2001.

Namboothiri, S. P., P. Kishore, Y. Murayama, and K. Igarashi, MF radar observations of terdiurnal tide in the mesosphere and lower thermosphere at Wakkanai (45.4°N,141.7°E), Japan, *Journal of Atmospheric and Terrestrial Physics*, *66*, 241–250, 2004.

Nielsen, K., et al., Propagation of short-period gravity waves at high-latitudes during the MaCWAVE winter campaign, *Annales Geophysicae*, *24*, 1277–1243, 2006.

Norton, W. A., and J. Thuburn, Sensitivity of mesospheric mean flow, planetary waves, and tides to strength of gravity wave drag, *Journal of Geophysical Research*, *104*(D24), 30,897–30,911, 1999.

Oznovich, I., R. L. Walterscheid, G. G. Sivjee, and D. J. McEwen, On krassovsky's ratio for ter-diurnal hydroxyl oscillations in the winter polar mesopause, *Planetary and Space Science*, *45*, 385–394, 1997.

Pancheva, D., Non-linear interactions of tides and Planetary waves in the Mesosphere and Lower Thermosphere: Observations over Europe, *Physics and Chemistry of the Earth*, *26*(6), 411–418, 2001.

Pancheva, D., et al., Global-scale tidal variability during the PSMOS Campaign of June-August 1999: Interaction with Planetary Waves, *Journal of Atmospheric and Solar Terrestrial Physics*, *64*(17), 1865–1896, 2002.

Pendelton, W. R. J., M. J. Taylor, and L. C. Gardner, Terdiurnal oscillations in OH Meinel rotational temperatures for fall conditions at northern mid-latitude sites, *Geophysical Research Letters*, *27*(12), 1799–1802, 2000.

Ratnam, M. V., T. Tsuda, C. Jacobi, and Y. Aoyama, Enhancement of gravity wave activity observed during a major Southern Hemisphere stratospheric warming by CHAMP/GPS measurements, *Geophysical Research Letters*, *31*(16), 2004.

Reid, I. M., and R. A. Vincent, Measurements of mesospheric gravity wave momentum fluxes and mean flow accelerations at Adelaide, Australia, *Journal of Atmospheric and Terrestrial Physics*, *49*, 443–460, 1987.

Salby, M. L., *Fundamentals of Atmospheric Physics*, vol. 61, Academic Press, 1996.

Sandford, D. J., H. G. Muller, and N. J. Mitchell, Observations of lunar tides in the mesosphere and lower thermosphere at Arctic and middle latitudes, *Atmospheric Chemistry and Physics*, *6*, 4117–4127, 2006.

Sandford, D. J., N. J. Mitchell, and R. A. Vincent, The lunar tides in the Arctic mesosphere and lower thermosphere, *Journal of Atmospheric and Solar Terrestrial Physics*, *69*(7-8), 2219–2237, 2007.

Singer, W., U. von Zahn, and J. Weiss, Diurnal and annual variations of meteor rates at the Arctic circle, *Atmospheric Chemistry and Physics*, *4*, 1355–1363, 2004.

Smith, A. K., Structure of the Terdiurnal Tide at 95 km, *Geophysical Research Letters*, *27*(2), 177–180, 2000.

Smith, A. K., and D. A. Ortland, Modelling and Analysis of the Structure and Generation of the Terdiurnal Tide, *Journal of Atmospheric and Solar Terrestrial Physics*, *58*(21), 3116–3134, 2001.

Snively, J. B., V. P. Pasko, M. J. Taylor, and W. K. Hocking, Doppler ducting of short-period gravity waves by midlatitude tidal wind structure, *Journal of Geophysical Research*, *112*, A03,304, doi:10.1029/2006JA011895, 2007.

Tang, J., A. Z. Liu, and G. R. Swenson, High frequency gravity waves observed in OH airglow at Starfire Optical Range, NM- Seasonal variations in momentum flux, *Geophysical Research Letters*, *29*(20), 2002.

Taylor, M. J., Bouyancy and bouyance waves - optical observations, in *Encyclopedia of Atmospheric Sciences*, vol. 1, edited by J. R. Holton, J. A. Curry, and J. A. Pyle, pp. 323–330, Academic Press, 2002.

Taylor, M. J., E. H. Ryan, T. F. Tuan, and R. Edwards, Evidence of the Preferential Directions for Gravity Wave Propagation Due to Wind Filtering in the Middle Atmosphere, *Journal of Geophysical Research*, *98*(A4), 6047–6057, 1993.

Teitelbaum, H., and F. Vial, On tidal variability induced by nonlinear-interaction with planetary waves, *Journal of Geophysical Research*, *96*(A8), 14,169 – 14,178, 1991.

Teitelbaum, H., F. Vial, A. H. Manson, R. Giraldez, and M. Masseboeuf, Nonlinear interaction between the diurnal and semidiurnal tides: Terdiurnal and diurnal secondary waves, *Journal of Atmospheric and Terrestrial Physics*, *51*(7/8), 627–634, 1989.

Thayaparan, T., The terdiurnal tide in the mesosphere and lower thermosphere over London, Canada (43°N 81°W), *Journal of Geophysical Research*, *102*(D18), 21,695–21,708, 1997.

Thayaparan, T., W. K. Hocking, and J. MacDougall, Observational evidence of tidal / gravity wave interactions using the UWO 2 MHz radar, *Geophysical Research Letters*, *22*(4), 373–376, 1995.

Thomas, G. E., Global change in the mesosphere-lower thermosphere region: Has it already arrived?, *Journal Atmospheric and Solar-Terrestrial Physics*, *58*, 1629–1656, 1996.

Thorsen, D., and S. J. Franke, Climatology of mesospheric gravity wave activity over Urbana, Illinois (40 °N, 88 °W), *Journal of Geophysical Research - Atmospheres*, *103*(D4), 3767–3780, 1998.

Tsuda, T., Y. Murayama, T. Nakamura, R. A. Vincent, A. H. Manson, C. E. Meek, and R. L. Wilson, Variations of the gravity wave characteristics with height, season and latitude revealed by comparative observations, *Journal of Atmospheric and Terrestrial Physics*, *56*(5), 555–568, 1994.

Vial, F., Causes of tidal variability, in *Coupling processes in the lower and middle atmosphere*, edited by E. V. Thrane, T. A. Blix, and D. C. Fritts, pp. 137–152, Kluwer Academic, 1993.

Vincent, R. A., Gravity-wave motions in the mesosphere and lower thermosphere observed at Mawson, Antarctica, *Journal of Atmospheric and Terrestrial Physics*, *56*(5), 593–602, 1994.

Vincent, R. A., and D. C. Fritts, A Climatology of Gravity Wave Motions in the Mesosphere Region at Adelaide, Australia, *Journal of the Atmospheric Sciences*, *44*(4), 1987.

von Zahn, U., and J. Höffner, The mesopause altitude: only two distinctive levels worldwide?, *Geophysical Research Letters*, *23*, 1996.

Walterscheid, R. L., Inertio-gravity wave induced accelerations of mean flow having an imposed periodic component: Implications for tidal observations in the meteor region, *Journal Geophysical Research*, *86*(C10), 9698–9706, 1981.

Williams, B. P., M. A. White, D. A. Krueger, and C. Y. She, Observation of a large amplitude wave and inversion layer leading to covective instability in the mesopause region over fort collins, CO (41°N, 105°W), *Geophysical Research Letters*, *29*(17), 1850–1854, doi:10.1029/ 2001GL014514, 2002.

Williams, B. P., D. C. Fritts, and R. A. Goldberg, Gravity Wave propagation through a large semidiurnal tide and instabilities in the mesosphere and lower thermosphere during the winter MaCWAVE rocket campaign, *Annales Geophysicae*, *24*, 1199–1208, 2006.

Wu, D. L., P. Preusse, S. D. Eckermann, J. H. Jiang, M. de la Torre Juarez, L. Coy, and D. Y. Wang, Remote sounding of atmospheric gravity waves with satellite limb and nadir techniques, *Advances in Space Research*, *37*, 2267–2277, 2006.

Wu, Q., N. J. Mitchell, T. L. Killeen, S. C. Solomon, and P. T. Younger, A high-latitude 8-hour wave in the mesosphere and lower thermosphere, *Journal of Geophysical Research - Space Physics*, *110*(A9), 2005.

Younger, P. T., D. Pancheva, H. R. Middleton, and N. J. Mitchell, The 8-hour tide in the Arctic mesosphere and lower thermosphere, *Journal of Geophysical Research*, *107*, 1420, 2002.